AEROELASTIC ANALYSIS OF COMPOSITE WINGS AND WIND TURBINE BLADES INCLUDING GEOMETRICAL NONLINEARITY AND COMPRESSIBILITY

A THESIS SUBMITTED TO
THE GRADUATE SCHOOL OF NATURAL AND APPLIED SCIENCES
OF
MIDDLE EAST TECHNICAL UNIVERSITY

BY

TOURAJ FARSADI

IN PARTIAL FULFILLMENT OF THE REQUIREMENTS
FOR
THE DEGREE OF DOCTOR OF PHILOSOPHY
IN
AEROSPACE ENGINEERING

APRIL 2018

Approval of the thesis:

AEROELASTIC ANALYSIS OF COMPOSITE WINGS AND WIND TURBINE BLADES INCLUDING GEOMETRICAL NONLINEARITY AND COMPRESSIBILTY

submitted by **TOURAJ FARSADI** in partial fulfillment of the requirements for the degree of **Doctoral in Aerospace Engineering Department, Middle East Technical University** by,

Prof. Dr. Halil Kalıpçılar
Dean, Graduate School of **Natural and Applied Sciences** _____

Prof. Dr. Ozan Tekinalp
Head of Department, **Aerospace Engineering** _____

Prof. Dr. Altan Kayran
Supervisor, **Aerospace Engineering Dept., METU** _____

Examining Committee Members:

Prof. Dr. Ismail Hakkı Tuncer
Aerospace Engineering Dept., METU _____

Prof. Dr. Altan Kayran
Aerospace Engineering Dept., METU _____

Prof. Dr. Levend Parnas
Mechanical Engineering Dept.,
TED University _____

Assoc. Prof. Dr. Ender Ciğeroğlu
Mechanical Engineering Dept., METU _____

Asst. Prof. Dr. Mustafa Kaya
Aeronautical Engineering Dept.,
Ankara Yıldırım Beyazıt University _____

Date: 19/04/2018

I hereby declare that all information in this document has been obtained and presented in accordance with academic rules and ethical conduct. I also declare that, as required by these rules and conduct, I have fully cited and referenced all material and results that are not original to this work.

Name, Last name : TOURAJ FARSADI

Signature :

ABSTRACT

AEROELASTIC ANALYSIS OF COMPOSITE WINGS AND WIND TURBINE BLADES INCLUDING GEOMETRICAL NONLINEARITY AND COMPRESSIBILTY

Farsadi, Touraj
Ph.D., Department of Aerospace Engineering
Supervisor : Prof. Dr. Altan Kayran

April 2018, 333 pages

Aeroelastic behaviour of composite wings and wind turbine blades in the incompressible and compressible flow regimes is investigated utilizing a geometrically nonlinear Thin Wall Beam (TWB) theory incorporating non uniform geometric features such as sweep, taper, pretwist, warping inhibition and transverse shear strain. The structural equations of motion are obtained in the most general form based on the kinematic relations governing thin walled beams, including the nonlinear strain displacement relations, and utilizing the principles of analytical dynamics. Unsteady aerodynamic loads in the incompressible and compressible flow regime are expressed using indicial functions in the time-domain. The aeroelastic system of equations is augmented by the differential equations governing the aerodynamics lag states to come up with the final coupled fluid-structure equations of motion. Time response of the nonlinear aeroelastic system is obtained via the Runge-Kutta direct integration algorithm.

The effect of the compressibility on the flutter characteristics of aeroelastically tailored bend-twist coupled (BTC) composite blades designed for the MW sized wind turbine is investigated. Flutter analyses are performed for the baseline blade and the BTC

blades designed for the MW sized wind turbine. Beam model of the blade is developed by making analogy with the structural model of the prewisted rotating TWB and utilizing the Variational Asymptotic Beam Section (VABS) method for the calculation of sectional properties of the blades designed. To investigate the effect of compressibility on the flutter characteristics of the wind turbine blades, aeroelastic analyses are performed in frequency and time domain utilizing both incompressible and compressible unsteady aerodynamics via indicial function approach.

Keywords: Composite wing; Composite wind turbine blade; Aeroelastic instability; Flutter; Compressibility; Bending-twisting coupling; Limit cycle oscillation (LCO)

ÖZ

GEOMETRİK DOĞRUSALSIZLIK VE SIKIŞTIRILABİLİRLİK İÇEREN KOMPOZİT KANAT VE RÜZGAR TÜRBİN KANATLARININ AEROELASTİK ANALİZİ

Farsadi, Touraj
Doktora, Havacılık ve Uzay Mühendisliği Bölümü
Tez Yöneticisi : Prof. Dr. Altan Kayran

Nisan 2018, 333 sayfa

Kompozit kanatlar ve rüzgar türbin kanatlarının sıkıştırılabilir ve sıkıştırılamaz akış rejimlerindeki aeroelastik davranışları, ok açısı, sivrilme, ön burulma, eğrilme engelleme ve enine kesme gerinimi gibi geometrik özellikleri bünyesinde barındıran geometrik olarak doğrusal olmayan ince cidarlı kiriş (TWB) teorisi kullanılarak incelenmştir. Yapısal hareket denklemleri, ince cidarlı kirişler için geçerli, doğrusal olmayan gerinim – yer değiştirme etkileşimlerini içeren ve analitik dinamiğin ilkelerini kullanan kinematik ilişkilerin üzerine kurulu en genel biçimde elde edilmiştir. Sıkıştırılamaz ve sıkıştırılabilir akış rejimindeki kararsız aerodinamik yükler, zaman bölgesinde indisiyel fonksiyonlar kullanılarak ifade edilmiştir. Aeroelastik denklemler sistemi, akışkan – yapısal bağlaşık hareket denklemlerine ulaşmak için, aerodinamik gecikme durumlarını yöneten diferansiyel denklemlerle genişletilmiştir. Doğrusal olmayan aeroelastik sistemin zamana bağlı cevabı, Runge-Kutta doğrudan integrasyon algoritması ile elde edilmiştir.

Sıkıştırılabilirliğin, MW kapasiteli rüzgar türbini için tasarlanmış, aeroelastik olarak uyarlanmış eğilme-burulma etkileşimine sahip (BTC) kompozit kanatların çırpma karakteristikleri üzerindeki etkisi incelenmiştir. MW türbin için tasarlanan referans kanat ve BTC kanatların çırpma analizleri gerçekleştirilmiştir. Kanadın kiriş modeli,

ön burulmalı döner ince cidarlı kirişin yapısal modeli ile benzeşim yapılarak ve tasarlanmış kanatların kesitsel özelliklerinin hesaplanması için varyasyonel asimtotik kiriş kesiti (VABS) metodu kullanılarak geliştirilmiştir. Sıkıştırılabilirliğin rüzgar türbin kanatlarının çırpma karakteristikleri üzerindeki etkisini incelemek için, indisiyel fonksiyon yaklaşımı yoluyla hem sıkıştırılamaz hem de sıkıştırılabilir kararsız aerodinamik kullanılarak, frekans ve zaman bölgelerinde aeroelastik analizler gerçekleştirilmiştir.

Anahtar kelimeler: Kompozit kanat; Kompozit rüzgar türbin kanadı; Aeroelastik kararsızlık; Çırpma; Sıkıştırılabilirlik; Eğilme-burulma bağlaşımı; Limit çevrim salınımı

To my family

ACKNOWLEDGMENTS

First and foremost, I would like to thank my supervisor Prof. Dr. Altan Kayran for his constant support, guidance, and patience for the last four years.

I would like to thank Professor Ismail Hakkı Tuncer and Professor Ender Ciğeroğlu for their helpful and effective comments during thesis progress meetings. Professor Demirkan Çöker assisted me to stay motivated through hard times that I truly appreciate.

I would also like to thank my office mates from METUWind: Mustafa Sahin, Can Muyan, Aydin Amireghbali, Miraç Onur Bozkurt, Ahmet Çevik, Özgün Şener, Onur Çakmak and Oğuz Atalay for their companionship and understanding throughout the time we have shared together.

I would like to thank Dr. Mohammad Rahmanian for his willingness to help, our insightful discussions and fruitful collaborations specially in the case of nonlinear aeroelasticity.

I want to express my gratitude for the dearest people who made me who I am. I am deeply indebted to my beloved mother, father and sister for their continuous support and positive attitude in my time of life.

I would like to express my deepest gratitude to Nardin Avishan, for her company during my graduate study. Her love and the happiness she brings to my life give me the strength to work hard and reach for my goals.

TABLE OF CONTENTS

LIST OF TABLES

TABLES

LIST OF FIGURES

FIGURES

NOMENCLATURE

AR	Aspect ratio
$A_{ij}, \mathrm{B}_{ij}, \mathrm{D}_{ij}, \mathrm{F}_{ij}, \mathrm{H}_{ij}$	first and higher order stiffness coupling coefficients
a_{ij}	1-D stiffness coefficients (Eqn. (2-89))
BTC	Bend-Twist coupling
B_w, Λ_z	Bimoment and higher order stress couple
b_i	mass density of the wing per unit span
b, l, d, h, L	Half chord, width, heigth, thickness, length
b_w	bimoment of the external force per unit span
C_{ij}	elastic modulus of the material
$C_{L\phi}$	local lift curve slope
CAS	circumferentially asymmetric stiffness, lay-up configuration
CUS	circumferentially uniform stiffness, lay-up configuration
GFRP, CFRP	glass fibre reinforced plastic, carbon fibre reinforced plastic
D/Dt	derivative with respect to dimensional time
E_i, G_{ij}	Young's moduli of orthotropic materials
F_w	measure of primary warping function
F_C	Centrifugal force
$H(\tau)$	Heaviside's step function

I_i, f_i	Inertia terms, centrifugal effect terms
K_{ij}	reduced stiffness coefficients (Eqn. (2-35))
L_{ae}, T_{ae}	Unsteady aerodynamic lift and moment
$L_{zz}, L_{sz}, N_{zz}, N_{sz}, \Gamma_{zz}$	Stress resultants
M	Mach number
M_x, M_y, M_z	1-D stress couples
M_s, C_s, K_s	Structural mass, damping and stiffness matrices
M_{ae}, C_{ae}, K_{ae}	aerodynamic mass, damping and stiffness matrices
m_l	Number of modes shape
n	Number of aerodynamic lag terms
N	Number of trial functions
$N^2_{u,v,w,x,y,\phi}, \quad N^3_{u,v,w,x,y,\phi}$	Second and third order nonlinear terms
PSD	power spectral density
Q_x, Q_y, Q_z	shear forces in *x, y, z* directions
R_0	Root to hub length
$R^{u,v,w,x,y,\phi}, \quad L^{u,v,w,x,y,\phi}$	right eigenvectors, left eigenvectors
s, z, n	Local coordinate system
TWB	Thin wall beam
T, V, V_{cf}, W	kinetic energy, internal elastic potential and work of external forces, respectively

T, V, V_{cf}, W	kinetic energy, internal elastic potential and work of external forces, respectively
T_z	generalized beam axial force
t, t_0, τ	dimensional; non-dimensional time variables
U_r, U_i	Relative speed, inflow speed
U_n	Normal wind speed
u_0, v_0, w_0	rigid body translations along *x, y, z* directions measured from shear center
θ_x, θ_y, ϕ	rotations of the cross section with respect to *x, y, z* axes
$\dot{X}, \ddot{X}$	$\frac{\partial X}{\partial t}, \frac{\partial^2 X}{\partial t^2}$
X', X''	$\frac{\partial X}{\partial z}, \frac{\partial^2 X}{\partial z^2}$
X, Y, Z	Inertial coordinate system
x, y, z	Rotating coordinate system
x^p, y^p, z^p	Curvilinear coordinate system
x_{ae}, z_{ae}	Aerodynamic coordinate system
$\alpha_{ic}, \alpha_{icq}, \alpha_{icM}, \alpha_{icMq}$	Indicial Mach dependent coefficients
β_i	Indicial Mach independent coefficients
γ_{zy}, γ_{zx}	transverse shear measures of the cross section
γ_0, γ_w	vortex on the blade surface, vortex on the blade wake
δ	operator of variation
$\varepsilon_{zz}^0, \varepsilon_{zz}^1, \varepsilon_{zz}^2$	on and off-contour axial normal strains, respectively

θ	Fiber angle
λ_r, w_r, G_r	r[th] eigenvalue, natural frequency and eigenfunction
Λ	Sweep angle
$\nu_{12},\nu_{13},\nu_{23}$	Poisson ratio
ρ_∞	mass density of the free stream
$\rho_{(k)}$	mass density of the k[th] layer
$\varepsilon_{ij}, \sigma_{ij}$	strain and stress components
σ_l, σ_d	Width and height taper ratio
ϕ_W	Wagner's function
$\phi_c, \phi_{cq}, \phi_{cM}, \phi_{cMq}$	Compressible plunging and pitching lift and moment indicial functions
$\eta^u,\eta^v,\eta^w,\eta^x,\eta^y,\eta^z$	time dependent variables
$\psi^u, \psi^v, \psi^w, \psi^x, \psi^y, \psi^z$	Trial functions
$w_{0.5c}, w_{0.75c}$	downwash at the semi-chord, three quarter chord, respectively
β, β_0	Pretwist angle along the beam span, pretwist at root section
Ψ	torsional function
Ω	Rotating speed
$\oint_C$	Integral operator around the cross section

CHAPTER 1

INTRODUCTION

1.1 Wind Turbines

Wind turbines are machines that convert wind's kinetic energy to rotary mechanical energy, resulting in the production of electricity. The first wind turbines were windmills that were used for the purpose of grinding in ancient Persia around 900 A.D. At the end of the 19th century, people started to generate electricity from the wind turbines and today, 4% [1] of the total electricity in the world is generated from wind turbines. Small wind turbines are used to recharge batteries and illuminate lamps where the larger ones in the industry are used to supply electricity.

In the wind turbine industry, the energy required from wind turbines has risen due to the increased demand for renewable energy. Blades are one of the main components responsible for the power produced. In order to obtain higher power from the turbines, the necessity of optimum control of the pitch angle and the increase in the length of the blades have boosted. The newly designed wind turbine blades have already reached the 100 meter border as shown in Figure 1-1. Due to the increase in the length, the weight of the blades increase. Moreover, active control mechanism for the pitch angle requires feedback system and mechanical parts to be installed on the blades which result in additional cost and weight. Longer blades necessitate better optimized blade structures which bring about challenges to the design process to develop innovative design solutions.

Higher energy extraction from wind turbine systems requires larger turbines, with blades in the border of 100 m, and associated optimized structural and mechanical components to accomplish improved stiffness, increased fatigue life, and reliability. To attain these goals, loads that occur due to the aeroelastic effects on the wind turbine blades must be reduced. This can also be achieved passively by utilizing anisotropy of composite materials. Due to the anisotropic behavior of composite materials, aeroelastic tailoring of the rotor blades as a passive control mechanism can be succeeded. Induced twist due to bending on the blades which occurs as a result of anisotropic behavior of composite materials as a passive control mechanism may reduce the loads in the whole wind turbine system [2-7].

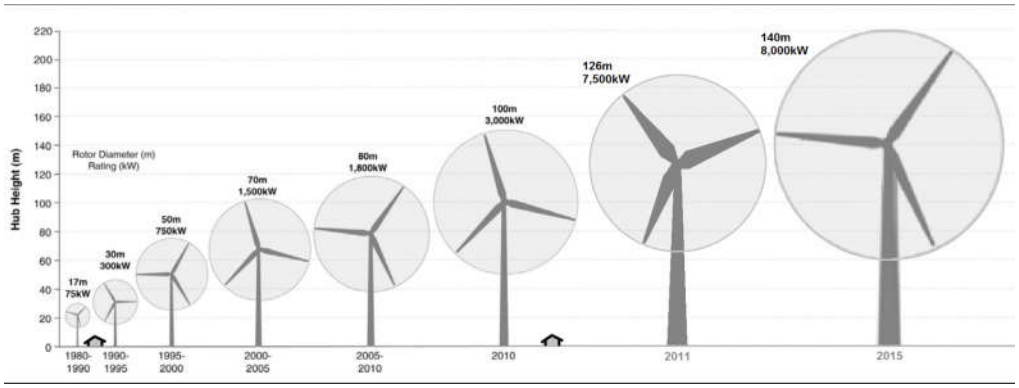

Figure 1-1 Wind turbine size increase 1980-2015, showing relative size of the swept area, as turbine size increased from 75 kW to 8 MW [8]

Aeroelasticity of Wind Turbine Blade Aeoroelasticity is the interaction of elasticity, inertia and aerodynamic loads. Elastic structures can be deformed by the external aerodynamic loads. On the other hand, the structural deformations change the aerodynamic loads. This interplay between the structural deformation and the aerodynamic loads leads to sophisticated physical problems. Several types of structures are exposed to aeroelastic phenomena due to the elasticity of the structure and airflow passing around the body. Bridges, tall buildings, aircraft wings, turbo-machinery and wind turbines all encounter aeroelastic instability. The nature of the aeroelasticity is either steady (static) aeroelasticity or dynamic aeroelasticity. The

static aeroelasticity studies only the steady interaction between elasticity and aerodynamic loads whereas dynamic aeroelasticity considers time dependent response of elastic structures and includes the inertia forces as well. Instabilities investigated under the static aeroelasticity mainly involve divergence and control surface reversal. Aerodynamic loads acting on lifting surface cause deflection in the structure. With the increase in applied loads, the twist increases. The increased loads deform the structure further, finally taking it to its critical load and complete failure.

The phase difference between the deformations of the structure and the aerodynamic loads causes energy absorption by the structure from the air. The energy transmission from aerodynamic loads to the structure may result in oscillations with growing amplitude. The worst case scenario is the failure of the structure. Flutter instability is a kind of dynamic aeroelasticity which involves flapwise and torsional modes of structure. For wind turbine blades these modes are shown in Figure 1-2,

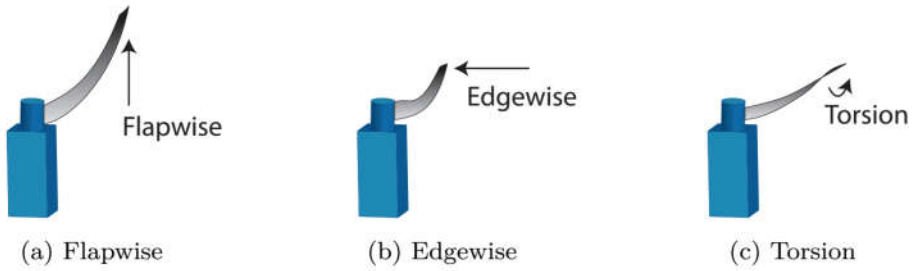

Figure 1-2 Degrees of freedom of a blade [9]

Classical flutter is a dynamic aeroelastic instability generated by coupling of torsion and flapwise deformations. When classical flutter arises, time response grows exponentially till the failure. Classical flutter is well known in aerospace and civil engineering. Occurrence of the classical flutter event has not been reported for commercial wind turbine so far. With an increase in length of wind turbine's blade in the future wind turbines, it is more likely to happen [9].

For large wind turbine's blade in low angle of attacks and attached flow, the classical flutter becomes a serious danger. It is recommended by [10] to include classical flutter

calculations in the preliminary design for 50 m blades and above due to decrease in the flapwise and the torsional stiffness.

Obtaining accurate and efficient aerodynamic models has been an important goal of research efforts in wind turbine industry over the past years. Aerodynamic models are necessary to design the wind turbine blade, to evaluate aeroelastic stability and the response. The unsteady aerodynamics provides a good level of accuracy in prediction of the flutter rotational speeds of the wind turbine blade when the correct models with both circulatory and non-circulatory components are employed [11]. Among the wide range of unsteady aerodynamic models in the literature the classical models of Theodorsen in frequency domain and its time domain counterpart, indicial aerodynamics remain widely used and provide a benchmark for the linear models both in fixed and rotary blades. Several studies have been conducted with the use of these approaches to investigate the aeroelastic characteristics of the wind turbine blades [12-20].

Janetzke [21] at the NASA Lewis Research Centre published the first paper directly related to the aeroelasticity of the wind turbine. Kooijman [22] indicated that the aeroelastic tailoring technique is promissory in the wind turbines rotor blade designs. Lobitz [23] utilized aeroelastic tailoring of the blades to shape the power curve and reduce load. Chaviaropoulos et al. [24] addressed flapping-edgewise coupling effects on the aeroelasticity of the wind turbine blade using viscous CFD techniques.

Lobitz [12] conducted one of the pioneer works to address the classical flutter instability phenomenon in a small size wind turbine blade system. Later, Lobitz [13] investigated the flutter limit of a MW sized wind turbine blade based on isolated blade. In this study, it is shown that the predicted flutter rotational speed of the blade using quasi-steady aerodynamics is lower than the flutter rotational speed obtained using unsteady Theodorsen aerodynamics. Owens et al. [14] performed an examination on the very large wind turbine blade's flutter problem. In this work, BLAST tool, which is a program based on FE model and Theodorsen's unsteady theory in MATLAB, is used to investigate the aeroelastic stability of a turbine blade. The p-k iteration method is employed to estimate instability boundaries of the aeroelastic system. Owens and

Griffith [15] employed Theodorsen unsteady airfoil aerodynamic theory to predict the aeroelastic instability boundaries of a large sized vertical axis wind turbine blade. The aeroelastic characteristics of the bend-twist coupled blade model in a linear state space formulation using frequency response diagrams are investigated by Stablein et al. [16]. The 2D linear blade section structural mode with 3 degree of freedom (flapwise, torsion and edgewise) is derived by means of Lagrange's theory while the Theodorsen's unsteady aerodynamic model in time domain is coupled with the structure model. Pourazarm et al. [17,18] predicted the dynamic instability onset of three different MW sized wind turbine blade WindPACT 1.5 MW, NREL 5 MW and SNL 100-00. The coupled bending-torsion simple continuous beam formulations subjected to Theodorsen's unsteady aerodynamic model are derived and solved using the Galerkin method. It is found out that the torsional natural frequency has the highest impact on the instability speed. The ratio of the torsional natural frequency to the flapwise natural frequency is brought up as a major blade design parameter to deal with the occurrence of the risk of the structural dynamic instability.

Jeong et al. [19] investigated the effect of torsional stiffness on aeroelastic instability of a large horizontal axis wind turbine. A finite element method based on the large deflection beam theory and Greenberg's extension of Theodorsen's aerodynamic strip theories are integrated in an aeroelastic system. For the stability analysis, a proposed aerodynamic approach was employed in conjunction with a structural model. They claimed that a low torsional stiffness of the wind turbine blade considerably affects the possibility of classical flutter instability. Buhl et al. [20] studied the passive suppression of the wind turbine blade's aeroelastic instability. They showed that the critical relative wind speed can be significantly improved with the increase of the blade torsional frequency. Hayat et al. [25,26] studied the flutter performance of large bend-twist coupled wind turbine blade in time domain. Aerodyn/ADAMS commercial code is used to verify the flutter results. It is shown that reduction in torsional stiffness results in a decrease in the flutter rotational speed.

Vatne [27] studied the aeroelastic instabilities of a 10 MW wind turbine blade using aeroelastic stability tool HAWCStab2 in time domain. Analysis has been performed in

two cases; isolated blade and entire wind turbine analysis. Results showed that the flutter rotational speed is slightly higher in the isolated blade analysis compared with the entire turbine analysis, but the results are close enough to avoid total turbine investigation due to the complexity.

In order to enhance the performance and aeroelastic characteristics of the rotary blades of wind turbine systems, pretwist is applied to the blades during the manufacturing. Pretwist which varies from the root of the blade to the tip of the blade is also called as geometric twist. An experimental aeroelastic analysis including geometric nonlinearity and pretwist effects are performed by Ladge et al. [28] on a small-scale wind turbine. It is seen that with the increase in twist angle by 35%, flutter rotational speed increased by 23%. Li et al. [29] studied the aeroelastic stability of the wind turbine blade considering bending-twist coupling and composite thin walled beam with pretwist in the structural model. The governing system of equations have been solved by the Galerkin method and time –marching approach. The time response analysis is performed for the wind speed of 20 m/s, ply angle of 30° for three pretwist angles; $0^{\circ}, 5^{\circ}$ and 10°. Results showed that by increasing the pretwist angle, response amplitude decreases and aeroelastic stability improves significantly.

In the case of computational aeroelasticity instability analysis of wind turbine blades, Yu and Kwon [30] numerically examined the aeroelastic response of a turbine blade using combined CFD-CSD method. Due to the aeroelastic torsional deformation, the aerodynamic loads on the blade are considerably increased. Baxevanou et al. [31] studied the classical flutter of the wind turbine airfoil using incompressible Navier–Stokes CFD solver.

Formerly, wind turbines were often analysed using incompressible aerodynamic models. But nowadays, compressibility effect becomes a significant factor in investigating the aeroelastic instability of wind turbine blades due to the increase in the size of the blade and higher tip speed ratio [32]. For the 5 MW and higher MW wind turbines, the tip speed at flutter point could exceed Mach number of 0.3 and compressibility effects cannot be ignored. So far, many CFD based analysis have been

performed to study the aeroelastic analysis of wind turbine using Navier Stokes subsonic compressible equations [33-35]. Almost all of them emphasized that in order to increase the accuracy of the aerodynamic model of the MW sized wind turbines, considering compressibility effects is inevitable. The nature of the method is not well-matched for wind turbine applications, due to the low Mach numbers around the blade root where the flow is usually incompressible. Some remedies such as preconditioned and artificial compressibility methods have been reported to deal with this problem which may increase the cost of computations and complexity of the simulation [36].

For a fixed wing, compressibility has a significant influence on the classical flutter speed such that at high subsonic speeds (M=0.7), compressibility can yield a drop of the flutter speed by about 45%. [37]. Sina and Farsadi [38], Farsadi [39] developed novel exponential approximation of indicial aerodynamic functions in the subsonic compressible flow regime.

1.1.1 Composite Thin Walled Beam

For the preliminary investigation of the aeroelasticity of the wind turbine blade, the simplified structure can be useful. Box structure of wind turbine blades and aircraft wings shown in Figure 1-3, is the load carrying part and in a conservative way it can be assumed that almost all the aerodynamic loads are resisted by the box beam. Thus, the structural design of box beam is very crucial in designing aircraft wings and wind turbine blades. Box beam structure can be considered as a TWB. TWB structures have found their extensive applications in a variety of engineering products such as aircraft wings, helicopter blades, wind turbine blades, tilt rotor aircrafts, space deployable antennas and turbo machinery/jet engine components. In fact, the design of flight vehicle structures is mainly based on the principles of thin walled beams [40]. The cross section of TWBs is made up from thin panels connected among themselves to create closed or open cross sections of a beam. From the strength of materials perspective, TWBs have a higher gyration radius and hence provide higher bending

stiffness to weight ratios compared with the traditional solid beams. Their structural efficiency may be even further improved by proper composite laminations.

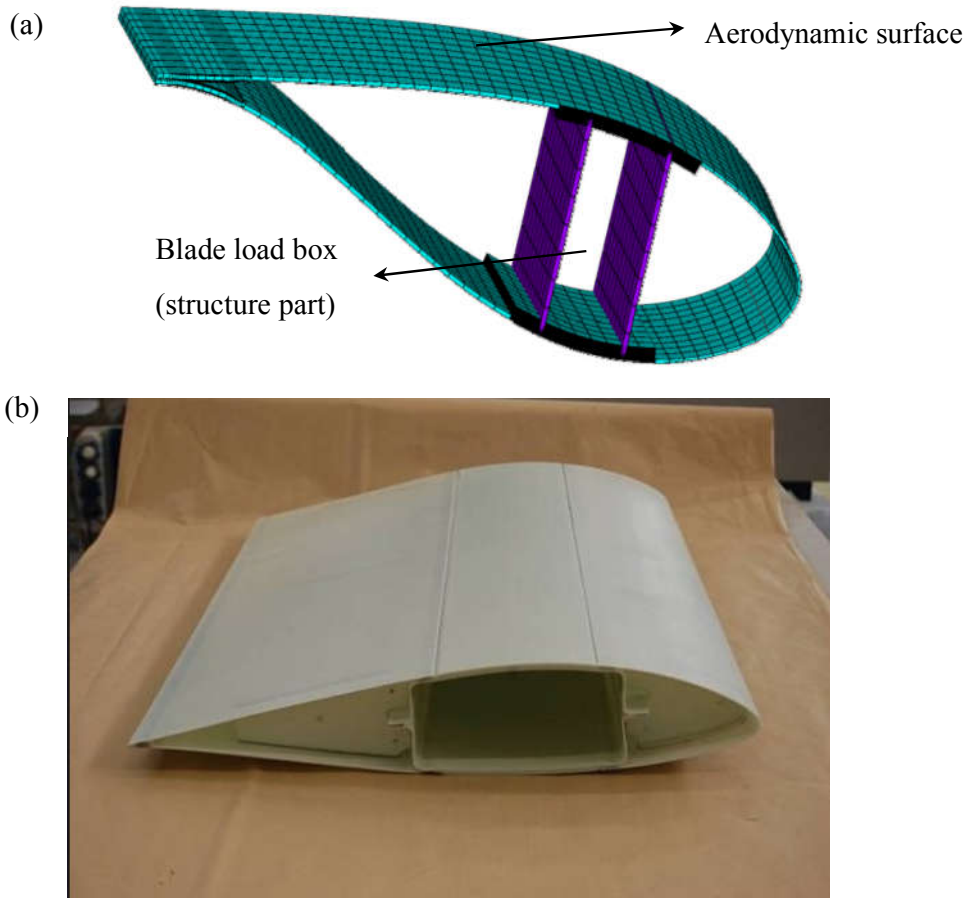

Figure 1-3 (a) Wind turbine blade and (b) aircraft wing cross section [41]

Composites provide the best specific stiffness (stiffness to weight) and specific strength (strength to weight), compared with nearly all modern materials. They also provide the possibility to perform aeroelastic tailoring to get the exact mechanical properties. Consequently, by using TWB structures wisely, the structural efficiency can be maximized. A most spectacular product of this technology is the possibility to eliminate, without weight penalties, the occurrence of the chronic aeroelastic

divergence instability that has prevented for a long time the use of swept-forward wings in aircraft such as the Grumman X-29 swept-forward wing experimental aircraft [42].

Having maximized the structural efficiency, the overall weight is minimized. This fact has led to extensive research studies to determine the critical loading/working conditions and bottlenecks of a design. The literature in this field is too vast to review hence only a few major studies are mentioned in this section. Both isotropic and composite material models are sufficiently studied. The key point in the studies of composite TWBs is that they exhibit significant non-classical effects, which include transverse shear, warping restraint, three-dimensional strain effect and contour-wise shear stiffness variations.

A comprehensive theory to deal with TWB was first developed in the late thirties by Vlasov [43]. Timoshenko [44,45] and later Gjelsvik [46] has extended the theory to include other complicating effects. Specifically speaking, Vlasov [43] introduced the concept of cross sectional primary warping by using a new variable, being the rate of twist along the beam; Timoshenko [44] obtained a general theory of TWB with open cross-section and then introduced the effect of shear transverse strain as a new kinematic variable [45]; and Gjelsvik [46] extended the theory to take into account both open and closed cross-section cases and incorporated the secondary warping effect for the first time. Several scientists have then contributed to evolving the theory of TWBs [47-52] to include single/multicellular configurations, composite lamination tailoring, transverse shear effects, open/closed cross sections and other complicating effects. A higher-order shear deformation theory for the static and dynamic analysis of thin-walled composite beams of arbitrary lay-up and cross section was also presented by J.K. Suresh et al. [53] . Z. Qin and L. Librescu [54] then proposed a refined model to account for the three-dimensional strain effect and non-uniformity effect of the contour-wise shear stiffness which are significantly effective in laminated composite beams. The model was later validated by the same authors for three distinct layup configurations [55]. The comprehensive book by L. Librescu and O. Song [56] gives

a full description of the governing equations of motion and their solution methodologies.

Nonlinear formulations to the problems of TWBs have also been reported in the literature both for isotropic [57-59] and laminated structures [60]. K. Bhaskar and L. Librescu [60] followed a systematic approach based on the Lagrangian description and Hamilton's principle to formulate the geometrically nonlinear theory. Their theory accounts for anisotropy, transverse shear deformation, constrained warping and bending stiffness of the beam-wall. Wang and Qin [61], performed nonlinear analysis of composite thin walled beams in the presence of simultaneous 1:2 internal and 1:1 external resonance. Their solution method is based on the extended Galerkin method and the method of multiple scales. The saturation and jump phenomena are well discussed and verified with the commercial code ABAQUS.

1.1.2 Aeroelasticity of Composite Thin Walled Beam

Due to the applicability of TWBs in aerospace vehicles and the importance of aeroelastic stability in the design of long wind turbine blades and modern flexible aircraft, a great deal of studies is devoted to the aeroelastic investigation of wings and blades structurally modeled as beams or TWBs. The first studies regarding this issue were published by L. Librescu et al. [62-66], Hong et al. [67] and Cesnik et al. [68]. In the latter study by Cesnik et al. [68], aeroelastic stability of high aspect ratio composite wings is performed. The structural model is based on an asymptotically correct cross-sectional formulation and a nonlinear geometric exact beam analysis. For the aerodynamic model, the 2-D unsteady inflow finite-state theory as well as the Theodorsen's theory are implemented. Z. Qin and L. Libresccu [69] incorporated the effects of transverse shear, material anisotropy, warping inhibition, and rotatory inertia in the structural modeling of an aircraft wing and utilized the unsteady incompressible aerodynamic model in the time domain according to the concept of indicial functions. Aeroelastic instability of aircraft wings by a composite TWB model is further studied by Z. Qin and L. Librescu [70]. They employed the incompressible unsteady aerodynamics using an indicial formulation. Haddadpour et al. [71] have also

performed aeroelastic analysis of anisotropic TWBs which represent aircraft wings. Unsteady incompressible aerodynamics is modeled in the time domain by the Wagner's function approximation. Na et al. [72] have provided a more comprehensive model, including active aeroelastic control of TWBs under specific loading conditions. They used an indicial formulation, being typical in compressible flow problems, to approximate the unsteady compressible aerodynamic loading in the time domain. The extensive research papers in the field of rotating composite beams have been reviewed in depth by Li [73] and Chakravarty [74,75]. Li et al. [73] proposed an innovative methodology for design of composite rotor blade cross sections. The concept of using adaptive, bend-twist coupled, composite blades in order to improve energy capture as well as decrease design complexity are considered in [75].

1.1.3 Nonlinear Aeroelasticity

1.1.3.1 Limit cycle oscillations

Flutter speed is normally calculated using linear governing equations of motion. Flutter speed is the borderline and the small disturbances in the flow results in exponential growth of the oscillations of the structure. In the vicinity of the flutter speed, the so-called limit cycle oscillations (LCO) occur if nonlinearities exist in the structure of fluid flow. LCOs have been observed in wind turbine blades and aircraft wings [76]. Figure 1-4 shows the time response of a typical LCO. As seen in Figure 1-4, amplitude increases up to a certain level beyond which the nonlinearities in the system do not permit the amplitude of the oscillations to increase any further. In this respect, nonlinearities in the system may prevent diverging oscillations.

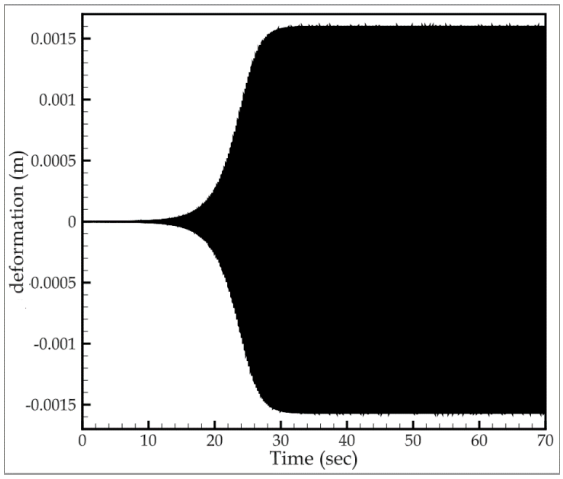

Figure 1-4 Time response of a typical LCO

Nonlinearities which result in LCOs, have either structural nature or aerodynamic origin. Structural nonlinearities which are the subject of present study, involve the geometrical nonlinearity, nonlinear stiffness (e.g. free play and contact) and nonlinear damping (e.g. friction). In case of aerodynamic nonlinearities, flow separation and shock phenomena can be mentioned. LCOs due to structural nonlinearity have been vastly studied both experimentally and theoretically [77-79]. Comprehensive research on the subject of LCOs due to aerodynamic nonlinearities has been performed [80,81]. Flutter speed is normally calculated using linear governing equations of motion. But the post flutter behavior and LCO caused by structural nonlinearities are investigated using nonlinear aeroelasticity. There exist two kinds of LCOs when considering structural nonlinearities. LCOs which occur beyond the flutter point and have a stable nature are called as benign LCOs. These LCOs are normally due to geometrical nonlinearities such as strain nonlinearity. Detrimental LCOs occur below the flutter point. Stiffness nonlinearities (such as free play and contact) and damping nonlinearities (such as friction) are the common source of detrimental LCOs. Figure 1-5 shows the difference of these two type of LCOs. Figure 1-5 is called as the bifurcation diagram which is very beneficial in interpreting post flutter response and the LCO behavior. Variation of the maximum LCO constant amplitude and the free stream speed are the axes of the bifurcation diagram. Benign LCOs occur outside the

flutter point. In benign LCO, maximum response amplitude increase with an increase of the velocity. Benign nonlinearity itself is divided into two forms. In the weak form, the LCO amplitude grows fast when the flow velocity is increased. On the other hand, in the strong form, the LCO amplitude grows rather gradually and LCOs can be observed in a wider post flutter region. For this kind of LCO, abrupt amplitude changes due to a disturbance terminates with LCO.

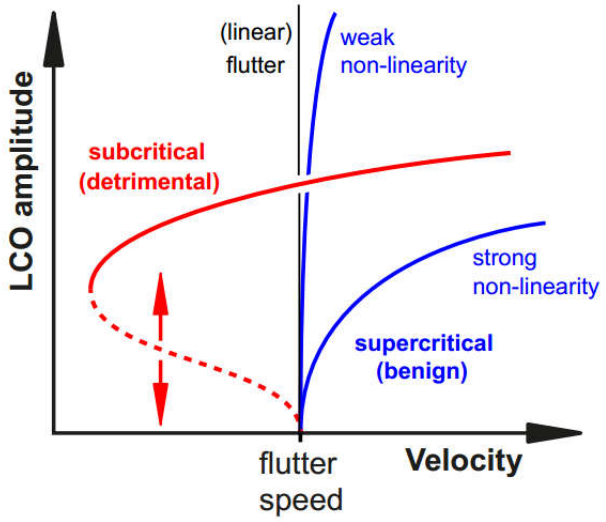

Figure 1-5 Types of LCOs described by Dowell [82]

LCOs come into existence due to the nonlinear modeling in aeroelastic problems of the wings [83-85]. Nonlinearities in wing structures usually arise from the structural stiffness, contacts and free plays of the control surfaces and nonlinear unsteady aerodynamics. A comprehensive review of the structural and aerodynamic nonlinearity effects on the aeroelastic response is given in by Dowell et al. [82]. As a pioneer, Woolston et al. [86] investigated the effect of structural nonlinearity on the classical flutter of aircraft wings. In this study three relatively simple characteristic types of structural nonlinearities were studied—namely, free play, hysteresis, and a cubic spring. As a result, it was shown that nonlinearity has a significant effect on the flutter speed. The results are highly dependent on the amplitude of the initial disturbance. In many cases the flutter speed was lowered as the initial disturbance was

increased. Lee et al. [87] presented a method for nonlinear aeroelastic analysis of a two-dimensional airfoil, subjected to incompressible aerodynamic loading using a time-marching finite-difference scheme. In a later study, Price et al. [88] investigated the airfoil response and the possibility of chaotic behavior by using a variety of plots including power spectral density, phase space, Poincare map and Lyapunov exponent. It is commented that LCO due to aerodynamic nonlinearity occurs beyond the flutter speed while the structural nonlinearity may lead to LCO at an air speed smaller than the flutter speed [89]. Tang and Dowell [90] investigated the effect of geometric nonlinearity on the flutter and post flutter behavior of high aspect ratio 3-D wings. They used slender body assumptions and utilized quasi steady aerodynamic theory. Patil and Hodges [91] considered aerodynamic and geometric nonlinearities in a unified aeroelastic model for high-aspect ratio wings. They employed doublet-lattice aerodynamic theory and nonlinear finite element solution methodology.

1.2 Objective of the thesis

The main objective of the present thesis is to develop theoretical models capable of predicting the aeroelastic instability boundaries and the post flutter LCO response of aircraft wings as well as wind turbine blades modelled as geometrically nonlinear TWB. The theoretical outline of the structural part of the present work consists of two main parts. Firstly, the load carrying box of composite wings is modelled as TWB with 3D displacement domain including all non-classical effects such as warping and transverse shear in presence of geometrical nonlinear terms due to large twist angle and moderately large transverse deformations and second order strain nonlinearity. The effects of stiffness coupling terms induced by various layup configuration on the static and dynamic aeroelastic characteristics and LCO behavior of composite wings are investigated. New quadratic and cubic nonlinear stiffness terms are formulated and integrated into an aeroelastic governing equations of motion capable of calculating the dynamic characteristics of composite wings in the subcritical, critical and the supercritical inflow speeds. The next part of the thesis study deals with the aeroelastic response of a more realistic MW sized wind turbine blade made of glass fiber

reinforced plastic (GFRP) including bend-twist coupling. The inertia and stiffness properties of the inversely designed blade are calculated using the VABS. The aerodynamic loads acting on the blade structure is assumed to be attached unsteady aerodynamic flow and calculated by the indicial function method. Unsteady incompressible aerodynamics based on Wagner's aerodynamic function and unsteady subsonic compressible aerodynamics based on compressible indicial aerodynamic functions are used to simulate the aerodynamic loads which are incorporated into coupled aeroelastic governing equation of motions to predict more realistic dynamic performance of wind turbine blade under various rotational and inflow speeds.

The main result to be reached is to achieve highest critical aeroelastic boundaries by alleviating internal loads by exploiting bend-twist coupling and validate the bend-twist coupling effect in box-beam structures, which simulate the flange region between the spars in a wind turbine blade, through a) theoretical composite thin walled beam model based on Librescu nonlinear theory and b) finite element analysis using VABS software. Off-axis unidirectional lamina applied in the blade load carrying box tends to decrease angle of attack yields to load alleviation in blade and increase instability boundaries of the system. On the other hand, stiffness coupling originated by off-axis fiber layups in conjunction with strain-displacement nonlinear terms directly affect the response of post flutter behavior.

1.3 Scope of the thesis

Due to the fact that turbine blades and aircraft wings are critical aerospace structures, aeroelastic optimization and stability of these structures is very crucial. Box beam in wings and wind turbine blades must have low weight as much as possible, and loads incurred due to the flexing of the blades must be controlled in order to enhance aeroelastic instability. In the literature part, most of the work is dedicated to the aeroelastic analysis of linear structure in incompressible flow regime. Different from most of the work in the literature, in the present thesis, the aeroelastic dynamic response and instability of the wings and blades modeled as TWBs is studied by

including geometrical nonlinearity, structural non-uniformity (such as; pretwist, taper ratio and weep angle), non-classical effects (such as; material anisotropy, transverse shear, warping and rotary moment of inertia) as well as compressibility effects. Throughout the thesis, it is intended to establish the bend-twist coupling in composite structure by choosing proper layup configuration and to apply stiffness coupling term into aeroelastic governing equation of motion results to evaluate dynamic characteristics of wind turbine blade's system.

In Chapter 2, theory of the rotating TWB incorporating the non-uniform geometric features such as pretwist, warping inhibition and transverse shear effects is developed and free vibration analysis is performed to obtain natural frequencies and mode shapes of the thin walled beams. The beam is made of anisotropic materials in two different layup configurations known as circumferentially asymmetric stiffness (CAS) and circumferentially uniform stiffness (CUS). These layup configurations possess diverse elastic coupling such as, flapwise bending- torsion, extension-chordwise bending in CAS configuration and extension- torsion, flapwise bending-chordwise bending in CUS configuration.

In Chapter 3, the unsteady indicial aerodynamics is introduced in detail. Derivation methodology of the unsteady incompressible aerodynamic based on Theoderson's theory and Wagner function is described in the first section. Then, compressible unsteady aerodynamics based on indicial function is comprehensively explained. The novel aspect of this formulation is the Mach dependent exponential approximation of the indicial functions which makes it possible to perform direct stability analysis at any subsonic Mach number.

In Chapter 4, aeroelastic response characteristics of composite wings are investigated via a geometrically nonlinear TWB theory for the structural part incorporating warping inhibition and transverse shear strain effect. Using the aerodynamics lag states and indicial incompressible and compressible aerodynamics theory, explicit expressions for the aerodynamics loading are obtained in the time domain. The coupled field equations of motion are obtained by utilizing the Hamilton's principle. Nonlinear aeroelastic responses are then obtained for composite wings and blades with CAS

configuration TWB structural model by means of a Ritz based solution methodology utilizing the mode shapes of the linear structural system. In Section 4-1, the general aeroelastic governing equation of motion of composite TWB including the effect of angular velocity and up to third order nonlinearity are derived. In Section 4.2, By excluding angular velocity effect, nonlinear aeroelastic behavior of composite fix wings with pretwist and taper ratio (Figure 1-6a) are comprehensively studied. The nonlinear aeroelastic analysis are performed in incompressible flow regime using aerodynamic states and Wagner aerodynamics theory for various fiber angles. In Section 4.3, By including the angular velocity effect both in structural and aerodynamic models, the nonlinear aeroelastic analysis is accomplished for a geometry similar to realistic 5 MW NREL wind turbine box beam-blade (Figure 1-6b) in order to obtain flutter rotational speed at constant wind inflow. Linear flutter analysis is done for fiber angle while post flutter analysis is studied for fiber angle -75°. The indicial function in unsteady incompressible flow is used to simulate incompressible unsteady aerodynamic effects. Section 4.4 is devoted to investigate the effect of compressibility on the linear and nonlinear aeroelastic characteristics of the composite fix wings. The nonlinear aeroelasticity of composite wing is studied in compressible flow regime using aerodynamic lag terms and indicial aerodynamics theory for various fiber and sweep angles (Figure 1-6c).

This chapter in general gives the detailed derivation and the solution procedure of the nonlinear aeroelastic system of equations. Effects of pretwist, taper ratio, wing sweep angle and the fiber angle of the CAS configuration TWB on the post-flutter response of the composite fix wing and rotating blade are studied in depth by providing bifurcation diagrams, phase portraits, Poincare maps and one sided Power Spectral Density (PSD) plots. To the best of author's knowledge, integration of the nonlinear structural thin walled beam model and compressible unsteady aerodynamics via indicial functions in an aeroelastic system for the investigation of the post-critical aeroelastic response of composite wings and rotating blades, as presented in this thesis study has not been studied before.

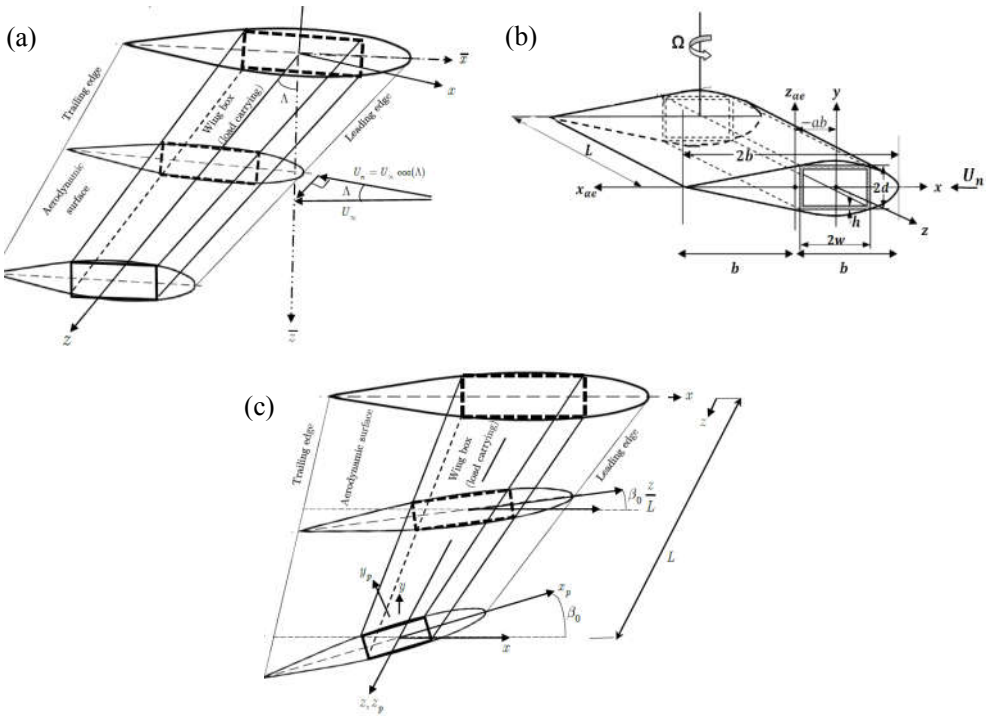

Figure 1-6 Schematic description of (a) pretwisted, tapered composite fix wing (b) rotating composite blade (c) swept composite fix wing

In Chapter 5, the effect of the compressibility on the flutter characteristics of BTC composite blades is investigated. Flutter analyses have been performed for the baseline blade and the BTC blades designed for the 5MW wind turbine of NREL (National Renewable Energy Laboratory). Beam model of the blade has been developed by making analogy with the structural model of the prewisted rotating TWB and utilizing the VABS method for the calculation of sectional properties of the blades designed. To investigate the effect of compressibility on the flutter characteristics of the blades, aeroelastic analyses have been performed both in frequency and time domain utilizing unsteady aerodynamics via indicial function approach.

CHAPTER 2

GENERAL NONLINEAR STRUCTURAL MODEL OF THE COMPOSITE ROTATING TWB

2.1 Preliminaries

TWB considered in the present study is composed of a single cell with straight edges as shown in Figure 2-1. However, the formulation can be extended to a general cross-section which is representative of a rotating blade. TWB model has a length L, width l, height d, wall thickness h and pretwist angle $\beta(z)$.

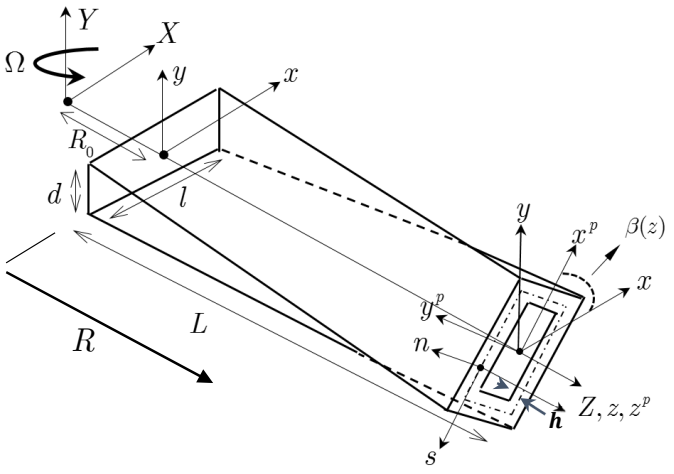

Figure 2-1 Schematic description of the rotating non-uniform TWB

For the derivation of the governing equations, four structural reference coordinates are considered. Inertial coordinate system (X,Y,Z) is attached to the hub center. The rotation vector is perpendicular to the (X,Z) plane and the TWB has angular velocity of $\Omega(\vec{\Omega} = \Omega j)$. Rotating coordinate system (x,y,z) is placed at the root of the TWB blade and R_0 is the offset between the hub center and the root of the blade. Curvilinear coordinate system (x^p, y^p, z^p) is used to define the complex contour of the cross section for the calculation of the cross-sectional properties. Local coordinate system (n,s,z) is defined at the mid plane of the cross section of the TWB such that the parameter *s* is the local coordinate axis tangent to the middle surface and *n* is the coordinate axis perpendicular to the tangential coordinate axis s and the origin is at the mid-plane of the wall thickness of the TWB (Figure 2-1).

The following assumptions are considered to model the composite rotating geometrically nonlinear TWB structural model [56,60];

a) The transverse displacements u and v in the x and y directions are finite but, the twist angle ϕ is considered to be moderately large.
b) The displacement w in the z direction is assumed to be much smaller than its counterparts in other directions (u,v).
c) The normal stress σ_{nn} can be ignored in developing the constitutive relations.
d) The form and geometry of the cross section remain invariant in its plane (i.e. $\varepsilon_{xx} = \varepsilon_{yy} = \varepsilon_{xy} = 0$), on the other hand, the cross section is permitted to warp out of its plane.
e) The transverse shear strains $(\gamma_{xz}, \gamma_{yz})$ are considered in the equation of motion, but, they remain uniform over the cross section of the TWB.
f) The torsional shear strain (γ_{sz}) is constant along the cell wall.
g) Shell force and moment resultants due to σ_{ss} and τ_{ns} are assumed to be small enough and omitted.

In the equations, dot ($\dot{}$) and prime ($'$) denote the derivatives with respect to time t and z axis, respectively.

2.2 Kinematics

For the large rotation of the cross section, based on assumption (a), the 3-D displacements $u(x,y,z,t), v(x,y,z,t), w(x,y,z,t)$ are described in terms of the displacements $u_0(z,t), v_0(z,t)$ and $w_0(z,t)$ and the twist angle $\phi(z,t)$ as [56],

$$
\begin{aligned}
u &= u_0 - \left(y - n\frac{dx}{ds}\right)\sin\phi - \left(x + n\frac{dy}{ds}\right)\left(1-\cos\phi\right) \\
v &= v_0 + \left(x + n\frac{dy}{ds}\right)\sin\phi - \left(y - n\frac{dx}{ds}\right)\left(1-\cos\phi\right) \\
w &= w_0 + \left(x + n\frac{dy}{ds}\right)\theta_y + \left(y - n\frac{dx}{ds}\right)\theta_x - \left[F_w(s) + na(s)\right]\phi'
\end{aligned}
\tag{2-1}
$$

Where, u_0, v_0, w_0 are the translations of the shear center of the thin walled beam in the x, y and z directions , respectively. $\theta_x(z,t), \theta_y(z,t)$ and $\phi(z,t)$ are the rotations about the x, y and z axes. $F_w(s)$ and $na(s)$ are the primary and secondary warping functions. Figure 2-2 shows the displacements and the rotations of the TWB with respect to the x, y, z coordinate system established at the root of the TWB.

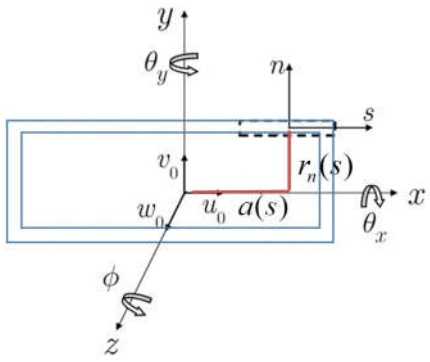

Figure 2-2 Cross-section of the TWB showing the displacements and rotations

The primary (contour) warping function $F_w(s)$ can be written as [17],

$$F_w = \int_0^s \left[r_n(s) - \Psi \right] ds \tag{2-2}$$

where the torsional function Ψ and the parameter $r_n(s)$ are given by,

$$\Psi = \frac{\oint_C \frac{r_n(s)}{h(s)} ds}{\oint_C \frac{ds}{h(s)}} \quad \overset{uniform\ \ thickness}{\Rightarrow} \quad \Psi = \frac{2A}{P} \tag{2-3}$$

$$r_n(s) = y \frac{dx}{ds} - x \frac{dy}{ds} \tag{2-4}$$

Where, A and P are the sectional area and perimeter, respectively. In the definition of the secondary (thickness) warping function referred to as $na(s)$, $a(s)$ is given by,

$$a(s) = x \frac{dx}{ds} + y \frac{dy}{ds} \tag{2-5}$$

As shown in Figure 2-2, $a(s)$ and $r_n(s)$ are the tangential and perpendicular distances from the shear center of cross-section of the TWB to a generic point in the mid-plane of the wall of the TWB.

In the present study, to be general, the approximation of the Green-Lagrange strain tensor is adopted to derive the strain-displacement relations. The nonzero components of the Lagrange' strain are defined by Equations (2-6)-(2-8) [17].

$$\varepsilon_{zz} = \frac{\partial w}{\partial z} + \frac{1}{2}\left[\left(\frac{\partial u}{\partial z} \right)^2 + \left(\frac{\partial v}{\partial z} \right)^2 \right] \tag{2-6}$$

$$\gamma_{sz} = \gamma_{xz} \frac{dx}{ds} + \gamma_{yz} \frac{dy}{ds} + \Psi(s)\phi' + 2n\phi' \tag{2-7}$$

$$\gamma_{nz} = \gamma_{xz} \frac{dy}{ds} - \gamma_{yz} \frac{dx}{ds} \tag{2-8}$$

For thicker walled composite structures, higher order shear deformation theories (HSDT) may be employed. For instance, for thick walled beam with quadratic variation of transverse shear strains through the wall thickness, Equations (2-7) and (2-8) should be modified as,

$$\gamma_{sz} = \left(1 - 4n^2/h^2\right)\gamma_{xz}\frac{dx}{ds} + \left(1 - 4n^2/h^2\right)\gamma_{zy}\frac{dy}{ds} + \Psi(s)\phi' + 2n\phi' \tag{2-9}$$

$$\gamma_{nz} = \left(1 - 4n^2/h^2\right)\gamma_{xz}\frac{dy}{ds} - \left(1 - 4n^2/h^2\right)\gamma_{zy}\frac{dx}{ds} \tag{2-10}$$

By substituting displacement components in Equation (2-1) into the axial strain expression given by Equation (2-6), the nonzero axial strain can be rewritten as given in,

$$\varepsilon_{zz} = \varepsilon_{zz}^{0} + n\varepsilon_{zz}^{1} + n^2\varepsilon_{zz}^{2} \tag{2-11}$$

where the strain components ε_{zz}^{0}, ε_{zz}^{1}, ε_{zz}^{2} include non-linear terms and their explicit expressions are given as follows.

$$\begin{aligned}\varepsilon_{zz}^{0} = {} & \theta_y' x + \theta_x' y + w_0' - F_w(s)\phi'' - u_0'\phi' y\cos\left(\phi\right) - u_0'\phi' x\sin\left(\phi\right) + \\ & v_0'\phi' x\cos\left(\phi\right) - v_0'\phi' y\sin\left(\phi\right) + \frac{1}{2}u_0'^2 + \frac{1}{2}v_0'^2 + \frac{1}{2}\phi'^2 x^2 + \frac{1}{2}\phi'^2 y^2\end{aligned} \tag{2-12}$$

$$\begin{aligned}\varepsilon_{zz}^{1} = {} & -\frac{dy}{ds}u_0'\phi'\sin\left(\phi\right) + \frac{dx}{ds}u_0'\phi'\cos\left(\phi\right) + \frac{dy}{ds}v_0'\phi'\cos\left(\phi\right) + \\ & \frac{dx}{ds}v_0'\phi'\sin\left(\phi\right) + r_n(s)\phi'^2 + \frac{dy}{ds}\theta_y' - \frac{dx}{ds}\theta_x' - \phi''a(s)\end{aligned} \tag{2-13}$$

$$\varepsilon_{zz}^{2} = \frac{1}{2}\phi'^2 \tag{2-14}$$

It should be noted that in the normal strain ε_{zz}, second order nonlinearity with arbitrary large twist deformation is taken into account.

In order to determine the expressions for the shear strains γ_{sz} and γ_{nz}, local shear strains in the yz plane γ_{yz} and xz plane γ_{xz} given by Equations (2-15) and (2-16)

are substituted into Equations (2-7) and (2-8). If a non-shear deformable theory were intended to be used, in the expressions the shear components γ_{yz}, γ_{xz} had to be nullified, consequently the number of dependent variables would reduce to four (u_0, v_0, w_0, ϕ).

$$\gamma_{yz} = \theta_x + v_0' \cos(\phi) - u_0' \sin(\phi) \tag{2-15}$$

$$\gamma_{xz} = \theta_y + u_0' \cos(\phi) + v_0' \sin(\phi) \tag{2-16}$$

Following the substitution, the transverse shear strains γ_{sz} and γ_{nz} can be expressed as,

$$\gamma_{sz} = \gamma_{sz}^0 + n\gamma_{sz}^1 \tag{2-17}$$

$$\gamma_{nz} = \gamma_{nz}^0 \tag{2-18}$$

where the explicit expressions of the shear strain components $\gamma_{sz}^0, \gamma_{sz}^1, \gamma_{nz}^0$ including the nonlinear terms are given as,

$$\gamma_{sz}^0 = \left[\theta_y + u_0' \cos(\phi) + v_0' \sin(\phi)\right]\frac{dx}{ds} + \left[\theta_x + v_0' \cos(\phi) - u_0' \sin(\phi)\right]\frac{dy}{ds} + \Psi(s)\phi' \tag{2-19}$$

$$\gamma_{sz}^1 = 2\phi' \tag{2-20}$$

$$\gamma_{nz}^0 = \left[\theta_y + u_0' \cos(\phi) + v_0' \sin(\phi)\right]\frac{dy}{ds} - \left[\theta_x + v_0' \cos(\phi) - u_0' \sin(\phi)\right]\frac{dx}{ds} \tag{2-21}$$

2.3 Constitutive Relations

The relationship between the stresses and strains in a layer in contracted form can be expressed in terms of the reduced stiffness coefficients $\bar{Q}_{ij}$ of the k^{th} layer of the composite TWB by Equation (2-22).

$$\begin{Bmatrix} \sigma_{ss} \\ \sigma_{zz} \\ \sigma_{nz} \\ \sigma_{sn} \\ \sigma_{sz} \end{Bmatrix}_{(k)} = \left[\bar{Q}_{ij}\right]_{(k)} \begin{Bmatrix} \varepsilon_{ss} \\ \varepsilon_{zz} \\ \gamma_{nz} \\ \gamma_{sn} \\ \gamma_{sz} \end{Bmatrix}_{(k)} \tag{2-22}$$

$$\left[\bar{Q}_{ij}\right]_{(k)} = \begin{bmatrix} \bar{Q}_{11} & \bar{Q}_{12} & 0 & 0 & \bar{Q}_{16} \\ \bar{Q}_{21} & \bar{Q}_{22} & 0 & 0 & \bar{Q}_{26} \\ 0 & 0 & \bar{Q}_{44} & \bar{Q}_{45} & 0 \\ 0 & 0 & \bar{Q}_{54} & \bar{Q}_{55} & 0 \\ \bar{Q}_{61} & \bar{Q}_{62} & 0 & 0 & \bar{Q}_{66} \end{bmatrix}_{(k)} \tag{2-23}$$

The $\bar{Q}_{ij}$ components are used to transform the stiffness coefficients from the problem axes to the material axes and all components are defined explicitly in Appendix A. The 2D first order stress resultants (N_{ij}) and couple resultants (L_{ij}) as well as higher order stress couple resultant (Γ_{ij}) of the cross-section of the TWB are defined in Equations (2-24)- (2-27) in terms of the 3D stresses by integrating the 3D stresses along the wall thickness of the cross section of the TWB and then summed up to form the total resultants. In Equations (2-24)- (2-27), it is assumed that the bounds of the k^{th} ply varies between $(h_{k-1} - h_k)$ and m_l is the total number of plies in the laminate of the TWB.

a) the membrane stress resultants

$$\begin{Bmatrix} N_{ss} \\ N_{zz} \\ N_{sz} \end{Bmatrix} = \sum_{k=1}^{m_l} \int_{h_{k-1}}^{h_k} \begin{Bmatrix} \sigma_{ss} \\ \sigma_{zz} \\ \sigma_{sz} \end{Bmatrix}_{(k)} dn \tag{2-24}$$

b) the transverse shear resultants

$$\begin{Bmatrix} N_{zn} \\ N_{sn} \end{Bmatrix} = \sum_{k=1}^{m_l} \int_{h_{k-1}}^{h_k} \begin{Bmatrix} \sigma_{zn} \\ \sigma_{sn} \end{Bmatrix}_{(k)} dn \tag{2-25}$$

c) the stress couples

$$\begin{Bmatrix} L_{ss} \\ L_{zz} \\ L_{sz} \end{Bmatrix} = \sum_{k=1}^{m_l} \int_{h_{k-1}}^{h_k} \begin{Bmatrix} \sigma_{ss} \\ \sigma_{zz} \\ \sigma_{sz} \end{Bmatrix}_{(k)} n dn \tag{2-26}$$

d) the higher order stress couple

$$\Gamma_{zz} = \sum_{k=1}^{m_l} \int_{n_{(k-1)}}^{n_{(k)}} \sigma_{zz} n^2 dn \tag{2-27}$$

The stress resultants and stress couples on shell elements are displayed in Figure 2-3.

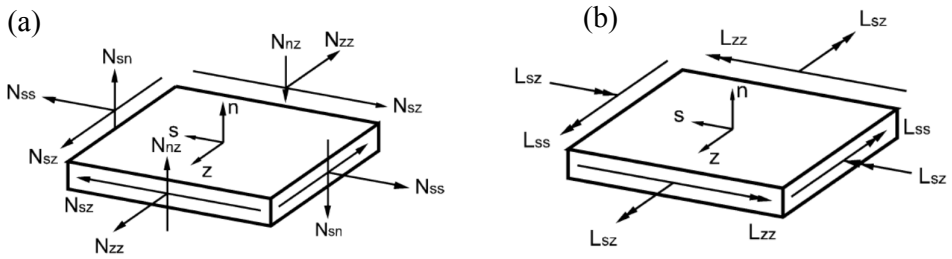

Figure 2-3 (a) Stress resultants and (b) Stress couples [92]

A simplifying assumption is sometimes applied at this stage by letting $\varepsilon_{ss} = \gamma_{ns} = 0$, but this has proved to overestimate the stiffness [46]. So, a more realistic assumption is usually applied by omitting the in-plane force and moment resultants $(N_{ss} = L_{ss} = N_{ns} = 0)$. Using this assumption, the strain components $\varepsilon_{ss}, \gamma_{ns}$ are

eliminated from the stress-strain relation. Accordingly, with no loss of generality one may assume the unknowns ε_{ss} to be linearly varying with the thickness coordinate *n* and γ_{ns} a constant with respect to the thickness coordinate n. This assumption is required for our proceeding simplifications, so one may express $\varepsilon_{ss}, \gamma_{ns}$ as given in Equations (2-28) and (2-29),

$$\varepsilon_{ss} = \varepsilon_{ss}^{0} + n\varepsilon_{ss}^{1} \tag{2-28}$$

$$\gamma_{ns} = \gamma_{ns}^{0} \tag{2-29}$$

Substituting the strain definitions from Equations (2-11), (2-17) and (2-18) in the stress-strain definition in Equation (2-22) and employing Equations (2-24)-(2-27) and (2-28), (2-29) the constitutive relations are obtained,

$$\begin{Bmatrix} N_{zz} \\ L_{zz} \\ \Gamma_{zz} \\ N_{sz} \\ L_{sz} \end{Bmatrix} = \underbrace{\begin{bmatrix} A_{22} & B_{22} & D_{22} & A_{26} & B_{26} \\ B_{22} & D_{22} & F_{22} & B_{26} & D_{26} \\ D_{22} & F_{22} & H_{22} & D_{26} & F_{26} \\ A_{62} & B_{62} & D_{62} & A_{66} & B_{66} \\ B_{62} & D_{62} & F_{62} & B_{66} & D_{66} \end{bmatrix}}_{M_1} \begin{Bmatrix} \varepsilon_{zz}^{0} \\ \varepsilon_{zz}^{1} \\ \varepsilon_{zz}^{2} \\ \gamma_{sz}^{0} \\ \gamma_{sz}^{1} \end{Bmatrix} + \underbrace{\begin{bmatrix} A_{21} & B_{21} \\ B_{21} & D_{21} \\ D_{21} & F_{21} \\ A_{61} & B_{61} \\ B_{61} & D_{61} \end{bmatrix}}_{M_2} \begin{Bmatrix} \varepsilon_{ss}^{0} \\ \varepsilon_{ss}^{1} \end{Bmatrix} \tag{2-30}$$

$$\begin{Bmatrix} N_{ss} \\ L_{ss} \end{Bmatrix} = \begin{bmatrix} A_{12} & B_{12} & D_{12} & A_{16} & B_{16} \\ B_{12} & D_{12} & F_{12} & B_{16} & D_{16} \end{bmatrix} \begin{Bmatrix} \varepsilon_{zz}^{0} \\ \varepsilon_{zz}^{1} \\ \varepsilon_{zz}^{2} \\ \gamma_{sz}^{0} \\ \gamma_{sz}^{1} \end{Bmatrix} + \underbrace{\begin{bmatrix} A_{11} & B_{11} \\ B_{11} & D_{11} \end{bmatrix}}_{M_3} \begin{Bmatrix} \varepsilon_{ss}^{0} \\ \varepsilon_{ss}^{1} \end{Bmatrix} \tag{2-31}$$

$$\begin{Bmatrix} N_{sn} \\ N_{zn} \end{Bmatrix} = \begin{bmatrix} A_{44} & A_{45} \\ A_{45} & A_{55} \end{bmatrix} \begin{Bmatrix} \gamma_{sn}^{0} \\ \gamma_{zn}^{0} \end{Bmatrix} \tag{2-32}$$

where the stiffness coefficients including both first and higher order coupling coefficients are defined as $(A_{ij}, B_{ij}, D_{ij}, F_{ij}, H_{ij})$ in Equation (2-33) [18].

$$\left(A_{ij}, \mathrm{B}_{ij}, \mathrm{D}_{ij}, \mathrm{F}_{ij}, \mathrm{H}_{ij}\right) = \sum_{k=1}^{M} \int_{h_{k-1}}^{h_k} \bar{Q}_{ij}^{(k)} \left(1, n, n^2, n^3, n^4\right) dn, \tag{2-33}$$

The 5×5 and 5×2 matrices in Equation (2-30), are named as, M_1, M_2, respectively. Also, the 2×2 matrix in Equation (2-31) is named as M_3. As mentioned earlier, omitting the in-plane force and moment resultants $(N_{ss} = L_{ss} = N_{ns} = 0)$ one can eliminate $\varepsilon_{ss}^0, \varepsilon_{ss}^1, \gamma_{ns}^0$ and constitutive relation given by Equation (2-34) is obtained,

$$\begin{Bmatrix} N_{zz} \\ L_{zz} \\ \Gamma_{zz} \\ N_{sz} \\ L_{sz} \end{Bmatrix} = \left[K_{ij}\right] \begin{Bmatrix} \varepsilon_{zz}^0 \\ \varepsilon_{zz}^1 \\ \varepsilon_{zz}^2 \\ \gamma_{sz}^0 \\ \gamma_{sz}^1 \end{Bmatrix}, \qquad N_{nz} = \left(A_{44} - \frac{A_{45}^2}{A_{55}}\right) \gamma_{zn}^0 \tag{2-34}$$

where the square and symmetric matrix K is defined as,

$$\left[K_{ij}\right] = \left[M_1\right] - \left[M_2\right]\left[M_3\right]^{-1}\left[M_2\right]^T \tag{2-35}$$

All the elements of K_{ij} are explicitly given in Appendix A.

2.4 Governing Dynamic System of Equations

For a rotating TWB, the governing equations of motion can be analytically derived using the Hamilton's principle in the absence surface shear forces, and thermal loadings as,

$$\int_{t_1}^{t_2} (\delta T - \delta\left(V + V_{cf}\right) + \delta W) dt = 0 \tag{2-36}$$
$$at \quad t = t_1, t_2,$$
$$\delta u_0 = \delta v_0 = \delta w_0 = \delta\theta_x = \delta\theta_y = \delta\phi = 0$$

where, T, V, V_{cf} and W are the kinetic energy, strain energy, strain energy due to the centrifugal force and the work done by external loads, respectively. For the free vibration problem, work done by the external forces is omitted.

2.4.1 Strain Energy

The strain energy in terms of the 3-D stress and nonzero strain field can be expressed as,

$$V = \frac{1}{2}\int_0^L \oint_C \sum_{k=1}^{N} \int_{h(k)} \left[\sigma_{zz}\varepsilon_{zz} + \sigma_{sz}\varepsilon_{sz} + \sigma_{nz}\varepsilon_{nz}\right]_{(k)} dndsdz = \tag{2-37}$$
$$= \frac{1}{2}\int_0^L \oint_C \sum_{k=1}^{N} \int_{h(k)} \begin{bmatrix} \sigma_{zz}^{(k)}\left(\varepsilon_{zz}^0 + n\varepsilon_{zz}^1 + n^2\varepsilon_{zz}^2\right) + \\ \sigma_{sz}^{(k)}\left(\gamma_{sz}^0 + n\gamma_{sz}^1\right) + \sigma_{nz}^{(k)}\gamma_{nz}^0 \end{bmatrix}_{(k)} dndsdz$$

Taking integral along the wall thickness and utilizing the shell stress resultants and stress couples, one gets,

$$V = \frac{1}{2}\int_0^L \oint_C \left[N_{zz}\varepsilon_{zz}^0 + L_{zz}\varepsilon_{zz}^1 + \Gamma_{zz}\varepsilon_{zz}^2 + N_{sz}\gamma_{sz}^0 + L_{sz}\gamma_{sz}^1 + N_{nz}\gamma_{nz}^0\right] dsdz \tag{2-38}$$

Utilizing the constitutive relation given by Equations (2-30), (2-31) and (2-32) and the strain displacement relations Equation (2-38), integrating Equation (2-38) along the contour of the cross-section of the TWB, strain energy can be obtained as,

$$\begin{aligned} V = & \\ & \frac{1}{2}\int_0^L \Big(T_z\left(w_0' + \frac{1}{2}u_0'^2 + \frac{1}{2}v_0'^2\right) + Q_y\left(\theta_x + v_0'\cos(\phi) - u_0'\sin(\phi)\right) + \\ & Q_x\left(\theta_y + u_0'\cos(\phi) + v_0'\sin(\phi)\right) + M_y\left(\theta_y' - u_0'\phi'\sin(\phi) + v_0'\phi'\cos(\phi)\right) + \\ & M_x\left(\theta_x' - u_0'\phi'\cos(\phi) - v_0'\phi'\sin(\phi)\right) + M_z\left(\phi'\right) - B_w\left(\phi''\right) + \frac{1}{2}\Lambda_z\phi'^2\Big)dz \end{aligned} \tag{2-39}$$

where the 1-D stress resultants (T_z, Q_x, Q_y) and the stress couples $(M_x, M_y, M_z, B_w, \Lambda_z)$ are defined in Equations (2-40)-(2-47) .

$$T_z = \oint_C N_{zz} ds \tag{2-40}$$

$$Q_x = \oint_C \left(N_{sz} \frac{dx}{ds} + N_{zn} \frac{dy}{ds} \right) ds \tag{2-41}$$

$$Q_y = \oint_C \left(N_{sz} \frac{dy}{ds} - N_{zn} \frac{dx}{ds} \right) ds \tag{2-42}$$

$$M_y = \oint_C \left(x N_{zz} + L_{zz} \frac{dy}{ds} \right) ds \tag{2-43}$$

$$M_x = \oint_C \left(y N_{zz} - L_{zz} \frac{dx}{ds} \right) ds \tag{2-44}$$

$$M_z = \oint_C \left(N_{sz} \Psi + 2L_{sz} \right) ds \tag{2-45}$$

$$B_w = \oint_C \left(N_{zz} F_w(s) + a(s) L_{zz} \right) ds \tag{2-46}$$

$$\Lambda_z = \oint_C \left(N_{zz} \left(x^2 + y^2 \right) + 2L_{zz} r_n + \Gamma_{zz} \right) ds \tag{2-47}$$

In Equations (2-40)-(2-47), T_z is the axial force, Q_x and Q_y correspond to the chordwise and flapwise shear forces, M_x, M_y are associated with the flapwise bending moment (moment about the x direction) and chordwise bending moment (moment about the y direction), M_z corresponds to the Saint –Venant twist moment, B_w is the bimoment (warping torque) and $\Gamma_z (\Gamma_z = \oint \Gamma_{zz} ds)$ is the torque due to the higher order stress couple.

To obtain the equations of motion and the associated natural boundary conditions via the Hamilton's principle, variation of the strain energy is taken. In the application of the Hamilton's principle, integration by parts is applied to get rid of the derivatives on the variations of the displacements, rotations and the twist angle and the variation of the strain energy is obtained as given in Equation (2-48).

$$
\delta V = \int_0^L \begin{bmatrix}
\left(-T_z'\right)\delta w_0 + \\
\begin{pmatrix} -T_z' u_0' - T_z u_0'' + M_y' \phi' \sin\phi + M_y \phi'' \sin\phi + M_y \phi'^2 \cos\phi + \\ M_x' \phi' \cos\phi + M_x \phi'' \cos\phi - M_x \phi'^2 \sin\phi - Q_x' \cos\phi + \\ Q_x \phi' \sin\phi + Q_y' \sin\phi + Q_y \phi' \cos\phi \end{pmatrix} \delta u_0 + \\
\begin{pmatrix} -T_z' v_0' - T_z v_0'' - M_y' \phi' \cos\phi - M_y \phi'' \cos\phi + M_y \phi'^2 \sin\phi + \\ M_x' \phi' \sin\phi + M_x \phi'' \sin\phi + M_x \phi'^2 \cos\phi - Q_x' \sin\phi - \\ Q_x \phi' \cos\phi - Q_y' \cos\phi + Q_y \phi' \sin\phi \end{pmatrix} \delta v_0 + \\
\begin{pmatrix} M_y' u_0' \sin\phi + M_y u_0'' \sin\phi - M_y' v_0' \cos\phi - M_y v_0'' \cos\phi + \\ M_x' u_0' \cos\phi + M_x u_0'' \cos\phi + M_x' v_0' \sin\phi + M_x v_0'' \sin\phi \\ -M_z' - B_w'' - \Lambda_z' \phi' - \Lambda_z \phi'' - Q_x u_0' \sin\phi + Q_x v_0' \cos\phi - \\ Q_y v_0' \sin\phi - Q_y u_0' \cos\phi \end{pmatrix} \delta\phi + \\
\left(-M_y' + Q_x\right)\delta\theta_y + \left(-M_x' + Q_y\right)\delta\theta_x
\end{bmatrix} dz + \\
\begin{bmatrix}
\left(T_z\right)\delta w_0 + \begin{pmatrix} T_z u_0' - M_y \phi' \sin\phi - M_x \phi' \cos\phi + Q_x \cos\phi - \\ Q_y \sin\phi \end{pmatrix} \delta u_0 + \\
\left(T_z v_0' + M_y \phi' \cos\phi - M_x \phi' \sin\phi + Q_x \sin\phi + Q_y \cos\phi\right)\delta v_0 + \\
M_y \delta\theta_y + M_x \delta\theta_x + \begin{pmatrix} +M_y v_0' \cos\phi - M_y u_0' \sin\phi - M_x u_0' \cos\phi \\ -M_x v_0' \sin\phi + M_z + B_w' + \Lambda_z \phi' \end{pmatrix} \delta\phi \\
-B_w \delta\phi'
\end{bmatrix}_0^L
\tag{2-48}
$$

2.4.2 Kinetic Energy

Variation of the kinetic energy is expressed as,

$$
T = \frac{1}{2}\iiint \rho \dot{R}^2 \quad dndsdz \tag{2-49}
$$

$$
\delta T = \iiint \rho \dot{R}\delta\dot{R} \quad dndsdz = \iiint \rho \ddot{R}\delta R \quad dndsdz
$$

where, the position vector $(\vec{R})$ shown in Figure 2-1 of an arbitrary point in the deformed rotating pretwisted TWB, calculated with respect to the centroid located at the middle of the hub, is given by,

$$\vec{R} = (x+u)\hat{i} + (y+v)\hat{j} + (z+w+R_0)\hat{k} \tag{2-50}$$

Considering that the angular velocity Ω about the global or the rotating y axis $(\Omega J = \Omega j)$, the acceleration of the arbitrary point $(\ddot{\vec{R}})$ in the deformed rotating TWB can be written as,

$$\ddot{\vec{R}} = a_x\hat{i} + a_y\hat{j} + a_z\hat{k} \tag{2-51}$$

where,

$$\begin{aligned} a_x &= \left[\ddot{u} + \underbrace{2\dot{w}\Omega}_{Coriolis} - \underbrace{(x+u)\Omega^2}_{Centrifugal}\right], \qquad a_y = \ddot{v}, \\ a_z &= \left[\ddot{w} - \underbrace{2\dot{u}\Omega}_{Coriolis} - \underbrace{\left(z+w+R_0\right)\Omega^2}_{Centrifugal}\right] \end{aligned} \tag{2-52}$$

where, the effects of the Coriolis and centrifugal terms induced by angular velocity are clearly identified.

The variation of the kinetic energy can then be expressed after carrying out an integration by parts whenever necessary.

$$\begin{aligned} \delta T = &-\int\left[\left(I_1\right)\delta u_0 + \left(I_2\right)\delta v_0 + \left(I_3\right)\delta w_0 + \left(I_4\right)\delta\theta_x + \left(I_5\right)\delta\theta_y + \left(I_6\right)\delta\phi\right]dz - \\ &\left[\begin{pmatrix} b_7\left(-\ddot{w}_0 + 2\dot{u}_0\Omega\right) + \left(b_8 - b_{14}\right)\left(-\ddot{\theta}_x\right) + \left(b_9 + b_{15}\right)\left(-\ddot{\theta}_y\right) + \\ \left(b_{10} + b_{16}\right)\left(\ddot{\phi}' - \Omega^2\phi'\right) \end{pmatrix}\delta\phi\right]_0^L \end{aligned} \tag{2-53}$$

where, the inertia terms (I_i) are defined as,

$$I_1 = b_1\left(\ddot{u}_0 + 2\dot{w}_0\Omega - u_0\Omega^2\right) - b_3A\left(\phi\right) - b_2B\left(\phi\right) \tag{2-54}$$

$$I_2 = b_1\left(\ddot{v}_0\right) + b_3B\left(\phi\right) - b_2A\left(\phi\right) \tag{2-55}$$

$$I_3 = b_1\left(\ddot{w}_0 - 2\dot{u}_0\Omega - \left(z + w_0 + R_0\right)\Omega^2\right) + b_2\ddot{\theta}_x + b_3\ddot{\theta}_y - b_7\ddot{\phi}' \tag{2-56}$$

$$
\begin{aligned}
I_4 = &\left(b_4 + b_{12}\right)\left(\ddot{\theta}_x - \Omega^2\theta_x + 2\cos\phi\Omega\dot{\phi}\right) + \\
&\left(b_6 - b_{18}\right)\left(\ddot{\theta}_y + 2\sin\phi\Omega\dot{\phi} - \Omega^2\theta_y\right) + \\
&b_2\left(\ddot{w}_0 - 2\dot{u}_0\Omega - \left(z + w_0 + R_0\right)\Omega^2\right) - \left(b_8 - b_{14}\right)\left(\ddot{\phi}'\right)
\end{aligned} \tag{2-57}
$$

$$
\begin{aligned}
I_5 = &\left(b_5 + b_{11}\right)\left(\ddot{\theta}_y - \Omega^2\theta_y + 2\sin\phi\Omega\dot{\phi}\right) + \\
&\left(b_6 - b_{18}\right)\left(\ddot{\theta}_x + 2\cos\phi\Omega\dot{\phi} - \Omega^2\theta_x\right) + \\
&b_3\left(\ddot{w}_0 - 2\dot{u}_0\Omega - \left(z + w_0 + R_0\right)\Omega^2\right) - \left(b_9 + b_{15}\right)\left(\ddot{\phi}'\right)
\end{aligned} \tag{2-58}
$$

$$
\begin{aligned}
I_6 = &\, b_3\left(\ddot{v}_0\cos\phi - \ddot{u}_0\sin\phi\right) + b_2\left(-\ddot{v}_0\sin\phi - \ddot{u}_0\cos\phi\right) + \\
&\left(b_6 - b_{18}\right)\left(-2\Omega\dot{\theta}_x\sin\phi - 2\Omega\dot{\theta}_y\cos\phi + \Omega^2\left(\cos^2\phi - \sin^2\phi\right)\right) + \\
&\left(b_4 + b_{12}\right)\left(A\left(\phi\right)\sin\phi + B\left(\phi\right)\cos\phi - 2\Omega\dot{\theta}_x\cos\phi - \Omega^2\cos\phi\sin\phi\right) + \\
&\left(b_5 + b_{11}\right)\left(A\left(\phi\right)\sin\phi + B\left(\phi\right)\cos\phi - 2\Omega\dot{\theta}_y\sin\phi + \Omega^2\cos\phi\sin\phi\right) + \\
&b_7\left(\ddot{w}_0' - 2\dot{u}_0'\Omega\right) + \left(b_8 - b_{14}\right)\left(\ddot{\theta}_x'\right) + \left(b_9 + b_{15}\right)\left(\ddot{\theta}_y'\right) + \left(b_{10} + b_{16}\right)\left(-\ddot{\phi}'' + \Omega^2\phi''\right)
\end{aligned} \tag{2-59}
$$

In Equations (2-54)-(2-59), b_i terms represent the reduced masses and are expressed as,

$$
\begin{aligned}
&\left\{b_1, b_2, b_3, b_4, b_5, b_6, b_7, b_8, b_9, b_{10}\right\} = \\
&\qquad \int_s m_0\left\{1, y, x, y^2, x^2, xy, F_w(s), yF_w(s), xF_w(s), F_w^2(s)\right\}ds \\
&\left\{b_{11}, b_{12}, b_{13}, b_{14}, b_{15}, b_{16}\right\} = \\
&\qquad \int_s m_2\left\{\left(\frac{dy}{ds}\right)^2, \left(\frac{dx}{ds}\right)^2, \left(\frac{dx}{ds}\right)\left(\frac{dy}{ds}\right), a(s)\frac{dx}{ds}, a(s)\frac{dy}{ds}, a^2(s)\right\}ds
\end{aligned} \tag{2-60}
$$

where the mass terms (m_0, m_2) are defined in Equation (2-61).

$$
\left\{m_0, m_1, m_2\right\} = \sum_{k=1}^{N}\int_{h_{k-1}}^{h_k}\rho_k\left\{1, n, n^2\right\}dn \tag{2-61}
$$

Moreover, $A(\phi), B(\phi)$ in Equations (2-54)-(2-59) is defined in Equation (2-62),

$$
\begin{aligned}
A\left(\phi\right) &= \ddot{\phi}\sin\phi + \dot{\phi}^2\cos\phi \\
B\left(\phi\right) &= \ddot{\phi}\cos\phi - \dot{\phi}^2\sin\phi
\end{aligned} \tag{2-62}
$$

It should be noted that for a symmetrically laminated TWB, the mass terms which include the coefficient m_1 are all zero.

2.4.3 Strain Energy Due to the Centrifugal Force

Rotary blades are subjected to centrifugal forces and in the present study the effect of centrifugal forces are also taken into account. The centrifugal force acting on the rotating beam at a spanwise location z can be expressed as,

$$F_c = \int_z^L \rho A \Omega^2 \left(R_0 + z \right) dz = \rho A \Omega^2 R(z) \tag{2-63}$$

where, $R(z)$ is defined as,

$$R\left(z \right) = \left[R_0 \left(L - z \right) + \frac{1}{2}\left(L^2 - z^2 \right) \right] \tag{2-64}$$

The contribution of the centrifugal force to the strain energy in the TWB can be expressed as,

$$V_{cf} = \frac{1}{2}\int_0^L \oint_C \sum_{k=1}^{N} \int_{h(k)} F_c \left[\left(u' \right)^2 + \left(v' \right)^2 \right] dn ds dz \tag{2-65}$$

where, u, v are the 3-D displacements in the edgewise and flapwise directions (Figure 2-1), respectively and F_c is the centrifugal force. By substituting the displacements defined by Equation (2-1) and the centrifugal force defined by Equation (2-63) into Equation (2-65), strain energy due to centrifugal force can be determined.

$$V_{cf} = \frac{1}{2}\int_0^L \Omega^2 R(z) \begin{bmatrix} b_1\left(u_0'^2 + v_0'^2 \right) + \left(b_4 + b_{12} \right)\left(\phi'^2 \cos\phi \sin\phi + \phi' \right) + \\ \left(b_5 + b_{11} \right)\left(\phi'^2 \cos\phi \sin\phi + \phi' \right) - \\ 2b_2\phi'\left(u_0' \cos\phi + v_0' \sin\phi \right) - 2b_3\phi'\left(u_0' \sin\phi - v_0' \cos\phi \right) \end{bmatrix} dz \tag{2-66}$$

By taking the variation of Equation (2-66) and applying integration by parts to get rid of the derivatives on the variations of the displacements, rotations and the twist angle, variation of the strain energy due to the centrifugal force can be expressed as,

$$\begin{aligned}\delta V_{cf} = -\int \left[\left(f_1\right)\delta u_0 + \left(f_2\right)\delta v_0 + \left(f_3\right)\delta\phi\right]dz + \\ \left[\left(f_{b1}\right)\delta u_0 + \left(f_{b2}\right)\delta v_0 + \left(f_{b3}\right)\delta\phi\right]_0^L\end{aligned} \tag{2-67}$$

where, f_i and f_{bi} are defined in Equations (2-68)-(2-70) and (2-71)-(2-73).

$$\begin{aligned}f_1 = b_1\Omega^2\left(R(z)u_0'' + R'(z)u_0'\right) + \\ b_2\Omega^2\left(R(z)\left(-\phi''\cos\phi + \phi'^2\sin\phi\right) - R'(z)\phi'\cos\phi\right) - \\ b_3\Omega^2\left(R(z)\left(\phi''\sin\phi + \phi'^2\cos\phi\right) + R'(z)\phi'\cos\phi\right)\end{aligned} \tag{2-68}$$

$$\begin{aligned}f_2 = b_1\Omega^2\left(v_0''R(z) + R'(z)v_0'\right) + \\ b_3\Omega^2\left(R(z)\left(\phi''\cos\phi + \phi'^2\sin\phi\right) + R'(z)\phi'\cos\phi\right) - \\ b_2\Omega^2\left(R(z)\left(\phi''\sin\phi + \phi'^2\cos\phi\right) + R'(z)\phi'\sin\phi\right)\end{aligned} \tag{2-69}$$

$$\begin{aligned}f_3 = -b_2\Omega^2\left(R(z)\left(u_0''\cos\phi + v_0''\sin\phi\right) + R'(z)\left(u_0'\cos\phi + v_0'\sin\phi\right)\right) - \\ b_3\Omega^2\left(R(z)\left(u_0''\sin\phi - v_0''\cos\phi\right) + R'(z)\left(u_0'\sin\phi - v_0'\cos\phi\right)\right) + \\ \left(b_4 + b_{12}\right)\Omega^2\left(R(z)\phi'' + R'(z)\phi'\right) + \left(b_5 + b_{11}\right)A\Omega^2\left(R(z)\phi'' + R'(z)\phi'\right)\end{aligned} \tag{2-70}$$

$$f_{b1} = b_1\Omega^2\left(u_0'R(z)\right) - b_2\Omega^2\left(R(z)\phi'\cos\phi\right) - b_3\Omega^2\left(R(z)\phi'\sin\phi\right) \tag{2-71}$$

$$f_{b2} = b_1\Omega^2\left(v_0'R(z)\right) + b_3\Omega^2\left(R(z)\phi'\cos\phi\right) - b_2\Omega^2\left(R(z)\phi'\sin\phi\right) \tag{2-72}$$

$$\begin{aligned}f_{b3} = -b_2\Omega^2\left(R(z)u_0'\cos\phi + R(z)v_0'\sin\phi\right) - \\ b_3\Omega^2\left(R(z)u_0'\sin\phi - R(z)v_0'\cos\phi\right) + \\ \left(b_4 + b_{12}\right)\Omega^2\left(R(z)\phi'\right) + \left(b_5 + b_{11}\right)\Omega^2\left(R(z)\phi'\right)\end{aligned} \tag{2-73}$$

2.4.4 Governing Equation of Motion and the Boundary Conditions

To obtain the equations of motion and the associated natural boundary conditions via the Hamilton's principle, variations of the strain energy due to deformation, strain energy due to centrifugal force and kinetic energy are taken. In the application of the Hamilton's principle, integration by parts is applied to get rid of the derivatives on the variations of the displacements, rotations and the twist angle and the nonlinear equations of the rotating TWB are derived. Euler–Lagrange equations of the TWB given by Equations (2-74)-(2-79).

$$\begin{aligned}&\delta u_0 : T_z' u_0' + T_z u_0'' - M_y' \phi' \sin\phi - M_y \left(\phi'' \sin\phi + \phi'^2 \cos\phi\right) - \\ &M_x' \phi' \cos\phi - M_x \left(\phi'' \cos\phi - \phi'^2 \sin\phi\right) + Q_x' \cos\phi - Q_x \phi' \sin\phi - Q_y' \sin\phi - \\ &Q_y \phi' \cos\phi + f_1 - I_1 = 0\end{aligned} \tag{2-74}$$

$$\begin{aligned}&\delta v_0 : T_z' v_0' + T_z v_0'' + M_y' \phi' \cos\phi + M_y \left(\phi'' \cos\phi - \phi'^2 \sin\phi\right) - \\ &M_x' \phi' \sin\phi - M_x \left(\phi'' \sin\phi + \phi'^2 \cos\phi\right) + Q_x' \sin\phi + Q_x \phi' \cos\phi + Q_y' \cos\phi - \\ &Q_y \phi' \sin\phi + f_2 - I_2 = 0\end{aligned} \tag{2-75}$$

$$\delta w_0 : T_z' - I_3 = 0 \tag{2-76}$$

$$\delta\theta_x : M_x' - Q_y - I_4 = 0 \tag{2-77}$$

$$\delta\theta_y : M_y' - Q_x - I_5 = 0 \tag{2-78}$$

$$\begin{aligned}&\delta\phi : M_y' \left(v_0' \cos\phi - u_0' \sin\phi\right) + M_y \left(v_0'' \cos\phi - u_0'' \sin\phi\right) - \\ &M_x' \left(v_0' \sin\phi + u_0' \cos\phi\right) - M_x \left(v_0'' \sin\phi + u_0'' \cos\phi\right) + \\ &M_z' + B_w'' + \Lambda_z' \phi' + \Lambda_z \phi'' + Q_x \left(u_0' \sin\phi - v_0' \cos\phi\right) + \\ &Q_y \left(v_0' \sin\phi + u_0' \cos\phi\right) + f_3 - I_6 = 0\end{aligned} \tag{2-79}$$

Boundary conditions at the root and the tip $(z = 0, L)$ section of the rotating TWB can be obtained by setting the coefficients of variation of the displacements and rotations $\delta u_0, \delta v_0, \delta w_0, \delta\theta_x, \delta\theta_y, \delta\phi, \delta\phi'$ in the non-integral terms to zero individually.

$$\delta u_0 = 0, or \quad T_z u_0' - M_y \phi' \sin\phi - M_x \phi' \cos\phi + Q_x \cos\phi - Q_y \sin\phi + f_{b1} = 0 \tag{2-80}$$

$$\delta v_0 = 0, or \quad T_z v_0' + M_y \phi' \cos\phi - M_x \phi' \sin\phi + Q_x \sin\phi + Q_y \cos\phi + f_{b2} = 0 \tag{2-81}$$

$$\delta w_0 = 0, \quad or \quad T_z = 0 \tag{2-82}$$

$$\delta \theta_x = 0, \quad or \quad M_x = 0 \tag{2-83}$$

$$\delta \theta_y = 0, \quad or \quad M_y = 0 \tag{2-84}$$

$$\begin{aligned} &\delta\phi = 0, or \quad M_y v_0' \cos\phi - M_y u_0' \sin\phi - M_x u_0' \cos\phi - M_x v_0' \sin\phi + M_z + \\ &B_w' + \Lambda_z \phi' + f_{b3} + B_7\left(-\ddot{w}_0 + 2\dot{u}_0\Omega\right) + B_8\left(-\ddot{\theta}_x\right) + B_9\left(-\ddot{\theta}_y\right) + B_{10}\left(\ddot{\phi}' - \Omega^2\phi'\right) = 0 \end{aligned} \tag{2-85}$$

$$\delta\phi' = 0, \quad or \quad B_w = 0 \tag{2-86}$$

2.4.5 Strain Energy Expression in Matrix Form

By considering the relationships between the shell stress resultants and couples (i.e. Equations (2-40)-(2-47)) and their generalized strain counterparts shown in Equation (2-39) in the matrix form, the generalized shell stresses are related to the generalized displacements by Equation (2-87).

$$\{F\} = [A]\{D\} \tag{2-87}$$

Where, the F, A, D are the generalized shell stresses, the 8×8 stiffness matrix of the cross-section of the TWB and the generalized displacements, respectively. For the composite TWB, by incorporating the geometrical nonlinearities, F, A, D are expressed as,

$$F^T = \begin{Bmatrix} T_z & Q_x & Q_y & M_y & M_x & M_z & B_w & \Lambda_z \end{Bmatrix} \tag{2-88}$$

$$A = \begin{bmatrix} a_{11} & a_{12} & a_{13} & a_{14} & a_{15} & a_{16} & a_{17} & a_{18} \\ & a_{22} & a_{23} & a_{24} & a_{25} & a_{26} & a_{27} & a_{28} \\ & & a_{33} & a_{34} & a_{35} & a_{36} & a_{37} & a_{38} \\ & & & a_{44} & a_{45} & a_{46} & a_{47} & a_{48} \\ & & & & a_{55} & a_{56} & a_{57} & a_{58} \\ & & & & & a_{66} & a_{67} & a_{68} \\ & sym & & & & & a_{77} & a_{78} \\ & & & & & & & a_{88} \end{bmatrix} \tag{2-89}$$

$$D = \begin{Bmatrix} w_0' + \frac{1}{2}u_0'^2 + \frac{1}{2}v_0'^2 \\ \theta_y + u_0'\cos(\phi) + v_0'\sin(\phi) \\ \theta_x + v_0'\cos(\phi) - u_0'\sin(\phi) \\ \theta_y' - u_0'\phi'\sin(\phi) + v_0'\phi'\cos(\phi) \\ \theta_x' - u_0'\phi'\cos(\phi) - v_0'\phi'\sin(\phi) \\ \phi' \\ -\phi'' \\ \phi'^2/2 \end{Bmatrix} \tag{2-90}$$

Substituting the terms of the constitutive law written in terms of the reduced stiffness coefficients K_{ij} given by Equation (2-35), into the 1D stress and moment resultants given by Equations (2-40)-(2-47) and expressing the resulting equations in the matrix form Equation (2-87), the 8×8 stiffness matrix of the cross section of the TWB is extracted. The coefficients of the stiffness matrix *A* are given in APPENDIX B. The strain energy of the anisotropic rotating TWB in terms of cross section stiffness is then obtained as,

$$V = \int_0^L \hat{V}\, dz \tag{2-91}$$

Where $\hat{V}$ is the strain energy per unit beam span, and it is written in matrix form in terms of the generalized displacements D and the stiffness matrix A as given in Equation (2-92) .

$$\hat{V} = \frac{1}{2} D^T A D \tag{2-92}$$

2.5 Composite Layup Configurations Studied

In the present study, two composite layup configurations are considered to establish proper structural couplings. These configurations are known as CAS and CUS and they are first discussed by Rehfield [93]. These two configurations are shown in Figure 2-4 a and b.

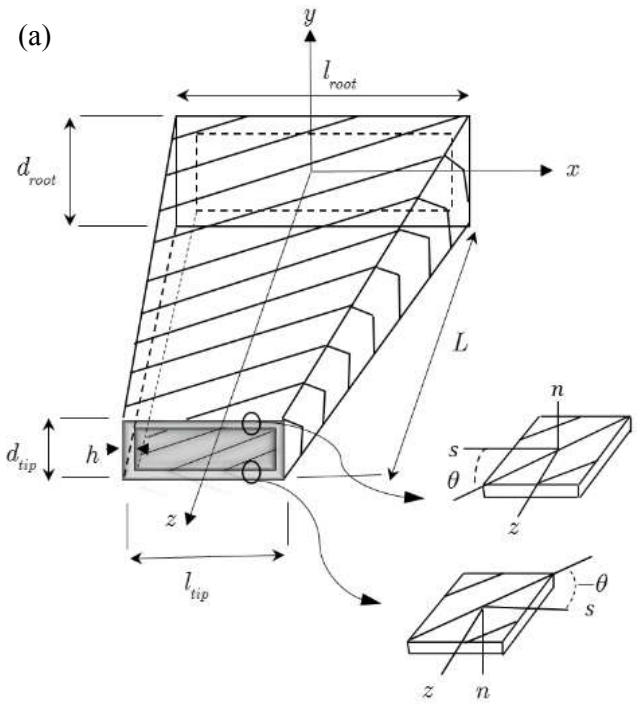

Figure 2-4a Layup configurations for the present structural model
Circumferentially asymmetric stiffness (CAS)

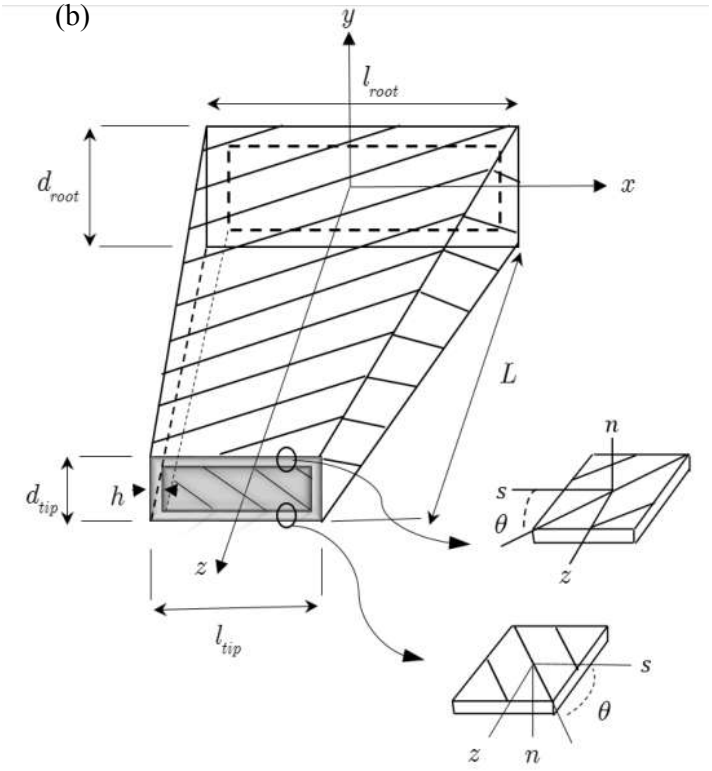

Figure 2-4b Layup configurations for the present structural model

Circumferentially uniform stiffness CUS

2.5.1 Circumferentially Asymmetric Stiffness Configuration (CAS)

In the CAS configuration, fiber angles in the top and bottom flanges of the TWB have opposite sign $\theta(y) = -\theta(-y)$, as shown in Figure a. Similarly, fiber angles in the side walls have opposite sign $\theta(x) = -\theta(-x)$. CAS layup configuration induces strong bending-torsion coupling which may be exploited in load alleviation in wind turbine blades. In the CAS configuration, the non-vanishing stiffness terms are $(a_{11}, a_{22}, a_{33}, a_{44}, a_{55}, a_{66}, a_{77}, a_{88})$ and non-vanishing coupling stiffness terms are

$(a_{12}, a_{18}, a_{28}, a_{56}, a_{37})$. The definition of the non-vanishing stiffness terms are made in Table 2-1 and Table 2-2. In addition to the stiffness terms, a number of mass terms also vanish in the CAS configuration. The non- vanishing mass/inertia terms are $(b_1, b_4, b_5, b_{10}, b_{11}, b_{12})$.

2.5.2 Circumferentially Uniform Stiffness Configuration (CUS)

In the CUS configuration, fiber angles in the top and bottom flanges of the TWB have same sign $\theta(y) = \theta(-y)$, as shown in Figure 4b. Similarly, fiber angles in the side walls have same sign $\theta(x) = \theta(-x)$. CUS layup configuration induces strong extension-torsion coupling which may be exploited in the design of moderate size wind turbine blades as well as helicopter blades. In the CUS configuration, the non-vanishing stiffness terms include $(a_{11}, a_{22}, a_{33}, a_{44}, a_{55}, a_{66}, a_{77}, a_{88})$ and non-vanishing coupling stiffness terms are $(a_{16}, a_{18}, a_{25}, a_{34}, a_{68})$. The definition of the stiffness terms are made in Table 2-1 and Table 2-3. The non-vanishing mass/inertia terms for the CUS configuration are $(b_1, b_4, b_5, b_{10}, b_{11}, b_{12}, b_{16})$.

Table 2-1 Description of the common non-vanishing stiffness terms for both CUS and CAS configurations

a_{11}	Extensional	a_{22}	Chordwise shear
a_{33}	Flapwise shear	a_{44}	Chordwise bending
a_{55}	Flapwise bending	a_{66}	Torsion
a_{77}	Warping	a_{88}	Higher order stress coupling

Table 2-2 Description of the non-vanishing coupling stiffness terms for the CAS configuration

a_{12}	Extension / chordwise shear	a_{18}	Extension / higher order
a_{28}	Chordwise shear / higher order stress	a_{56}	Flapwise bending / torsion
a_{37}	Flapwise shear / warping		

Table 2-3 Description of the non-vanishing coupling stiffness terms for the CUS configuration

a_{16}	Extension / torsion	a_{18}	Extension / higher order
a_{25}	Chordwise shear / flapwise bending	a_{34}	Flapwise shear / chordwise
a_{68}	Torsion / higher order stress		

The effect of fiber orientation on cross sectional stiffness properties for the composite TWB with geometric and material properties given in Table 2-4 for CAS and CUS configurations are investigated in Figure 2-5-Figure 2-8. Figure 2-5 shows the common non-vanishing stiffness terms for both CUS and CAS configurations. Figure 2-6 indicates the non-vanishing coupling stiffness terms for the CAS configuration. Figure 2-7 depicts the non-vanishing coupling stiffness terms for the CUS configuration and Figure 2-8 gives the stiffness coefficients of the nonlinear terms.

Table 2-4 Geometric and material properties of the graphite/epoxy composite rotating TWB[1]

Material properties		**Geometric[1] properties**	
$E_1\ (GPa)$	206.8e9	$L\ (m)$	2.03
$E_2\ (GPa)$	5.17e9	$l\ (m)$	0.254
$E_3\ (GPa)$	5.17e9	$d\ (m)$	0.0681
$G_{12}\ (GPa)$	2.55e9	$h\ (m)$	0.0102
$G_{13}\ (GPa)$	2.55e9	$\beta\ (deg.)$	0
$G_{23}\ (GPa)$	1.38e9	$\theta\ (deg.)$	0-180
$\vartheta_{21} = \vartheta_{32}$	0.25	$\rho\ (kg/m^3)$	1528
ϑ_{31}	0.25	$R_0\ (m)$	0

[1] For the geometric parameters refer to Figure 2-1.

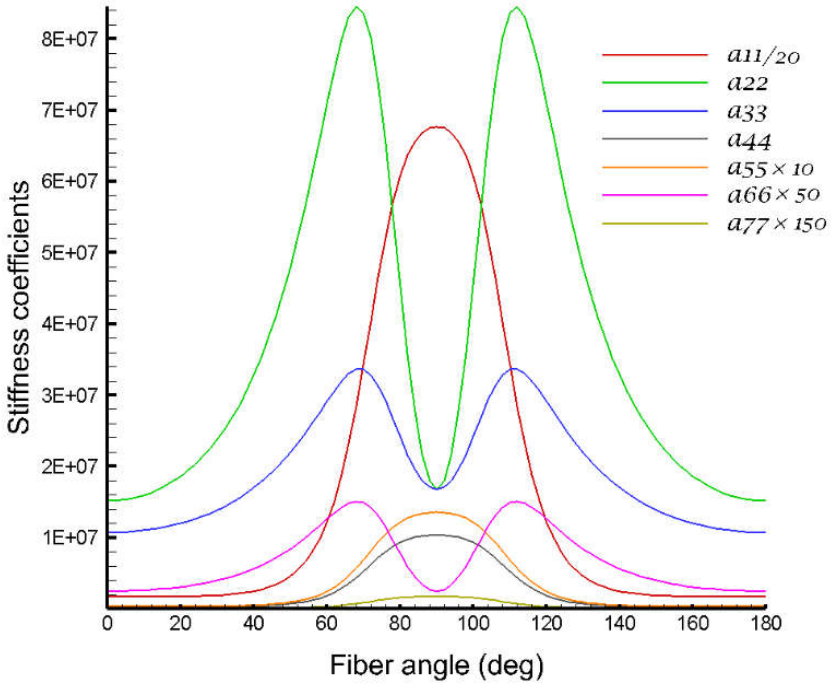

Figure 2-5 Variations of the extensional (a_{11}), chordwise shear (a_{22}), flapwise shear (a_{33}), chordwise bending (a_{44}), flapwise bending (a_{55}), torsion (a_{66}), and the warping (a_{77}) stiffness coefficients versus the ply angle for the uniform TWB for CUS and CAS configurations at zero angular velocity($(\times n \; or \; /n)$ indicates n times magnified or reduced stiffness coefficients)

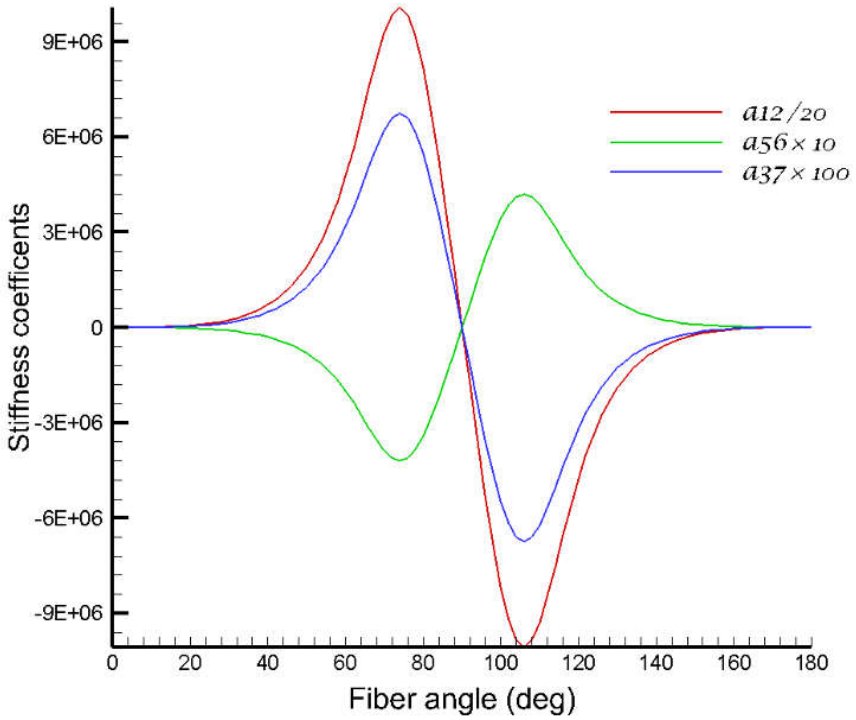

Figure 2-6 Variations of the extension / chordwise shear (a_{12}), flapwise bending / torsion (a_{56}), flapwise shear / warping (a_{37}) coupling stiffness coefficients versus the ply angle for uniform TWB with CAS configuration at zero angular velocity($(\times n \; or \; /n)$ indicates *n* times magnified or reduced stiffness coefficients)

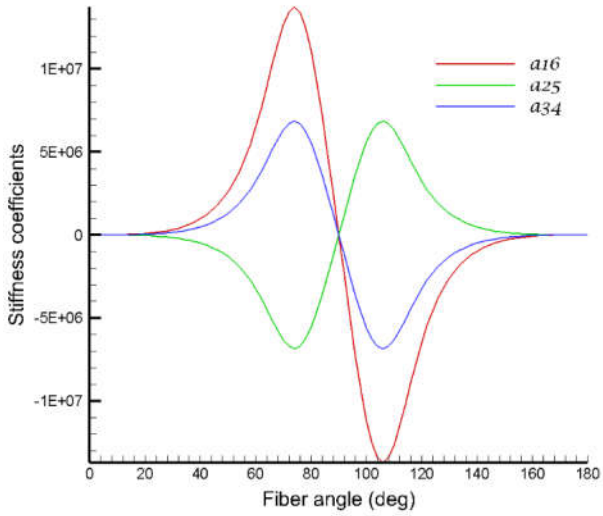

Figure 2-7 Variations of the extension / torsion (a_{16}), chordwise shear / flapwise bending (a_{25}), flapwise shear / chordwise bending (a_{34}) coupling stiffness coefficients versus the ply angle for uniform TWB with CUS configuration at zero angular velocity

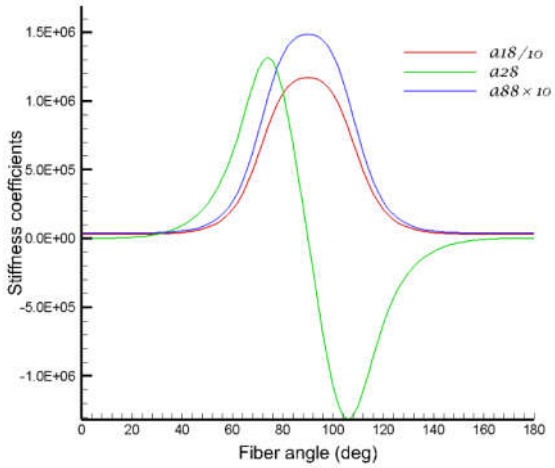

Figure 2-8 Variations of the extension / higher order (a_{18}), chordwise shear / higher order stress (a_{28}) coupling and higher order stress coupling (a_{88}) stiffness coefficients versus the ply angle for uniform TWB at zero angular velocity($(\times n \; or \; /n)$ indicates *n* times magnified or reduced stiffness coefficients)

In the following, in order to investigate the linear dynamic characteristics of rotating composite TWB, by ignoring the nonlinear terms, the governing equations for the CAS and CUS layup configurations are derived in terms of the non-vanishing 8×8 cross section stiffness coefficients (a_{ij}).

For the CAS configuration, the governing system of equations including the flapwise bending / torsion and extension / chordwise transverse shear coupling, are obtained and given by Equations (2-93)-(2-98). It should be noted that in deriving Equations (2-93)-(2-98), beam constitutive equation Equation (2-87) is utilized to obtain the equations in terms of displacement and rotations of the TWB and also non-linear terms in Equations (2-74)-(2-79) and Equation (2-87) are omitted.

$$\delta u_0 : a_{12}\left(w_0''\right) + a_{22}\left(u_0' + \theta_y\right)' - b_1\begin{pmatrix}\ddot{u}_0 + 2\dot{w}_0\Omega - u_0\Omega^2 - \\ \Omega^2\left[R\left(z\right)u_0'' + R'\left(z\right)u_0'\right]\end{pmatrix} + p_x = 0 \tag{2-93}$$

$$\delta v_0 : a_{33}\left(v_0' + \theta_x\right)' - a_{37}\left(\phi''\right)' - b_1\left(\ddot{v}_0 - \Omega^2\left[v_0''R\left(z\right) + R'\left(z\right)v_0'\right]\right) + p_y = 0 \tag{2-94}$$

$$\delta w_0 : a_{11}w_0'' + a_{12}\left(u_0' + \theta_y\right)' - b_1\left(\ddot{w}_0 - 2\dot{u}_0\Omega - \left(z + w_0 + R_0\right)\Omega^2\right) + p_z = 0 \tag{2-95}$$

$$\begin{aligned}&\delta\theta_x : -a_{33}\left(v_0' + \theta_x\right) + a_{37}\left(\phi'\right)' + a_{55}\left(\theta_x'\right)' + a_{56}\left(\phi'\right)' - \\ &\left(b_4 + b_{12}\right)\left(\ddot{\theta}_x - \Omega^2\theta_x + 2\Omega\dot{\phi}\right) + m_x = 0\end{aligned} \tag{2-96}$$

$$\delta\theta_y : -a_{12}\left(w_0'\right) - a_{22}\left(u_0' + \theta_y\right) + a_{44}\left(\theta_y'\right)' - \left(b_5 + b_{11}\right)\left(\ddot{\theta}_y - \Omega^2\theta_y\right) + m_y = 0 \tag{2-97}$$

$$\begin{aligned}&\delta\phi : a_{37}\left(v_0''' + \theta_x''\right) + a_{56}\left(\theta_x'\right)' + a_{66}\left(\phi'\right)' - a_{77}\left(\phi''\right)'' + \\ &\left(b_4 + b_{12}\right)\Omega^2\left(R\left(z\right)\phi'' + R'\left(z\right)\phi'\right) + \left(b_5 + b_{11}\right)\Omega^2\left(R\left(z\right)\phi'' + R'\left(z\right)\phi'\right) - \\ &\left(b_4 + b_{12}\right)\left(\ddot{\phi} - 2\Omega\dot{\theta}_x - \Omega^2\phi\right) - \left(b_5 + b_{11}\right)\left(\ddot{\phi} + \Omega^2\phi\right) - b_{10}\left(-\ddot{\phi}'' + \Omega^2\phi''\right) + m_z = 0\end{aligned} \tag{2-98}$$

For the rotating TWB clamped at the root $(z = 0)$ and free at the tip $(z = L)$ the corresponding boundary conditions are obtained from Equations (2-80)-(2-86) and presented by Equations (2-99)-(2-105).

$$\begin{aligned} &at \quad z = 0 \qquad \delta u_0 = 0, or \\ &at \quad z = L \qquad a_{12}\left(w_0'\right) + a_{22}\left(u_0' + \theta_y\right) + b_1\Omega^2 u_0' R\left(z\right) = 0 \end{aligned} \tag{2-99}$$

$$\begin{aligned} &at \quad z = 0 \qquad \delta v_0 = 0, or \\ &at \quad z = L \qquad a_{33}\left(\theta_x + v_0'\right) - a_{37}\left(\phi'\right)' + b_1\Omega^2 v_0' R\left(z\right) = 0 \end{aligned} \tag{2-100}$$

$$\begin{aligned} &at \quad z = 0 \qquad \delta w_0 = 0, or \\ &at \quad z = L \qquad a_{11}\left(w_0'\right) + a_{12}\left(u_0' + \theta_y\right) = 0 \end{aligned} \tag{2-101}$$

$$\begin{aligned} &at \quad z = 0 \qquad \delta\theta_x = 0, or \\ &at \quad z = L \qquad a_{55}\left(\theta_x'\right) + a_{56}\left(\phi'\right) = 0 \end{aligned} \tag{2-102}$$

$$\begin{aligned} &at \quad z = 0 \qquad \delta\theta_y = 0 \\ &at \quad z = L \qquad a_{44}\left(\theta_y' + v_0'\phi'\right) = 0 \end{aligned} \tag{2-103}$$

$$\begin{aligned} &at \quad z = 0 \qquad \delta\phi = 0, or \\ &at \quad z = L \qquad a_{37}\left(\theta_x + v_0'\right)' + a_{56}\left(\theta_x'\right) + a_{66}\left(\phi\right)' - a_{77}\left(\phi''\right)' + \\ &\left(b_4 + b_{12} + b_5 + b_{11}\right)\Omega^2 R\left(z\right)\phi' = 0 \end{aligned} \tag{2-104}$$

$$\begin{aligned} &at \quad z = 0 \qquad \delta\phi' = 0, or \\ &at \quad z = L \qquad a_{37}\left(\theta_x + v_0'\right) - a_{77}\left(\phi'\right)' = 0 \end{aligned} \tag{2-105}$$

Similarly, linear equations of motion and the related boundary conditions of composite TWB for the CUS configuration including extension / torsion and chordwise shear / flapwise bending coupling are derived and presented in Equations (2-106)-(2-111).

$$\delta u_0 : a_{22}\left(\theta_y + u_0'\right)' + a_{25}\left(\theta_x'\right)' - b_1\begin{pmatrix}\ddot{u}_0 + 2\dot{w}_0\Omega - u_0\Omega^2 - \\ \Omega^2\left[R\left(z\right)u_0'' + R'\left(z\right)u_0'\right]\end{pmatrix} + p_x = 0 \tag{2-106}$$

$$\delta v_0 : a_{33}\left(\theta_x + v_0'\right)' + a_{34}\left(\theta_y'\right)' - b_1\left(\ddot{v}_0 - \Omega^2\left[v_0'' R\left(z\right) + R'\left(z\right)v_0'\right]\right) + p_y = 0 \tag{2-107}$$

$$\delta w_0 : a_{11}\left(w_0''\right) + a_{16}\left(\phi'\right)' - b_1\left(\ddot{w}_0 - 2\dot{u}_0\Omega - \left(z + w_0 + R_0\right)\Omega^2\right) + p_z = 0 \tag{2-108}$$

$$\delta\theta_x : a_{25}\left(u_0' + \theta_y\right)' - a_{33}\left(v_0' + \theta_x\right) - a_{34}\left(\theta_y'\right) + a_{55}\left(\theta'\right)' - \left(b_4 + b_{12}\right)\left(\ddot{\theta}_x - \Omega^2\theta_x + 2\Omega\dot{\phi}\right) + m_x = 0 \tag{2-109}$$

$$\delta\theta_y : -a_{22}\left(u_0' + \theta_y\right) + a_{25}\left(-\theta_x'\right) + a_{34}\left(v_0' + \theta_x\right)' + a_{44}\left(\theta_y'\right)' - \left(b_5 + b_{11}\right)\left(\ddot{\theta}_y - \Omega^2\theta_y\right) + m_y = 0 \tag{2-110}$$

$$\delta\phi : a_{16}\left(w_0''\right) + a_{66}\left(\phi'\right)' - a_{77}\left(\phi''\right)'' + \left(b_4 + b_{12}\right)\Omega^2\left(R\left(z\right)\phi'' + R'\left(z\right)\phi'\right) + \left(b_5 + b_{11}\right)\Omega^2\left(R\left(z\right)\phi'' + R'\left(z\right)\phi'\right) - \left(b_4 + b_{12}\right)\left(\ddot{\phi} - 2\Omega\dot{\theta}_x - \Omega^2\phi\right) - \left(b_5 + b_{11}\right)\left(\ddot{\phi} + \Omega^2\phi\right) - \left(b_{10} + b_{16}\right)\left(-\ddot{\phi}'' + \Omega^2\phi''\right) + m_z = 0 \tag{2-111}$$

The associated boundary conditions for the clamped $(z = 0)$ free $(z = L)$ rotating TWB with the CUS configuration are given by Equations (2-112)-(2-118).

$$\begin{aligned} &at \quad z = 0 \qquad \delta u_0 = 0, or \\ &at \quad z = L \qquad a_{22}\left(u_0' + \theta_y\right) + a_{25}\left(\theta_x'\right) + b_1\Omega^2 u_0' R\left(z\right) = 0 \end{aligned} \tag{2-112}$$

$$\begin{aligned} &at \quad z = 0 \qquad \delta v_0 = 0 \\ &at \quad z = L \qquad a_{33}\left(v_0' + \theta_x\right) + a_{34}\left(\theta_y'\right) + b_1\Omega^2 v_0' R\left(z\right) = 0 \end{aligned} \tag{2-113}$$

$$\begin{aligned} &at \quad z = 0 \qquad \delta w_0 = 0, or \\ &at \quad z = L \qquad a_{11}\left(w_0'\right) + a_{16}\left(\phi\right)' = 0 \end{aligned} \tag{2-114}$$

$$\begin{aligned} &at \quad z = 0 \qquad \delta\theta_x = 0, or \\ &at \quad z = L \qquad a_{25}\left(u_0' + \theta_y\right) + a_{55}\left(\theta_x'\right) = 0 \end{aligned} \tag{2-115}$$

$$\begin{aligned} &at \quad z = 0 \qquad \delta\theta_y = 0, or \\ &at \quad z = L \qquad a_{34}\left(v_0' + \theta_x\right) + a_{44}\left(\theta_y'\right) = 0 \end{aligned} \tag{2-116}$$

$$\begin{aligned} &at \quad z = 0 \qquad \delta\phi = 0, or \\ &at \quad z = L \qquad 2a_{16}\left(w_0'\right) + a_{66}\left(\phi'\right) - a_{77}\left(\phi''\right)' + \left(b_4 + b_{12} + b_5 + b_{11}\right)\Omega^2 R\left(z\right)\phi' = 0 \end{aligned} \tag{2-117}$$

$$\begin{aligned} &at \quad z = 0 \qquad \delta\phi' = 0, or \\ &at \quad z = L \qquad a_{77}\left(\phi'\right)' = 0 \end{aligned} \tag{2-118}$$

2.6 Non-Uniform Geometric Features

In the preceding section, effects of taper ratio and pretwist angle were ignored and the governing equations of motion are obtained for an untwisted and untapered thin walled beam. Now, in this section two geometric nonuniformities (linear taper and pretwist) are mathematically described to help better understanding of the effect of these nonuniformity in structural dynamics of composite TWB.

2.6.1 Tapered Rotating TWB

In order to model the tapered TWB, width and height of the TWB are assumed to vary as given in Equation (2-119),

$$\begin{Bmatrix} l(\eta) \\ d(\eta) \end{Bmatrix} = \begin{bmatrix} 1-\eta(1-\sigma_l) & 0 \\ 0 & 1-\eta(1-\sigma_d) \end{bmatrix} \begin{Bmatrix} l_{root} \\ d_{root} \end{Bmatrix} \tag{2-119}$$

Where $l(\eta)$ and $d(\eta)$ are the width and the height of local cross section, respectively, η is the non-dimensional spanwise coordinate $(0 < \eta < 1)$ shown in Figure 2-4. Parameters $\sigma_l(\sigma_l = l_{tip}/l_{root})$ and $\sigma_d(\sigma_d = d_{tip}/d_{root})$ represent the ratio of the tip width and the tip height of the TWB to the root tip and root height of the TWB, respectively.

2.6.2 Pretwisted Rotating TWB

In order to enhance the performance and aeroelastic characteristics of the rotary blades of turbomachinery, helicopter and wind turbine systems, pretwist is applied to the blades during the manufacturing. Pretwist which varies from the root of the blade to the tip of the blade is also called as geometric twist. In the present study, the pretwist model of Song et al. [94] and Librescu [92] is adopted, and the pretwist is applied before any deformation takes place. In the pretwisted TWB, the inertia and stiffness

quantities of the cross section are determined in the rotated coordinate system (x^p, y^p, z^p) shown in Figure 2-1. At a section of the TWB, the coordinate system (x^p, y^p, z^p) is obtained by rotating the coordinate system (x, y, z) about the beam axis z by the local twist angle $\beta(z)$. The transformation relations between the coordinate systems (x, y, z) and (x^p, y^p, z^p) are given by Equation (2-120).

$$\begin{aligned} x &= x^p(s)\cos\Big(\beta(z)\Big) - y^p(s)\sin\Big(\beta(z)\Big) \\ y &= x^p(s)\sin\Big(\beta(z)\Big) + y^p(s)\cos\Big(\beta(z)\Big) \\ z &= z^p \end{aligned} \tag{2-120}$$

In the pretwisted model of the TWB, cross section form is preserved, and primary and secondary warping as well as transverse shear and rotary inertia are included in the structural model. Due to the pretwist, stiffness (a_{ij}) and the inertia (b_i) terms of the TWB become a function of the twist angle $\beta(z)$ $(\beta(z) = \beta_0\, z/L)$, with β_0 being the pretwist angle at tip section of the TWB, and in the present study pretwist is assumed to vary linearly along of the span of the TWB. In this respect, stiffness coefficients a_{ij} and inertia terms b_i are expressed with respect to the twisted coordinate system (x^p, y^p, z^p) instead of the original coordinate system (x, y, z) by applying the transformation given by Equation (2-120). Resulting relations between the stiffness coefficients and reduced mass/inertia terms defined with respect to the coordinate system at the root of the TWB (x, y, z) and the local pretwisted coordinate system (x^p, y^p, z^p) are explicitly given in APPENDIX C.

2.7 Free Vibration Analysis of the Geometrically Linear TWB

2.7.1 Extended Galerkin Method

Due to the complex boundary conditions and complex couplings involved in the above equations, it is difficult to generate proper comparison functions that fulfil all the geometric and natural boundary conditions. The difficulty can be bypassed utilizing the modified Galerkin method, where the discretization process is performed directly in the extended Hamilton's principle in Equation (2-36) [95]. Therefore, in order to solve the governing partial differential equation of motion for the natural frequencies and the associated mode shapes, the Extended Galerkin Method (EGM) in conjunction with the separation of variation method are applied. The main feature of this method is to choose appropriate trial functions that only satisfy the essential boundary conditions, while the effect of the natural boundary conditions is kept in the governing system.

The linear combination of the shape functions is used and the number of terms in the series is incremented gradually until convergence is achieved. Application of the EGM results symmetric structural mass and stiffness matrices. In the EGM, the unknown deformation variables are approximated in series form by,

$$\begin{aligned} u_0(z,t) &= \sum_{i=1}^{N} \eta_i^u(t)\psi_i^u(z), \qquad v_0(z,t) = \sum_{i=1}^{N} \eta_i^v(t)\psi_i^v(z) \\ w_0(z,t) &= \sum_{i=1}^{N} \eta_i^w(t)\psi_i^w(z), \qquad \theta_x(z,t) = \sum_{i=1}^{N} \eta_i^x(t)\psi_i^x(z) \\ \theta_y(z,t) &= \sum_{i=1}^{N} \eta_i^y(t)\psi_i^y(z), \qquad \phi(z,t) = \sum_{i=1}^{N} \eta_i^\phi(t)\psi_i^\phi(z) \end{aligned} \tag{2-121}$$

where, the trial functions $\psi^u, \psi^v, \psi^w, \psi^x, \psi^y, \psi^\phi$ have to be reasonably chosen to satisfy the essential boundary conditions, and N is the number of terms in the series which is chosen suitably to achieve converge. Admissible functions are assumed in the form of N degree polynomial $(\psi_i = z^i, i = 1,2,...,N)$ and the coefficients of the

polynomial are taken as one for the solution of the free vibration problem. The state vector of the time dependent variables is defined by Equation (2-122).

$$\eta = \left\{ \left\{\eta^u\right\}^T \quad \left\{\eta^v\right\}^T \quad \left\{\eta^w\right\}^T \quad \left\{\eta^x\right\}^T \quad \left\{\eta^y\right\}^T \quad \left\{\eta^\phi\right\}^T \right\}^T \tag{2-122}$$

Inserting Equation (2-121) into Equation (2-49), one can write the kinetic energy in the linear and discrete form,

$$T = \frac{1}{2}\dot{\eta}^T M_s \dot{\eta} \tag{2-123}$$

Similarly, by inserting Equation (2-121) into Equations (2-39) and (2-66) in linear form, the total strain energy can be written as,

$$V_{total} = V + V_{cf} = \frac{1}{2}\eta^T K_s \eta \tag{2-124}$$

Where M_s and K_s are the structural mass and stiffness matrices defined in Appendix D for the CAS and CUS configurations.

Introducing Equations (2-123) and (2-124) in Hamilton principle given in Equation (2-36), integrating with respect to time, and knowing $\delta\eta = 0$ at $t = t_1, t_2$, we can obtain the discrete governing equations of motion as,

$$\left[M_s\right]\left\{\ddot{\eta}\right\} + \left[K_s\right]\left\{\eta\right\} = 0 \tag{2-125}$$

If the state vector is redefined as,

$$G = \left\{ \left\{\eta\right\} \quad \left\{\dot{\eta}\right\} \right\} \tag{2-126}$$

Equation (2-125) can be expressed in state space form as given in Equation (2-127).

$$\begin{aligned} &\dot{G} = \mathbb{R}G, \\ &\mathbb{R} = \begin{bmatrix} 0 & I \\ -M_s^{-1}K_s & 0 \end{bmatrix} \end{aligned} \tag{2-127}$$

For the eigenvalue analysis, state vector can be expressed as,

$$G = \bar{G} e^{\lambda t} \tag{2-128}$$

Where $\bar{G}$ is a constant vector of amplitudes and λ is the eigenvalue. Substituting Equation (2-128) into Equation (2-127), the eigenvalue problem given by Equation (2-129) is obtained.

$$\left(\mathbb{R} - I\lambda\right)\bar{G} = 0 \tag{2-129}$$

Equation (2-129) can be solved for the eigenvalues λ_r and the corresponding eigenvectors $\bar{G}_r$. For the free vibration problem, eigenvalues are obtained as complex conjugate roots without the real part $(\lambda_r = \pm iw_r)$.

2.7.2 Results and Discussion

In this section results are presented for the free vibration characteristics of CAS and CUS configuration pretwisted rotating TWBs. Using 3D plots, the effects of fiber angle, pretwist, angular velocity on the first five natural frequencies, and mode shapes for both CAS and CUS configuration TWBs are displayed. It should be noted that the TWB model developed in the present study forms the structural model of the aeroelastic system which is used for the aeroelastic stability analysis of composite wings and rotor blades.

In order to validate the structural model, natural frequencies and mode shapes are compared with the results obtained by finite element (FE) analysis software MSC. Nastran. For this purpose, the first four natural frequencies of the non-rotating TWB are compared with Nastran results for the untwisted and pretwisted cases. In the FE model, 2D shell elements with drilling degrees of freedom are utilized with 3D orthotropic material definition. The structures are clamped at the root and let free at the tip. For modal analysis in MSC. Nastran solution sequence SOL 103 is used. For pretwisted model, twist distribution varies linearly with respect to *z* while at the tip is $40^{\circ}\left(\beta_0 = 40^{\circ}\right)$.

2.7.2.1 Case 1: CAS Configuration

For the material and geometric properties of the TWB given in Table 2-4, Table 2-5 and Table 2-6 compare the first four natural frequencies and dominant modes with the ones calculated by MSC Nastran for the untwisted and the pretwisted, nonrotating TWB, respectively. It is seen that the results obtained with the TWB model are in reasonable agreement with the results of the FE model for the untwisted and the twisted models.

Table 2-5 First four natural frequencies for the fiber angle $\theta = 45°, \Omega = 0°, \beta_0 = 0°$ for the CAS configuration untwisted TWB

	Present study		**MSC NASTRAN**	
	Frequency (Hz)	Dominant mode	Frequency (Hz)	Dominant mode
1	9.15	1st flapwise bending	9.24	1st flapwise bending
2	27.7	1st chordwise bending	25.58	1st chordwise bending
3	56.7	2nd flapwise bending	56.17	2nd flapwise bending
4	151	Torsion	148.14	Torsion

Table 2-6 First four natural frequencies for the fiber angle $\theta = 45°, \Omega = 0°$ for the CAS configuration TWB with pretwist $\beta_0 = 40°$

	Present study		**MSC NASTRAN**	
	Frequency (Hz)	Dominant mode	Frequency (Hz)	Dominant mode
1	10.05	1st flapwise bending	9.37	1st flapwise bending
2	27.2	1st chordwise bending	24.32	1st chordwise bending
3	62.68	2nd flapwise bending	59.77	2nd flapwise bending
4	148	Torsion	146.12	Torsion

In order to compare the mode shapes, 2nd flapwise – torsion mode shape of untwisted TWB with CAS configuration and $\theta = 45^0$ are obtained using present code and Nastran are compared in Figure 2-9.

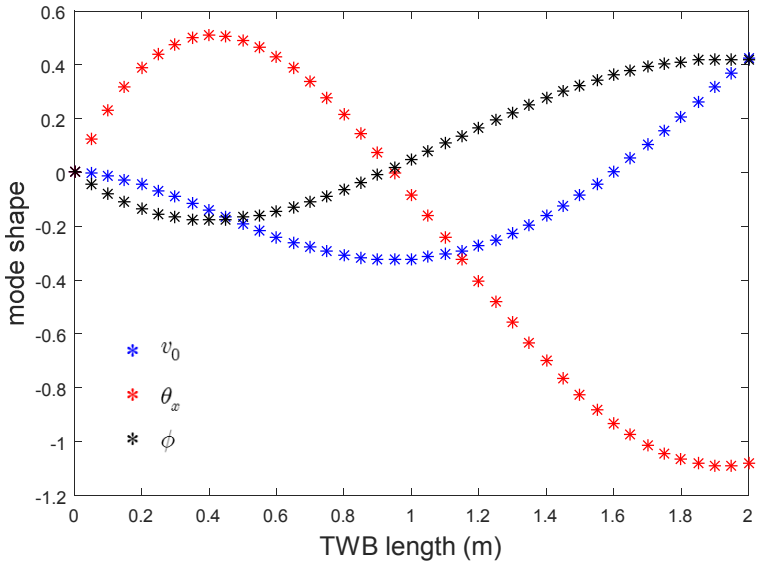

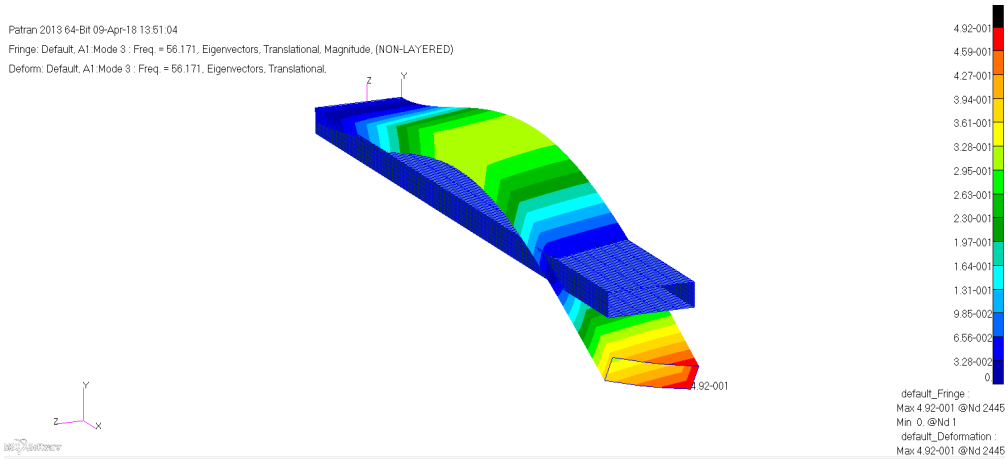

Figure 2-9 second flapwise-torsion mode shape of TWB for CAS configuration with fiber angle 45 degree (a) present model (natural frequency =56.7 Hz) (b)MSC NASTRAN (natural frequency =56.17 Hz)

2.7.2.1.1 Effects of the Fiber Angle on the Natural Frequencies and the Mode Shapes

Figure 2-10a-d show the variation of first four natural frequencies of the TWB with no pretwist with the fiber angle and the rotational speed in 3D plots. Since the natural frequencies are symmetric with respect to fiber angle in the range 0° - -90° in Figure 2-10a-d, the results are just shown for fiber angles between 0° and -90°. Generally, all natural frequencies increase by increasing the angular velocity. It is seen that the dominant mode varies with the angular velocity for each natural frequency, and in Figure 2-10a-d they are indicated by the capitals C for chordwise bending, F for flapwise bending and T for torsion.

Figure 2-10a-d also show that, natural frequencies of the modes which are dominant in flapwise bending increase with angular velocity at a higher rate compared to the torsion or chordwise bending dominant modes. This observation shows that the centrifugal stiffening effect plays more important role in the flapwise dominant modes. On the other hand, centrifugal stiffening has slightly greater effect on the torsion dominant modes than the chordwise bending mode.

In Figure 2-10a, it is seen that for the fiber angles in the range [0° - -60°], fundamental natural frequency related to the flapwise bending mode grows with the increase in the angular velocity until a certain angular velocity at which dominant mode changes from flapwise bending to chordwise bending. After the switching of the modes, the effect of centrifugal stiffening on the chordwise bending mode is seen to lessen than the effect of centrifugal stiffening on the flapwise bending mode. For the fibers angle of -75° and -90°, the fundamental mode remains flapwise bending also in the higher angular velocities. In general, all natural frequencies of the flapwise bending mode increase with the increase in the ply angle. This trend can be seen as well in the torsion and chordwise bending modes in the fiber angle range of $0° < \theta < -75°$. However, in 2nd and 3rd natural frequencies, the opposite trend is seen at higher fiber angles. This phenomenon may be explained by referring to Figure 2-5 and Figure 2-6 which give the stiffness variation versus the fiber angle.

(a) 1st mode

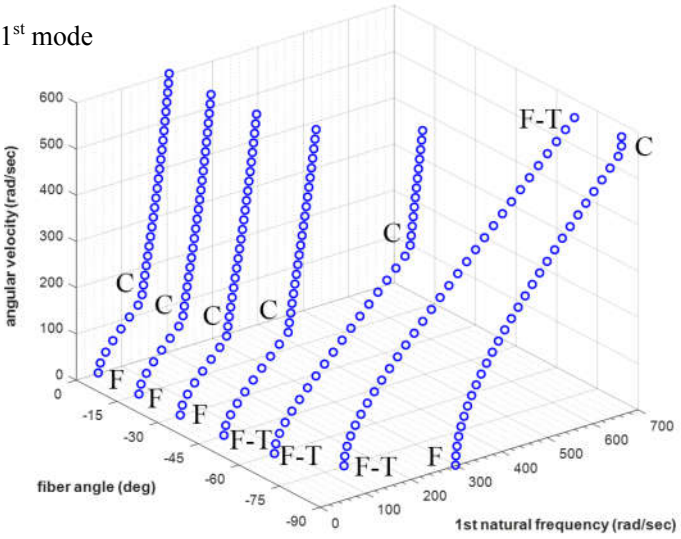

(b) 2nd mode

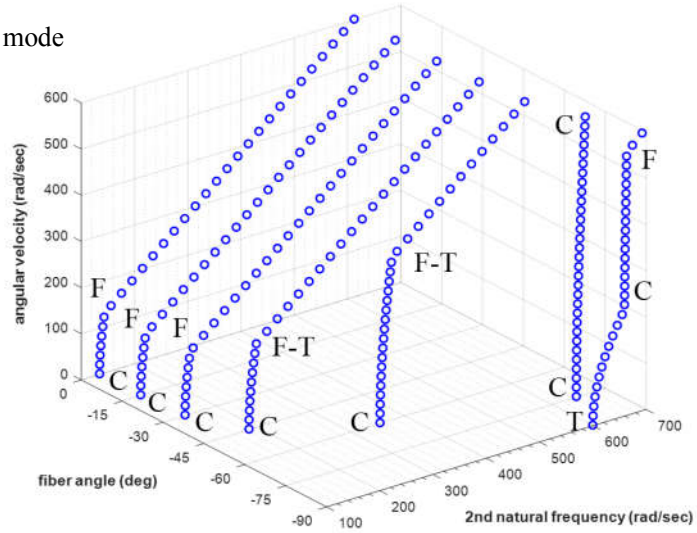

(c) 3rd mode

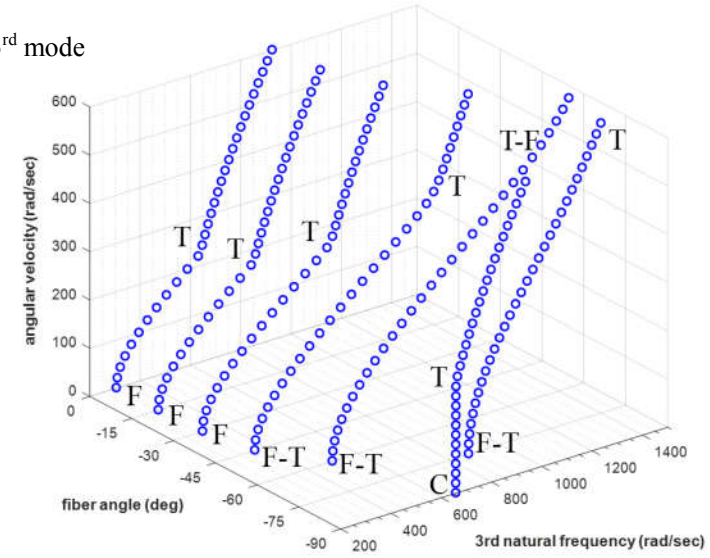

(d) 4th mode

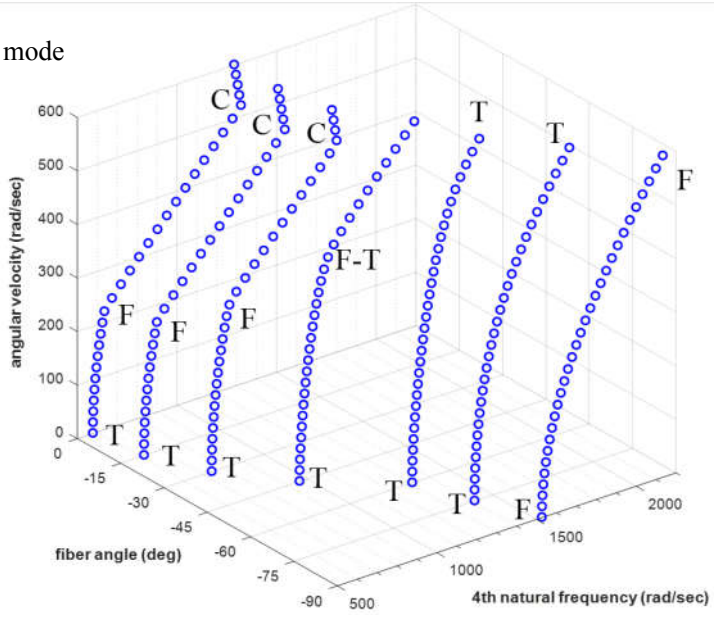

Figure 2-10 First four coupled natural frequencies versus the fiber angle for different angular velocities for the CAS configuration untwisted TWB / Dominant modes: C: Chordwise bending, F: Flapwise bending, T:Torsion

2.7.2.1.2 Effect of the PreTwist on the Natural Frequencies and Mode Shapes

For the CAS configuration TWB, Figure 2-11a-d display the variation of the first four natural frequencies of the rotating beam as a function of the fiber angle and the angular velocity for TWBs with and without pretwist. In Figure 2-11a-d, the blue symbols show the data for the TWB without pretwist and the red symbols show the data for the TWB with the tip pretwist angle of $40^{\circ}\left(\beta_0 = 40^{\circ}\right)$. To aid the discussion the natural frequency results, the variation of the flapwise bending (a_{55}), chordwise bending (a_{44}), torsion (a_{66}), and flapwise bending-torsion coupling (a_{56}), stiffness coefficients with the fiber angle for the uniform and the pretwisted beam are plotted in Figure 2-12. Figure 2-11a and Figure 2-11b show that for the first and the second modes which are flapwise bending and chordwise bending, the effect of pretwist is not considerable on the natural frequencies except for higher fiber angles $(\theta = -75^{\circ}, -90^{\circ})$. In general, it is seen that stiffening effect of the pretwist is higher at low angular velocities and for higher fiber angles. Figure 2-12 clearly shows that at higher fiber angles, the effect of pretwist on the flapwise bending stiffness of the TWB is more pronounced. With the increase in the angular velocity, the effect of pretwist on the first natural frequency becomes insignificant. The effect of pretwist on the 3rd natural frequency appears to be more pronounced for the whole range of the fiber angle but for a limited fiber angle ranges (-75° - -90°) for the 4th natural frequency. For the 3rd natural frequency, for the range of angular velocity in which the dominant mode is the flapwise bending mode, pretwist has a stiffening effect and pretwisted TWB has higher natural frequencies than the TWB without pretwist. As Figure 2-11c shows, for the fiber angle of -75° the effect of pretwist on the natural frequencies of the TWB is significant. When the modes switches from flapwise bending to torsional at high angular velocities (Figure 2-11c), it is seen that the pretwist has softening effect on the natural frequency. For the fiber angle of -90°, vibration mode is chordwise bending at lower angular velocities and pretwist has insignificant effect on the natural frequency. However, at higher angular velocities, mode switches to torsion and for the torsional mode pretwist has softening

effect and natural frequencies decrease for the pretwisted TWB. For the 4th lowest mode, and for the fiber angles of $-75°$ and $-90°$ flapwise bending mode is dominant and the stiffening effect of pretwist is clear. In general, it can be concluded that at higher angular velocities, the effect of pretwist on the natural frequencies decreases.

(a) 1st mode

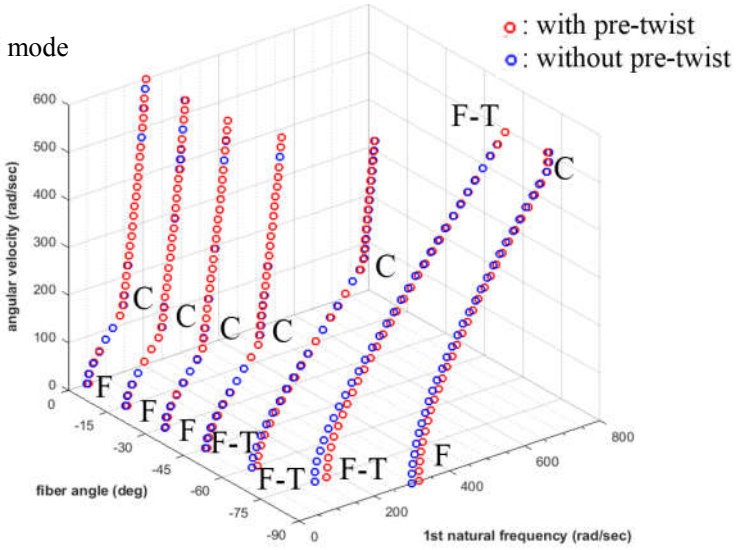

(b) 2nd mode

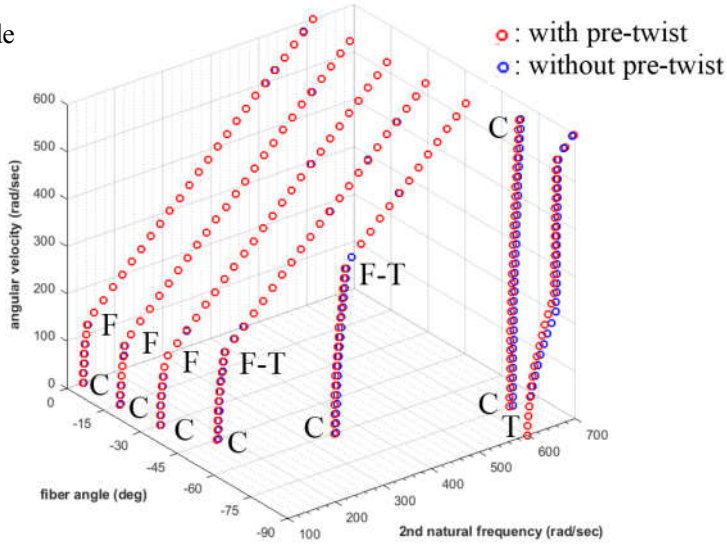

(c) 3rd mode

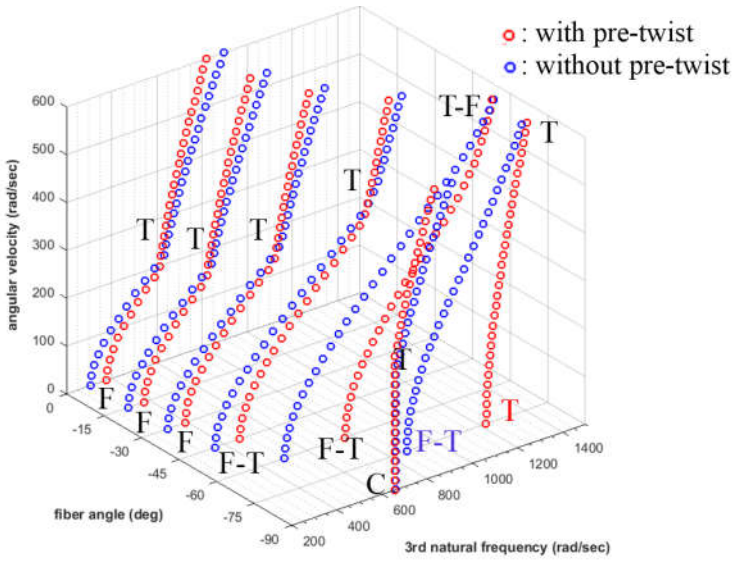

(d) 4th mode

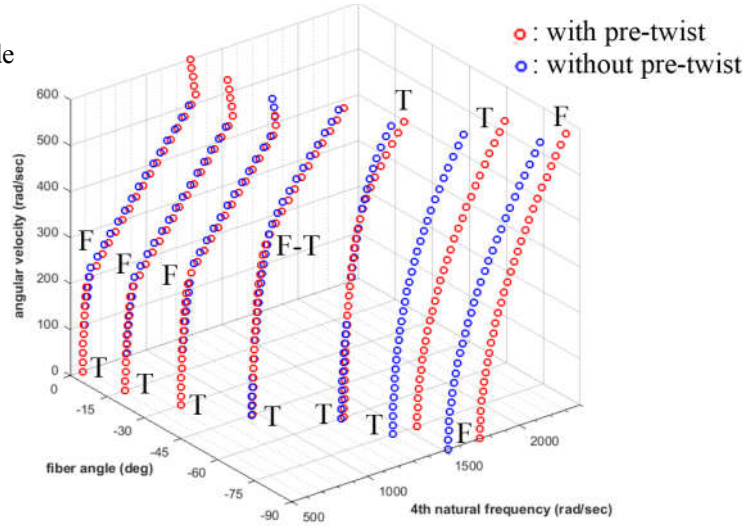

Figure 2-11 Comparison of the natural frequencies of CAS configuration TWBs with pretwist (red circle) and without pretwist (blue circle) versus the fiber angle and angular velocity (/ Dominant modes; C: Chordwise bending, F: Flapwise bending, T:Torsion

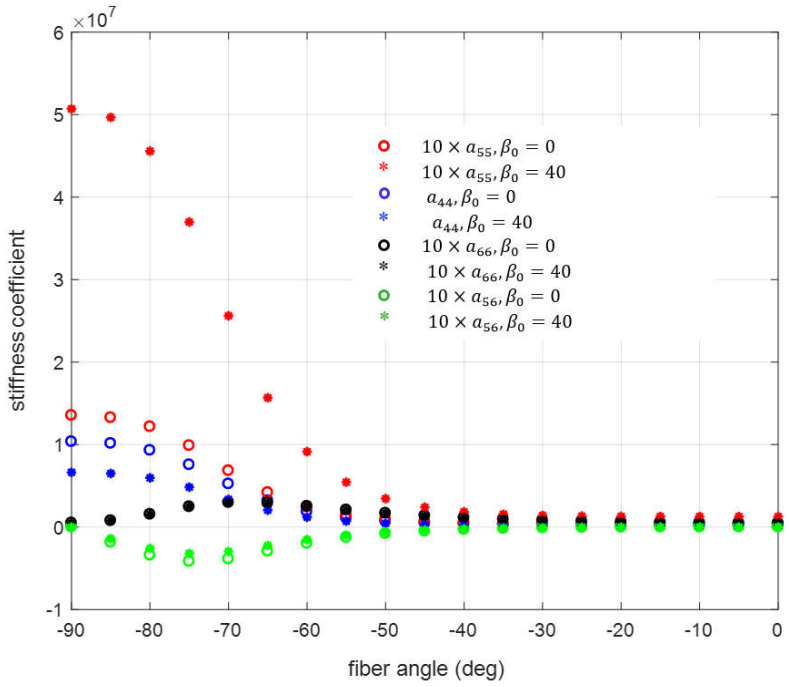

Figure 2-12 Variation of flapwise bending(a_{55}), chordwise bending(a_{44}), torsion (a_{66}), and flapwise bending -torsion(a_{56}) stiffness coefficients versus the fiber for uniform and tapered TWB with CAS configuration at zero angular velocity ($\times 10$) indicates 10 times magnified stiffness coefficients)

2.7.2.2 Case 2: CUS Configuration

For the material and geometric properties of the TWB given in Table 2-4, Table 2-7 and Table 2-8 compare the first four natural frequencies and dominant modes with the ones calculated by MSC Nastran for the untwisted and the pretwisted, nonrotating TWB, respectively. It is seen that the results obtained with the TWB model are in reasonable agreement with the results of the FE model for the untwisted and TWB with pretwist.

Table 2-7 First four natural frequencies for the fiber angle $\theta = 45°, \Omega = 0°, \beta_0 = 0°$ for the CUS configuration untwisted TWB

	Present study		MSC NASTRAN	
	Frequency (Hz)	Dominant mode	Frequency (Hz)	Dominant mode
1	9.39	1st flapwise bending	9.22	1st flapwise bending
2	27.63	1st chordwise bending	25.32	1st chordwise bending
3	59.19	2nd flapwise bending	56.74	2nd flapwise bending
4	125.56	Torsion	125.32	Torsion

Table 2-8 natural frequencies for the fiber angle $\theta = 45°, \Omega = 0°$ for the CAS configuration TWB with pretwist $\beta_0 = 40°$

	Present study		MSC NASTRAN	
	Frequency(Hz)	Dominant mode	Frequency (Hz)	Dominant mode
1	10.02	1st flapwise bending	9.24	1st flapwise bending
2	26.12	1st chordwise bending	23.94	1st chordwise bending
3	64.26	2nd flapwise bending	61.82	2nd flapwise bending
4	122.01	Torsion	120.4	Torsion

2.7.2.2.1 Effect of the Fiber Angle on the Natural Frequencies and Mode Shapes

Figure 2-13a-d illustrate the variation of the first four natural frequencies of rotating TWB without pretwist as a function of the fiber angle and angular velocity. For the first natural frequency, for fiber angles $0° < \theta < -60°$, with the increase in the angular velocity mode switching occurs from flapwise bending to chordwise bending beyond a certain angular velocity. This pattern of mode switching has also been detected in 2nd, 3rd and 4th modes. In the second mode, mode switching occurs from chordwise bending to flapwise bending, and in the third mode switching occurs from flapwise bending to torsion. The nature of the fundamental vibration mode (mode 1) for the CUS and the CAS configurations is the same throughout the range of the angular velocity. As in the CAS configuration, natural frequency of the flapwise bending mode is affected the most from the increase of the angular velocity. For a wide range of fiber angles, second vibration modes at low angular velocities are mostly chordwise bending except for the fiber angles $-75°$ and $-90°$. By increasing the angular velocity, the second mode switches from highly chordwise bending to highly flapwise bending, and the rate of frequency increase with the angular velocity becomes greater compared to

the rate of increase of the natural frequency of the dominant chordwise bending mode with the angular velocity.

(a) 1st mode

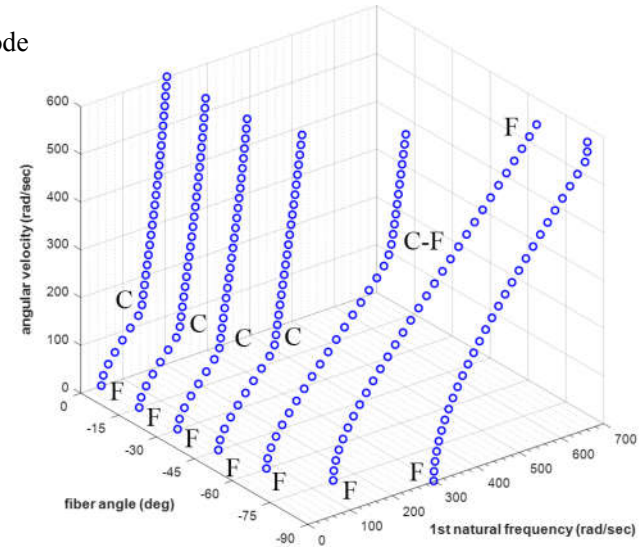

(b) 2nd mode

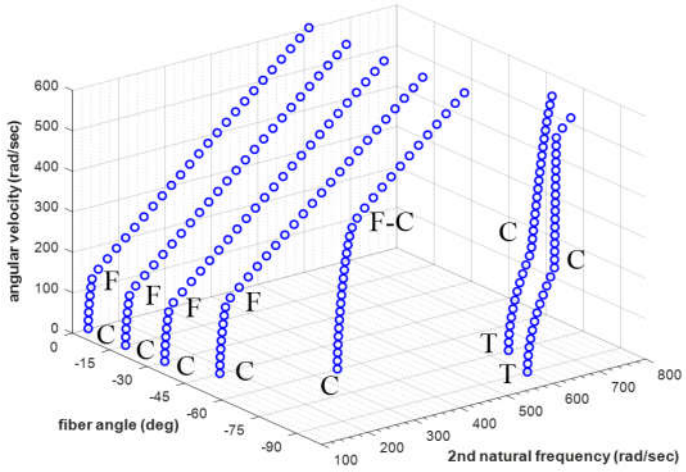

(c) 3rd mode

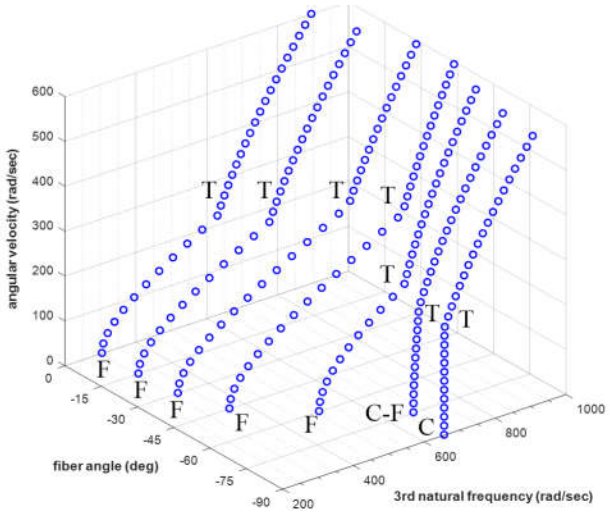

(d) 4th mode

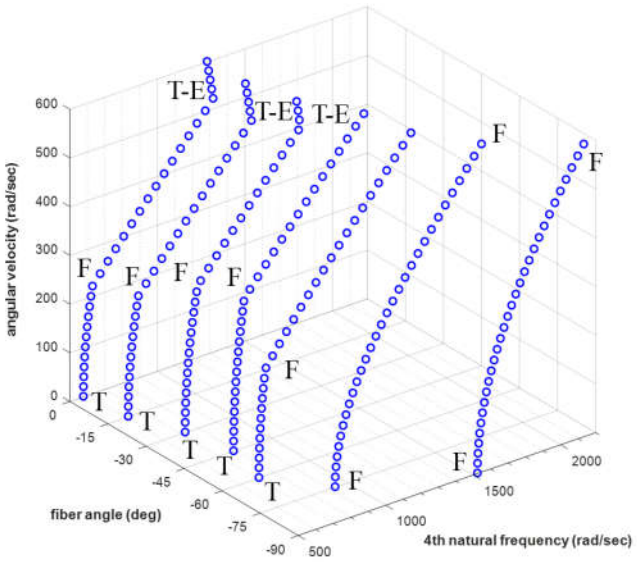

Figure 2-13 First four coupled natural frequencies versus the fiber angle for different angular velocities for the CUS configuration TWB / Dominant modes: C: Chordwise bending, F: Flapwise bending, T:Torsion, E: Extension

In general, all natural frequencies of the flapwise bending mode increase with the increase in the ply angle. This trend can be seen as well in the torsion and chordwise bending modes in the fiber angle range of $0° < \theta < -75^{\circ}$. Figure 2-5 shows the variation of the flapwise (a_{55}), chordwise (a_{44}), and torsion (a_{66}), stiffnesses.

Flapwise and chordwise stiffness coefficients gradually increasing while torsion stiffness has a maximum value at $\theta = -75^{\circ}$ and then it decreases. It is deemed that the decrease in torsion natural frequencies at high fiber angles is mainly caused by the decrease in torsion stiffness, as shown in Figure 2-5.

2.7.2.2.2 Effect of the Pretwist on the Natural Frequencies and Mode Shapes

Figure 2-14a-d present the variation of the first four natural frequencies of the rotating TWB as a function of the fiber angle and the angular velocity for CUS configuration TWB with and without pretwist. The blue symbols show the data for the TWB without pretwist and the red symbols show the data for the TWB with pretwist with the tip pretwist angle of $40^{\circ}\left(\beta_0 = 40^{\circ}\right)$. The variation of the flapwise bending (a_{55}), chordwise bending (a_{44}), torsion (a_{66}), and extension-torsion coupling (a_{16}), chordwise shear - flapwise bending (a_{25}), stiffness coefficients with the fiber angle for the uniform and the pretwisted beam are plotted in Figure 2-15. Figure 2-14a and b indicate that for the first and the second modes which are the flapwise bending and the chordwise bending, the effect of pretwist is not significant on the natural frequencies except for higher fiber angles $(\theta = -75^{\circ}, -90^{\circ})$. In general, it is seen that stiffening effect of the pretwist is higher at low angular velocities and for higher fiber angles, the same trend seen in CAS model. Figure 2-15 clearly shows the major effects of the pretwist on the flapwise bending stiffness. At higher fiber angles $(\theta = -75^{\circ}, -90^{\circ})$, Figure 2-15 shows that the flapwise bending stiffness of TWB with pretwist increases significantly compare to lower fiber angle which leads increasing the flapwise dominant natural frequency in higher fiber angles. In general, with the increase in the angular velocity, the effect of pretwist becomes negligible. The effect of pretwist on the 3rd natural frequency appears to be more pronounced for the whole range of the fiber angle. For fiber angle $\theta = -60^{\circ}$, with the increase in the pretwist mode switching

occurs from flapwise bending to torsion. For the 3rd natural frequency, for the range of angular velocity in which the dominant mode is the flapwise bending mode, pretwist has a stiffening effect whereas for the torsion dominant mode, pretwist has a softening effect. For $\theta = -75^{\circ}, -90^{\circ}$, pretwist has minor effect on the natural frequencies at low angular velocities. For the 4th natural frequency (Figure 2-14d), the effect of pretwist looks to be more distinct for $-60^{\circ} < \theta < -90^{\circ}$, where For fiber angle $\theta = -60^{\circ}$, mode switching occurs from torsion to flapwise bending.

(a) 1st mode

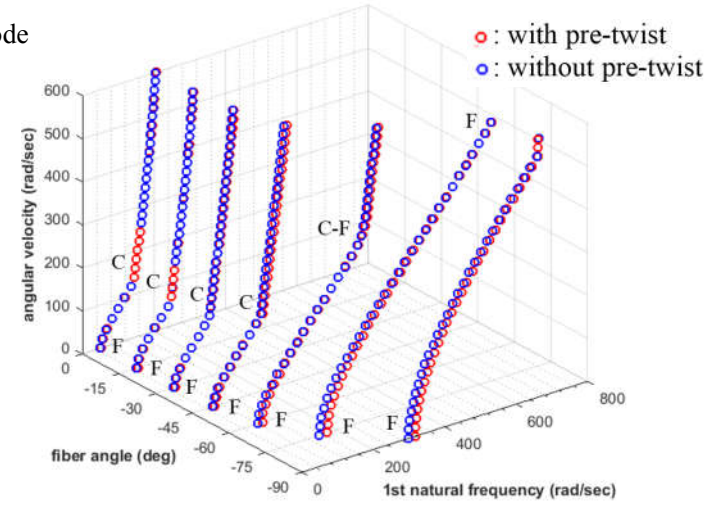

(b) 2nd mode

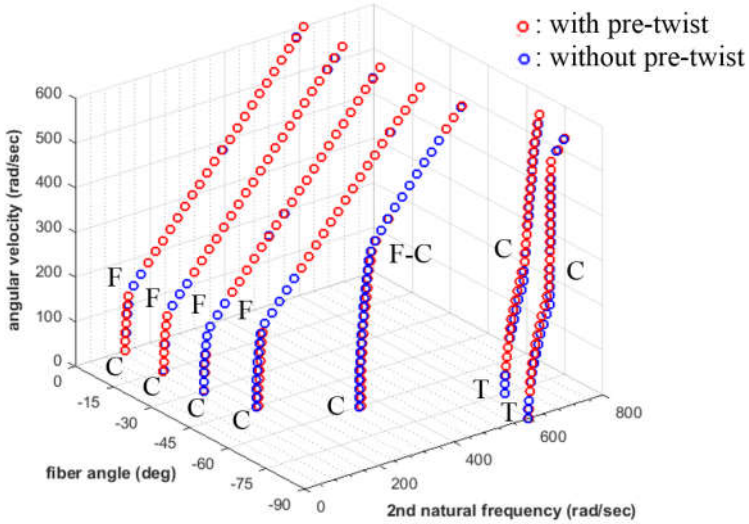

(c) 3rd mode

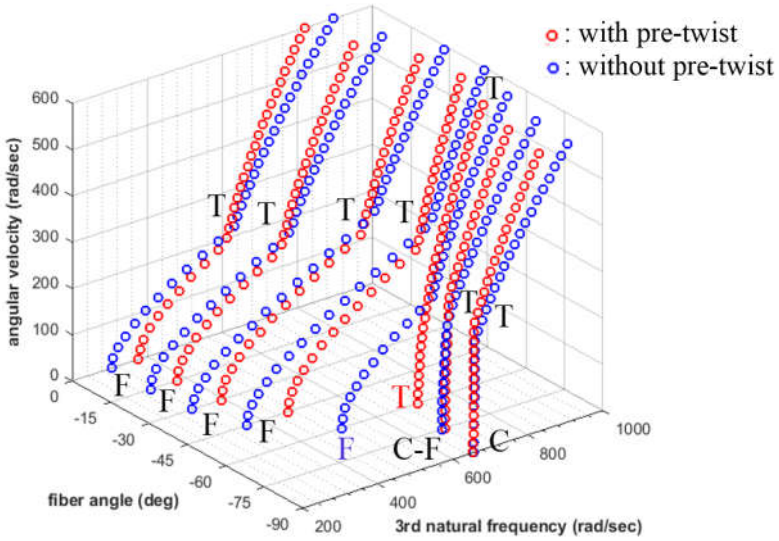

(d) 4th mode

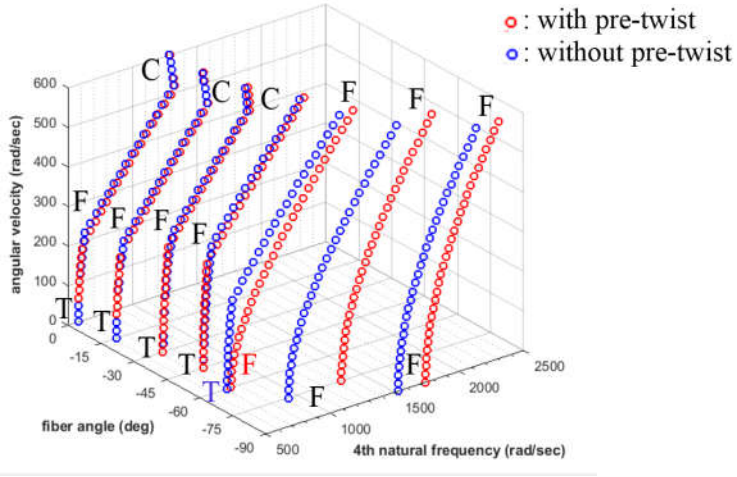

Figure 2-14 Comparison of the natural frequencies of CUS configuration TWBs with pretwist (red circle) and without pretwist (blue circle) versus the fiber angle and angular velocity (/ Dominant modes; C: Chordwise bending, F: Flapwise bending, T:Torsion

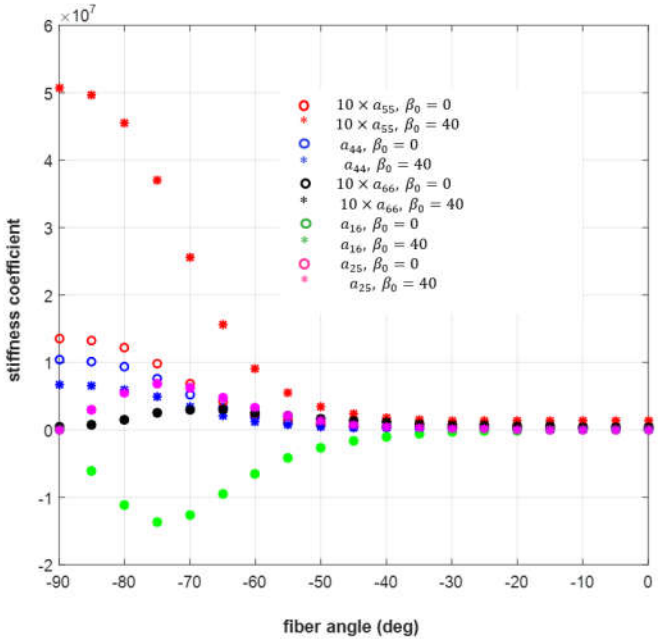

Figure 2-15 Variation of flapwise bending(a_{55}), chordwise bending(a_{44}), twist(a_{66}), extension-torsion(a_{16}), and chordwise shear-flapwise bending(a_{25}) stiffness coefficients versus the fiber angle for uniform and tapered TWB with CUS configuration at zero angular velocity($(\times 10)$ indicates 10 times magnified stiffness coefficients)

Figure 2-16-Figure 2-18 show the variation of the natural frequencies of the dominant modes of the CAS configuration TWB with respect to the angular velocity. For the TWB with the CAS layup configuration and the fiber angle of 90°, with an increase in the rotational speed, the natural frequencies of the 1st flapwise bending, 1st torsion and 2nd flapwise bending modes increase, but natural frequencies of the 1st chordwise bending mode remain more or less constant as the angular speed increases. However, in general natural frequencies of TWBs increase with the rotational speed irrespective of the fiber angle of the CAS configuration. Torsional frequencies are very influential on the aeroelastic stability of wings and blades. Among the TWBs with the fiber angles of 90º, 60º and 45º, TWB with the fiber angle of 60º has the highest torsional frequency. Figure 2-17 shows that torsional stiffness of the CAS configuration TWB with the fiber angle of 60º is higher than the torsional stiffness of the TWBs with the fiber angles of 90º and 45º. In this respect, torsional frequencies and torsional

frequencies have the same trend for the TWBs with the fiber angles of 90º, 60º and 45º.

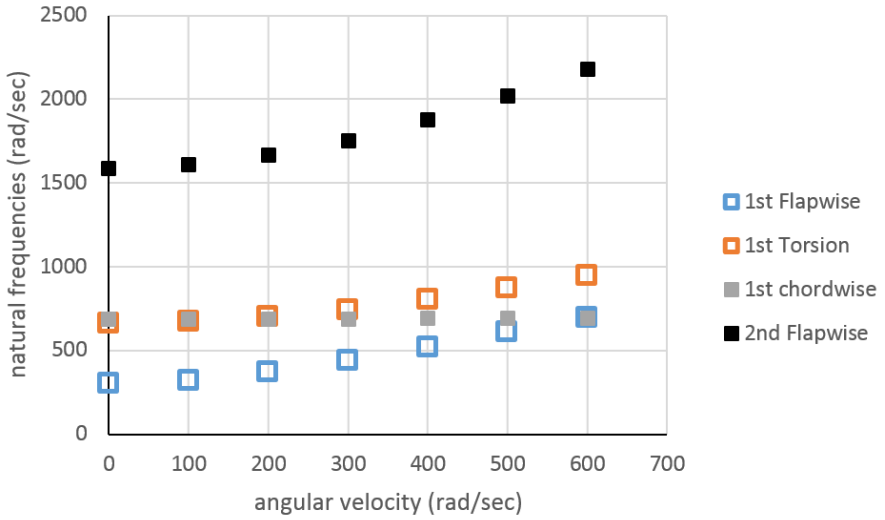

Figure 2-16 Variation of natural frequencies of four principle modes angle versus the angular velocity for the CAS configuration TWB without pretwist / Fiber angle = 90°

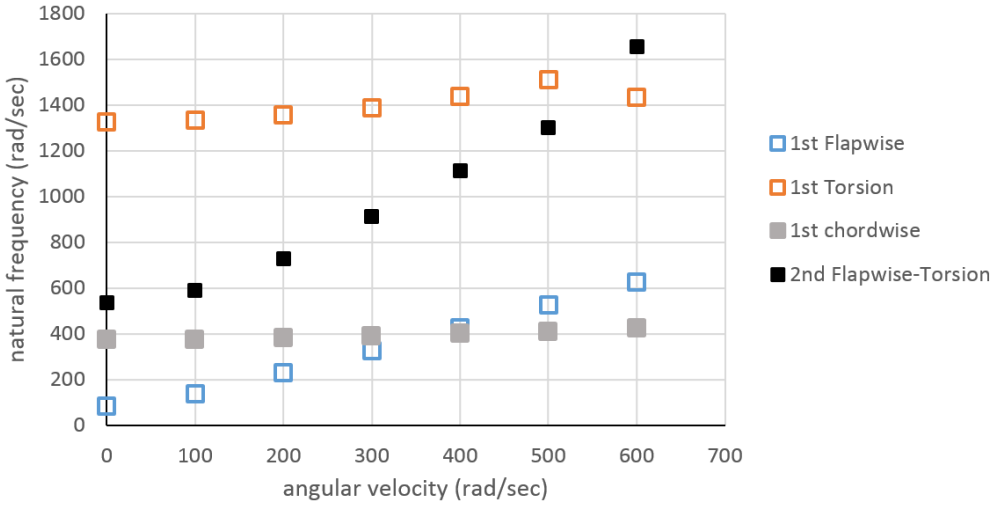

Figure 2-17 Variation of natural frequencies of four principle modes angle versus the angular velocity for the CAS configuration TWB without pretwist / Fiber angle = 60°

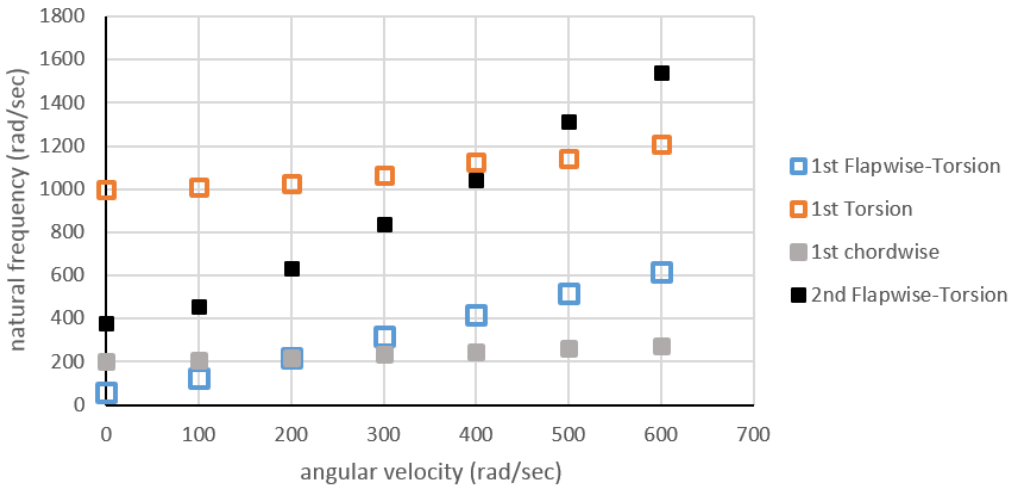

Figure 2-18 Variation of natural frequencies of four principle modes angle versus the angular velocity for the CAS configuration TWB without pretwist / Fiber angle = 45°

In this chapter, the dynamic characteristics of the pretwisted composite rotating TWB is investigated. To this end, a computer code has been developed to simulate the free vibration of the composite rotating TWB. The structural models are developed for the CAS and the CUS layup configurations. The extended Galerkin's method has been utilized to construct the proper state space form of the governing equations of motion. The effect of the fiber angle, the pretwist, and the angular velocity on the free vibration characteristics of the TWB have been comprehensively analyzed. A careful analysis of the numerical results obtained from this study revealed the following conclusions:

- Major improvement in eigenfrequencies are obtainable for studied ply angles. At zero angular velocity, by changing the fiber angle from 0° to -70°, natural frequencies increase both for the CAS and the CUS model. For the 2nd, 3rd and 5th modes and for fiber angles $-70° < \theta < -90^{\circ}$, reductions in natural frequencies are observed.
- Centrifugal stiffening causes mode switching at high angular velocities.

- Angular velocity has stiffening effect particularly on flapwise dominant mode. In general, increase in angular velocity results in increases in the natural frequencies of TWBs with CAS and CUS configurations.
- From the results, it is obvious that the effect of pretwist on enhancement in natural frequencies, particularly for the higher modes, is significant at low angular velocities as well as high fiber angles.
- Structural model of the TWB developed in the present study is a suitable model for the aeroelastic system which can be used for the aeroelastic stability analysis of composite rotor blades and composite wings.
- The main difference in between two configurations is the torsion and chordwise bending mode's contribution in the nature of modes. The presence of torsion mode in CAS model and chordwise bending mode in CUS model are impressive

CHAPTER 3

UNSTEADY SUBSONIC AERODYNAMICS BASED ON INDICIAL FUNCTION APPROACH

The key point in an effective aeroelastic analysis is to apply an accurate and efficient unsteady aerodynamics model. Aerodynamic loads can be modeled in various ways such as: strip theory, UVLM: unsteady Vortex-Lattice method, indicial response theory or in more modern aerodynamic techniques like CFD: computational fluid dynamics through Euler and Navier Stokes fluid theories. Aerodynamic loads can be introduced into the analysis in either frequency or time domain. Instability boundaries of an aeroelastic system are easily determined by using an aerodynamic model in frequency domain and performing eigenvalue analysis. However, in order to investigate the response of nonlinear aeroelastic systems and apply closed loop control systems aerodynamic loads are usually expressed in time domain. The classical solutions for 2-D aerodynamic lift and pitching moment in time and frequency domains are given by Theoderson [96], Loewy [97], Greenberg [98] and Wagner [99].

Considering simple harmonic motion, Theoderson's and Greenberg's theories are valid just in flutter speeds and limited to frequency domain approach. On the other hand, indicial response approach proposed by Wagner in the time domain is inefficient in the compressible flow regime. Although, Unsteady Vortex-Lattice Method and CFD methods are very precise and accurate in calculating aeroelastic response of lifting surfaces, but these methods are normally avoided in aeroelasticity due to the intrinsic complexity and high computational power requirement. Therefore, unsteady aerodynamic models in time domain which includes compressibility effects and

arbitrary change in pitch rate and which are not CFD based are preferred in aeroelastic analysis.

Generally, there are three viewpoints in modeling the aerodynamic loads in aeroelastic systems; steady flow, quasi steady flow and unsteady flow. Deriving comprehensive flow model needs a vast knowledge of fluid dynamics which is not the scope of the present study. Among the steady, quasi steady and unsteady flows, it is proved that steady and quasi steady flows are accompanied with errors in predicting the flutter speeds of aeroelastic systems. Consequently, the unsteady aerodynamic model is opted as the aerodynamic model which has higher accuracy and complexity. In this chapter, the unsteady incompressible and compressible aerodynamic models are studied. Strip theory is applied to extend the present model to a 3D wing and wind turbine blade models.

In indicial aerodynamics theory response of the system is obtained to a step function disturbance. In the present study, the disturbance is the pitching and plunging motion of the airfoil. If the indicial response is known, then the unsteady loads to arbitrary changes in angle of attack can be obtained through the superposition of indicial responses using Duhamel's integral in an incompressible or compressible flow.

The indicial aerodynamics theory results are an effective, comprehensive and appropriate approach to characterize subsonic unsteady flow. However, the indicial aerodynamic theory is valid for the simulation of attached flow over the airfoil since it is based on small disturbance theory. For both incompressible and compressible flows, appropriate indicial functions are available. In the compressible flow regime, indicial functions are Mach dependent and obtained for certain Mach numbers in the literature. In the present study, an approach is also presented to determine the indicial function for any Mach number utilizing the available data for certain Mach numbers.

3.1 Unsteady Incompressible Aerodynamics Model

Based on the strip theory and incompressible unsteady aerodynamics model, the aerodynamic lift and pitching moment about the reference axis which is positioned at the mid chord shown in Figure 3-1 are expressed as,

$$L_{ae}(z,t) = \rho_\infty U\Gamma_0(z,y) - \rho_\infty \frac{d}{dt}\int_{-b}^{b}\gamma_0(x,z,t)xdx + \rho_\infty U\int_{-b}^{\infty}\frac{\gamma_w(x,z,t)}{\sqrt{x^2-b^2}}dx \qquad (3\text{-}1)$$

$$M_{ae}(z,t) = -\rho_\infty U\int_{-b}^{b}\gamma_0(x,z,t)xdx + \frac{1}{2}\rho_\infty \frac{d}{dt}\int_{-b}^{b}\gamma_0(x,z,t)(x^2-\frac{1}{2}b^2)dx \qquad (3\text{-}2)$$
$$+\frac{1}{2}\rho_\infty Ub^2\int_{-b}^{\infty}\frac{\gamma_w(x,z,t)}{\sqrt{x^2-b^2}}dx$$

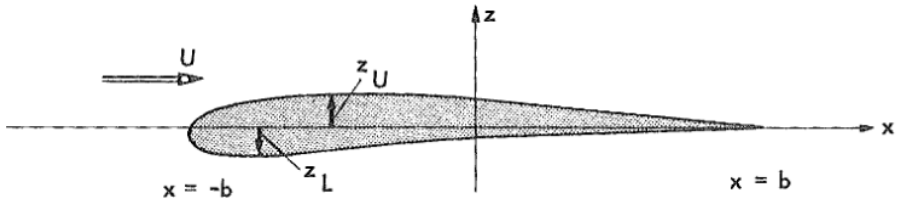

Figure 3-1 Cross section of a thin airfoil in *xy* plane [100]

where, $\gamma_0(x,y,z)$ is the quasi vortex on the wing surface (see Figure 3-2), $\gamma_w(x,y,z)$ is the vortex on the wake and $\Gamma_0(z,t)$ is the quasi circulation. $\gamma_0(x,z,t)$ and $\gamma_w(x,z,t)$ are obtained based on no-penetration and Kutta conditions. Continuation is devoted to explain derivation process of mentioned vortices.

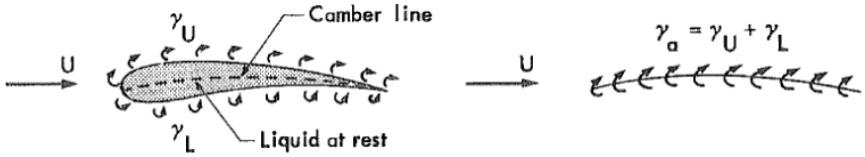

Figure 3-2 Two stages in the replacement of a thin airfoil by vortex sheets on the wing surface [100]

The vertical position of any points on the surface of the blade cross section is expressed as,

$$z_a(x,z,t) = v_0(z,t) - \phi(z,t)(x_{ac} - ab) \tag{3-3}$$

Where, the x axis of the aerodynamic coordinates is in the opposite side of the x axis of the structural coordinate $(x_{ae} = -x)$, y_{ae}coincident with z axis and z_{ae} coincident with y axis. $v_0(z,t)$ and $\phi(z,t)$ are the flapwise transverse and torsion deformations and ab indicates the offset between the shear center of wing box beam and mid chord. Let's define $F(x,y,z,t)$ as,

$$F(x,y,z,t) = z_a(x,z,t) - v_0(z,t) - \phi(z,t)(x - ba) \tag{3-4}$$

The flow no-penetration condition can be stated as,

$$\begin{aligned} &\frac{DF(x,y,t)}{Dt} = \frac{\partial F}{\partial t} + U.\nabla F = 0; \\ &\frac{\partial F}{\partial t} + (U + u_b + u_w)\frac{\partial F}{\partial x} + v\frac{\partial F}{\partial y_{ac}} + (w_b + w_w)\frac{\partial F}{\partial z_{ac}} = 0 \end{aligned} \tag{3-5}$$

Where, $u_b = \frac{\partial \Phi_b}{\partial x}, u_w = \frac{\partial \Phi_w}{\partial x}, w_b = \frac{\partial \Phi_b}{\partial z_{ae}}, u_w = \frac{\partial \Phi_w}{\partial z_{ae}}$. Φ_b and Φ_w are the bound vortex function and the wake. Based on the thin airfoil theory and small disturbance theory [100], we have,

$$w_b(x, y_{ac}, z_{ac}, t) \mid_{z_{ac}\to 0} = \frac{\partial \Phi_b}{\partial z_{ac}} \mid_{z_{ac}\to 0} = -\frac{1}{2\pi}\int_{-b}^{b} \frac{\gamma_b(\xi, y_{ac}, t)d\xi}{x - \xi} \tag{3-6}$$

$$w_w(x, y_{ac}, z_{ac}, t) \mid_{z_{ac}\to 0} = \frac{\partial \Phi_w}{\partial z_{ac}} \mid_{z_{ac}\to 0} = -\frac{1}{2\pi}\int_{b}^{\infty} \frac{\gamma_w(\xi, y_{ac}, t)d\xi}{x - \xi} \tag{3-7}$$

The downwash is calculated as follows,

$$w_a(x,z,t) = \frac{\partial z_a}{\partial t} + U\frac{\partial z_a}{\partial x} \\ = \dot{v}_0 - (x - ba)\dot{\phi} - U\phi = -\frac{1}{2\pi}\int_{-b}^{b}\frac{\gamma_b(\xi,z,t)d\xi}{x-\xi} - \frac{1}{2\pi}\int_{b}^{\infty}\frac{\gamma_w(\xi,z,t)d\xi}{x-\xi} \tag{3-8}$$

The airfoil may move in vertical translation $v_0(t)$ and rotate about an axis at $x = ba$ through an angle $\phi(t)$. The directions of these variables are depicted in Figure 3-3.

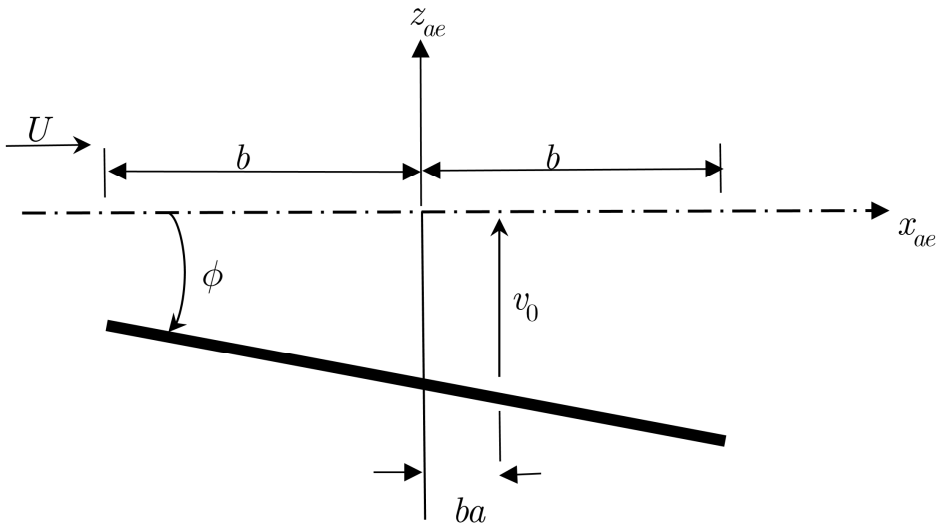

Figure 3-3 Mean line of chordwise-rigid airfoil. v_0 is the downward displacement of the axis $(x = ba)$ of rotation ϕ

In Equations (3-6)-(3-8), it is assumed that the wake is on the flat plate. The downwash at the middle of airfoil (mid chord) and a quarter of airfoil is calculated from Equation (3-8) as given in Equation (3-9).

$$w_{0.5c}(z,t) = \dot{v}_0 + ba\dot{\phi} - U\phi \\ w_{0.75c}(z,t) = \dot{v}_0 - (\frac{1}{2} - a)b\dot{\phi} - U\phi \tag{3-9}$$

Methodology brought in the next part follows researches performed by Theodorsen [96], Von Karman [101] and bisplinghoff [100]. For quasi steady part of the solution we have,

$$w_a(x,z,t) = \dot{v}_0 - (x - ba)\dot{\phi} - U\phi = -\frac{1}{2\pi}\int_{-b}^{b}\frac{\gamma_0(\xi,z,t)d\xi}{x-\xi} \tag{3-10}$$

$$\Gamma_0(z,t) = \int_{-b}^{b}\gamma_0(\xi,z,t)d\xi \tag{3-11}$$

While, for the effect of wake, one can be stated as

$$0 = -\frac{1}{2\pi}\int_{-b}^{b}\frac{\gamma_1(\xi,z,t)d\xi}{x-\xi} - \frac{1}{2\pi}\int_{b}^{\infty}\frac{\gamma_\infty(\xi,z,t)d\xi}{x-\xi} \tag{3-12}$$

$$\Gamma_1(z,t) = \int_{-b}^{b}\gamma_1(\xi,z,t)d\xi = \int_{b}^{\infty}[\sqrt{\frac{\xi+b}{\xi-b}} - 1]\gamma_w(\xi,z,t)d\xi \tag{3-13}$$

The total circulation on the airfoil is written in this form,

$$\Gamma_b(z,t) = \Gamma_0(z,t) + \Gamma_1(z,t) \tag{3-14}$$

The Kutta condition on the trailing edge of the airfoil is satisfied in Equation (3-15).

$$\Gamma_0(z,t) + \int_{b}^{\infty}\sqrt{\frac{\xi+b}{\xi-b}}\gamma_w(\xi,z,t)d\xi = 0 \tag{3-15}$$

The Sohngen inversion formula [102] is used to solve the Equation (3-10) in order to obtain $\gamma_0(x,z,t)$ and $\Gamma_0(x,z,t)$ given in Equations (3-10) and (3-11). Substituting $\Gamma_0(x,z,t)$ into Equation (3-15) and solving it, $\gamma_w(x,z,t)$ is calculated. After using spatial Laplace transform and some manipulations, eventually, we get,

$$\begin{aligned}\Gamma_0(z,t) &= -2b\int_{-1}^{1}\sqrt{\frac{1+\xi}{1-\xi}}[\dot{v}_0 - U - b\xi\dot{\phi}] \\ &= -2\pi b[\dot{v}_0 - U\phi - \frac{1}{2}b\dot{\phi}] = -2\pi b w_{0.75c}(z,t)\end{aligned} \tag{3-16}$$

3.1.1 Arbitrary Motion of Thin Airfoil in Incompressible Flow (Wagner Function)

The function $\phi_W(Ut/b)$ is the indicial function for incompressible flow which is usually referred to as Wagner's function. Wagner's function is evaluated via inverse Laplace transform of the generalized Theodorsen function which is defined in frequency domain. Based on Theodorsen frequency domain aerodynamics, for the general motion of thin airfoil of chord length $2b$ undergoing a combination of pitching and plunging motion in a flow of steady velocity U, unsteady lift and pitching moment about the reference axis are given by Equations (3-17) and (3-18), respectively [100].

$$L_{ae} = \underbrace{\pi\rho b^2(-\ddot{v}_0 + ba\ddot{\phi} + U\dot{\phi})}_{noncirculatory} + \underbrace{2\pi\rho bU^2C(k)(U\phi + b(\frac{1}{2}-a)\dot{\phi} + \dot{v}_0]}_{circulatory} \tag{3-17}$$

$$T_{ae} = \underbrace{\pi\rho b^3(-a\ddot{v}_0 - U(\frac{1}{2}-a)\dot{\phi} + b(\frac{1}{8}+a^2)\ddot{\phi})}_{noncirculatory} + \underbrace{2\pi\rho Ub^2(\frac{1}{2}+a)C(k)(\dot{v}_0 + U\phi + b(\frac{1}{2}-a)\dot{\phi})}_{circulatory} \tag{3-18}$$

The first term in Equations (3-17) and (3-18) is the non-circulatory or apparent mass part, which results from the flow acceleration effect. The second group of terms is the circulatory components arising from the generation of circulation about the airfoil. Theodorsen's function, also named as lift deficiency function, $C(k)$ is a complex-valued function which depends on the reduced frequency k $(k = wb/U)$. Theodorsen's function has a complex value as,

$$C(k) = F(k) - iG(k) \tag{3-19}$$

By using inverse Laplace transform, the time domain counterpart of Theoderson Function can be calculated as given in Equation (3-20) [100].

$$\phi_W(Ut/b) = \frac{1}{2\pi i}\int_{-\infty}^{\infty}\frac{C(k)}{k}e^{ik(Ut/b)}dk \tag{3-20}$$

Separating $e^{ik(Ut/b)}$ and $C(k)$ into their real and imaginary parts, the Wagner's function for $(Ut/b) > 0$ can be rewritten as,

$$\phi_W(Ut/b) = \frac{2}{\pi}\int_0^\infty \frac{F(k)}{k}\sin ksdk = 1 + \frac{2}{\pi}\int_0^\infty \frac{G(k)}{k}\cos ksdk \tag{3-21}$$

In many aeroelastic applications it is convenient to use $\phi_W(Ut/b)$ when writing the circulatory lift and moment due to arbitrary motion. The $\phi_W(Ut/b)$ has a relatively simple form which it is often referred to certain convenient approximation, such as,

$$\phi_W(Ut/b) \cong 1 - 0.165e^{-0.0455(Ut/b)} - 0.335e^{(Ut/b)} \tag{3-22}$$

A plot of $\phi_W(Ut/b)$ is shown in Figure 3-4.

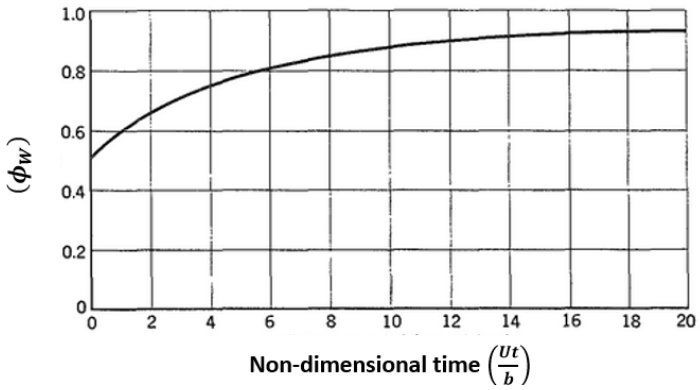

Figure 3-4 Wagner's function $\phi_W(Ut/b)$ for indicial lift [99]

The general form of the aerodynamic lift L_{ae} and pitching moment M_{ae} given in Equations (3-23) and (3-24) are calculated by substituting the expression of $\Gamma_0, \gamma_0, \gamma_w$ given in Equations (3-9), (3-10), (3-11) and (3-15) into Equations (3-1) and (3-2).

$$L_{ae}(z,t) = -\pi\rho b^2 \ddot{w}_{0.5c}(z,t) - C_{L\phi}\rho U b\left\{ w_{0.75c}(z,0)\phi_W(\frac{U}{b}t) + \int_0^t \left[\frac{dw_{0.75c}(z,\tau)}{d\tau}\phi_W\left(\frac{U}{b}(t-\tau)\right)\right] d\tau \right\} \quad (3\text{-}23)$$

$$M_{ae}(z,t) = -\pi\rho b^3\left[\frac{U}{2}\dot{\phi} - Ua\dot{\phi} + a\ddot{v}_0 + b\left(\frac{1}{8}+a^2\right)\ddot{\phi}\right] - C_{L\phi}\rho U b^2\left(\frac{1}{2}+a\right)\left\{ w_{0.75}(z,0)\phi_W(\frac{U}{b}t) + \int_0^t \left[\frac{dw_{0.75c}(z,\tau)}{d\tau}\phi_W\left(\frac{U}{b}(t-\tau)\right)\right] d\tau \right\} \quad (3\text{-}24)$$

In Equations (3-23) and (3-24), ρ_∞, U, b are the mean flow density, the air speed, semi-chord length of the blade, respectively. Also, $w_{0.5c}, w_{0.75c}$ are the downwash at the mid-chord and three-quarter chord of the wing, respectively.

The terms in curly brackets in Equations (3-23) and (3-24) are circulatory part of the aerodynamic lift and moment [100]. The circulatory part depends on the motion history and wake influences, and is the most influential term in an unsteady analysis [103].

In order to avoid complex numerical computations regarding the inverse Laplace transform, Wagner proposed the following quasi-polynomial approximation [69],

$$\phi_W(\frac{U}{b}t) = \left(1 - \sum_{i=1}^{2}\alpha_i e^{-\beta_i\frac{U}{b}t}\right)H(\frac{U}{b}t) \quad (3\text{-}25)$$

where $H(\frac{U}{b}t)$ represents the step function and $\alpha_1 = 0.165 \quad \alpha_2 = 0.335 \quad \beta_1 = 0.0455$ $\beta_2 = 0.3$ [104].

In order to handle the integral appearing in Equations (3-23) and (3-24), Wagner's function is replaced by the quasi polynomial approximation of the Wagner's function, Equation (3-25), and the resulting integral is defined as a new variable $D(z,t)$.

$$D(z,t) = \int_0^t \frac{dw_{0.75c}(z,\tau)}{dt_0}\phi_W\left(\frac{U}{b}(t-\tau)\right)d\tau \quad (3\text{-}26)$$

The first term of the integral in Equation (3-26) yields the downwash at the three-quarter chord provided that the wing is at rest at time zero. If the second and the third terms of the integral in Equation (3-26) are defined as $B_1(z,t), B_2(z,t)$, which are in fact the aerodynamic lag terms, then Equation (3-26) can be rewritten as,

$$D(z,t) = w_{0.75c}(z,t) - \sum_{i=1}^{n} \alpha_i B_i(z,t) \tag{3-27}$$

where, by making use of the Leibniz integral rule, it can be shown that the B_i terms have to satisfy Equation (3-28).

$$\dot{B}_i + (\beta_i \frac{U}{b}) B_i = \dot{w}_{0.75c}(z,t); \qquad i = 1,2 \tag{3-28}$$

The present model can incorporate as many aerodynamic lag terms as required for an accurate solution. It is also worth to mention that this model is similar to the Roger's approximation method [105] in terms of the number of augmented states introduced in the solution.

The preceding expressions are valid only for 2-D airfoils. For 3-D blades with finite span, some modifications have to be implemented according to the modified strip theory [106]. To reflect the 3-D effects, lift curve slope and the position of the three-quarter chord position, where the downwash is calculated, have to be modified according to Equation (3-29) only in the circulatory lift and moment expressions in Equations (3-23) and (3-24) [70].

$$\begin{aligned} 2\pi \rightarrow C_{L\phi} &= \frac{dC_L}{d\phi} = \frac{AR}{AR\sqrt{1 + \left(\frac{2}{AR}\right)^2} + 2} 2\pi \\ \frac{1}{2}b &\rightarrow \frac{b}{2}\left[\frac{C_{L\phi}}{\pi} - 1\right] \end{aligned} \tag{3-29}$$

where, AR is the aspect ratio of the blade.

Thus, downwash at $3/4^{th}$ chord is modified by replacing 2π by $C_{L\phi}$ and $b/2$ by $b/2\left(C_{L\phi}/\pi - 1\right)$. By substituting the modified downwash, at the three-quarter chord position into Equation (3-27), and Equation (3-27) into Equations (3-23) and (3-24), the final form of the unsteady aerodynamic lift and pitching moment expressions can be obtained, as shown in the following relations,

$$L_{ae}(z,t) = -\pi\rho_\infty b^2[\ddot{v}_0 - U\dot{\phi} + ba\ddot{\phi}] - C_{L\phi}\rho_\infty Ub[\dot{v}_0 - U\phi + ba\dot{\phi} - \frac{b}{2}(\frac{C_{L\phi}}{\pi} - 1)\dot{\phi} - \sum_{i=1}^{2}\alpha_i B_i(z,t)], \tag{3-30}$$

$$M_{ae}(z,t) = -\pi\rho_\infty b^3[\frac{1}{2}(\frac{C_{L\phi}}{\pi} - 1)U\dot{\phi} - Ua\dot{\phi} + a\ddot{v}_0 + b(\frac{1}{8} + a^2)\ddot{\phi}] - C_{L\phi}\rho_\infty Ub^2\left(\frac{1}{2} + a\right)[\dot{v}_0 - U\phi + ba\dot{\phi} - \frac{b}{2}(\frac{C_{L\phi}}{\pi} - 1)\dot{\phi} - \sum_{i=1}^{2}\alpha_i B_i(z,t)] \tag{3-31}$$

where $B_i's$ should satisfy Equation (3-28).

3.2 Unsteady Compressible Aerodynamics Based on Indicial Model

Due to necessity of having explicit expressions for unsteady aerodynamic lift and moment in time domain including the effects of compressibility, indicial aerodynamics has been introduced and is now well accepted by the scientific community [100,107-109]. Indicial response is a mathematical concept which cannot be obtained directly from experiments. For incompressible and inviscid flows, closed form solutions are available for indicial responses [100] while for compressible subsonic flows, there is no such analytical solutions, even though approximate solutions may be obtained from inversions of periodic aerodynamic responses in the frequency domain [110]. For the compressible flow case, there does not exist a unique solution in entire time domain [110]. In the unsteady incompressible theory, the aerodynamic loadings originate from the two main sources which are circulatory and non-circulatory. Non-circulatory lift and moment depend on the instantaneous accelerations and velocities of the wing. However, in a compressible medium where the speed of sound is finite, the non-

circulatory flow does not adapt itself to the changes of the boundaries instantly, hence noncirculatory lift and moment do not only depend on the instantaneous values of acceleration and velocity but also on the history of motion. For compressible flows, it is not customary to make distinction between circulatory and non-circulatory flow since the history of the motion becomes important and apparent mass is no longer a meaningful concept [38,100,110]. Mazelsky [111,112] and mazelsky and Drischler [113] determined approximated indicial response function in exponential form for three Mach numbers, 0.5, 0.6 and 0.7.

In aeroelastic problems the pitching axis usually coincides the elastic axis but in the development of the compressible indicial functions the pitch axis is temporarily placed at the leading edge as shown in Figure 3-5 [113].

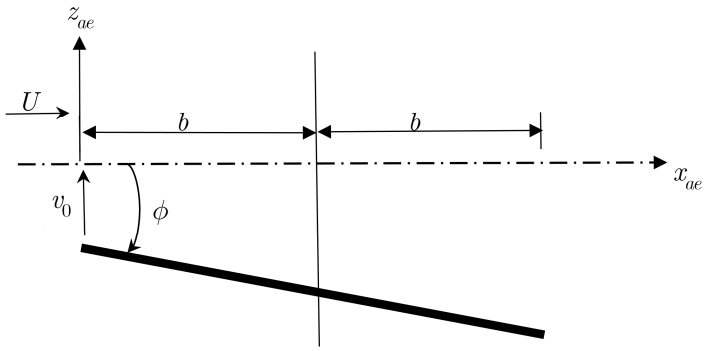

Figure 3-5 Wing performing vertical translation and pitching about an axis through the leading edge

In the present study, compressible indicial functions are employed to express the unsteady aerodynamic loading in the compressible flow regime. For arbitrary small motions of the thin airfoil in subsonic flow, with respect to the reference axis placed at the leading edge of the airfoil, downwash velocity at a distance x from the leading edge corresponding to pitching and plunging motions can be expressed as in Equation (3-32) [100]

$$w_a(x,z,t) = \underbrace{\left[\dot{v}_0(z,t) - U\,\phi(z,t)\right]}_{w_v(z,t)} - x\,\underbrace{\dot{\phi}(z,t)}_{w_\phi(z,t)} \tag{3-32}$$

The downwash velocity is divided into two parts; $w_v = (\dot{v}_0 - U\phi)$ indicates the plunging motion and $w_\phi = \dot{\phi}$ yields a linear variation of w_a with x.

The indicial lift function $\phi_c(t)$ and indicial moment function about the reference axis located in the leading edge $\phi_{cM}(t)$ are defined as the responses to the unit step change of the plunging motion w_a at the leading edge. Consequently, the lift and moment distributions due to this unit step excitation are defined by Equations (3-33) and (3-34), [100]

$$L'_T\left(z,t\right) = -C_{L\phi}\rho U b\left[w_v(z,0)\phi_c(t) + \int_0^t \frac{d\left(w_v(z,\tau)\right)}{d\tau}\phi_c(\frac{U}{b}(t-\tau))\,d\tau\right], \tag{3-33}$$

$$M'_T\left(z,t\right) = -2C_{L\phi}\rho U_r b^2\left[w_v(z,0)\phi_{cM}\left(t\right) + \int_0^t \frac{d\left(w_v(z,\tau)\right)}{d\tau}\phi_{cM}(\frac{U}{b}(t-\tau))\,d\tau\right], \tag{3-34}$$

In a similar fashion, $\phi_{cq}(t), \phi_{cMq}(t)$ are introduced as the indicial lift and moment functions about the leading edge due to unit step change of the pitching rate $(\dot{\phi})$ at the leading edge. As a result, the lift and moment distributions are defined by Equations (3-35) and (3-36),

$$L'_q\left(z,t\right) = 2C_{L\phi}\rho U b^2\left[w_\phi(z,0)\phi_{cq}(t) + \int_0^t \frac{d\left(w_\phi(z,\tau)\right)}{d\tau}\phi_{cq}(\frac{U}{b}(t-\tau))\,d\tau\right], \tag{3-35}$$

And

$$M'_q\left(z,t\right) = 4C_{L\phi}\rho U b^3\left[w_\phi(z,0)\phi_{cMq}(t) + \int_0^t \frac{d\left(w_\phi(z,\tau)\right)}{d\tau}\phi_{cMq}(\frac{U}{b}(t-\tau))\,d\tau\right]. \tag{3-36}$$

Considering the four indicial functions defined in Equations (3-33)-(3-36) the total aerodynamics lift (positive upward) and pitching moment (positive nose-up) about the leading edge are obtained by summing Equations (3-33)-(3-36) as stated in Equation (3-37),

$$L'(z,t) = L'_T(z,t) + L'_q(z,t)$$
$$M'(z,t) = M'_T(z,t) + M'_q(z,t) \tag{3-37}$$

In Equation (3-37), the prime symbol indicates that the aerodynamic loads are evaluated in the reference coordinate located at the leading edge of the wing. Aerodynamic loads in the so called Theodorsen's coordinate, which is located at a distance $b(a+1)$ behind the leading edge, are then defined by Equations (3-38)-(3-41) which are obtained by employing the general law for transferring the axis of a moment. [100]

$$L_T(z,t) = L'_T(z,t) = -C_{L\phi}\rho U b\left[w_v(z,0)\bar{\phi}_c(t) + \int_0^t \frac{d\left(w_v(z,\tau)\right)}{d\tau}\bar{\phi}_c\left(\frac{U}{b}(t-\tau)\right)d\tau\right] \tag{3-38}$$

$$M_T(z,t) = M'_T(z,t) + b(a+1)L'_T(z,t) = -2C_{L\phi}\rho U_r b^2\left[w_v(z,0)\bar{\phi}_{cM}(t) + \int_0^t \frac{d\left(w_v(z,\tau)\right)}{d\tau}\bar{\phi}_{cM}\left(\frac{U}{b}(t-\tau)\right)d\tau\right] \tag{3-39}$$

$$L_q(z,t) = L'_q(z,t) - C_{L\phi}\rho U b^2(a+1)\left[w_\phi(z,0)\phi_c(t) + \int_0^t \frac{d\left(w_\phi(z,\tau)\right)}{d\tau}\phi_c\left(\frac{U}{b}(t-\tau)\right)d\tau\right] = 2C_{L\phi}\rho U_r b^2\left[w_\phi(z,0)\bar{\phi}_{cq}(t) + \int_0^t \frac{d\left(w_\phi(z,\tau)\right)}{d\tau}\bar{\phi}_{cq}\left(\frac{U}{b}(t-\tau)\right)d\tau\right] \tag{3-40}$$

$$M_q(z,t) = M'_q(z,t) - 2C_{L\phi}\rho U b^3(a+1)\left[w_\phi(z,0)\phi_{cM}(\tau) + \int_0^t \frac{d\left(w_\phi(z,\tau)\right)}{d\tau}\phi_{cM}\left(\frac{U}{b}(t-\tau)\right)d\tau\right] + L_q(z,t)b(a+1) = 4C_{L\phi}\rho U b^3\left[w_\phi(z,0)\bar{\phi}_{cMq}(t) + \int_0^t \frac{d\left(w_\phi(z,\tau)\right)}{d\tau}\bar{\phi}_{cMq}\left(\frac{U}{b}(t-\tau)\right)d\tau\right] \tag{3-41}$$

In Equations (3-38)-(3-41) a new set of aerodynamic indicial functions for compressible flow are defined in the Theodorsen's coordinate as given by Equation (3-42), [100]

$$\begin{aligned}
&\bar{\phi}_c(t) = \phi_c(t), \\
&\bar{\phi}_{cM}(t) = \phi_{cM}(t) + \left(\frac{a}{2} + \frac{1}{2}\right)\phi_c(t), \\
&\bar{\phi}_{cq}(t) = \phi_{cq}(t) - \left(\frac{a}{2} + \frac{1}{2}\right)\phi_c(t), \\
&\bar{\phi}_{cMq}(t) = \phi_{cMq}(t) + \left(\frac{a}{2} + \frac{1}{2}\right)\left(\phi_{cq}(t) - \phi_{cM}(t)\right) - \left(\frac{a}{2} + \frac{1}{2}\right)^2 \phi_c(t).
\end{aligned} \tag{3-42}$$

In the literature, compressible indicial functions are available only in limited Mach numbers $(M = 0.5, 0.6, 0.7, 0.8)$ [100,112,113]. For instance, Figure 3-6-Figure 3-9 gives the indicial lift and moment functions $\hat{\phi}_c, \hat{\phi}_{cM}, \hat{\phi}_{cq}, \hat{\phi}_{cMq}$ for both incompressible $(M = 0)$ and three subsonic compressible Mach numbers $(M = 0.5, 0.6, 0.7)$. By considering Figure 3-6-Figure 3-9, it is concluded that the magnitude of lift and moment at any non-dimensional time increases with the Mach number. The results shown in Figure 3-6-Figure 3-9 are obtained by Mazelsky and Drischler [112,113].

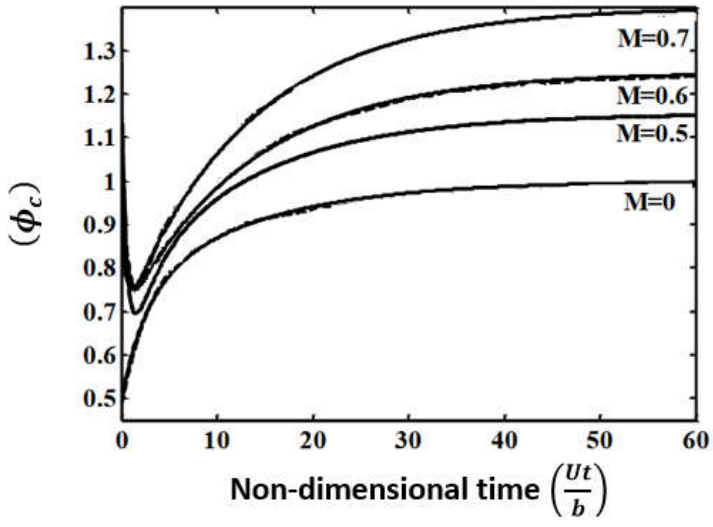

Figure 3-6 Indicial lift functions for plunging airfoil about the leading edge in compressible flow

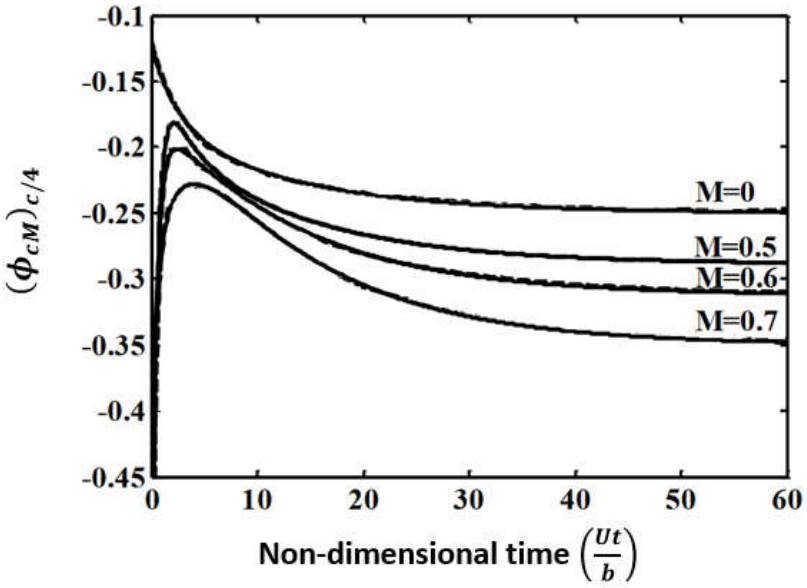

Figure 3-7 Indicial moment functions for plunging airfoil about the quarter-chord axis in compressible flow

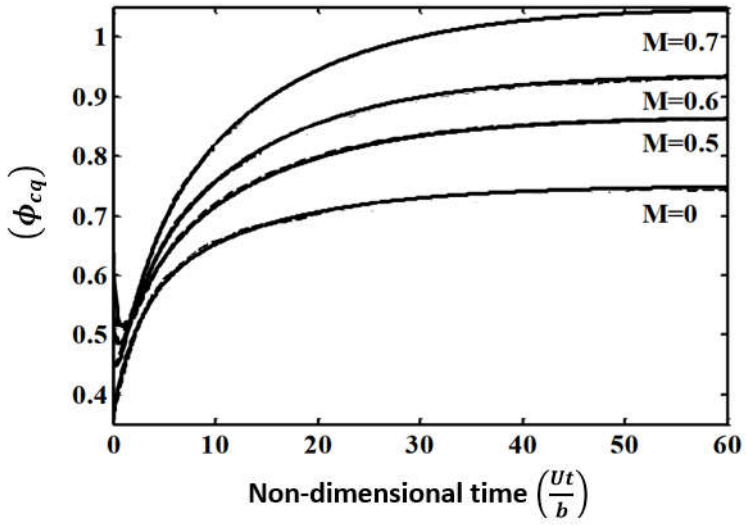

Figure 3-8 Indicial lift functions for pitching airfoil about the leading edge in compressible flow

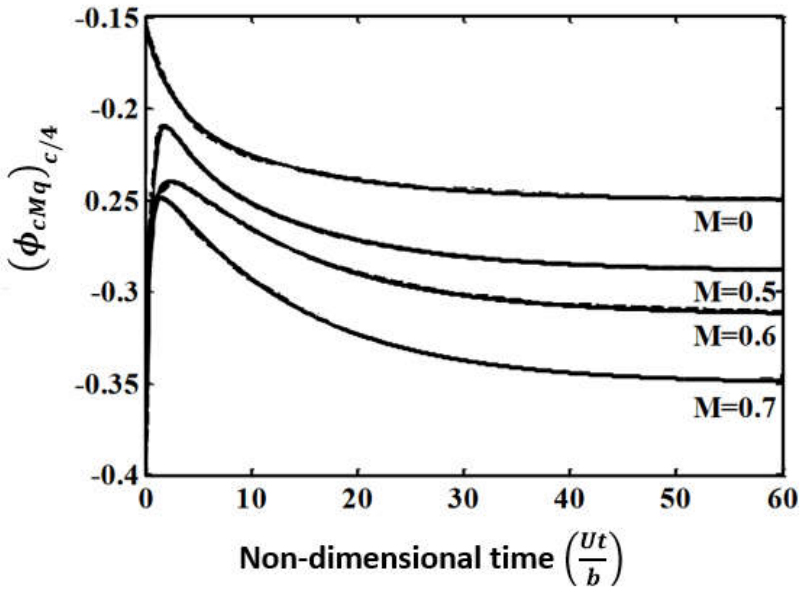

Figure 3-9 Indicial moment functions for pitching airfoil about the quarter-chord axis in compressible flow

Figure 3-7 and Figure 3-9 give the indicial moment functions for plunging and pitching motions about the quarter-chord axis. In order to obtain the indicial moment functions for plunging and pitching about the leading edge, the axis is transferred from quarter chord to leading edge and new equations are derived as,

$$\phi_{cM} = \left(\phi_{cM}\right)_{c/4} - \frac{1}{4}\phi_c \tag{3-43}$$

$$\phi_{cMq} = \left(\phi_{cMq}\right)_{c/4} - \frac{1}{4}\phi_{cq} \tag{3-44}$$

In order to handle the integrals appearing in Equations (3-38)-(3-41), compressible indicial functions are represented by their exponential approximations just like the Wagner's function. For the compressible flow case, in the literature he indicial functions, which are defined with respect to the leading edge of the airfoil, are assumed to be in the form of four term Mach dependent exponentially growing functions given by,

$$\phi_c(Ut/b) = b_{0c} + b_{1c}e^{-\beta_{1c}\frac{Ut}{b}} + b_{2c}e^{-\beta_{2c}\frac{Ut}{b}} + b_{3c}e^{-\beta_{3c}\frac{Ut}{b}} \quad (3\text{-}45)$$

$$\phi_{cM}(Ut/b) = b_{0cM} + b_{1cM}e^{-\beta_{1cM}\frac{Ut}{b}} + b_{2cM}e^{-\beta_{2cM}\frac{Ut}{b}} + b_{3cM}e^{-\beta_{3cM}\frac{Ut}{b}} \quad (3\text{-}46)$$

$$\phi_{cq}(Ut/b) = b_{0cq} + b_{1cq}e^{-\beta_{1cq}\frac{Ut}{b}} + b_{2cq}e^{-\beta_{2cq}\frac{Ut}{b}} + b_{3cq}e^{-\beta_{3cq}\frac{Ut}{b}} \quad (3\text{-}47)$$

$$\phi_{cMq}(Ut/b) = b_{0cMq} + b_{1cMq}e^{-\beta_{1cMq}\frac{Ut}{b}} + b_{2cMq}e^{-\beta_{2cMq}\frac{Ut}{b}} + b_{3cMq}e^{-\beta_{3cMq}\frac{Ut}{b}} \quad (3\text{-}48)$$

The coefficients associated with the indicial functions for plunging motion are listed in the Table 3-1 [112] [100].

Table 3-1 Exponential representations of compressible indicial functions for the plunging airfoil different Mach numbers

	M	ϕ_c	$\left(\phi_{cM}\right)_{(1/4)c}$
$b_{0\,c,cM}$	0.5	1.155	0
	0.6	1.25	0
	0.7	1.4	0
	0.8	1.667	-
$b_{1\,c,cM}$	0.5	-0.406	0.0557
	0.6	-0.452	-0.1
	0.7	-0.5096	-0.2425
	0.8	-6.322	-
$b_{2\,c,cM}$	0.5	-0.249	-1
	0.6	-0.63	-1.502
	0.7	-0.567	0.084
	0.8	6.538	-
$b_{3\,c,cM}$	0.5	0.773	0.6263
	0.6	0.893	1.336
	0.7	0.5866	-0.069
	0.8	-1.095	-
$\beta_{1\,c,cM}$	0.5	0.0754	2.555
	0.6	0.0646	1.035
	0.7	0.0536	0.974
	0.8	2.111	-

Table 3-1 continued …

$\beta_{2\ c,cM}$	0.5	0.372	3.308
	0.6	0.481	4.04
	0.7	0.357	0.668
	0.8	2.049	-
$\beta_{3\ c,cM}$	0.5	1.89	6.09
	0.6	0.958	5.022
	0.7	0.902	0.438
	0.8	0.082	-

As shown in Table 3-1, approximate representations of the compressible indicial functions are only available for certain Mach numbers [100,113]. However, in an aeroelastic analysis usually iterative methods are used and for an airspeed damping of the system is traced. To take the compressibility effects into account properly, compressible indicial functions have to be evaluated for the Mach number which corresponds to the input airspeed. However, since the compressible indicial functions are known for discrete Mach numbers in the literature, an appropriate interpolation method is required to evaluate the compressible indicial functions for any Mach number.

In the present study, a novel exponential approximation is presented which represent the coefficients of approximations as functions of Mach number less than 0.85. This technique in conjunction with the state-space representation of the aerodynamic loads [37,114] enables one to perform direct stability analysis of aircraft wings for different subsonic Mach numbers. For this purpose, with respect to the axis passing from the leading edge of the airfoil, exponential representations of the Mach dependent compressible indicial functions are re-defined as,

$$\phi_c\left(M, Ut/b\right) = \left[\alpha_{0c}(M) - \sum_{i=1}^{3} \alpha_{ic}(M)\, \mathrm{e}^{-\beta_i Ut/b}\right] H\left(Ut/b\right) \tag{3-49}$$

$$\phi_{cM}\left(M, Ut/b\right) = \left[\alpha_{0cM}(M) - \sum_{i=1}^{3} \alpha_{icM}(M)\, \mathrm{e}^{-\beta_i Ut/b}\right] H\left(Ut/b\right) \tag{3-50}$$

$$\phi_{cq}\left(M,Ut/b\right)=\left[\alpha_{0cq}(M)-\sum_{i=1}^{3}\alpha_{icq}(M)\mathrm{e}^{-\beta_i Ut/b}\right]H\left(Ut/b\right) \tag{3-51}$$

$$\phi_{cMq}\left(M,Ut/b\right)=\left[\alpha_{0cMq}(M)-\sum_{i=1}^{3}\alpha_{icMq}(M)\mathrm{e}^{-\beta_i Ut/b}\right]H\left(Ut/b\right) \tag{3-52}$$

where $H(Ut/b)$ is the unit step function. α_i coefficients are Mach dependent coefficients but β_i coefficients are Mach independent power coefficients.

It is further assumed that for all exponential representations of the indicial functions, Mach-independent power coefficients β_i are equal to their counterparts in the exponential approximation of the plunging indicial function for the lift for $M=0.5$ and they are given by $\beta_1=0.0754,\beta_2=0.372,\beta_3=1.89$ [100]. Thus, for each indicial function in Equations (3-49)-(3-52), there are only four Mach-dependent base coefficients $(\alpha_{ic,icM,icq,icMq}(M),i=0,1,2,3)$ to be determined. To obtain the unknown Mach dependent base coefficients the following procedure is pursued.

The asymptotic values of the indicial functions are computed by multiplying their counterparts in incompressible flow by the Prandtl-Glauert factor $1/\sqrt{1-M^2}$. It should be noted that these asymptotic values are equal to the sectional lift and moments coefficients in steady flow. Hence,

$$\begin{aligned}\phi_c(\infty)&=\frac{1}{\sqrt{1-M^2}},\phi_{cM}(\infty)=\frac{-1}{4\sqrt{1-M^2}},\\ \phi_{cq}(\infty)&=\frac{3}{4\sqrt{1-M^2}},\phi_{cMq}(\infty)=\frac{-1}{4\sqrt{1-M^2}}.\end{aligned} \tag{3-53}$$

Utilizing Equation (3-53), the first base coefficients of the lift and moment indicial functions for the plunging and the pitching motion ($\alpha_{0c,0cq,0cM,0cMq}(M)$) are found. As a matter of fact, first base coefficients are identically equal to the asymptotic values of the indicial functions given by Equation (3-53). It should be noted that asymptotic values of the indicial functions, which are equal to the first base coefficients, are independent of the power coefficients $(\beta_i,i=1,2,3)$.

With the assumption that for all exponential representations of the indicial functions, Mach-independent power coefficients β_i are equal to their counterparts in the exponential approximation of the plunging indicial function for the lift for $M = 0.5$, and with the already determined first base coefficients of the lift and moment indicial functions for the plunging and the pitching motion, the compressible indicial functions are expressed by Equations

$$\phi_c\left(Ut/b\right) = \frac{1}{\sqrt{1-M^2}} + \alpha_{1c}e^{-0.0754\frac{Ut}{b}} + \alpha_{2c}e^{-0.372\frac{Ut}{b}} + \alpha_{3c}e^{-1.89\frac{Ut}{b}} \quad (3\text{-}54)$$

$$\phi_{cM}\left(Ut/b\right) = \frac{-1}{4\sqrt{1-M^2}} + \alpha_{1cM}e^{-0.0754\frac{Ut}{b}} + \alpha_{2cM}e^{-0.372\frac{Ut}{b}} + \alpha_{3cM}e^{-1.89\frac{Ut}{b}} \quad (3\text{-}55)$$

$$\phi_{cq}\left(Ut/b\right) = \frac{3}{4\sqrt{1-M^2}} + \alpha_{1cq}e^{-0.0754\frac{Ut}{b}} + \alpha_{2cq}e^{-0.372\frac{Ut}{b}} + \alpha_{3cq}e^{-1.89\frac{Ut}{b}} \quad (3\text{-}56)$$

$$\phi_{cMq}\left(Ut/b\right) = \frac{-1}{4\sqrt{1-M^2}} + \alpha_{1cMq}e^{-0.0754\frac{Ut}{b}} + \alpha_{2cMq}e^{-0.372\frac{Ut}{b}} + \alpha_{3cMq}e^{-1.89\frac{Ut}{b}} \quad (3\text{-}57)$$

At this step, for each compressible indicial function, there are three base Mach dependent base coefficients $(\alpha_{ic,icM,icq,icMq}(M), i = 0,1,2,3)$, to be determined.

For the determination of the remaining three base coefficients for each indicial function three equations are needed. Lomax et al. [108] have solved the wave equation in the 2-D unsteady compressible flow to obtain the chordwise pressure loading on the airfoil in the time range of the non-dimensional time $0 \le Ut/b \le 2M/(M+1)$ are given by Equation ,

$$\phi_c\left(Ut/b\right)=\frac{2}{\pi M}\left[1-\frac{Ut/b}{2M}\left(1-M\right)\right],$$
$$\phi_{cM}\left(Ut/b\right)=\frac{-1}{\pi M}\left[1-\frac{Ut/b}{2M}\left(1-M\right)+\frac{\left(Ut/b\right)^2}{8M}\left(M-2\right)\right], \quad (3\text{-}58)$$
$$\phi_{cq}\left(Ut/b\right)=\frac{1}{\pi M}\left[1-\frac{Ut/b}{2M}\left(1-M\right)+\frac{\left(Ut/b\right)^2}{4M}\left(1-\frac{M}{2}\right)\right],$$
$$\phi_{cMq}\left(Ut/b\right)=\frac{-2}{3\pi M}\left[1-\frac{3\left(Ut/b\right)}{4M}\left(1-M\right)+\frac{3\left(Ut/b\right)^2}{32M^2}\left(1-M\right)^2+\frac{\left(Ut/b\right)^3}{16M^3}\left[M+\frac{1}{4}\left(1-M\right)^3\right]\right].$$

Two of the equations required for the solution of the three base coefficients come from the evaluation of the indicial functions at the non-dimensional times $Ut/b=0$ and $Ut/b=2M/M+1$.

The following procedure is implemented to obtain the third equation required for the solution of the three base coefficients for each indicial function $(\alpha_{ic,icM,icq,icMq}(M), i=0,1,2,3)$.

The remaining third equation is obtained by fitting polynomials to the already known exponential representations of the indicial functions at Mach numbers 0.5,0.6,0.7 and 0.8. It should be noted that for the lift indicial function for the plunging motion $(\tilde{\phi}_c)$, exponential representation of the indicial function is known at Mach numbers 0.5,0.6,0.7 and 0.8 whereas for the remaining indicial functions $(\tilde{\phi}_{cM},\tilde{\phi}_{cq},\tilde{\phi}_{cMq})$ exponential representations are known at Mach numbers 0.5,0.6 and 0.7. The aim is to obtain polynomial form of indicial functions $(\tilde{\phi}_c,\tilde{\phi}_{cM},\tilde{\phi}_{cq},\tilde{\phi}_{cMq})$ in terms of non-dimensional time (Ut/b) using the data given for the compressible indicial functions.

In this respect, indicial lift function for lift for the plunging motion of the airfoil is approximated by a third order polynomial given by,

$$\tilde{\phi}_c\left(Ut/b\right) = a_{c3}\left(Ut/b\right)^2 + a_{c2}\left(Ut/b\right)^2 + a_{c1}\left(Ut/b\right) + a_{c0} \qquad (3\text{-}59)$$

where, M is the Mach number, t is time, and b is the half chord. $a_{c0}, a_{c1}, a_{c2}, a_{c3}$ are the unknown coefficients which are obtained using the available data for the lift indicial function for the plunging motion $(\tilde{\phi}_c)$ The known exponential representations of the lift indicial function for the plunging motion for Mach numbers 0.5,0.6,0.7 and 0.8 are evaluated at four different non-dimensional times and the four unknown coefficients of the polynomial approximation of the indicial function ϕ_c are determined. For this purpose, four non-dimensional times are considered $\left(Ut_1/b = 4, Ut_2/b = 4.8, Ut_3/b = 5.6, Ut_4/b = 6.4\right)$ as a target values, and Equation (3-45) is set equal to Equation (3-59) at the indicated non-dimensional times as shown in Equation (3-60). From the four equations given by Equation (3-60), four undetermined coefficients $a_{c0}, a_{c1}, a_{c2}, a_{c3}$ are determined.

$$\phi_c = \tilde{\phi}_c \rightarrow$$

$$\begin{cases} for \qquad M = 0.5 \\ b_{0c} + b_{1c}e^{-\beta_{1c}(Ut_1/b)} + b_{2c}e^{-\beta_{2c}(Ut_1/b)} + b_{3c}e^{-\beta_{3c}(Ut_1/b)} = \\ \qquad\qquad a_{c3}(Ut_1/b)^3 + a_{c2}(Ut_1/b)^2 + a_{c1}(Ut_1/b) + a_{c0} \end{cases}$$

$$\begin{cases} for \qquad M = 0.6 \\ b_{0c} + b_{1c}e^{-\beta_{1c}(Ut_2/b)} + b_{2c}e^{-\beta_{2c}(Ut_2/b)} + b_{3c}e^{-\beta_{3c}(Ut_2/b)} = \\ \qquad\qquad a_{c3}(Ut_2/b)^3 + a_{c2}(Ut_2/b)^2 + a_{c1}(Ut_2/b) + a_{c0} \end{cases} \qquad (3\text{-}60)$$

$$\begin{cases} for \qquad M = 0.7 \\ b_{0c} + b_{1c}e^{-\beta_{1c}(Ut_3/b)} + b_{2c}e^{-\beta_{2c}(Ut_3/b)} + b_{3c}e^{-\beta_{3c}(Ut_3/b)} = \\ \qquad\qquad a_{c3}(Ut_3/b)^3 + a_{c2}(Ut_3/b)^2 + a_{c1}(Ut_3/b) + a_{c0} \end{cases}$$

$$\begin{cases} for \qquad M = 0.8 \\ b_{0c} + b_{1c}e^{-\beta_{1c}(Ut_4/b)} + b_{2c}e^{-\beta_{2c}(Ut_4/b)} + b_{3c}e^{-\beta_{3c}(Ut_4/b)} = \\ \qquad\qquad a_{c3}(Ut_4/b)^3 + a_{c2}(Ut_4/b)^2 + a_{c1}(Ut_4/b) + a_{c0} \end{cases}$$

The same process is repeated for the other moment indicial function ϕ_{cM} for the plunging motion of the airfoil, but second order polynomials are fitted since the exponential representations for the indicial functions ϕ_{cM} are available for Mach number 0.5, 0.6 and 0.7. For this purpose, second order polynomial for the moment indicial function in plunging motion $\left(\tilde{\phi}_{cM}\right)$ is introduced as,

$$\tilde{\phi}_{cM}\left(Ut/b\right) = a_{cM2}\left(Ut/b\right)^2 + a_{cM1}\left(Ut/b\right) + a_{cM0} \qquad (3\text{-}61)$$

where unknown coefficients $a_{cM0}, a_{cM1}, a_{cM2}$ are determined using the available data for the moment indicial function for the plunging motion $\left(\phi_{cM}\right)$ using Figure 3-7, Table 3-1 and Equation (3-7) at certain values of the non-dimensional time $\left(Ut/b\right)$ for

Mach numbers 0.5, 0.6 and 0.7 respectively . Three values of the non-dimensional time $\left(Ut_1/b = 4, Ut_2/b = 4.8, Ut_3/b = 5.6\right)$ are considered as target values and Equation (3-46) is set equal to Equation (3-61) at the indicated non-dimensional times, as shown in Equation (3-62). From the three equations given by Equation (3-62), three undetermined coefficients $a_{cM0}, a_{cM1}, a_{cM2}$ are determined.

$$\phi_{cM} = \tilde{\phi}_{cM} \rightarrow$$

$$\begin{cases} for \qquad M = 0.5 \\ b_{0cM} + b_{1cM} e^{-\beta_{1cM}(Ut_1/b)} + b_{2cM} e^{-\beta_{2cM}(Ut_1/b)} + b_{3cM} e^{-\beta_{3cM}(Ut_1/b)} = \\ \qquad\qquad a_{cM2}(Ut_1/b)^2 + a_{cM1}(Ut_1/b) + a_{cM0} \end{cases}$$

$$\begin{cases} for \qquad M = 0.6 \\ b_{0cM} + b_{1cM} e^{-\beta_{1cM}(Ut_2/b)} + b_{2cM} e^{-\beta_{2cM}(Ut_2/b)} + b_{3cM} e^{-\beta_{3cM}(Ut_2/b)} = \\ \qquad\qquad a_{cM2}(Ut_2/b)^2 + a_{cM1}(Ut_2/b) + a_{cM0} \end{cases} \tag{3-62}$$

$$\begin{cases} for \qquad M = 0.7 \\ b_{0cM} + b_{1cM} e^{-\beta_{1cM}(Ut_3/b)} + b_{2cM} e^{-\beta_{2cM}(Ut_3/b)} + b_{3cM} e^{-\beta_{3cM}(Ut_3/b)} = \\ \qquad\qquad a_{cM2}(Ut_3/b)^2 + a_{cM1}(Ut_3/b) + a_{cM0} \end{cases}$$

Similarly, second order polynomial for the lift indicial function in pitching motion $\left(\tilde{\phi}_{cq}\right)$ is introduced as,

$$\tilde{\phi}_{cq}\left(Ut/b\right) = a_{cq2}\left(Ut/b\right)^2 + a_{cq1}\left(Ut/b\right) + a_{cq0} \tag{3-63}$$

The unknown coefficients $a_{cq0}, a_{cq1}, a_{cq2}$ are calculated using data given in Table 3-2 extracted from Figure 3-8 at certain values of the non-dimensional time $\left(Ut_1/b = 4, Ut_2/b = 4.8, Ut_3/b = 5.6\right)$. By setting the values given in Table 3-2 equal to Equation (3-63) at the indicated non-dimensional times and solving the three

equations given in Equation (3-64), the unknown coefficients $a_{cq0}, a_{cq1}, a_{cq2}$ are obtained. It should be noted that the values of the indicial functions in Table 3-2 are obtained.

Table 3-2 Lift indicial function in pitching motion at three non-dimensional times for Mach numbers 0.5, 0.6 and 0.7

Mach number	Indicial function	Value of the indicial function
0.5	$\phi_{cq}(4)$	0.598
0.6	$\phi_{cq}(4.8)$	0.629
0.7	$\phi_{cq}(5.6)$	0.709

$$\phi_{cq} = \tilde{\phi}_{cq} \rightarrow$$

$$\begin{cases} for \qquad M = 0.5 \\ \phi_{cq}(Ut_1/b) = a_{cq2}(Ut_1/b)^2 + a_{cq1}(Ut_1/b) + a_{cq0} \end{cases}$$

$$\begin{cases} for \qquad M = 0.6 \\ \phi_{cq}(Ut_2/b) = a_{cq2}(Ut_2/b)^2 + a_{cq1}(Ut_2/b) + a_{cq0} \end{cases} \tag{3-64}$$

$$\begin{cases} for \qquad M = 0.7 \\ \phi_{cq}(Ut_3/b) = a_{cq2}(Ut_3/b)^2 + a_{cq1}(Ut_3/b) + a_{cq0} \end{cases}$$

Lastly, second order polynomial for moment indicial function in pitching motion $\left(\tilde{\phi}_{cMq}\right)$ is introduced as in Equation (3-65).

$$\tilde{\phi}_{cMq}\left(Ut/b\right) = a_{cMq2}\left(Ut/b\right)^2 + a_{cMq1}\left(Ut/b\right) + a_{cMq0} \tag{3-65}$$

The unknown coefficients $a_{cMq0}, a_{cMq1}, a_{cMq2}$ are calculated using data given in Table 3-3 extracted from Figure 3-9 at certain values of the non-dimensional time

$\left(Ut_1/b = 4, Ut_2/b = 4.8, Ut_3/b = 5.6\right)$. By setting the values given in Table 3-3 equal to Equation (3-65) at the indicated non-dimensional times and solving the three equations given in Equation (3-66), the unknown coefficients are obtained. The values of the indicial function in Table 3-3 are obtained

Table 3-3 Moment indicial function in pitching motion at three non-dimensional times for Mach numbers 0.5, 0.6 and 0.7

Mach number	Indicial function	values
0.5	$\phi_{cMq}(4)$	-0.322
0.6	$\phi_{cMq}(4.8)$	-0.31
0.7	$\phi_{cMq}(5.6)$	-0.286

$$\phi_{cMq} = \tilde{\phi}_{cMq} \rightarrow$$

$$\begin{cases} for \qquad M = 0.5 \\ \phi_{cMq}(Ut_1/b) = a_{cMq2}(Ut_1/b)^2 + a_{cMq1}(Ut_1/b) + a_{cMq0} \end{cases}$$

$$\begin{cases} for \qquad M = 0.6 \\ \phi_{cMq}(Ut_2/b) = a_{cMq2}(Ut_2/b)^2 + a_{cMq1}(Ut_2/b) + a_{cMq0} \end{cases} \qquad (3\text{-}66)$$

$$\begin{cases} for \qquad M = 0.7 \\ \phi_{cMq}(Ut_3/b) = a_{cMq2}(Ut_3/b)^2 + a_{cMq1}(Ut_3/b) + a_{cMq0} \end{cases}$$

In the end, the polynomial approximations of the compressible indicial functions with known coefficients are obtained and presented in Equations (3-67)-(3-70). For each compressible indicial function, Equations (3-67)-(3-70) give the third equation needed to solve for the Mach dependent base coefficients $(\alpha_{ic,icM,icq,icMq}(M), i = 0,1,2,3)$.

$$\tilde{\phi}_c\left(Ut/b\right) = -0.01093\left(Ut/b\right)^3 + 0.1719\left(Ut/b\right)^2 - 0.794\left(Ut/b\right) + 1.9233 \qquad (3\text{-}67)$$

$$\tilde{\phi}_{cM}\left(Ut/b\right) = -0.00149\left(Ut/b\right)^2 + 0.01366\left(Ut/b\right) - 0.2439 \tag{3-68}$$

$$\tilde{\phi}_{cq}\left(Ut/b\right) = 0.03742\left(Ut/b\right)^2 - 0.29024\left(Ut/b\right) + 1.16058 \tag{3-69}$$

$$\tilde{\phi}_{cMq}\left(Ut/b\right) = 0.00841\left(Ut/b\right)^2 - 0.0586\left(Ut/b\right) - 0.2225 \tag{3-70}$$

In the following, the process of obtaining the Mach dependent base coefficients is explained for the lift indicial function for the plunging motion $\left(\phi_c\right)$. The first two equations come from the evaluation of the compressible indicial functions, which are determined by Lomax in the range of the non-dimensional time $0 \le Ut/b \le 2M/(M+1)$, given by Equation (3-58). Compressible lift indicial function is evaluated at non-dimensional times $Ut/b = 0$ and $Ut/b = 2M/(M+1)$ and they are given by Equations (3-71) and (3-72).

$$\phi_c(0) = \frac{2}{\pi M} \tag{3-71}$$

$$\phi_c\left(\frac{2M}{M+1}\right) = \frac{4}{\pi(1+M)} \tag{3-72}$$

The third equation is obtained by equating the proposed approximation of the lift indicial function given by Equation (3-54) to the polynomial approximation Equation (3-67) at a later time. As seen in Figure 3-6, compressible indicial functions are shown for non-dimensional times up to 60. As the non-dimensional time increases, all indicial functions level out. Therefore, for all indicial functions proposed approximation of the lift indicial function given by Equation (3-54) is equated to the polynomial approximation Equation (3-67) at the non-dimensional time 40, as shown in Equations (3-73) and (3-74).

$$\phi_c(40) = \tilde{\phi}(40) \tag{3-73}$$

$$\frac{1}{\sqrt{1-M^2}} + \alpha_{1c}e^{-0.0754\times 40} + \alpha_{2c}e^{-0.372\times 40} + \alpha_{3c}e^{-1.89\times 40} = \\ -0.01093\times 40^3 + 0.1719\times 40^2 - 0.794\times 40 + 1.9233 \tag{3-74}$$

For the proposed approximation of the lift indicial function for the plunging motion, Equations (3-71), (3-72) and (3-74) are solved for the three unknown Mach dependent base coefficients $(\alpha_{ic}, i = 1,2,3)$.

For the moment indicial function in plunging motion ϕ_{cM}, the three equations for the solution of the Mach dependent base coefficients $(\alpha_{icM}, i = 1,2,3)$ are given by Equations (2-69)-(2-71).

$$\phi_{cM}(0) = \frac{-1}{\pi M} \tag{3-75}$$

$$\phi_{cM}\left(\frac{2M}{M+1}\right) = \frac{-1}{\pi M}\left(1 - \frac{1-M}{1+M} + \frac{M(M-2)}{2(1+M)^2}\right) \tag{3-76}$$

$$\phi_{cM}(40) = \tilde{\phi}_{cM}(40) \\ \frac{-1}{4\sqrt{1-M^2}} + \alpha_{1cM}e^{-0.0754\times 40} + \alpha_{2cM}e^{-0.372\times 40} + \alpha_{3cM}e^{-1.89\times 40} = \\ -0.00149\times 40^2 + 0.01366\times 40 - 0.2439 \tag{3-77}$$

For the lift indicial function in pitching motion ϕ_{cq}, the three equations for the solution of the Mach dependent base coefficients $(\alpha_{icq}, i = 1,2,3)$ are given by Equations (3-78)-(3-80).

$$\phi_{cq}(0) = \frac{1}{\pi M} \tag{3-78}$$

$$\phi_{cq}(\frac{2M}{M+1}) = \frac{1}{\pi M}\left(1 - \frac{1-M}{1+M} + \frac{M(1-M/2)}{2(1+M)^2}\right) \tag{3-79}$$

$$\begin{aligned} &\phi_{cq}(40) = \tilde{\phi}_{cq}(40) \\ &\frac{3}{4\sqrt{1-M^2}} + \alpha_{1cq}e^{-0.0754\times 40} + \alpha_{2cq}e^{-0.372\times 40} + \alpha_{3cq}e^{-1.89\times 40} = \\ &\qquad 0.0372\times 40^2 - 0.29024\times 40 + 1.16058 \end{aligned} \tag{3-80}$$

For the lift indicial function in pitching motion ϕ_{cMq}, the three equations for the solution of the Mach dependent base coefficients $(\alpha_{icMq}, i = 1,2,3)$ are given by Equations (3-81)-(3-83).

$$\phi_{cMq}(0) = \frac{-2}{3\pi M} \tag{3-81}$$

$$\phi_{cMq}(\frac{2M}{M+1}) = \frac{-2}{3\pi M}\left(1 - \frac{3(1-M)}{2(1+M)} + \frac{3(1-M)^2}{28} + \frac{M+1}{2(1+M)^3(1-M)^3}\right) \tag{3-82}$$

$$\begin{aligned} &\phi_{cMq}(40) = \tilde{\phi}_{cMq}(40) \\ &\frac{-1}{4\sqrt{1-M^2}} + \alpha_{1cMq}e^{-0.0754\times 40} + \alpha_{2cMq}e^{-0.372\times 40} + \alpha_{3cMq}e^{-1.89\times 40} = \\ &\qquad 0.00841\times 40^2 - 0.0586\times 40 - 0.2225 \end{aligned} \tag{3-83}$$

For any Mach number, after solution of the three Mach dependent coefficients $(\alpha_{ic,icM,icq,icMq}(M), i = 0,1,2,3)$ for each compressible indicial function for the plunging and pitching motions of the airfoil, compressible indicial functions can be calculated for any Mach number through Equations (3-54)-(3-57). With the proposed approach for the frequency domain solution of the aeroelastic instability problem one evaluate the compressible indicial functions at any Mach number in the Mach number range $0.5 \le M \le 0.8$. It should be noted that for Mach numbers less than 0.3, incompressible flow assumption is reasonable.

The variations of the Mach dependent coefficients of lift and moment indicial functions in plunging and pitching motions, which are calculated using the proposed method, with respect to Mach number are presented in Figure 3-10-Figure 3-13

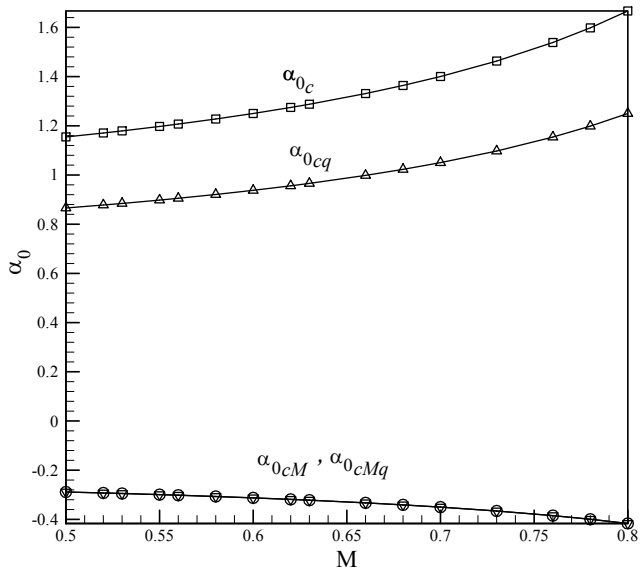

Figure 3-10 α_0 coefficients for approximating the indicial lift and moment at $0.5 \leq M \leq 0.8$

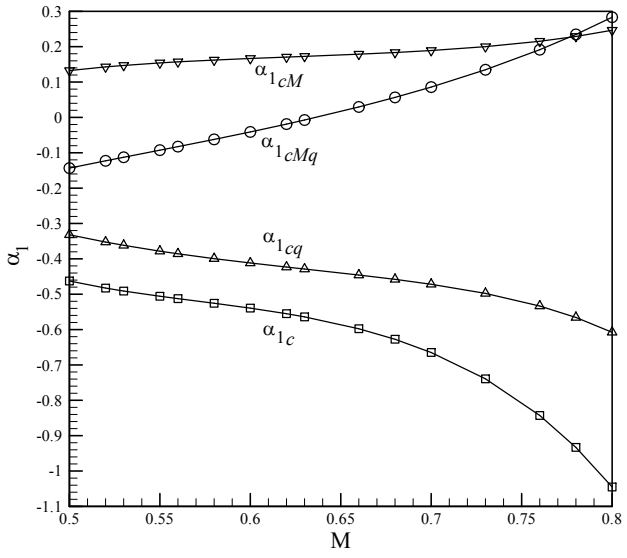

Figure 3-11 α_1 coefficients for approximating the indicial lift and moment at $0.5 \leq M \leq 0.8$

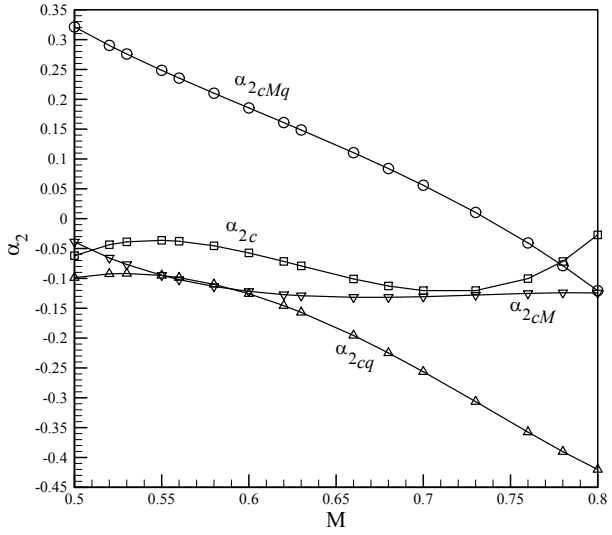

Figure 3-12 α_2 coefficients for approximating the indicial lift and moment at $0.5 \leq M \leq 0.8$

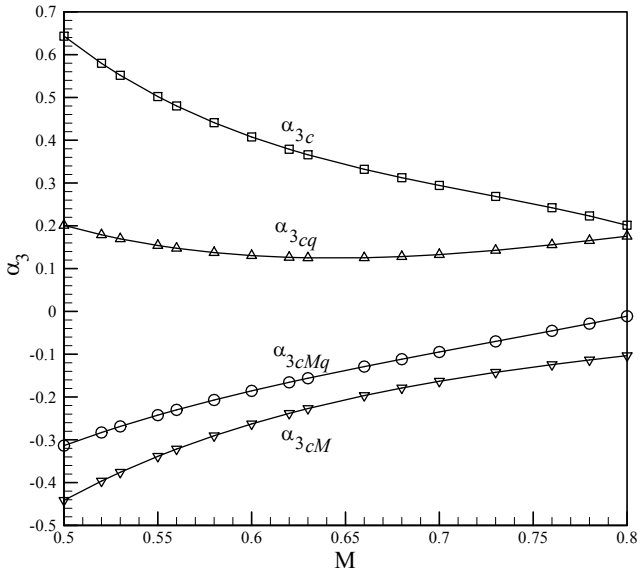

Figure 3-13 α_3 coefficients for approximating the indicial lift and moment at $0.5 \leq M \leq 0.8$

In Figure 3-14 and Figure 3-15, lift $\left(\phi_c\right)$ and moment $\left(\phi_{cMq}\right)$ indicial functions for the plunging motion are calculated by the proposed approach are compared with the available solutions of the lift and moment indicial functions in subsonic flow [115].

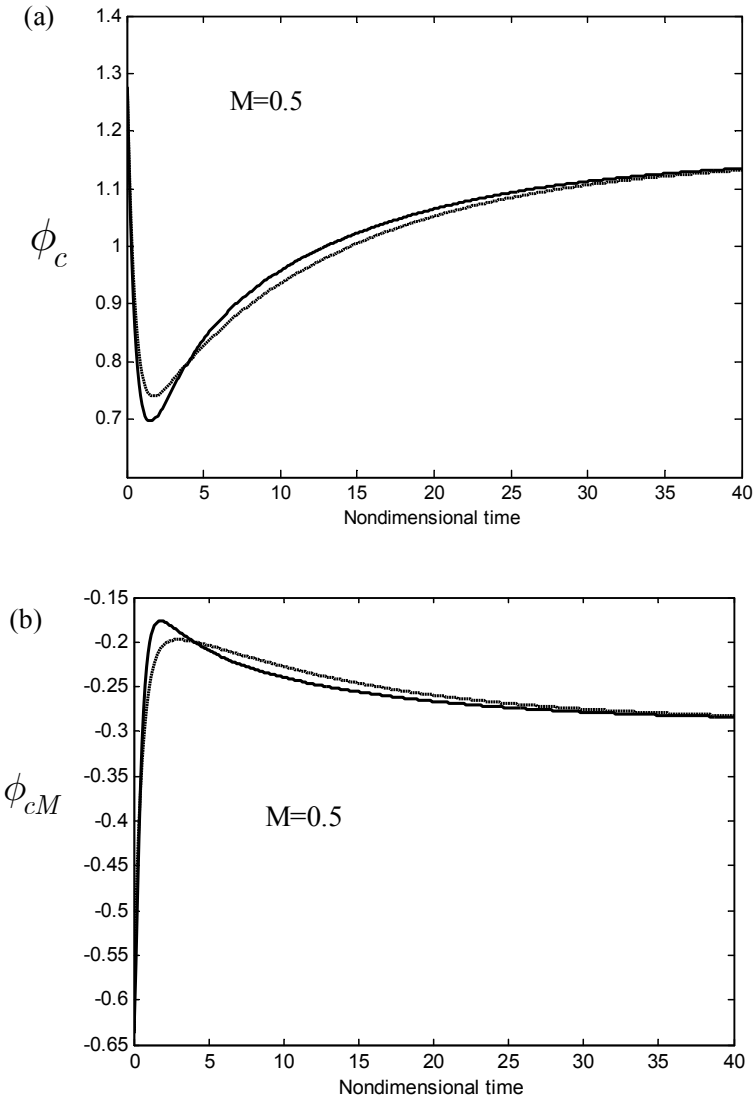

Figure 3-14 Comparison of indicial (a) lift and (b) moment functions for the plunging motion $M = 0.5$, dashed line: present study, solid line : Ref [115]

At the Mach numbers of 0.5 and 0.7. From Figure 3-14 and Figure 3-15, it is seen that in the range of the non-dimensional time $0 \leq Ut/b \leq 40$, the variations of the indicial functions calculated by the proposed approach are in reasonably good agreement with the available solution. It should be again stressed that with the proposed approach, the compressible indicial functions can be calculated at any Mach number in range $0.5 \leq M \leq 0.8$ which covers most of the subsonic compressible flow problems.

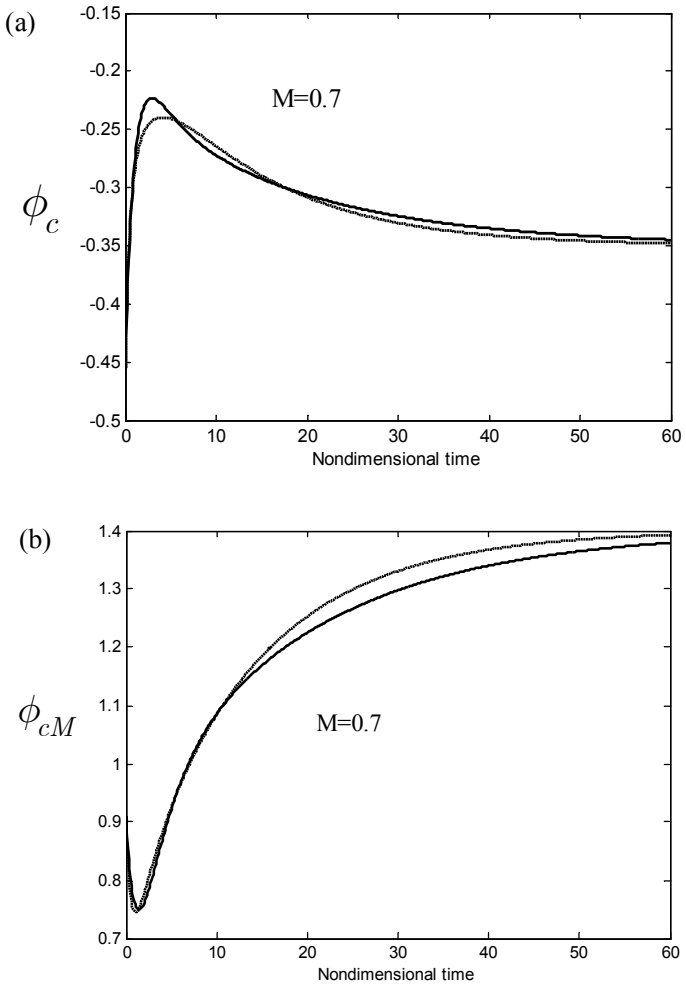

Figure 3-15 Comparison of indicial (a) lift and (b) moment functions for the plunging motion $M = 0.7$, dashed line: present study, solid line : Ref [115]

3.2.1 Explicit form of the subsonic compressible aerodynamics model

Once the Mach dependent base coefficients $(\alpha_{ic,icM,icq,icMq}(M), i = 0,1,2,3)$ of the lift and the moment compressible indicial functions for the plunging and pitching motion with respect to the coordinate system established at the leading edge of the airfoil are determined for any Mach number, base coefficients with respect to the axis located at $b(a+1)$ aft of the leading edge can be determined utilizing the relations given by Equation (3-84),

$$\begin{aligned}
&\bar{\alpha}_{ic}(M) = \alpha_{ic}(M) \\
&\bar{\alpha}_{icM}(M) = \alpha_{icM}(M) + \left(\frac{a}{2} + \frac{1}{2}\right)\alpha_{ic}(M) \\
&\bar{\alpha}_{icq}(M) = \alpha_{icq}(M) - \left(\frac{a}{2} + \frac{1}{2}\right)\alpha_{ic}(M) \\
&\bar{\alpha}_{icMq}(M) = \alpha_{icMq}(M) + \left(\frac{a}{2} + \frac{1}{2}\right)\left(\alpha_{icq}(M) - \alpha_{icM}(M)\right) - \left(\frac{a}{2} + \frac{1}{2}\right)^2 \alpha_{ic}(M)
\end{aligned} \tag{3-84}$$

where $i = 1,2,3$. It should be noted that these relations are the same as those given by Equation (3-42) for the indicial functions themselves owing to the fact that, the approximate exponential representation of the four indicial functions are defined with the same Mach-independent power coefficients $(\beta_i, i = 1,2,3)$.

The integrals in the lift and moment expressions in Equations (4-79) and (4-80) are re-expressed by substituting the exponential representations of the indicial functions, defined with respect to the axis located at $b(a+1)$ aft of the leading edge, in the integrals as shown in,

$$\begin{aligned}
&L^c_{ae}\left(z,t\right) = -C_{L\phi}\rho U b\left[w_v(z,0)\,\bar{\phi}_c(\frac{U}{b}t) + \int_0^t \frac{dw_v(z,\tau)}{d\tau}\,\bar{\phi}_c\left(\frac{U}{b}(t-\tau)\right)d\tau\right] + \\
&2C_{L\phi}\rho U b^2\left[w_\phi(z,0)\bar{\phi}_{cq}(\frac{U}{b}t) + \int_0^t \frac{dw_\phi\left(z,\tau\right)}{d\tau}\,\bar{\phi}_{cq}\left(\frac{U}{b}(t-\tau)\right)d\tau\right]
\end{aligned} \tag{3-85}$$

$$M_{ae}^{c}\left(z,t\right)=-2C_{L\phi}\rho Ub^{2}\left[w_{v}(z,0)\,\overline{\phi}_{cM}(\frac{U}{b}t)+\int_{0}^{t}\frac{dw_{v}(z,\tau)}{d\tau}\overline{\phi}_{c}\left(\frac{U}{b}(t-\tau)\right)dt_{0}\right]+ \quad (3\text{-}86)$$
$$4C_{L\phi}\rho Ub^{3}\left[w_{\phi}(z,0)\overline{\phi}_{cMq}(\frac{U}{b}t)+\int_{0}^{t}\frac{dw_{\phi}\left(z,\tau\right)}{d\tau}\overline{\phi}_{cMq}\left(\frac{U}{b}(t-\tau)\right)dt_{0}\right]$$

$$\begin{aligned}
D_{1}(z,t)&=\int_{0}^{t}\frac{dw_{v}(z,\tau)}{d\tau}\overline{\phi}_{c}\left(\frac{U}{b}(t-\tau)\right)d\tau=\int_{0}^{t}\frac{dw_{v}(z,\tau)}{d\tau}\left(\overline{\alpha}_{0c}(M)-\sum_{i=1}^{3}\overline{\alpha}_{ic}(M)\,\mathrm{e}^{-\beta_{i}\frac{U}{b}(t-\tau)}\right)d\tau\\
D_{2}(z,t)&=\int_{0}^{t}\frac{dw_{\phi}(z,\tau)}{d\tau}\overline{\phi}_{cq}\left(\frac{U}{b}(t-\tau)\right)d\tau=\int_{0}^{t}\frac{dw_{\phi}(z,\tau)}{d\tau}\left(\overline{\alpha}_{0cq}(M)-\sum_{i=1}^{3}\overline{\alpha}_{icq}(M)\,\mathrm{e}^{-\beta_{i}\frac{U}{b}(t-\tau)}\right)d\tau\\
D_{3}(z,t)&=\int_{0}^{t}\frac{dw_{v}(z,\tau)}{d\tau}\overline{\phi}_{cM}\left(\frac{U}{b}(t-\tau)\right)d\tau=\int_{0}^{t}\frac{dw_{v}(z,\tau)}{d\tau}\left(\overline{\alpha}_{0cM}(M)-\sum_{i=1}^{3}\overline{\alpha}_{icM}(M)\,\mathrm{e}^{-\beta_{i}\frac{U}{b}(t-\tau)}\right)d\tau\\
D_{4}(z,t)&=\int_{0}^{t}\frac{dw_{\phi}(z,\tau)}{d\tau}\overline{\phi}_{cqM}\left(\frac{U}{b}(t-\tau)\right)d\tau=\int_{0}^{t}\frac{dw_{\phi}(z,\tau)}{d\tau}\left(\overline{\alpha}_{0cqM}(M)-\sum_{i=1}^{3}\overline{\alpha}_{icqM}(M)\,\mathrm{e}^{-\beta_{i}\frac{U}{b}(t-\tau)}\right)d\tau
\end{aligned} \quad (3\text{-}87)$$

By defining the integrals involving the exponential terms in Equation (3-87) as the aerodynamic lag terms $B_{ic,icq,icM,icMq}\left(z,t\right)$, assuming that the wing is initially at rest ($w_{v}(z,0)=w_{\phi}(z,0)=0$) and making use of the Leibniz integral rule, Equation (3-87) is transformed into Equation (3-88).

$$\begin{aligned}
D_{1}\left(z,t\right)&=\overline{\alpha}_{0_{c}}w_{v}(z,t)-\sum_{i=1}^{3}\overline{\alpha}_{ic}B_{ic}\left(z,t\right)\\
D_{2}\left(z,t\right)&=\overline{\alpha}_{0_{cq}}w_{\phi}(z,t)-\sum_{i=1}^{3}\overline{\alpha}_{icq}B_{icq}\left(z,t\right)\\
D_{3}\left(z,t\right)&=\overline{\alpha}_{0_{cM}}w_{v}(z,t)-\sum_{i=1}^{3}\overline{\alpha}_{icM}B_{icM}\left(z,t\right)\\
D_{4}\left(z,t\right)&=\overline{\alpha}_{0_{cMq}}w_{\phi}(z,t)-\sum_{i=1}^{3}\overline{\alpha}_{icMq}B_{icMq}\left(z,t\right)
\end{aligned} \quad (3\text{-}88)$$

When the Leibniz integral rule is applied to the integrals involving the exponential terms in Equation (3-87) it can be shown that the aerodynamic lag terms $B_{ic,icq,icM,icMq}\left(z,t\right)$ are defined by,

$$\begin{aligned}
&\dot{B}_{ic}\left(z,t\right)+(\beta_i\frac{U}{b})B_{ic}\left(z,t\right)=\frac{dw_v\left(z,t\right)}{dt}\\
&\dot{B}_{icq}\left(z,t\right)+(\beta_i\frac{U}{b})B_{icq}\left(z,t\right)=\frac{dw_\phi\left(z,t\right)}{dt}\\
&\dot{B}_{icM}\left(z,t\right)+(\beta_i\frac{U}{b})B_{icM}\left(z,t\right)=\frac{dw_v\left(z,t\right)}{dt}\\
&\dot{B}_{icMq}\left(z,t\right)+(\beta_i\frac{U}{b})B_{icMq}\left(z,t\right)=\frac{dw_\phi\left(z,t\right)}{dt}
\end{aligned}\tag{3-89}$$

It should be noted that three aerodynamic lag terms are used for each indicial function so a total number of twelve aerodynamic lag terms would exist in the description of the 3D unsteady aerodynamic loads in the subsonic compressible flow. Finally, unsteady compressible aerodynamic lift $L_{ae}^{c}(z,t)$ and pitching moment $M_{ae}^{c}(z,t)$ about the Theodorsen's coordinate in terms of indicial functions are expressed as,

$$\begin{aligned}
L_{ae}^{c}(z,t)=-C_{L\phi}\rho Ub\left[\overline{\alpha}_{0c}(M)w_v\left(z,t\right)-\sum_{i=1}^{3}\overline{\alpha}_{ic}(M)B_{ic}\left(z,t\right)\right]+\\
2C_{L\phi}\rho Ub^2\left[\overline{\alpha}_{0cq}(M)w_\phi\left(z,t\right)-\sum_{i=1}^{3}\overline{\alpha}_{icq}(M)B_{icq}\left(z,t\right)\right]
\end{aligned}\tag{3-90}$$

$$\begin{aligned}
M_{ae}^{c}(z,t)=-2C_{L\phi}\rho Ub^2\left[\overline{\alpha}_{0cM}(M)w_v\left(z,t\right)-\sum_{i=1}^{3}\overline{\alpha}_{icM}(M)B_{icM}\left(z,t\right)\right]+\\
4C_{L\phi}\rho Ub^3\left[\overline{\alpha}_{0cMq}(M)w_\phi\left(z,t\right)-\sum_{i=1}^{3}\overline{\alpha}_{icMq}(M)B_{icMq}\left(z,t\right)\right]
\end{aligned}\tag{3-91}$$

To incorporate the 3-D effects of the finite span wing, lift curve slope $C_{L\phi}$ is obtained from Diederich's general formula as [116],

$$C_{L\phi}=\frac{ARc_{l\phi}}{AR\sqrt{1-M^2}\sqrt{1+\left(\frac{c_{l\phi}}{\pi AR\sqrt{1-M^2}}\right)^2}+\frac{c_{l\phi}}{\pi}}\tag{3-92}$$

where M is the Mach number and $c_{l\phi}$ is the 2D lift curve slope.

CHAPTER 4

NONLINEAR DYNAMIC AEROELASTIC RESPONSE OF COMPOSITE WINGS STRUCTURALLY MODELED AS TWB

Geometrically nonlinear aeroelastic behavior of pretwisted, tapered composite wings, structurally modeled as TWB is studied. The structural equations of motion are obtained in the most general form based on the kinematic relations governing thin walled beams, including the nonlinear strain displacement relations, and utilizing the principles of analytical dynamics. Unsteady aerodynamic loads in the incompressible flow regime are expressed using Wagner's function in the time domain (Section 4.2) and unsteady aerodynamic loads in the subsonic compressible flow regime are expressed using indicial's function (Section 4.4). The aeroelastic system of equations is augmented by the differential equations governing the aerodynamics lag states to come up with the final coupled fluid-structure equations of motion. The governing system of equations of the aeroelastic system is solved, for the TWB with CAS composite layup, by means of a Ritz based solution methodology utilizing the mode shapes of the linear structural system to approximate the spatial variation of the degrees of freedom of the thin walled beam. Time response of the nonlinear aeroelastic system is obtained via the Runge-Kutta direct integration algorithm. Effects of the fiber angle, pretwist angle, taper ratio and sweep angle of the CAS layup configuration on the nonlinear aeroelastic stability margins and LCO behavior are studied in depth.

The aim of the present study is to investigate the effect of geometrical nonlinearity on the post flutter behavior of composite high aspect ratio wings in subsonic flight regime, with both incompressible and compressible aerodynamics. In this flow regime, the

medium fidelity aerodynamic model of the unsteady strip theory with indicial functions provide acceptable accuracy compared to high fidelity CFD models. In the literature, several studies have been performed using non-linear beam dynamic equations coupled with 2D unsteady aerodynamics models with or without modelling stall phenomenon [117-121].

In the present work, it is assumed that the torsional deformation is finite and moderately large while the flow still remains attached to the surface. The assumption of considering nonlinearity in torsion degree of freedom is due to establishing stiffness coupling among the degrees of freedom which affects the post flutter behavior significantly. On the other hand, for large torsional deformations, dynamic stall could be a major problem. For many types of airfoils, the critical value of angle of attack is usually between 15-20 degrees [122]. In our analyses, twist angle is nowhere near the stall region.

In summary, in this study, small disturbance theory, which is valid for attached flow, is used. For impending aeroelastic instability, using small disturbance theory suffices since in the initial phase of the flutter phenomenon deformations are small. In the current study, post-flutter response has been investigated for very small values for the initial conditions which makes the small disturbance theory still acceptable for the investigation of nonlinear aeroelasticity of wings and blades. Intrinsic character of the nonlinear aeroelastic system has been investigated by exciting the wing by a very small initial disturbance and utilizing linear unsteady aerodynamics. The current model can be improved by including stall aerodynamics using models such as ONERA stall aerodynamics as a future work.

4.1 Aeroelastic Governing Equation of Motion

Due to complicate boundary conditions derived in Chapter 2, it is challenging to find appropriate comparison functions that satisfy both geometric and natural boundary conditions. Therefore, in order to avoid dealing with complexity of boundary conditions effects, they are not extracted from the governing equations of motion by

applying integration by parts. Symbolic composite wing with structural and aerodynamic coordinates and parameters is shown in Figure 4-1.

the nonlinear structural model based on Librescu and Song [56] is representative for advanced rotating wings with general cross section, for the sake of convenience a single-cell, fiber-reinforced composite thin walled box beam with a length L, width l, height d, thickness h, wing chord $2b$ (see Figure 4-2a) . The 3-D displacement parameters, u_0, v_0 and w_0 are mid-surface displacements in x, y and z directions, respectively. Also, θ_x , θ_y and ϕ are section normal vector rotations about x, y and z directions, respectively (Figure 4-2b).

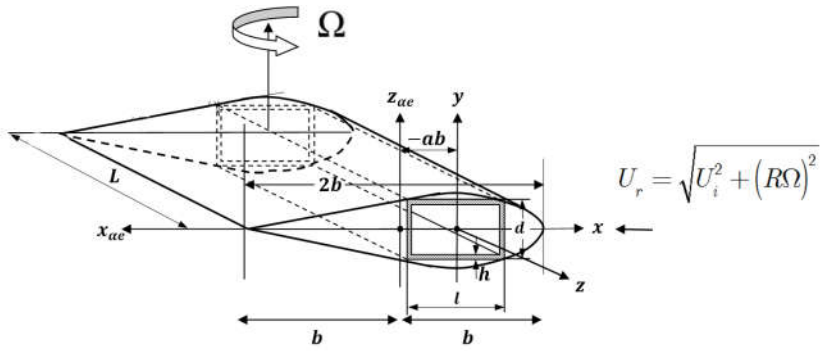

Figure 4-1 Schematic description of the rotating wing structure and it's cross section

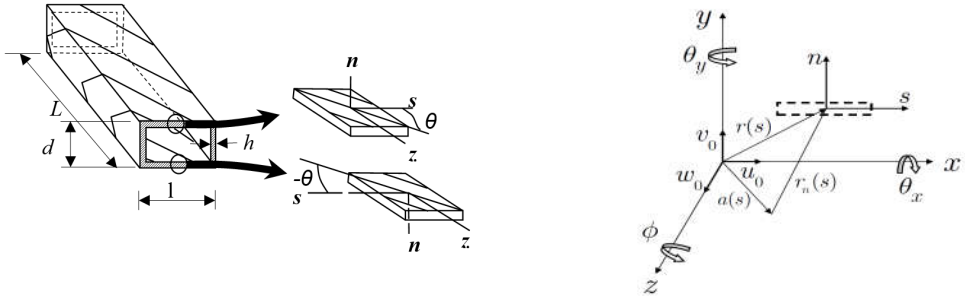

Figure 4-2 (a) Composite TWB (b) Cross section coordinate to define complex cross sections of CAS configuration

Energy Expression

Having introduced all the preliminary concepts and energy definitions in Chapter 2 for composite nonlinear TWB, it is now time to use the Hamilton's principle to obtain integral equations of motion. According to the Hamilton dynamics, variations of the Lagrangian of the system in stationary over any interval of motion $[t_1 \quad t_2]$m

$$\begin{aligned} &\int_{t_1}^{t_2} (\delta T - \delta V - \delta V_{cf} + \delta W) dt = 0 \\ &at \quad t = t_1, t_2, \\ &\delta u_0 = \delta v_0 = \delta w_0 = \delta \theta_x = \delta \theta_y = \delta \phi = 0 \end{aligned} \tag{4-1}$$

where, T, V, V_{cf} are the kinetic energy, potential energy due to large strains and centrifugal force, respectively and W stands for the work done by external loads.

Theses energies are comprehensively studied in Chapter 2. The variational form of strain energy, kinetic energy and the work done by the external force are utilized to establish the integral form of general governing system of equations.

Variation of the strain potential energy due to large strain is obtained be used in Equation (4-1). The variation of the strain potential energy of TWB shown in Figure 4-2 is given by,

$$\delta V = \int_0^L \begin{bmatrix} \left(T_z u_0' - M_y \phi' \sin(\phi) - M_x \phi' \cos(\phi) + Q_x \cos(\phi) - Q_y \sin(\phi)\right) \delta u_0' + \\ \left(T_z v_0' + M_y \phi' \cos(\phi) - M_x \phi' \sin(\phi) + Q_x \sin(\phi) + Q_y \cos(\phi)\right) \delta v_0' + \\ \left(T_z\right) \delta w_0' + Q_y \delta \theta_x + Q_x \delta \theta_y + \left(M_y\right) \delta \theta_y' + \left(M_x\right) \delta \theta_x' + \\ \begin{pmatrix} -M_y u_0' \phi' \cos(\phi) - M_y v_0' \phi' \sin(\phi) + M_x u_0' \phi' \sin(\phi) - \\ M_x v_0' \phi' \cos(\phi) - Q_x u_0' \sin(\phi) + Q_x v_0' \cos(\phi) - \\ Q_y v_0' \sin(\phi) - Q_y u_0' \cos(\phi) \end{pmatrix} \delta \phi + \\ \begin{pmatrix} M_y v_0' \cos(\phi) - M_y u_0' \sin(\phi) - M_x u_0' \cos(\phi) - \\ M_x v_0' \sin(\phi) + M_z + \Lambda_z \phi' \end{pmatrix} \delta \phi' + \\ \left(-B_w\right) \delta \phi'' \end{bmatrix} dz \tag{4-2}$$

On the other hand the variation of the kinetic energy in terms of the position vector R is given by,

$$\delta T = \int_0^L \oint_C \sum_{k=1}^{m_l} \int_{n_{k-1}}^{n_k} \rho \ddot{R} \delta R \quad dn ds dz \tag{4-3}$$

Since the position vector of any generic point on the TWB with respect to the root coordinate system is given in Equation (4-4),

$$R = (x+u)\hat{i} + (y+v)\hat{j} + (z+w+R_0)\hat{k} \tag{4-4}$$

Noting that the displacement field (u, v, w) is defined in Equation (2-1), considering angular velocity $\Omega(\Omega J = \Omega j)$ (Figure 2-1), one can determine the acceleration vector as shown in Equation (4-5).

$$\ddot{R} = \left[\ddot{u} + \underbrace{2\dot{w}\Omega}_{Coriolis} - \underbrace{(x+u)\Omega^2}_{Centrifugal} \right] \hat{i} + \ddot{v}\hat{j} + \left[\ddot{w} - \underbrace{2\dot{u}\Omega}_{Coriolis} - \underbrace{\left(z+w+R_0\right)\Omega^2}_{Centrifugal} \right] \hat{k} \tag{4-5}$$

Substituting the acceleration components from Equation (2-1) into Equation (4-5) and using the result in Equation (4-3) one eventually obtains the variation of the kinetic energy as,

$$\delta T = -\int \left[I_1 \delta u_0 + I_2 \delta v_0 + I_3 \delta w_0 + I_4 \delta \theta_x + I_5 \delta \theta_y + I_6 \delta \phi + I_7 \delta \phi' \right] dz \tag{4-6}$$

where,

$$
\begin{aligned}
I_1 &= b_1\left(\ddot{u}_0 + 2\dot{w}_0\Omega - u_0\Omega^2\right) - b_3\left(\ddot{\phi}\sin\phi + \dot{\phi}^2\cos\phi\right) - \\
&\quad b_2\left(\ddot{\phi}\cos\phi - \dot{\phi}^2\sin\phi\right) \\
I_2 &= b_1\ddot{v}_0 + b_3\left(\ddot{\phi}\cos\phi - \dot{\phi}^2\sin\phi\right) - b_2\left(\ddot{\phi}\sin\phi + \dot{\phi}^2\cos\phi\right) \\
I_3 &= b_1\left(\ddot{w}_0 - 2\dot{u}_0\Omega - \left(z + w_0 + R_0\right)\Omega^2\right) + b_2\ddot{\theta}_x + b_3\ddot{\theta}_y - b_7\ddot{\phi}' \\
I_4 &= \left(b_4 + b_{12}\right)\left(\ddot{\theta}_x - \Omega^2\theta_x + 2\cos\phi\Omega\dot{\phi}\right) + \\
&\quad \left(b_6 - b_{13}\right)\left(\ddot{\theta}_y - \Omega^2\theta_y + 2\sin\phi\Omega\dot{\phi}\right) + \\
&\quad b_2\left(\ddot{w}_0 - 2\dot{u}_0\Omega - \left(z + w_0 + R_0\right)\Omega^2\right) - \left(b_8 - b_{14}\right)\left(\ddot{\phi}'\right) \\
I_5 &= \left(b_5 + b_{11}\right)\left(\ddot{\theta}_y - \Omega^2\theta_y + 2\sin\phi\Omega\dot{\phi}\right) + \\
&\quad \left(b_6 - b_{13}\right)\left(\ddot{\theta}_x - \Omega^2\theta_x + 2\cos\phi\Omega\dot{\phi}\right) + \\
&\quad b_3\left(\ddot{w}_0 - 2\dot{u}_0\Omega - \left(z + w_0 + R_0\right)\Omega^2\right) - \left(b_9 + b_{15}\right)\ddot{\phi}' \\
I_6 &= b_3\left(\ddot{v}_0\cos\phi - \ddot{u}_0\sin\phi\right) + b_2\left(-\ddot{v}_0\sin\phi - \ddot{u}_0\cos\phi\right) + \\
&\quad \left(b_6 - b_{13}\right)\left(-2\Omega\dot{\theta}_x\sin\phi - 2\Omega\dot{\theta}_y\cos\phi + \Omega^2\left(\cos^2\phi - \sin^2\phi\right)\right) \\
&\quad + \left(b_4 + b_{12}\right)\left\{\begin{array}{l}\left(\ddot{\phi}\sin\phi + \dot{\phi}^2\cos\phi\right)\sin\phi + \\ \left(\ddot{\phi}\cos\phi - \dot{\phi}^2\sin\phi\right)\cos\phi - 2\Omega\dot{\theta}_x\cos\phi - \Omega^2\cos\phi\sin\phi\end{array}\right\} + \\
&\quad \left(b_5 + b_{11}\right)\left\{\begin{array}{l}\left(\ddot{\phi}\sin\phi + \dot{\phi}^2\cos\phi\right)\sin\phi + \\ \left(\ddot{\phi}\cos\phi - \dot{\phi}^2\sin\phi\right)\cos\phi - 2\Omega\dot{\theta}_y\sin\phi + \Omega^2\cos\phi\sin\phi\end{array}\right\} + \\
I_7 &= b_7\left(\ddot{w}_0 - 2\dot{u}_0\Omega\right) + \left(b_8 - b_{14}\right)\left(\ddot{\theta}_x\right) + \left(b_9 + b_{15}\right)\left(\ddot{\theta}_y\right) - \left(b_{10} + b_{16}\right)\left(\ddot{\phi}' - \Omega^2\phi'\right)
\end{aligned}
\tag{4-7}
$$

where all inertia terms b_i are defined in Equation (2-60).

Rotary blades are subjected to centrifugal force whose influence is more significant at high speeds. The centrifugal force acting on the rotating beam at a spanwise location *z* can be expressed as,

$$
F_c = \int_z^L \rho\Omega^2\left(R_0 + z\right)dz = \rho\Omega^2 R\left(z\right) \tag{4-8}
$$

where, $R(z)$ is defined as,

$$
R\left(z\right) = \left[R_0\left(L - z\right) + \frac{1}{2}\left(L^2 - z^2\right)\right] \tag{4-9}
$$

The variation of strain energy due to the centrifugal force is given by Equation (4-10),

$$\delta V_{cf} = \int_0^L \left[\left(f_1 \right) \delta u_0' + \left(f_2 \right) \delta v_0' + \left(f_3 \right) \delta \phi' + \left(f_4 \right) \delta \phi \right] dz \tag{4-10}$$

where f_i are defined in Equation (4-11)- (4-14).

$$f_1 = b_1 \Omega^2 R\left(z\right) u_0' - b_2 \Omega^2 R\left(z\right) \phi' \cos\phi - b_3 \Omega^2 R\left(z\right) \phi' \sin\phi \tag{4-11}$$

$$f_2 = b_1 \Omega^2 R\left(z\right) v_0' - b_2 \Omega^2 R\left(z\right) \phi' \sin\phi + b_3 \Omega^2 R\left(z\right) \phi' \cos\phi \tag{4-12}$$

$$\begin{aligned} f_3 = {} & \left(b_4 + b_{12} \right) \Omega^2 R\left(z\right) \phi' + \left(b_5 + b_{11} \right) \Omega^2 R\left(z\right) \phi' - \\ & b_2 \Omega^2 R\left(z\right) \left(u_0' \cos\left(\phi\right) + v_0' \sin\left(\phi\right) \right) + b_3 \Omega^2 R\left(z\right) \left(v_0' \cos\left(\phi\right) - u_0' \sin\left(\phi\right) \right) \end{aligned} \tag{4-13}$$

$$\begin{aligned} f_4 = {} & b_2 \Omega^2 R\left(z\right) \left(u_0' \phi' \sin\left(\phi\right) - v_0' \phi' \cos\left(\phi\right) \right) - \\ & b_3 \Omega^2 R\left(z\right) \left(u_0' \phi' \cos\left(\phi\right) + v_0' \phi' \sin\left(\phi\right) \right) \end{aligned} \tag{4-14}$$

The last portion of the Hamiltonian in Equation (4-1) is the variation of work done by the external loading. The only loading considered in this study is the one due to the unsteady aerodynamics. Hence, one can obtain δW as,

$$\delta W = \int_0^L \left(L_{ae}(z,t) \delta v_0(z) + M_{ae}(z,t) \delta \phi(z) \right) dz \tag{4-15}$$

where the explicit forms of the unsteady aerodynamic lift L_{ae} and the pitching moment about the reference axis M_{ae} are derived in Chapter 3.

The integral representation of the general governing system of equations is obtained by inserting the expressions of the variation of the potential energy (Equation (4-2)), the kinetic energy (Equation (4-6)) the strain energy due to centrifugal force (Equation (4-10)) and the work done by the unsteady aerodynamic forces (Equation (4-15)) into the Hamiltonian given by Equation (4-1).

In the rest of the article, the integral representation of the general governing system of equations is presented for the circumferentially asymmetric stiffness (CAS) layup

configuration to demonstrate the solution methodology for the study of the nonlinear aeroelastic behavior composite wing modelled as TWBs.

For the CAS layup, fiber angles in the top and bottom flanges as well as the side walls of the TWB have opposite sign $\theta(y) = -\theta(-y); \theta(x) = -\theta(-x)$, as shown in Figure a. It should be noted that CAS layup configuration accounts for flapwise bending-torsion and extension-chordwise bending couplings which are utilized in load alleviation in fixed and rotary wing structures. For the TWB with CAS layup, some of the stiffness coefficients in Equation (2-89) vanish and consequently some simplifications occur in the nonlinear system of equations. The non-zero stiffness coefficients in Equation (2-89) include the diagonal terms and off-diagonal coupling stiffness terms $a_{12}, a_{18}, a_{28}, a_{56}, a_{37}$. Among the non-zero stiffness coefficients a_{56} is the flapwise bending-torsion coupling stiffness which is exploited for load alleviation in flexible fixed and rotary wing structures. Moreover, for the TWB with CAS layup non-vanishing mass/inertia terms in Equation (2-60) include $b_1, b_4, b_5, b_{10}, b_{11}, b_{12}$. After expanding $\sin\phi$ and $\cos\phi$ in Taylor series about $\phi = 0$ in the Equations (4-2), (4-6) and (4-10) which define the variations of the strain energy (Equation (4-2)) and the kinetic energy (Equation (4-6)), in the resulting expressions only the terms with square and cubic nonlinearity are retained. The integral equation of motion for the CAS configuration with square and cubic nonlinearities is obtained using Equations (4-1), (4-2), (4-6), (4-10) and (4-15). By inserting energy expressions into Hamilton principle and simplifying the equation, the integral form of governing equation of motion derived as in the form given in Equation (4-16).

$$\int_0^L \begin{Bmatrix} f_1(\Delta)\delta u_0 + f_2(\Delta)\delta u_0' + \\ f_3(\Delta)\delta v_0 + f_4(\Delta)\delta v_0' + \\ f_5(\Delta)\delta w_0 + f_6(\Delta)\delta w_0' + \\ f_7(\Delta)\delta\theta_x + f_8(\Delta)\delta\theta_x' + \\ f_9(\Delta)\delta\theta_y + f_{10}(\Delta)\delta\theta_y' + \\ f_{11}(\Delta)\delta\phi + f_{12}(\Delta)\delta\phi' + f_{13}(\Delta)\delta\phi'' \end{Bmatrix} dz = 0 \qquad (4\text{-}16)$$

where Δ is defined as $\Delta \in \{u_0, v_0, w_0, \theta_x, \theta_y, \phi\}$; moreover, the function $f_i; i = 1...13$ are given by Equations (4-17)-(4-29).

$$f_1(\Delta) = b_1\ddot{u}_0 + 2b_1\dot{u}_0\Omega - b_1u_0\Omega^2 \tag{4-17}$$

$$f_2(\Delta) = a_{22}(\theta_y + u_0') + a_{12}w_0' + b_1\Omega^2R(z)u_0' + N_u^2 + N_u^3 \tag{4-18}$$

$$f_3(\Delta) = b_1\ddot{v}_0 - L_{ae} \tag{4-19}$$

$$f_4(\Delta) = a_{33}(\theta_x + v_0') - a_{37}\phi'' + b_1\Omega^2R(z)v_0' + N_v^2 + N_v^3 \tag{4-20}$$

$$f_5(\Delta) = b_1\ddot{w}_0 - 2b_1\dot{u}_0\Omega - b_1(z + u_0 + R_0)\Omega^2 \tag{4-21}$$

$$f_6(\Delta) = a_{11}w_0' + a_{12}(\theta_y + u_0') + N_w^2 + N_w^3 \tag{4-22}$$

$$f_7(\Delta) = a_{33}(v_0' + \theta_x) - a_{37}\phi'' + (b_4 + b_{12})(\ddot{\theta}_x - \Omega^2\theta_x + 2\Omega\dot{\phi}) + N_x^2\big|_1 + N_x^3\big|_1 \tag{4-23}$$

$$f_8(\Delta) = a_{55}\theta_x' + a_{56}\phi' + N_x^2\big|_2 + N_x^3\big|_2 \tag{4-24}$$

$$f_9(\Delta) = a_{12}w_0' + a_{22}(u_0' + \theta_y) + (b_5 + b_{11})(\ddot{\theta}_y - \Omega^2\theta_y) + N_y^2\big|_1 + N_y^3\big|_1 \tag{4-25}$$

$$f_{10}(\Delta) = a_{44}\theta_y' + N_y^2\big|_2 + N_y^3\big|_2 \tag{4-26}$$

$$f_{11}(\Delta) = (b_4 + b_{12})(\ddot{\phi} - 2\Omega\dot{\theta}_x - \Omega^2\phi) + (b_5 + b_{11})(\ddot{\phi} + \Omega^2\phi) + + N_\phi^2\big|_1 + N_\phi^3\big|_1 - M_{ae} \tag{4-27}$$

$$f_{12}(\Delta) = a_{66}\phi' + a_{56}\theta_x' - b_{10}\ddot{\phi}' + \left(b_4 + b_{12}\right)\Omega^2 R(z)\phi' + \left(b_5 + b_{11}\right)\Omega^2 R(z)\phi' + N_\phi^2\Big|_2 + N_\phi^3\Big|_2 \tag{4-28}$$

$$f_{13}(\Delta) = a_{37}\left(v_0' + \theta_x\right) - a_{77}\phi'' + N_\phi^2\Big|_3 + N_\phi^3\Big|_3 \tag{4-29}$$

where the square nonlinear terms N_Δ^2 are defined as,

$$N_u^2 = a_{22}\left(v_0'\phi\right) - a_{33}\left(v_0'\phi + \theta_x\phi\right) - a_{55}\left(\theta_x'\phi'\right) + \frac{1}{2}a_{28}\left(\phi'\right)^2 - a_{56}\left(\phi'\right)^2 \\ a_{12}\left(\frac{3}{2}\left(u_0'\right)^2 + \frac{1}{2}\left(v_0'\right)^2 + \theta_y u_0'\right) + a_{11}\left(u_0'w_0'\right) + a_{37}\left(\phi''\phi\right) \tag{4-30}$$

$$N_v^2 = a_{12}\left(u_0'v_0' + v_0'\theta_y + w_0'\phi\right) + a_{22}\left(u_0'\phi + \theta_y\phi\right) - \\ a_{33}\left(u_0'\phi\right) + a_{44}\left(\phi'\theta_y'\right) + a_{11}\left(v_0'w_0'\right) \tag{4-31}$$

$$N_w^2 = a_{11}\left(\frac{1}{2}\left(u_0'\right)^2 + \frac{1}{2}\left(v_0'\right)^2\right) + a_{12}\left(v_0'\phi\right) + \frac{1}{2}a_{18}\left(\phi'\right)^2 \tag{4-32}$$

$$N_x^2\Big|_1 = -a_{33}\left(u_0'\phi\right) \tag{4-33}$$

$$N_x^2\Big|_2 = -a_{55}\left(u_0'\phi'\right) \tag{4-34}$$

$$N_y^2\Big|_1 = a_{12}\left(\frac{1}{2}\left(u_0'\right)^2 + \frac{1}{2}\left(v_0'\right)^2\right) + a_{22}\left(v_0'\phi\right) + \frac{1}{2}a_{28}\left(\phi'\right)^2 + \\ 2\left(b_5 + b_{11}\right)\left(\Omega\phi\dot{\phi}\right) \tag{4-35}$$

$$N_y^2\Big|_2 = a_{44}\left(v_0'\phi'\right) \tag{4-36}$$

$$N_\phi^2\Big|_1 = a_{22}\left(u_0'v_0' + v_0'\theta_y\right) - a_{33}\left(u_0'v_0' + u_0'\theta_x\right) + a_{12}\left(v_0'u_0'\right) + a_{37}\left(u_0'\phi''\right) - \\ 2\left(b_5 + b_{11}\right)\left(\Omega\dot{\theta}_y\phi\right) \tag{4-37}$$

$$N_\phi^2\Big|_2 = a_{44}\left(v_0'\theta_y'\right) + a_{28}\left(u_0'\phi' + \theta_y\phi'\right) - 2a_{56}\left(u_0'\phi'\right) - a_{55}\left(u_0'\theta_x'\right) + a_{18}\left(u_0'\phi'\right) \tag{4-38}$$

$$N_\phi^2\Big|_3 = -a_{37}\left(u_0'\phi\right) \tag{4-39}$$

and the cubic nonlinear terms N_{Δ}^{3} are expressed as,

$$N_u^3 = -a_{22}\left(u_0'\phi^2 + \frac{1}{2}\theta_y\phi^2\right) - a_{12}\left(\frac{1}{2}w_0'(\phi)^2 + u_0'v_0'\phi\right) + \frac{a_{11}}{2}\left((u_0')^3 + u_0'(v_0')^2\right) + a_{55}\left(u_0'(\phi')^2\right) + a_{33}\left(u_0'\phi^2\right) - a_{44}\left(\theta_y'\phi'\phi\right) + \frac{1}{2}a_{18}\left(u_0'(\phi')^2\right) \tag{4-40}$$

$$N_v^3 = a_{22}\left(v_0'\phi^2\right) - a_{33}\left(\frac{1}{2}\theta_x\phi^2 + v_0'\phi^2\right) - \frac{a_{12}}{2}\left(\phi(u_0')^2 + 3\phi(v_0')^2\right) + \frac{a_{11}}{2}\left(v_0'(u_0')^2 + (v_0')^3\right) + \frac{a_{18}}{2}\left(v_0'(\phi')^2\right) + a_{44}\left(v_0'(\phi')^2\right) - a_{55}\left(\theta_x'\phi'\phi\right) - a_{56}\left(\phi(\phi')^2\right) \tag{4-41}$$

$$N_w^3 = -\frac{a_{12}}{2}\left(u_0'\phi^2\right) \tag{4-42}$$

$$N_x^3\Big|_1 = -\frac{a_{33}}{2}\left(v_0'(\phi)^2\right) \tag{4-43}$$

$$N_x^3\Big|_2 = -a_{55}\left(v_0'\phi'\phi\right) \tag{4-44}$$

$$N_y^3\Big|_1 = \frac{a_{22}}{2}\left(u_0'\phi^2\right) \tag{4-45}$$

$$N_y^3\Big|_2 = a_{44}\left(u_0'\phi'\phi\right) \tag{4-46}$$

$$N_\phi^3\Big|_1 = -a_{55}\left(v_0'\phi'\phi\right) - a_{56}\left(v_0'(\phi')^2\right) - \frac{a_{12}}{2}\left(v_0'(u_0')^2 + (v_0')^3 + u_0'w_0'\phi\right) - a_{44}\left(u_0'\phi'\theta_y'\right) - a_{22}\left(u_0'\theta_y\phi + \phi(u_0')^2 - \phi(v_0')^2\right) + a_{33}\left(v_0'\theta_x\phi + \phi(v_0')^2 - \phi(u_0')^2\right) \tag{4-47}$$

$$N_\phi^3\Big|_2 = a_{55}\left(\phi'\left(u_0'\right)^2 - v_0'\theta_x'\phi\right) + a_{44}\left(\phi'(v_0')^2 - u_0'\theta_y'\phi\right) - 2a_{56}\left(v_0'\phi'\phi\right) + \frac{a_{18}}{2}\left(\phi'(u_0')^2 + \phi'(v_0')^2\right) + \frac{a_{88}}{2}\left(\phi'\right)^3 \tag{4-48}$$

4.2 Nonlinear Aeroelastic Analysis of the Composite TWB-Wing Using Incompressible Unsteady Aerodynamic

By neglecting rotating speed $(\Omega = 0)$ in Equations (4-16)-(4-48), Nonlinear aeroelastic behavior of tapered and pretwisted *composite fix wings* shown in Figure 4-3 modeled as thin walled beams (TWB) and CAS configuration in the incompressible flow regime is studied in this section.

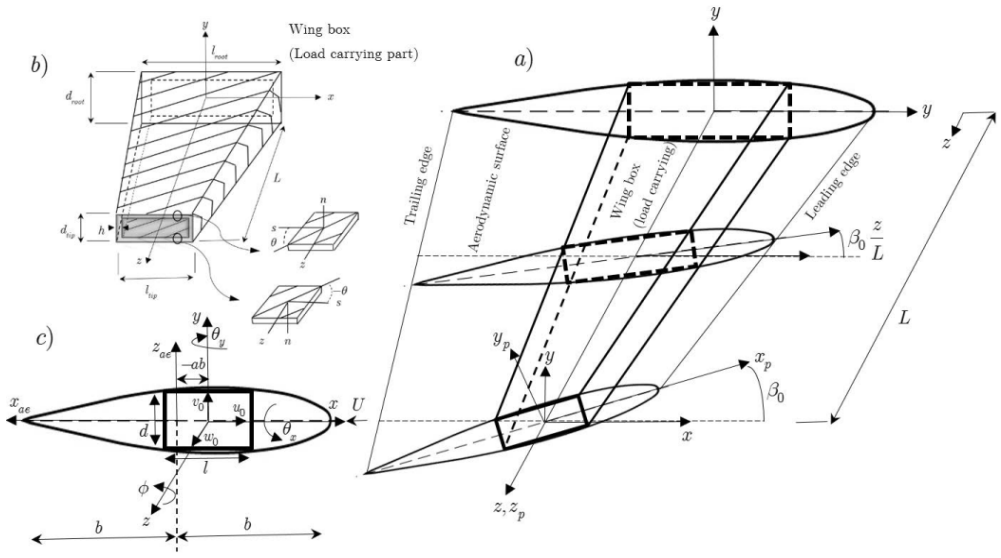

Figure 4-3 Schematic description of an aircraft wing modeled as a doubly tapered TWB with geometric pretwist and the associated CAS layup configuration.

The structural equations of motion are obtained in the most general form based on the kinematic relations governing thin walled beams, including the nonlinear strain displacement relations, and utilizing the principles of analytical dynamics. Unsteady aerodynamic loads in the incompressible flow regime are expressed using Wagner's function in the time-domain. The aerodynamic strip method based on Wagner's function in the unsteady incompressible flow has been used to calculate incompressible unsteady aerodynamic lift and pitching moment. The Wagner function based aerodynamic models provide an efficient, general, and convenient approach to describe the incompressible unsteady flows. The explicit form of incompressible

unsteady aerodynamic lift L_{ae} and pitching moment about the reference axis M_{ae} are obtained in Chapter 3, and they are given by (4-49) and (4-50),

$$L_{ae}\left(z,t\right) = -\pi\rho b^2\left(\ddot{v}_0 - U\dot{\phi} + ba\ddot{\phi}\right) - C_{L\phi}\rho Ub\left[\dot{v}_0 - U\phi + ba\dot{\phi} - \frac{b}{2}\left(\frac{C_{L\phi}}{\pi} - 1\right)\dot{\phi} - \sum_{i=1}^{2}\alpha_i B_i\left(z,t\right)\right] \tag{4-49}$$

$$M_{ae}\left(z,t\right) = -\pi\rho b^3\left[\frac{1}{2}\left(\frac{C_{L\phi}}{\pi} - 1\right)U\dot{\phi} - Ua\dot{\phi} + a\ddot{v}_0 + b\left(\frac{1}{8} + a^2\right)\ddot{\phi}\right] - C_{L\phi}\rho Ub^2\left(\frac{1}{2} + a\right)\left[\dot{v}_0 - U\phi + ba\dot{\phi} - \frac{b}{2}\left(\frac{C_{L\phi}}{\pi} - 1\right)\dot{\phi} - \sum_{i=1}^{2}\alpha_i B_i\left(z,t\right)\right] \tag{4-50}$$

As explained in Chapter 3, in the Equations (4-49) and (4-51), the quantities $B's$ are defined such that, they should satisfy the following expression in Equation (4-51),

$$\dot{B}_i + (\beta_i\frac{U}{b})B_i = \dot{w}_{0.75c}\left(z,t\right); i = 1,2 \tag{4-51}$$

Expressing the unsteady aerodynamic lift and moment by Equations (4-49) and (4-50) and using the quasi-polynomial approximation for the Wagner's function, the final nonlinear system of equations used in the time domain solution is obtained by augmenting the system of equations which come out of the integral expression (Equation(4-1)), by Equation(4-51) which has to be satisfied by the aerodynamic lag states $B_i(z,t); i = 1,2$. In what follows, the integral equation is given for CAS layup configuration, including nonlinear terms of the second and third order in the variational representation of the Hamiltonian definition.

The aeroelastic system of equations is augmented by the differential equations governing the aerodynamics lag states to come up with the final coupled fluid-structure equations of motion. The governing system of equations of the aeroelastic system is solved, for the TWB with circumferentially asymmetric stiffness (CAS) composite layup, by means of a Ritz based solution methodology utilizing the mode shapes of the linear structural system to approximate the spatial variation of the degrees of freedom of the thin walled beam. Time response of the nonlinear aeroelastic system is obtained

via the fourth order Runge-Kutta direct integration algorithm. Effects of taper ratio, pretwist angle and the fiber angle of the CAS layup configuration on the nonlinear aeroelastic stability margins and LCO behavior are studied in depth.

4.2.1 Method of Solution

Many algorithms exist that deal with the solution of nonlinear problems [123]. One common characteristic of most solution algorithms is that the mode shapes of the geometrically linear unloaded TWB are obtained and then used for the nonlinear aeroelastic analysis of the composite wing with the CAS layup configuration analysis. In the present study, the same solution procedure is adopted. In this respect, first a solution of the structural equations of motion is obtained for the mode shapes of the TWB utilizing the geometrically linear system of equations by following a Ritz based solution methodology. Then, the mode shapes of the TWB are employed in the nonlinear aeroelastic analysis of the composite wing.

4.2.1.1 Solution for the Mode Shapes of the TWB

In the present study, a Ritz based solution method is used for the solution of the eigenfunctions of the composite TWB with CAS layup. For the clamped-free wing structure, trial functions which satisfy the essential boundary conditions are picked and spatial semi-discretization is done as given in Equation (4-52) and [124],

$$\begin{aligned} u_0(z,t) &= \sum_{i=1}^{N} \psi_i^u(z)\eta_i^u(t), \qquad v_0(z,t) = \sum_{i=1}^{N} \psi_i^v(z)\eta_i^v(t) \\ w_0(z,t) &= \sum_{i=1}^{N} \psi_i^w(z)\eta_i^w(t), \qquad \theta_x(z,t) = \sum_{i=1}^{N} \psi_i^x(z)\eta_i^x(t) \\ \theta_y(z,t) &= \sum_{i=1}^{N} \psi_i^y(z)\eta_i^y(t), \qquad \phi(z,t) = \sum_{i=1}^{N} \psi_i^\phi(z)\eta_i^\phi(t) \end{aligned} \tag{4-52}$$

where N is the number of terms in the series which is chosen suitably to achieve convergence, and the spatial functions for all degrees of freedom satisfy the clamped boundary condition at the wing root $(z = 0)$. Spatial functions for all degrees of freedom are taken as identical as shown in Equation (4-53).

$$\psi_i^u(z) = \psi_i^v(z) = \psi_i^w(z) = \psi_i^x(z) = \psi_i^y(z) = \psi_i^\phi(z) = z^i; i = 1..N \tag{4-53}$$

To solve for the mode shapes of the TWB utilizing the geometrically linear system of equations, aerodynamic and nonlinear terms in Equation (4-16) are omitted, and the semi-discretized expansions of the degrees of freedom of the TWB, given by Equation (4-52), are substituted into the modified integral form of the governing equations of motion along with the test functions, which are the variations of the degrees of freedom $(\delta u_0, \delta v_0, \delta w_0, \delta\theta_x, \delta\theta_y, \delta\theta_y)$. Here, the test functions are again taken as the spatial functions given by Equation (4-53) such that they vanish at the root of the wing at $z = 0$, and their spatial derivatives are taken accordingly and substituted into Equation (4-16). Integrating Equation (4-16) over the axial coordinate, one obtains the following system of equations,

$$\left[\boldsymbol{M}_s\right]\left\{\ddot{\eta}\right\} + \left[\boldsymbol{K}_s\right]\left\{\eta\right\} = 0 \tag{4-54}$$

where $\boldsymbol{K}_s, \boldsymbol{M}_s$ are the structural stiffness and mass matrices, described in Appendix D, and the vector of state variables is defined as,

$$\eta_{6N\times 1} = \left\{\eta^{u^T} \quad \eta^{v^T} \quad \eta^{w^T} \quad \eta^{x^T} \quad \eta^{y^T} \quad \eta^{\phi^T}\right\}^T \tag{4-55}$$

Where, $\eta^{uT} = \left\{\eta_1^u(t) \quad \eta_1^u(t) \quad \ldots \quad \eta_1^u(t)\right\}$, etc.

The system of equations given by Equation (4-54) can be transformed into the state space form defining a vector of the state variables themselves and their time derivatives as shown in Equation (4-56).

$$G_{12N\times 1} = \left\{\eta^T \quad \dot{\eta}^T\right\}^T \tag{4-56}$$

Utilizing Equation (4-56), the state space form of the system of equations of motion for the TWB is obtained as shown in Equation (4-57).

$$\dot{G} = VG, \qquad V = \begin{bmatrix} 0 & I \\ -M_s^{-1}K_s & 0 \end{bmatrix} \tag{4-57}$$

Equation (4-57) can be recast to the standard form of an eigenvalue problem by introducing $G = \bar{G}e^{\lambda t}$, yielding,

$$\left(V - I\lambda\right)\bar{G} = 0 \tag{4-58}$$

where the eigenvalues (λ) and the corresponding eigenvectors $\bar{G}$ may be readily obtained.

4.2.1.2 Nonlinear Aeroelastic Analysis of the Composite Wing

Nonlinear aeroelastic analysis is conducted by means of a Ritz based solution methodology utilizing the mode shapes of the linear structural system to approximate the spatial variation of the degrees of freedom of the thin walled beam. Equation (4-59) gives the reduced modal matrix $\boldsymbol{R}$, which is extracted from the solution of Equation (4-58), for the dominant m right eigenvectors corresponding to the translational and rotational degrees of freedom of the linear system.

$$R_{6N\times m} = \begin{bmatrix} R_{m\times N}^{u^T} & R_{m\times N}^{v^T} & R_{m\times N}^{w^T} & R_{m\times N}^{x^T} & R_{m\times N}^{y^T} & R_{m\times N}^{\phi^T} \end{bmatrix} \tag{4-59}$$

One can then construct a reduced order model by expressing any of the six degrees freedom $\Delta \in \{u_0, v_0, w_0, \theta_x, \theta_y, \phi\}$ in terms of the relevant trial function ψ^{Δ}, relevant reduced modal matrix $\boldsymbol{R}^{\Delta}$ which is composed of dominant m right eigenvectors and the modal coordinates as,

$$\Delta(z,t) = \psi^{\Delta^T} R^{\Delta} \vartheta(t) \tag{4-60}$$

Where $\vartheta(t)$ is the generalized modal coordinate vector of dimension of $m \times 1$, $\boldsymbol{R}^{\Delta}$ is the reduced modal matrix of dimension $N \times m$ composed of dominant m right eigenvectors corresponding to any of the degrees of freedom Δ, and ψ^{Δ} is the vector

of trial functions, of dimension $N \times 1$, corresponding to any of the degrees of freedom Δ.

For the nonlinear system, the test functions for any of the degrees of freedom, which are the variations of the degrees of freedom, are defined by the premultiplication of the the vector of the trial functions ψ^{Δ} by the reduced modal matrix $\boldsymbol{L}^{\Delta T}$ which is composed of dominant m left eigenvectors corresponding to the translational and rotational degrees of freedom.

$$\delta\Delta(z) = L^{\Delta^T}\psi^{\Delta} \tag{4-61}$$

Modal expansions of the degrees of freedom of the TWB (Equation (4-60)) and the variations of the degrees of freedom (Equation (4-61)) are substituted into the integral form of the governing equations of motion Equation (4-16) resulting in the reduced order system of nonlinear equations,

$$M_t\ddot{\vartheta}(t) + C_t\dot{\vartheta}(t) + K_t\vartheta(t) - Z(t) + \bar{H}^{NL}(t) = 0 \tag{4-62}$$

Where $\boldsymbol{M}_t, \boldsymbol{C}_t, \boldsymbol{K}_t$ are the reduced order mass, aerodynamic damping and stiffness matrices of dimension $m \times m$, and Z and $\bar{H}_{NL}$ are the reduced order vectors of dimension $m \times 1$ and they include the aerodynamic lag states and the nonlinear terms, respectively.

In the resulting reduced order system of equations, if the modal matrices composed of the left $(\boldsymbol{L}^T)$ and the right eigenvectors $(\boldsymbol{R})$ are factored out, reduced order mass, damping and stiffness matrices in Equation (4-62) are defined by,

$$\begin{aligned} \boldsymbol{M}_t &= L^T(\boldsymbol{M}_s + \boldsymbol{M}_{ae})R \\ \boldsymbol{C}_t &= L^T\boldsymbol{C}_{ae}R \\ \boldsymbol{K}_t &= L^T(\boldsymbol{K}_s + \boldsymbol{K}_{ae})R \end{aligned} \tag{4-63}$$

where the structural mass $(\boldsymbol{M}_s)$ and stiffness $(\boldsymbol{K}_s)$, and the aerodynamic mass $(\boldsymbol{M}_{ae})$, stiffness $(\boldsymbol{K}_{ae})$ and damping $(\boldsymbol{C}_{ae})$ matrices of dimension $6N \times 6N$ are defined in Appendix D.

It should be noted that the aerodynamic damping matrix $\boldsymbol{C}_{ae}$ in Equation (4-63) does not include the aerodynamic lag terms defined in Equations (4-49) and (4-50), and these terms are collected in the aerodynamic lag vector Z. Aerodynamic lag vector Z is derived from the virtual work done by the aerodynamic lag states (B_i) in the unsteady lift and moment expressions in Equations (4-49) and (4-50) .

In the integral equation of motion Equation (4-16), virtual work done by the unsteady lift and moment due to aerodynamic lag states is given by,

$$\int_0^L \left\{ (L_{ae})_{Lag} \delta v_0 + (M_{ae})_{Lag} \delta\phi \right\} dz \tag{4-64}$$

where the unsteady lift and moment due to aerodynamic lag states are given by Equations (4-65) and (4-66) .

$$(L_{ae})_{Lag}(z,t) = C_{L\phi} \rho U b \left(\alpha_1 B_1(z,t) + \alpha_2 B_2(z,t) \right) \tag{4-65}$$

$$(M_{ae})_{Lag}(z,t) = C_{L\phi} \rho U b \left\{ b \left(\frac{1}{2} + a \right) \left(\alpha_1 B_1(z,t) + \alpha_2 B_2(z,t) \right) \right\} \tag{4-66}$$

Following the substitution of the unsteady lift and moment due to aerodynamic lag states in Equation (4-64), and expressing the variations δv_0 and $\delta\phi$ by Equation (4-61), after manipulations aerodynamic lag vector Z is defined as,

$$Z(t) = \begin{bmatrix} \alpha_1 I & \alpha_2 I \end{bmatrix} \begin{Bmatrix} \hat{B}_1(t) \\ \hat{B}_2(t) \end{Bmatrix} \tag{4-67}$$

Where $\boldsymbol{I}$ is the identity matrix of order $m \times m$ and $\hat{B}_1$ and $\hat{B}_2$ are vectors of order $m \times 1$ defined by,

$$\hat{B}_i(t) = \left\{ \int_0^L C_{L\phi} \rho U b \left(L^{v^T} \psi^v + b\left(\frac{1}{2} + a\right) L^{\phi^T} \psi^\phi \right) B_i(z,t) dz \right\} i = 1,2 \qquad (4\text{-}68)$$

where the term inside the curly bracket is a vector of dimension $m \times 1$ and so are the transformed aerodynamic lag state vectors $\hat{B}_i(t)$.

In Equation (4-62), vector of nonlinear terms $\bar{H}_{NL}$ originates from the integral equation of motion of the CAS configuration composite wing given by Equation (4-16). After the substitution of Equation (4-17)-(4-29) into Equation (4-16), the nonlinear terms can be grouped as shown in Equation (4-69).

$$H^{NL}(t) = \int_0^L \begin{bmatrix} \left(N_u^2 + N_u^3\right)\delta u_0' + \left(N_v^2 + N_v^3\right)\delta v_0' + \left(N_w^2 + N_w^3\right)\delta w_0' + \\ \left(N_x^2\big|_1 + N_x^3\big|_1\right)\delta\theta_x + \left(N_x^2\big|_2 + N_x^3\big|_2\right)\delta\theta_x' + \left(N_y^2\big|_1 + N_y^3\big|_1\right)\delta\theta_y + \\ \left(N_y^2\big|_2 + N_y^3\big|_2\right)\delta\theta_y' + \left(N_\phi^2\big|_1 + N_\phi^3\big|_1\right)\delta\phi + \left(N_\phi^2\big|_2 + N_\phi^3\big|_2\right)\delta\phi' + \\ \left(N_\phi^2\big|_3 + N_\phi^3\big|_3\right)\delta\phi'' \end{bmatrix} dz \qquad (4\text{-}69)$$

To obtain the reduced order vector of nonlinear terms $\bar{H}^{NL}$ in Equation (4-62), nonlinear terms N_Δ^2, N_Δ^3 defined by Equations (4-30)-(4-39) and Equations (4-40)-(4-48), modal expansions of the degrees of freedom given by Equation (4-60), and the variations of the degrees of freedom given by Equation (4-61) are substituted into Equation (4-70), resulting in,

$$\bar{H}^{NL}(t) = \int_0^L \begin{bmatrix} L^{u^T}\psi'^u\left(\bar{N}_u^2 + \bar{N}_u^3\right) + L^{v^T}\psi'^v\left(\bar{N}_v^2 + \bar{N}_v^3\right) + \\ L^{w^T}\psi'^w\left(\bar{N}_w^2 + \bar{N}_w^3\right) + L^{x^T}\psi^x\left(\bar{N}_x^2\big|_1 + \bar{N}_x^3\big|_1\right) + \\ L^{x^T}\psi'^x\left(\bar{N}_x^2\big|_2 + \bar{N}_x^3\big|_2\right) + L^{y^T}\psi^y\left(\bar{N}_y^2\big|_1 + \bar{N}_y^3\big|_1\right) + \\ L^{y^T}\psi'^y\left(\bar{N}_y^2\big|_2 + \bar{N}_y^3\big|_2\right) + L^{\phi^T}\psi^\phi\left(\bar{N}_\phi^2\big|_1 + \bar{N}_\phi^3\big|_1\right) + \\ L^{\phi^T}\psi'^\phi\left(\bar{N}_\phi^2\big|_2 + \bar{N}_\phi^3\big|_2\right) + L^{\phi^T}\psi''^\phi\left(\bar{N}_\phi^2\big|_3 + \bar{N}_\phi^3\big|_3\right) \end{bmatrix} dz \qquad (4\text{-}70)$$

where the algebraic expressions for the nonlinear coefficients $\bar{N}^2_\Delta, \bar{N}^3_\Delta$, which are expressed in terms of the trial functions and derivatives of the trial functions $(\psi^{\Delta T})$, reduced modal matrices $(\boldsymbol{R}^\Delta)$ and the modal coordinates $\vartheta_i(t)$ are given in Appendix E.

With the introduction of the aerodynamic lag states, there are $2m$ number of additional unknowns in Equation (4-62), and to perform the nonlinear aeroelastic analysis of the composite wing, additional $2m$ number of additional equations are needed. To this end, the system of nonlinear equations Equation (4-62) is augmented by the differential equations that the aerodynamic lag states $B_i(z,t), i = 1,2$ must satisfy (Equation (4-51)). Since in the system of nonlinear equations, given by Equation (4-62), aerodynamic lag states are defined by the transformed aerodynamic lag state vectors $\hat{B}_i(z,t), i = 1,2$, Equation (4-51) is manipulated such that it is also expressed in terms of the the transformed vectors $\hat{B}_i(z,t), i = 1,2$. For this purpose, both sides of Equation (4-51) are multiplied by the expression given in Equation (4-71),

$$C_{L\phi}\rho U b\left(\delta v_0 + b\left(\frac{1}{2}+a\right)\delta\phi\right) \tag{4-71}$$

the variations δv_0 and $\delta\phi$ are expressed by Equation (4-61), modal expansions of the degrees of freedom (Equation (4-60)) which appear in the right hand side of Equation (4-51) are substituted, and both sides of Equation (4-51) are integrated along the span of the wing as shown in Equation (4-72).

$$\int_0^L C_{L\phi}\rho U b\left(L^{v^T}\psi^v + b\left(\frac{1}{2}+a\right)L^{\phi^T}\psi^\phi\right)\left(\dot{B}_i(z,t) + \beta_i\frac{U}{b}B_i(z,t)\right)dz = RHS \qquad i = 1,2 \tag{4-72}$$

After manipulations the right hand side RHS in Equation (4-72) can be simplified as,

$$RHS = D_1\dot{\vartheta}(t) + D_2\ddot{\vartheta}(t) \tag{4-73}$$

Where $\boldsymbol{D}_1$ and $\boldsymbol{D}_2$ are the $m \times m$ coefficient matrices defined by,

$$\left[D_1\right]_{m\times m}=\int_0^L C_{L\phi}\rho U^2 b\left[L^{vT}\psi^v\psi^{\phi T}R^\phi+b\left(a+\frac{1}{2}\right)L^{\phi T}\psi^\phi\psi^{\phi T}R^\phi\right]dz \tag{4-74}$$

$$\left[D_2\right]_{m\times m}=\int_0^L C_{L\phi}\rho U b\begin{bmatrix}L^{vT}\psi^v\psi^{vT}R^v+b\left(\frac{1}{2}+a\right)L^{\phi T}\psi^\phi\psi^{vT}R^v+\\ b^2\left(a^2-\frac{1}{4}\right)L^{\phi T}\psi^\phi\psi^{\phi T}R^\phi+b\left(a-\frac{1}{2}\right)L^{vT}\psi^v\psi^{\phi T}R^\phi\end{bmatrix}dz \tag{4-75}$$

Comparing Equation (4-68) and Equation (4-72), it is evident that since the terms multipying the time derivative of the aerodynamic lag state $B_i(z,t)$ in Equation (4-68) do not depend on time, Equation (4-72) can be written as,

$$\dot{\hat{B}}_i(t)+\beta_i\frac{U}{b}\hat{B}_i(t)=D_1\dot{\vartheta}(t)+D_2\ddot{\vartheta}(t)\qquad i=1,2 \tag{4-76}$$

Where $\hat{B}_i(t)$ is the transformed aerodynamic lag state vector of dimension $m\times 1$ defined by Equation (4-68). It should be noted that in passing from Equation (4-72) to Equation (4-76), it is assumed that the semi-chord length b in the U/b term is constant along the span of the wing, which is so for rectangular wings. For tapered wings, it suffices to use the mean semi-chord length only in the U/b term in Equation (4-76).

By augmenting Equation (4-62) with Equation (4-76) , the final form of the nonlinear aeroelastic system of equations of the CAS configuration composite wing modeled as TWB can be obtained in state space representation as shown in Equation (4-77).

$$\begin{bmatrix}C_t & M_t & 0 & 0\\ I & 0 & 0 & 0\\ D_1 & D_2 & -I & 0\\ D_1 & D_2 & 0 & -I\end{bmatrix}\frac{d}{dt}\begin{Bmatrix}\vartheta\\ \dot{\vartheta}\\ \hat{B}_1\\ \hat{B}_2\end{Bmatrix}+\begin{bmatrix}K_t & 0 & \alpha_1 I & \alpha_2 I\\ 0 & -I & 0 & 0\\ 0 & 0 & \left(-\beta_1 U/b\right)I & 0\\ 0 & 0 & 0 & \left(-\beta_2 U/b\right)I\end{bmatrix}\begin{Bmatrix}\vartheta\\ \dot{\vartheta}\\ \hat{B}_1\\ \hat{B}_2\end{Bmatrix}-\begin{Bmatrix}\bar{H}_{NL}\\ 0\\ 0\\ 0\end{Bmatrix}=0 \tag{4-77}$$

Equation (4-77) is in the form,

$$A\dot{q} + Bq + F^{NL} = 0 \tag{4-78}$$

Where q is the state vector of dimension $4m \times 1, F^{NL}$ is the vector of nonlinear terms of dimension $4m \times 1$, and $\boldsymbol{A}$ and $\boldsymbol{B}$ are $4m \times 4m$ coefficient matrices defined in Equation (4-77). Nonlinear aeroelastic respose of the composite wing modeled as TWB is performed in time domain by the direct integration of Equation (4-78) by the Runge-Kutta method for the prescribed initial conditions.

4.2.2 Numerical Results and Discussions

In this section, unsteady incompressible aerodynamics and the linear structural TWB models are first verified by comparing the results with the available test and analysis results in the literature. Then, numerical results are presented for the aeroelastic stability response of the CAS configuration composite wing utilizing both the linear and nonlinear structural models of the TWB.

In this section, unsteady aerodynamics and the linear structural TWB models are first verified by comparing the results with the available test and analysis results in the literature. Then, numerical results are presented for the aeroelastic stability response of the CAS configuration composite wing utilizing both the linear and nonlinear structural models of the TWB.

4.2.2.1 Verification Studies

Unsteady aerodynamics model based on the approximation of the Wagner's function with two aerodynamic lag states is verified by the well-known experimental study of Barmby et al. [125]. The experimental flutter speed and flutter frequency results obtained for the unswept aluminum alloy wing of NACA 16-1010 profile in the subsonic flow regime are compared with the classical flutter predictions involving only the flapwise bending displacement and the torsional rotation degrees of freedom of the present study. In the model of the present study used for the verification, structural model is based on geometrically linear equations, but exactly the same Ritz-based

methodology described for the nonlinear aeroelastic analysis of the composite wing is used. In this respect, seven trial functions $(N = 7)$ are used in the series given in Equation (4-52) for the flapwise deformation v_0 and torsional ϕ degrees of freedom and first seven $(m = 7)$ eigenfunctions are used for the modal reduction. Flutter speed and frequency comparisons are made for the unswept wing models 40A and 40B [125] which have the stiffness and mass/inertia properties given in Table 4-1. In order to adapt the present TWB structural model to the wing models of Barmby et al. [125], degrees of freedom are restricted to the flapwise bending deflection v_0 and the elastic twist ϕ and the assignments given by Equation (4-79) are made for the stiffness and mass properties. It should be noted that the *a* parameter in Table 4-1 specifies the nondimensional offset between the shear center and the mid-chord, as shown in Figure 4-3. A negative value of the *a* parameter indicates that the shear center is forward of the mid chord.

$$\begin{aligned} a_{66} &= GJ \\ a_{55} &= EI \\ b_4 + b_5 &= I_\alpha \\ b_1 &= m \end{aligned} \tag{4-79}$$

Table 4-1 Stiffness and mass/inertia properties of the wing models used in the verification study

Model	ρ	EI (Nm^2)	GJ (Nm^2)	L (m)	b (m)	a	$\frac{m}{\pi\rho b^2}$	$r_\alpha^2 = \frac{I_\alpha}{mb^2}$
40A	1.144	15	10.15	0.6299	0.1016	-0.2	36.5	0.277
40B	1.174	14.4	10.64	0.6299	0.1016	-0.2	35.5	0.297

Table 4-2 compares the experimentally determined flutter Mach numbers and the flutter frequencies of the wing models 40A and 40B with the linear aeroelastic analysis solutions of the present study.

Table 4-2 Comparison of the present linear aeroelastic analysis results with the experimental results of Barmby et al. [125]

Model	Air density (Kg/m^3)	Instability Mach No.		Frequency at the instability	
		Experiment [125]	Present	Experiment [125]	Present
40A	1.144	0.24	0.25	62	64
40B	1.174	0.23	0.24	61	59

Results given in Table 4-2 shows that present linear aeroelastic analysis results are in good agreement with the experimental results of Barmby et al. [125]. It is also noted that the effect of slight differences in the stiffness and mass terms between the wing models 40A and 40B on the flutter speed and the flutter frequency can be captured adequately with present solution methodology. As a second verification, flutter speed and frequency of a CAS configuration composite box beam studied by Haddadpour et al. [71] are calculated and compared with the results of Haddadpour [71] and MSC Nastran subsonic aeroelastic analysis results which are also reported in the study of Haddadpour et al. [71]. Table 4-3 gives the geometric and material properties of the box beam composed of graphite/epoxy.

Table 4-4 compares the flutter speeds and frequencies of the CAS configuration TWB with a fiber angle of −20 degree. It is seen that results of the present study are in good agreement with the results of Haddadpour et al. [71] and Msc Nastran results which are obtained by the finite element method involving Doublet-Lattice oscillatory aerodynamics.

Table 4-3 Geometric and material properties of the graphite/epoxy composite wing.

Material properties		**Geometric[1] properties**	
$E_1\ (GPa)$	206.8e9	$L\ (m)$	14
$E_2\ (GPa)$	5.17e9	$l\ (m)$	0.757
$E_3\ (GPa)$	5.17e9	$d\ (m)$	0.1
$G_{12}\ (GPa)$	3.1e9	$h\ (m)$	0.03
$G_{13}\ (GPa)$	3.1e9	$\beta\ (deg.)$	0, 5
$G_{23}\ (GPa)$	2.55e9	$\theta\ (deg.)$	-75,-60,-45
$\vartheta_{12} = \vartheta_{23}$	0.25	$\rho\ (kg/m^3)$	1528
ϑ_{13}	0.25	$R_0\ (m)$	0

Table 4-4 Comparison of the flutter speeds and frequencies

a	Flutter speed (m/s)			Flutter Frequency (Hz)		
	Haddadpour [71]	Msc NASTRAN	Present	Haddadpour [71]	Msc NASTRAN	Present
0	101	100	100	3.35	3.59	3.39
-0.2	127	124	128	3.53	3.62	3.57

As a final verification study, geometrically nonlinear TWB model is verified against the finite element solution. For this purpose, nonlinear transient analysis of a thin walled beam with the geometrical and mechanical properties given in Table 4-5 is performed by the present solution method and MSC Nastran using CBEAM beam elements which allow warping. Nonlinear transient analyses of the TWB and the beam models are performed for an initial flapwise tip displacement of $v_0(0) = -0.3m$. From the resulting time response plots shown in Figure 4-4, the first two dominant frequencies are determined via Fast-Fourier-Transform (FFT) and comparisons are made with the linear modal analysis results in Table 4-6. From Table 4-6, it is seen that the lowest two frequencies extracted from the nonlinear transient analysis results obtained by the present method and by MSC Nastran agree very well. Table 4-6 also gives the linear modal analysis results obtained by the present model and by MSC Nastran. It is seen that although the first lowest frequencies of the linear and the nonlinear models are very close to each other, the second lowest frequencies are

separate, and the present nonlinear TWB model captures this separation quite accurately.

Table 4-5 Geometric and material properties of the TWB in nonlinear validation

Parameter	Value
$L\ (m)$	5
$l\ (m)$	0.5
$d\ (m)$	0.2
$h\ (m)$	0.01
$E\ (GPa)$	70
ϑ	0.3
$\rho\ (kg/m^3)$	2700

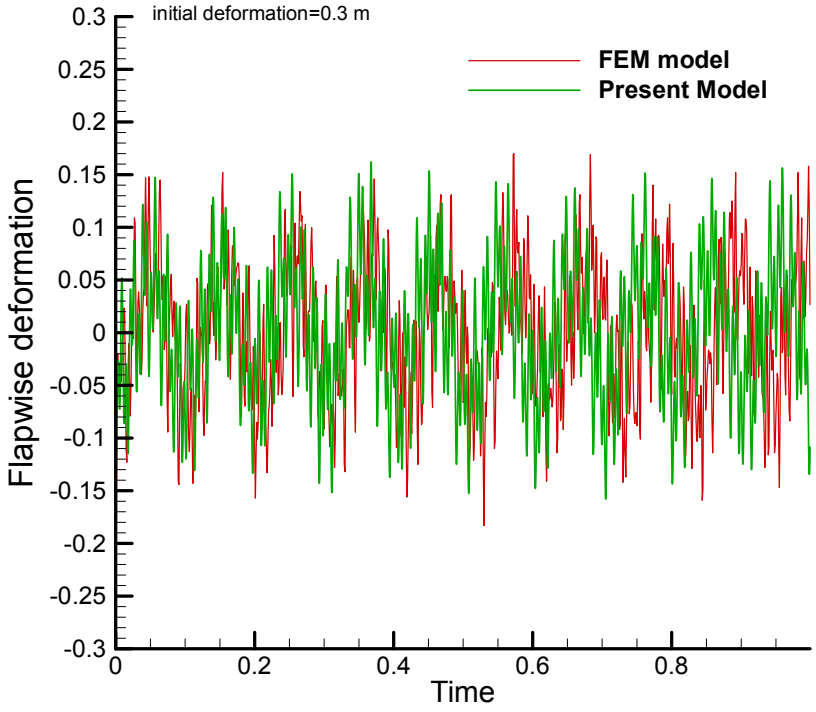

Figure 4-4 Comparison of the flapwise time response of nonlinear TWBs of MSC Nastran and current time history

Table 4-6 Comparison of the first two frequencies of nonlinear TWBs via FFT analysis of MSC Nastran and current time history results

Frequency	Linear frequency (Hz) (Eigenvalue Analysis)		Nonlinear frequency (Hz) (Transient Analysis)	
	MSC NASTRAN	Present	MSC NASTRAN	Present
1st	9.63	9.7	10.056	10.07
2nd	19.82	20.01	55.9	56.8

4.2.2.2 Linear Aeroelastic Analysis of Composite Wings

Before the nonlinear aeroelastic analysis of composite wings, linear aeroelastic analyses have been performed to predict the flutter and divergence instability conditions in order to better evaluate the results of nonlinear aeroelastic analysis. As discussed before, Ritz-based methodology described for the nonlinear aeroelastic analysis is also followed in the linear aeroelastic analysis of the CAS configuration composite wings, and seven trial functions $(N = 7)$ are used in the series for the six degrees of freedom of the TWB and first seven $(m = 7)$ eigenfunctions are used for the modal reduction. Setting $F^{NL} = 0$ in Equation (4-78) and considering $q = q_0 e^{\lambda t}$ one obtains the standard form of a generalized eigenvalue problem where the eigenvalues and eigenvectors correspond to the natural frequencies and mode shapes, respectively. It should be noted that with seven trial functions and seven eigenfunctions of the linear structural system, convergence has been achieved in every case and the frequency domain linear aeroelastic analyses are performed. For the composite TWB structure, geometric and material properties given in Table 4-3 are used and the nondimensional offset between the shear center and the mid chord is taken as $a = 0.3$, implying that the shear center is aft of the mid chord. Moreover, the spanwise and chordwise taper ratios are assumed to be identical and equal to 1 hereafter for simplification purposes $(\sigma_l = \sigma_d = 1)$. Figure 4-5 a and b give the variation of the aeroelastic instability speed and associated frequency of the rectangular composite wing with the fiber angle of the CAS configuration. Results are presented for an untwisted wing and for a wing with

linearly varying twist along the wing span with a tip twist of 5 degrees. It is noted that for positive fiber angles, flutter frequency is zero and the instability mode is divergence. In the CAS configuration TWB, for the positive fiber angles, fibers are oriented towards the leading edge, as seen in Figure 4-3. Hence, twist due to bending causes angle of attack to increase further resulting in an increase of the lift and moment and eventually causes divergence instability before the flutter occurrence. Negative fiber angles have just the opposite effect and since the fibers are oriented towards the leading edge, bending-twisting coupling works toward decreasing the angle of attack and divergence instability is deferred to higher speeds and flutter instability occurs earlier. As depicted, the maximum flutter speed corresponds to a fiber angle of $-45°$ while the minimum flutter speed occurs at a positive fiber angle of $45°$. This is in agreement with the physical interpretation provided in the previous paragraph which states that negative lamination angles act toward stabilizing the wing. For a better comprehension of the differences between stability margins of the two twist angles $\beta_0 = 0,5$, numerical results are tabulated in Table 4-7.

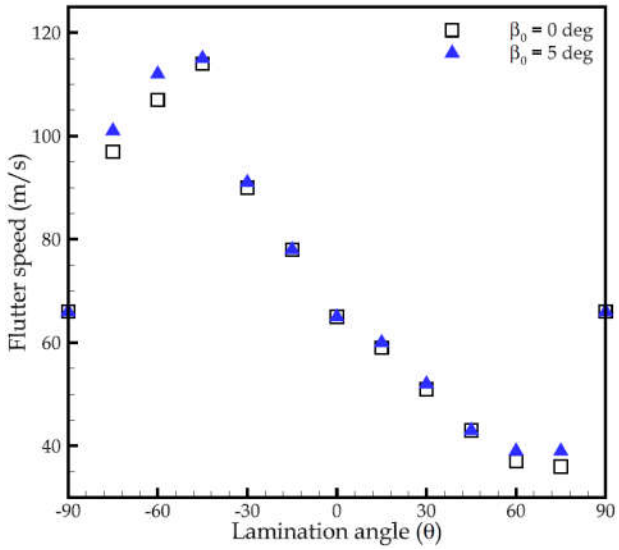

Figure 4-5a Variations of the flutter speed versus the fiber angle

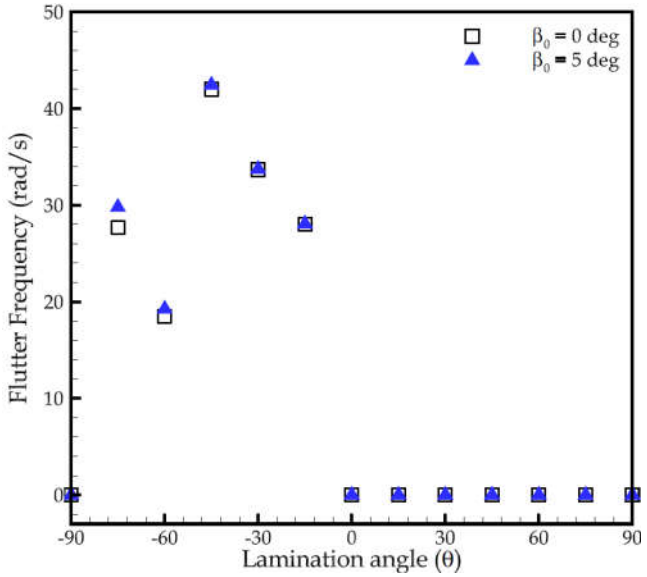

Figure 4-5b Variations of the flutter frequency versus the fiber angle

Table 4-7 Summary of flutter speed and frequency for different fiber and twist angles.

θ	Flutter speed (m/s)		Flutter Frequency (rad/sec)	
	$\beta_0 = 0$	$\beta_0 = 5$	$\beta_0 = 0$	$\beta_0 = 5$
-90	66	66	0	0
-75	97	101	27.7	29.8
-60	107	112	18.5	19.26
-45	114	115	42	42.4
-30	90	91	33.7	33.7
-15	78	78	28	28.1

Figure 4-6 and Figure 4-7 present the flutter speed and frequency results for doubly tapered wing $(\sigma = 0.8, 0.6)$. for the positive fiber angles, fibers are oriented towards the leading edge. Hence, twist due to bending causes angle of attack to increase further and eventually causes divergence instability before the flutter occurrence. the tapered wing has lower aerodynamic loading than the rectangular wing. It is deemed that the

combined effect of lower aerodynamic loading, lower mass and lower stiffness of the tapered wing compared to the rectangular wing is such that the tapered wing is prone to aeroelastic instability at higher air speed than the rectangular wing flutter speed is increased for all ply angles, while the corresponding frequencies experience a small increase at negative ply angles and remain intact at positive angles as shown in Figure 4-6 and Figure 4-7.

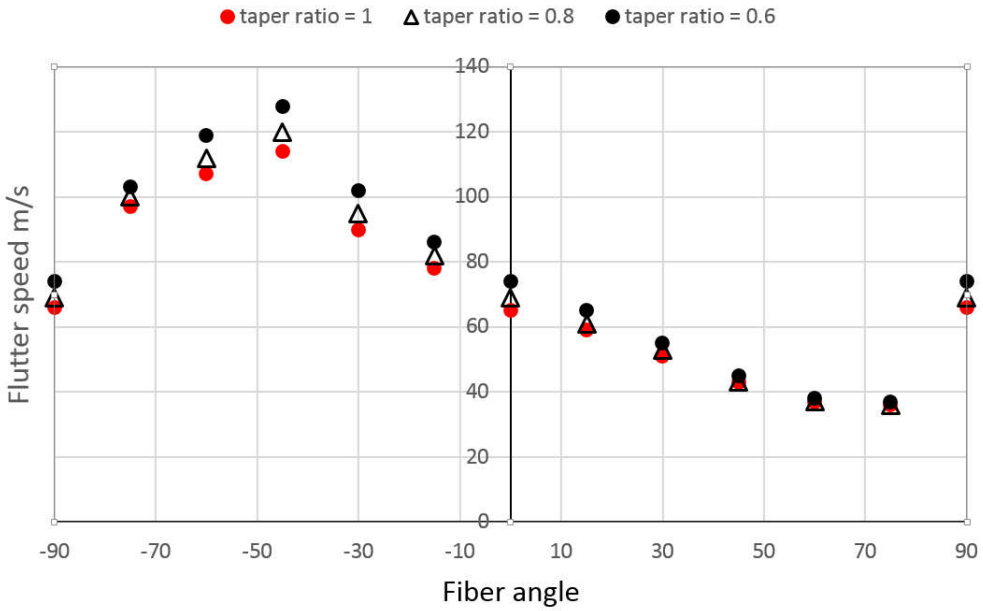

Figure 4-6 Variations of the flutter speed versus the fiber angle for taper ratios $\sigma_l = \sigma_d = \sigma = 1, 0.8, 0.6$

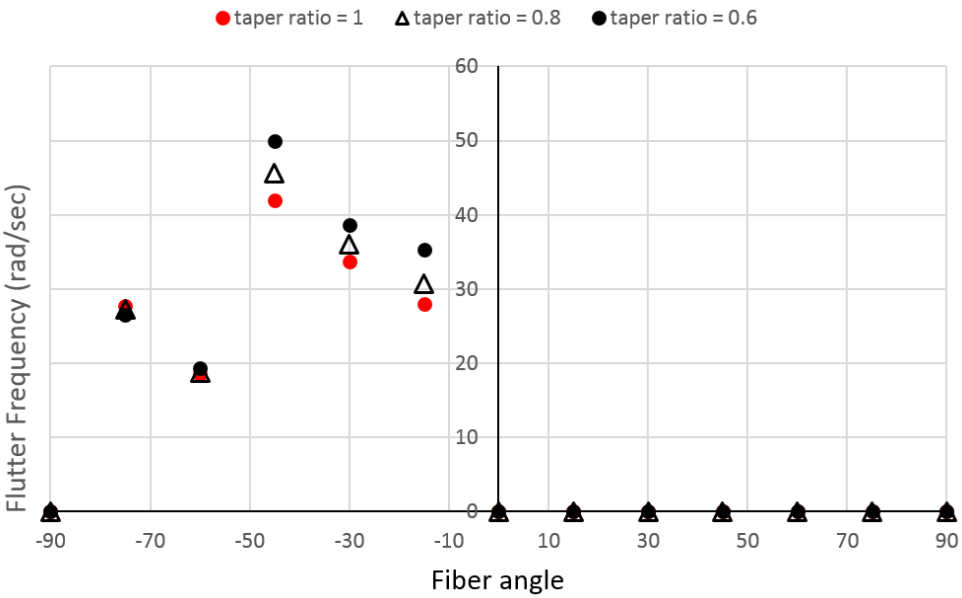

Figure 4-7 Variations of the flutter frequency versus the fiber angle for taper ratios $\sigma_l = \sigma_d = \sigma = 1, 0.8, 0.6$

4.2.2.3 Nonlinear Aeroelastic Analysis of Composite Wings

For the CAS configuration composite wings which are structurally modeled as TWBs, nonlinear aeroelastic analyses have been performed in time domain through the fourth order Runge-Kutta direct integration of the state representation of the governing nonlinear aeroelastic system of equations given by Equation (4-78). In the numerical simulations performed, it is assumed that the composite wing is initially at rest and the wing is given an initial disturbance by assigning an initial value of 1.0e-06 to all modal coordinates. With the very low initial conditions given to the modal coordinates, it is aimed to start self-excited oscillations, and depending on the intrinsic character of the aeroelastic system, the response of the system may attenuate or increase. In the following, time history plots and the associated phase plots, Poincare and Power Spectrum Density (PSD) diagrams are given for the response of the wing tip $(z = L)$.

Parameter a which defines the offset between the center of twist and the mid chord is taken as 0.3 in the time domain nonlinear aeroelastic simulations performed. Material and geometric properties for the following analysis are given in Table 4-3.

Initially, the nonlinear aeroelastic system of equations is verified by comparing the time domain solution obtained with the linear aeroelastic solution for a rectangular, untwisted wing which has a $-75°$ fiber angle in the CAS configuration. For this configuration, from Table 4-7, it is seen that the flutter speed is 97 m/s which is predicted by the linear aeroelastic analysis. Figure 4-7 shows the time history plots of the flapwise displacement of the wing tip obtained by the solution of the nonlinear system of Equation (4-78) for the subcritical speed of 94 m/s, for the critical speed of 96.7 m/s and for the supercritical speed of 98 m/s. The critical speed is obtained by gradually increasing the wind speed and ploting the time response until the appearance of constant amplitude response (flutter). It is seen that at the critical speed, LCO is observed in the nonlinear aeroelastic solution. For airspeeds less than the critical speed, disturbance generated by the initial conditions imposed, attenuate due to the aerodynamic damping (Figure 4-8a). With the increase in the airspeed, an exchange of energy between the wing structure and the aerodynamic flow commences at the bifurcation speed which corresponds to the flutter speed obtained by the linear aeroelastic analysis, and LCO starts . In the supercritical region, amplitude of the LCO increases substantially, and as Figure 4-8c shows the magnitude of oscillation of the flapwise deflection is much higher than the magnitude of the oscillations at the critical speed.

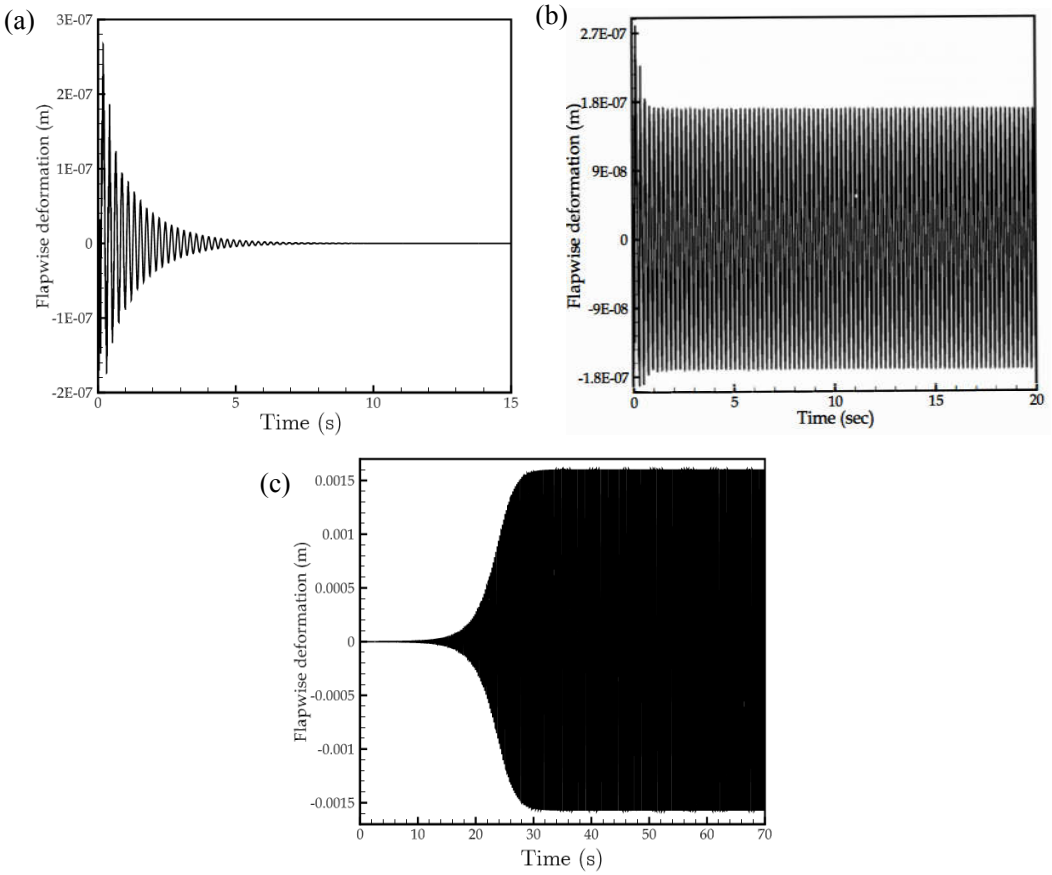

Figure 4-8 Nonlinear time history plots of the flapwise wing tip displacement for three air speeds (a) Subcritical ($U = 94\ m/s$) (b) Critical ($U = 96.72\ m/s$) and (c) Supercritical ($U = 98\ m/s$) .

It should be noted that the closeness of the flutter speeds determined by linear and nonlinear aeroelastic analysis has also been reported by Tang and Dowell [126]. In the current study, the intrinsic character of the nonlinear aeroelastic system has been investigated by exciting the wing by a very small initial disturbance and utilizing linear unsteady aerodynamics. Tang and Dowell [126] Coupled nonlinear beam model with strip theory with ONERA stall aerodynamic model and slender body theory for the wing tip slender body. It is observed that even with nonlinear aerodynamics associated with the stall model, flutter speeds determined by the nonlinear aeroelastic model are very close to those determined by the linear aeroelastic model.

Due to the geometric nonlinearity, the nonlinear aeroelastic equations should be solved by direct integration using a method such as Runge-Kutta for prescribed initial conditions to determine the dynamic response in time domain. In the present study, the static deformation of the blade and the mean steady aerodynamic loads are not considered, and the flutter occurrence is investigated with respect to the undeformed blade. It is assumed that the attached flow assumption holds since the aerodynamic models are based on small disturbance theory. Thus, intrinsic flutter characteristic of the wind turbine blade has been investigated for small deformation of the blade about a static deformation state utilizing linear or nonlinear unsteady aerodynamics. Hence, the magnitude of the initial conditions chosen in the present study is small and taken as 1e-6 for the for all modal coordinates.

It should be noted that structural vibrations occur about a static state condition. This means that the whole structure oscillates about a deformed state which can be large according to the flight scenario and the structural flexibility of the whole aircraft. The aim of the present study is to determine the dynamic (oscillatory) response about a static state which is taken as zero.

Self-excited vibrations require an initial condition. Even a very small deformation or velocity input is sufficient to trigger self-excited vibrations in an aeroelastic system. Solution of the nonlinear aeroelastic system of equations is performed in time domain by integrating the nonlinear system of equations. Therefore, an initial condition as an initial disturbance is needed to start the self-excited vibrations. This is achieved by a very small initial condition because the aim is to investigate the intrinsic character of the nonlinear aeroelastic system corresponding to a very small initial condition. It should be noted that behavior of nonlinear systems is sensitive to initial conditions and a small change in the initial condition may cause substantial changes in the response, especially in case of chaos dynamics where topological changes occur even for a small change in the initial conditions.

If the aeroelastic system characteristics fall within the subcritical region, response will attenuate after a certain time interval. In the subcritical region, larger values of initial conditions increase the time required for a complete attenuation of the response. On

the other hand, for an aeroelastic system in the supercritical region with a small initial condition, time to reach complete LCOs will take longer compared to the case for which larger initial conditions are specified. This is shown by the two plots given in Figure 4-9. For the plot shown in Figure 4-9b, initial condition is 100 times higher than for the case given in Figure 4-9a. It is clearly seen that LCO is reached faster when the initial condition is high.

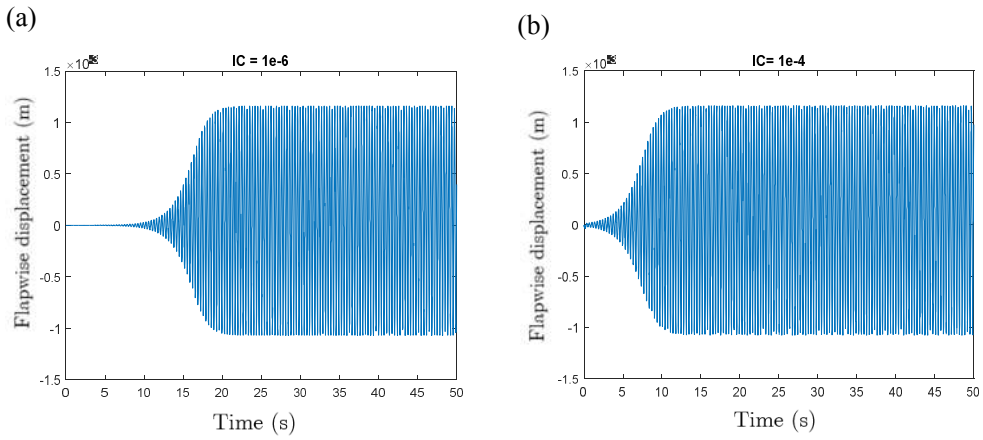

Figure 4-9 Transient time histories of supercritical Hopf-bifurcation (a) $U = 110\ m/s$ and $\vartheta = 1e-6$ (b) $U = 110\ m/s$ and $\vartheta = 1e-4$

4.2.2.3.1 Effect of Fiber Angle of the CAS Configuration TWB on the Nonlinear Aeroelastic Response

The effect of fiber angle of the CAS configuration TWB on the nonlinear aeroelastic response of the composite wing has been investigated for the rectangular wing with no pretwist and no taper, and for the fiber angles of $\theta = -75^{\circ}, -60^{\circ}, -45^{\circ}$. Bifurcation diagram of the torsional deformation (ϕ) and the flapwise deflection (v_0) degrees of freedom at the wing tip is presented in Figure 4-10a and b. Bifurcation diagrams shows that the bifurcation points for both degrees of freedom are nearly identical, and as the absolute value of the fiber angle is decreased, speed at which the bifurcation occurs increases. In this respect, flutter speeds determined by the nonlinear aeroelastic

solution confirm well to the flutter speeds obtained by the linear aeroelastic solution. Figure 4-10b reveals that for the fiber angle of $\theta = -45^{\circ}$, the center line of the bifurcation diagram for flapwise displacement moves upward. For $\theta = -45^{\circ}$, bifurcation angle is wide and amplitude of the LCO increases abruptly with slight increase in the airspeed compared to $\theta = -75^{\circ}, -60^{\circ}$ shown in Figure 4-10a. At this fiber angle nonlinearity is relatively weak and amplitude curves are nearly vertical compared to $\theta = -75^{\circ}, -60^{\circ}$. On the other hand, for the fiber angle of $\theta = -60^{\circ}$ shown in Figure 4-10a, bifurcation angle is narrow and before chaotic oscillations start, amplitude of the LCO is contained in a band as the airspeed increases. Such a post-flutter behavior is a desirable nonlinear aeroelastic response and it is a sign of strong nonlinearity. It should be noted that in Figure 4-10a and b, the average of the absolute values of the maximum and minimum amplitude of the deformations with respect to the center line is taken in drawing the bifurcation diagram. It should be noted that due to the nonlinear stiffness coupling for certain cases there is asymmetry in the amplitude response which is also observed in the literature such as in the work of Tang and Dowell [126]. In order to investigate the effect of fiber angle on the post-flutter response of composite wings, time response, time phase portraits, Poincare maps and one-sided power spectrum density (PSD) plots are obtained at three different post-flutter speeds. In the plots presented, Poincare maps are constructed for the flapwise bending displacement degree of freedom when the torsional deformation is zero at the wing tip by plotting crossings in both directions and PSD plots are generated for the flapwise wing tip deflection.

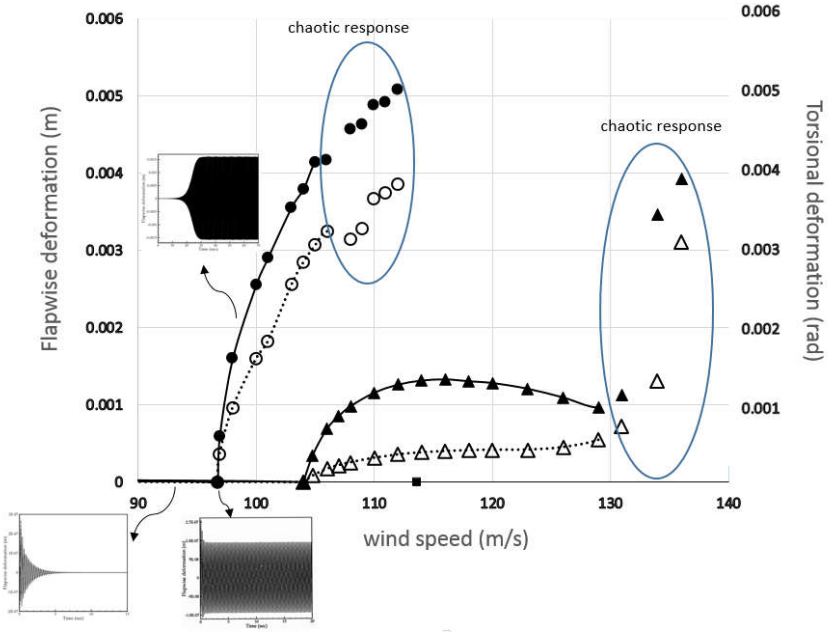

Figure 4-10a Bifurcation diagram of the flapwise bending (solid symbols) and torsional rotation (empty symbols) at fiber angles; circle: θ = -75°, triangle: θ = - 60°

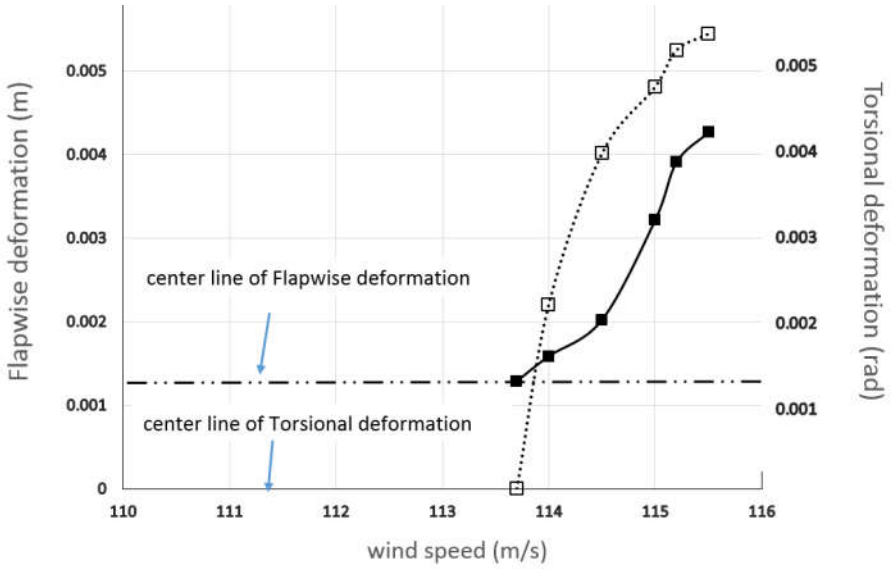

Figure 4-10b Bifurcation diagram of the flapwise bending (solid symbols) and torsional rotation (empty symbols) at fiber angle; rectangular: θ = - 45°

For the fiber angle of $\theta = -75^{\circ}$, Figure 4-11, Figure 4-12 and Figure 4-13 gives the time history plots and associated phase portraits, Poincare maps and one-sided power spectrum density (PSD) plots at the post-flutter speeds of $98\,m/s$, $108\,m/s$ and $112\,m/s$, respectively. For the TWB with the fiber angle of $\theta = -75^{\circ}$, flutter speed is $97\,m/s$ and for the slightly higher post-flutter speed of $98\,m/s$. Figure 4-11 depicts that time history plots of the flapwise displacement and the torsional deformation at the wing tip are smooth and phase portraits have closed narrow circuits representing periodic response. Poincare map given in Figure 4-11e has two dots indicating that the flapwise bending response is indeed periodic and the PSD plot shows the distinct frequency content clearly.

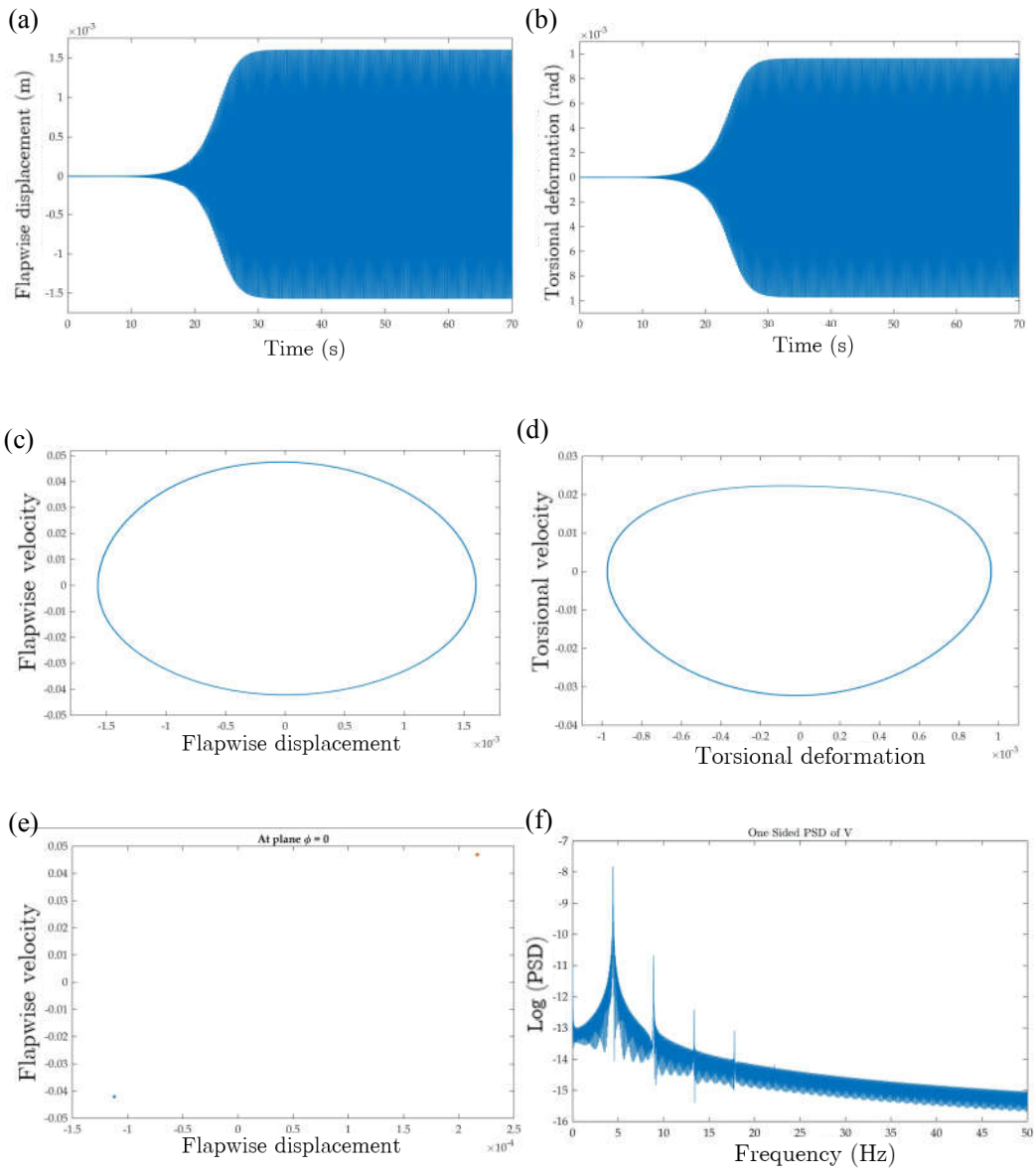

Figure 4-11 Response qualification at $\theta = -75^{\circ}, U = 98\frac{m}{s}, a = 0.3, \beta_0 = 0^{\circ}, \sigma = 1$ (a) Flapwise displacement time response, (b) Torsional deformation time response, (c) Flapwise displacement phase portrait, (d) Torsional deformation phase portrait, (e) Poincare map, (f) PSD.

At the higher post-flutter speed of $108\ m/s$, as seen in Figure 4-12, amplitude of the oscillations increase and time history plots of flapwise bending and torsional deformation are no longer smooth and higher frequency content of the response is evident in the time plots and also in the PSD of flapwise bending displacement. At this speed, phase plane plots have thicker intermittent circuits, as shown in Figure 4-12c-d, and Poincare map has more than one dot. These are indications of the quasi-periodic nonlinear aeroelastic response. Figure 4-13 shows the nonlinear aeroelastic flapwise bending and torsion response of the wing tip at the post flutter speed of 112 m/s. Time response plots Figure 4-13a-b and Phase portraits in Figure 4-13c-d clearly show that the response is chaotic, and broadband range of dominant frequencies exist as shown in the Poincare map given in Figure 4-13e. It should be noted that each separate dot on the Poincare map represents a distinct frequency content in the time response which is also evident in the PSD plot in Figure 4-13f.

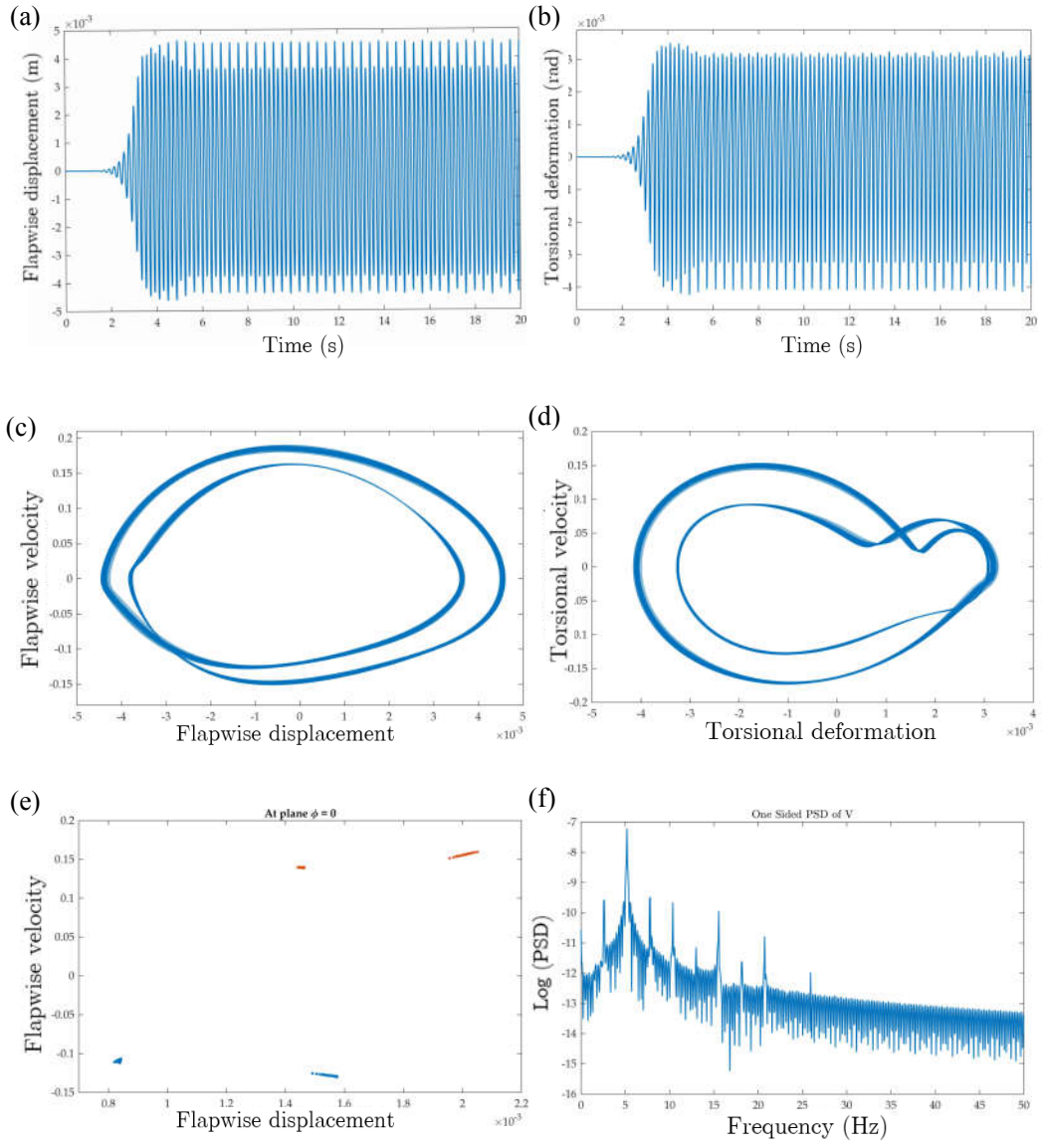

Figure 4-12 Response qualification at $\theta = -75^{\circ}, U = 108\frac{m}{s}, a = 0.3, \beta_0 = 0^{\circ}, \sigma = 1$ a) Flapwise displacement time response, b) Torsional deformation time response, c) Flapwise displacement phase portrait, d) Torsional deformation phase portrait, e) Poincare map, f) PSD.

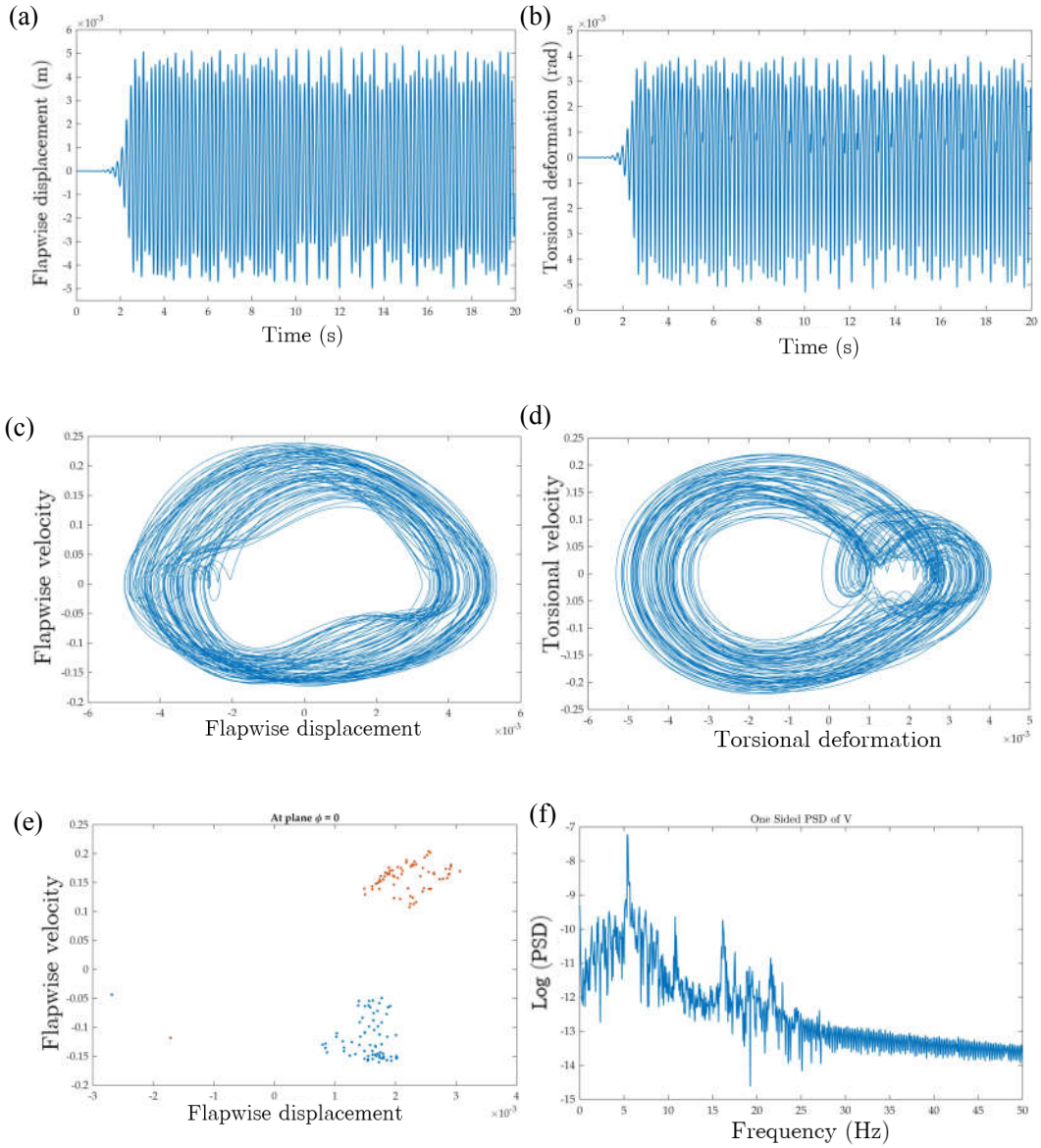

Figure 4-13 Response qualification at $\theta = -75^{\circ}, U = 112\frac{m}{s}, a = 0.3, \beta_0 = 0^{\circ}, \sigma = 1$ a) Flapwise displacement time response, b) Torsional deformation time response, c) Flapwise displacement phase portrait, d) Torsional deformation phase portrait, e) Poincare map, f) PSD.

For the fiber angle of $\theta = -60^{\circ}$, Figure 4-14, Figure 4-15 and Figure 4-16 give the phase portraits, Poincare maps and one-sided power spectrum density (PSD) plots at the post-flutter speeds of 106 *m/s*, 126 *m/s* and 138 *m/s*, respectively. For the TWB with the fiber angle of $\theta = -60^{\circ}$, flutter speed is 104 *m/s*. It is to be noted that since the post-flutter range for the -60° fiber angle case is wide as shown in Figure 4-10, the selected post-flutter speed increments are taken large on purpose. Phase portraits and the Poincare map given in Figure 4-14a-b-c clearly show that the response is purely periodic at 106 *m/s*. As the speed increases, the thickness of the phase plane circuits and the frequency content of the response increase and the periodic response degenerates. Phase portraits and the Poincare map clearly show the for the -60° fiber angle case, post-flutter response is more well behaved compared to the -75° fiber angle case and chaotic response is not encountered until 136 *m/s*.

It should be noted that the source of non-periodic/chaotic response is due to the nonlinear stiffness effect which originates from including geometric nonlinearity which is introduced through the nonlinear strain displacement relations and through the definition of the displacement degrees of freedom. There does not have to be aerodynamic nonlinearity to obtain nonperiodic/chaotic response. Mathematically speaking, a nonlinear system of PDEs with at least three degrees of freedom, may become chaotic for a specific set of parameter definitions. For the present problem, as the flow velocity increases, the rate of energy transfer from the fluid into the structure and vice versa increases up to a point where LCO appears. If geometric nonlinearities are neglected, analysis would fail just after the point of instability and the model predicts at most the threshold of instability. Nonlinearities on the other hand can control the post flutter response and make the system tolerant in the post flutter region. Beyond certain flow velocities, the transferred energy becomes sufficient to commence chaotic response.

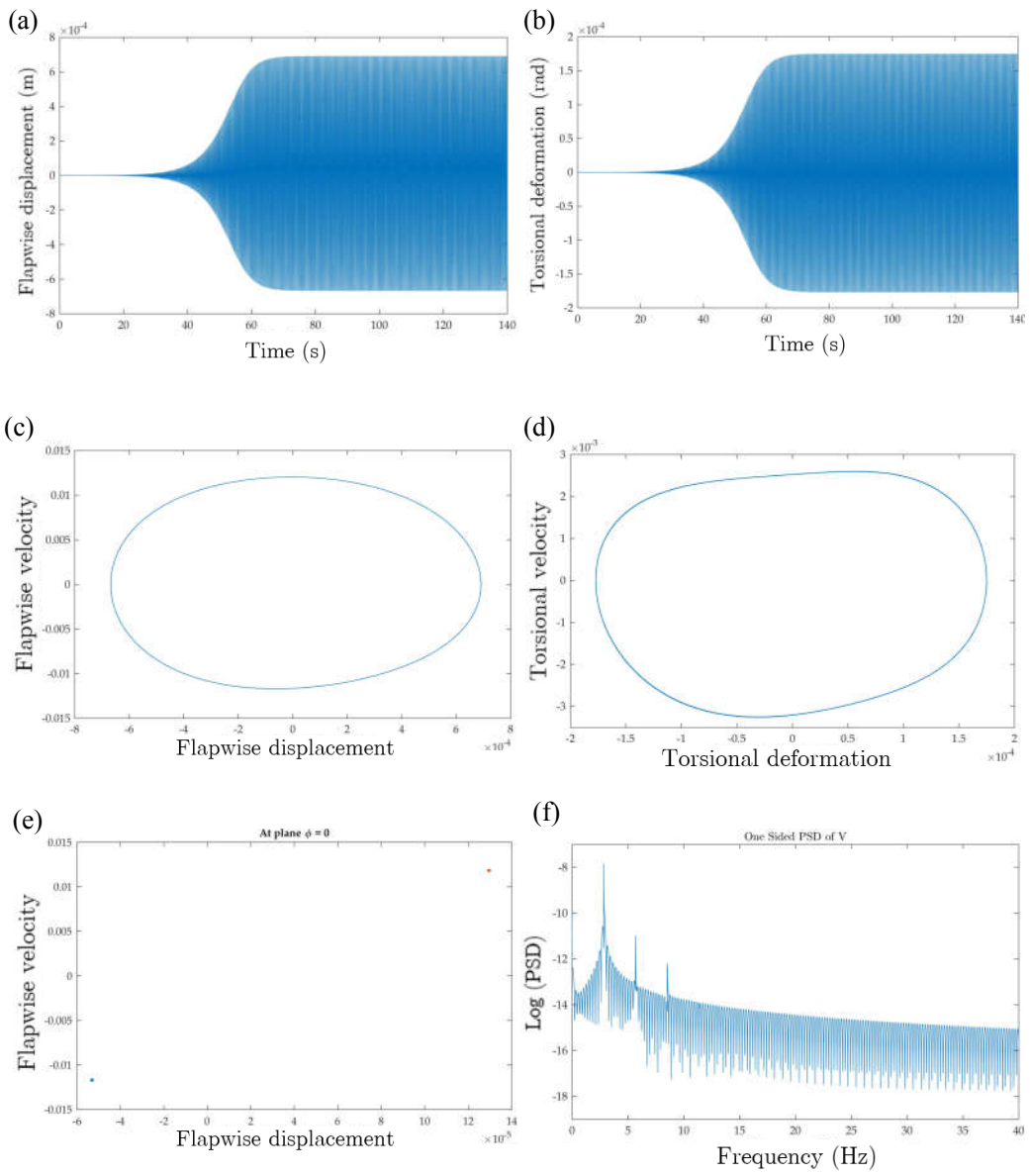

Figure 4-14 Response qualification at $\theta = -60^{\circ}, U = 106\frac{m}{s}, a = 0.3, \beta_0 = 0^{\circ}, \sigma = 1$ a) Flapwise displacement time response, b) Torsional deformation time response, c) Flapwise displacement phase portrait, d) Torsional deformation phase portrait, e) Poincare map, f) PSD.

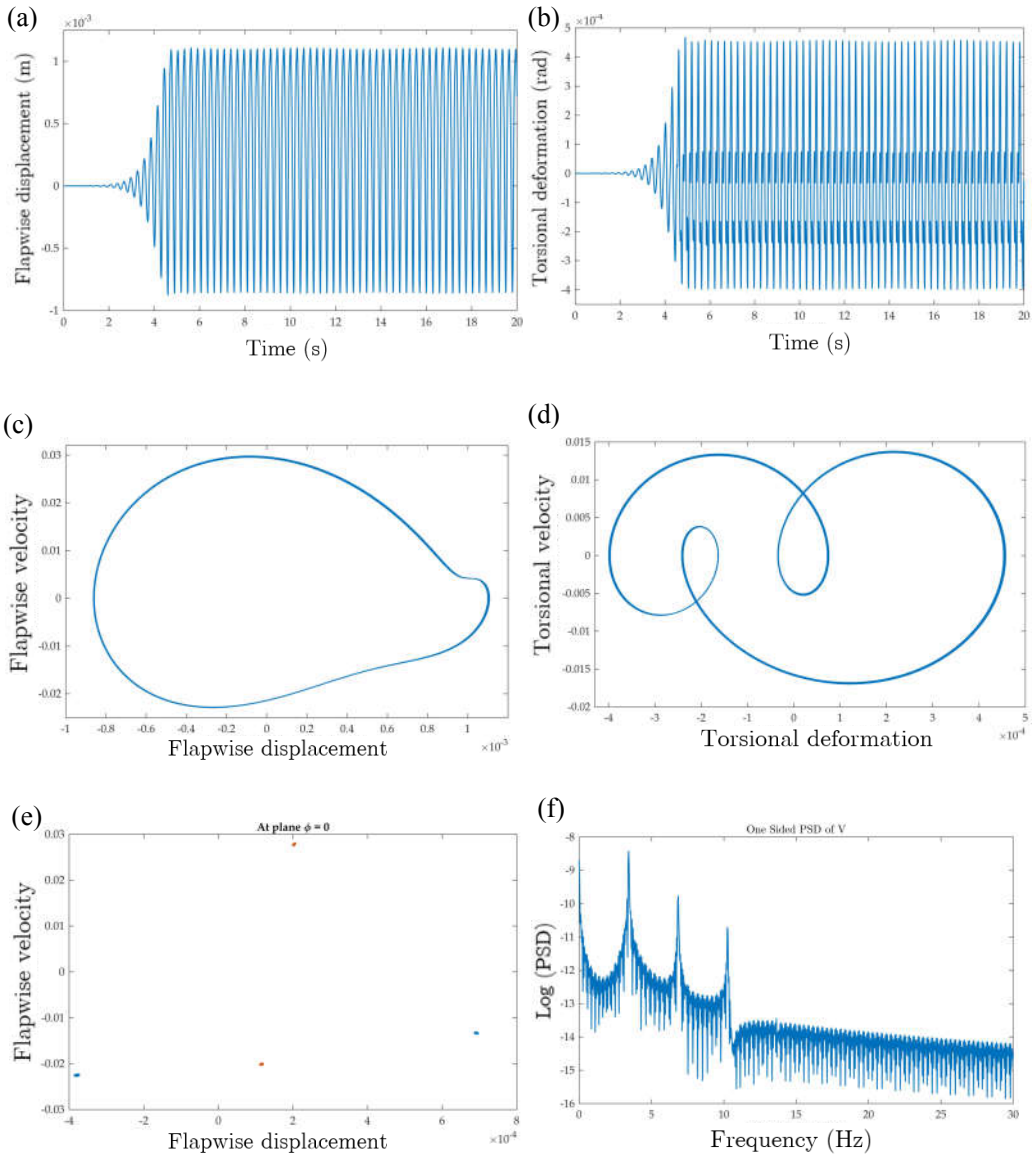

Figure 4-15 Response qualification at $\theta = -60^{\circ}, U = 126\frac{m}{s}, a = 0.3, \beta_0 = 0^{\circ}, \sigma = 1$ a) Flapwise time response, b) Torsion time response, c) Flapwise phase portrait, d) Torsion phase portrait, e) Poincare map, f) PSD.

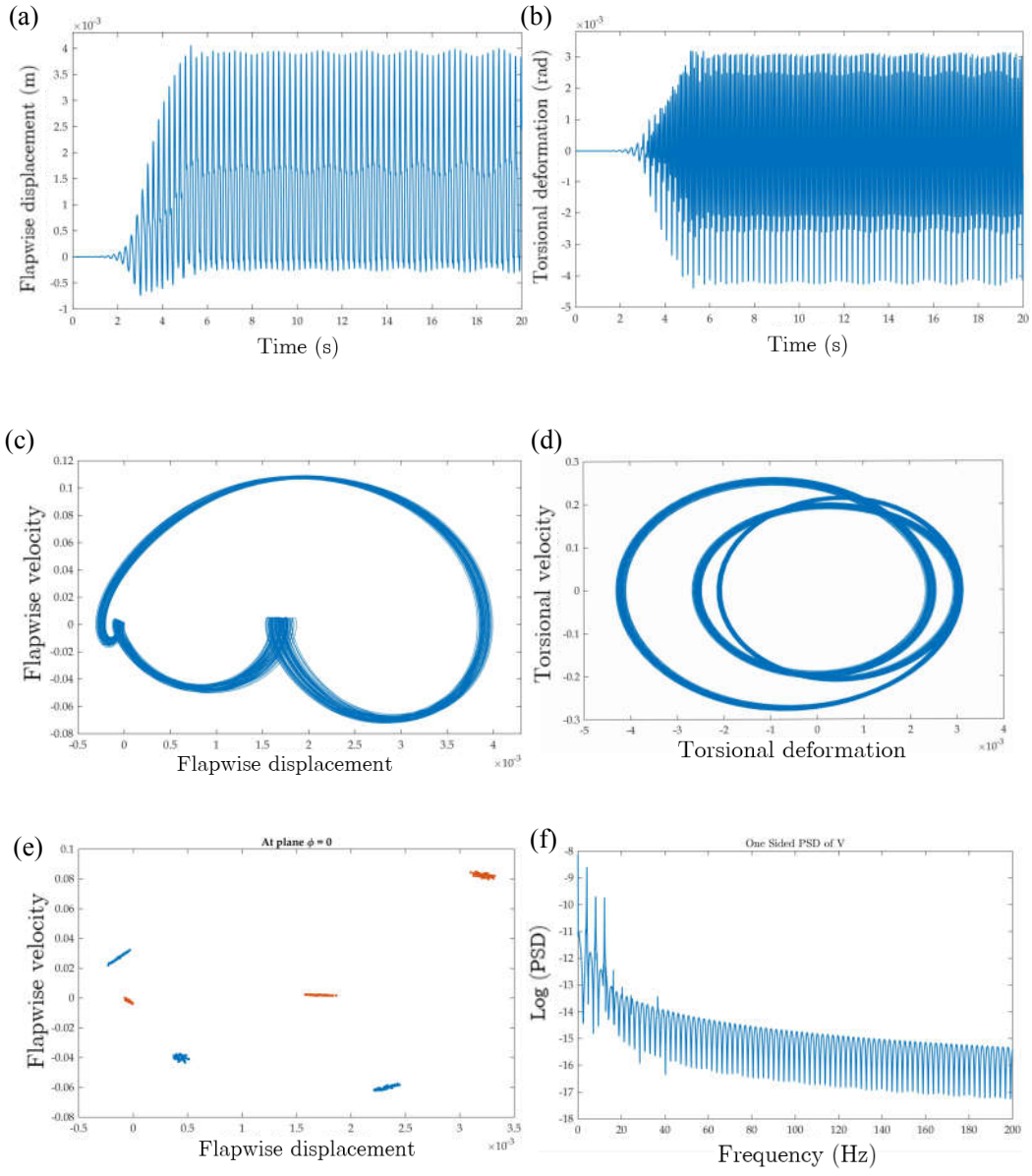

Figure 4-16 Response qualification at $\theta = -60^{\circ}, U = 136\frac{m}{s}, a = 0.3, \beta_0 = 0^{\circ}, \sigma = 1$ a) Flapwise time response, b) Torsion time response, c) Flapwise phase portrait, d) Torsion phase portrait, e) Poincare map, f) PSD.

To

Figure 4-17, Figure 4-18 and Figure 4-19 present the phase portraits, Poincare maps and one-sided power spectrum density (PSD) plots for the -45° fiber angle case. For this fiber angle, as Figure 4-10 shows the bifurcation angle is very wide and the amplitude of oscillations increase abruptly with the slight increase in the airspeed. Therefore, post-flutter speeds at which the nonlinear aeroelastic response is studied are selected as 114 *m/s*, 116 *m/s* and 118 *m/s* with small speed increments. For the -45° fiber angle case, flutter speed is 113.7 *m/s*.

Figure 4-17, Figure 4-18 and Figure 4-19 show that with 4 *m/s* increment in the airspeed, nonlinear aeroelastic responses of the flapwise displacement and the torsional deformation of the wing tip transform from almost periodic motion to chaotic motion. Phase portraits get thicker and thicker as the speed is increased and the Poincare maps get more crowded, indicating the broadband range of dominant frequencies existing in the response. Nonlinear aeroelastic responses of the composite wing with the CAS configuration TWB structural model at three different fiber angles showed that the fiber angle of the CAS configuration greatly affects post-flutter behavior of the composite wing. Although the flutter speed of the composite wing with -75° fiber angle is lower than the flutter speed of the -60° fiber angle case, from post-flutter response point of view, -60° fiber angle is preferable, since the well behaved post-flutter range is wide and the amplitudes of LCOs are low compared to the -75° and -45° fiber angle cases.

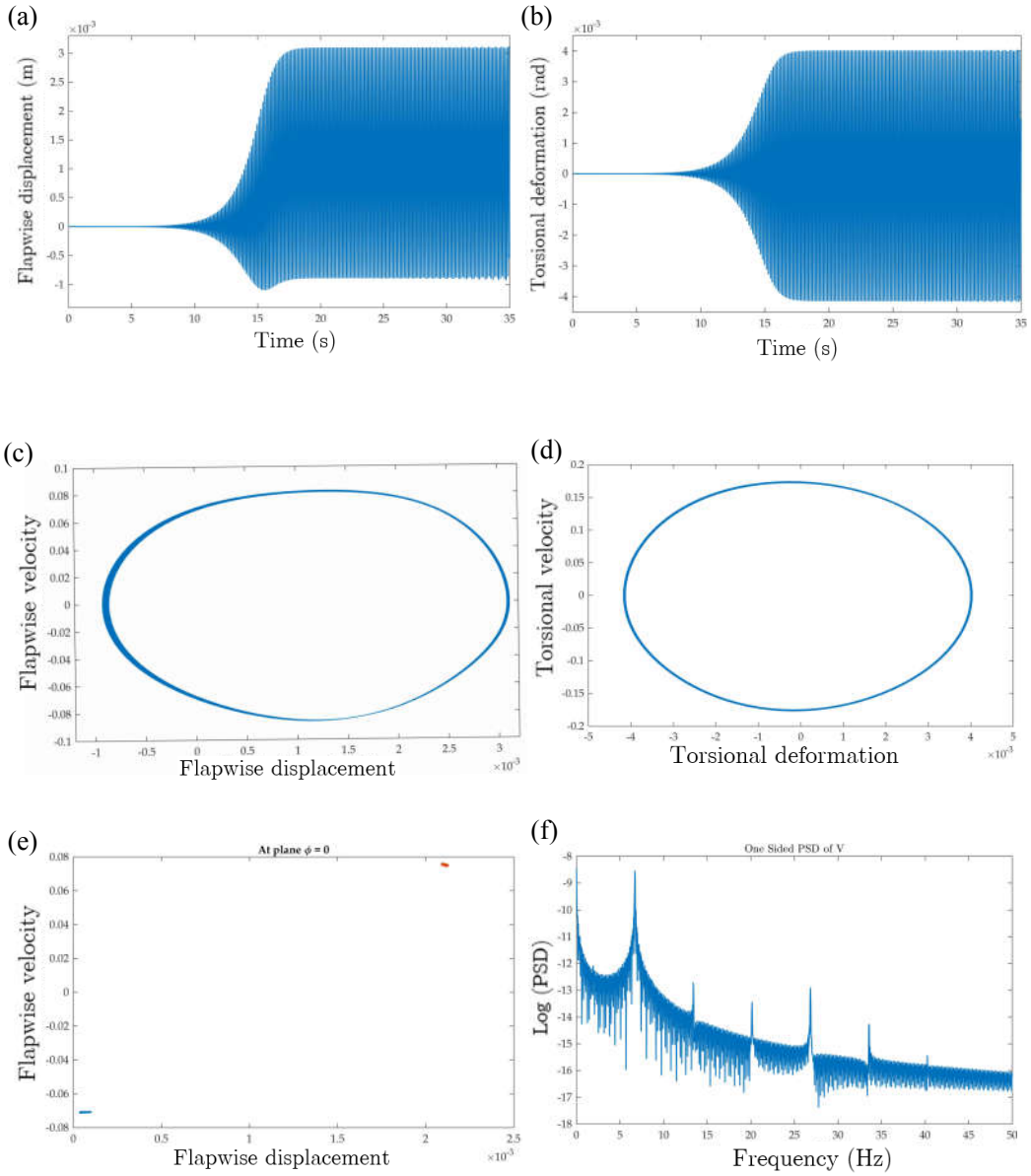

Figure 4-17 Response qualification at $\theta = -45^{\circ}, U = 114\frac{m}{s}, a = 0.3, \beta_0 = 0^{\circ}, \sigma = 1$ a) Flapwise displacement time response, b) Torsional deformation time response, c) Flapwise displacement phase portrait, d) Torsional deformation phase portrait, e) Poincare map, f) PSD.

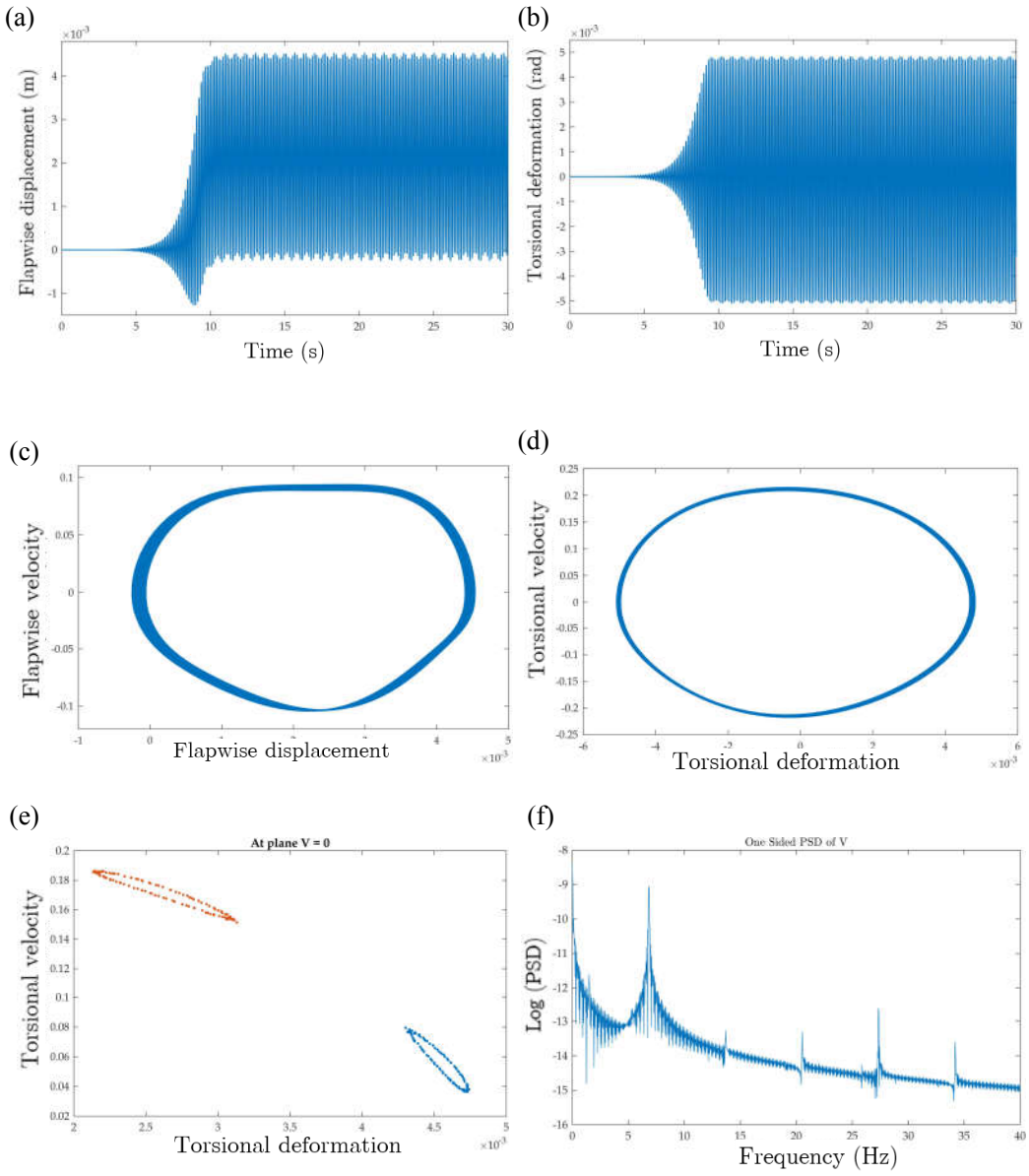

Figure 4-18 Response qualification at $\theta = -45^{\circ}, U = 116\frac{m}{s}, a = 0.3, \beta_0 = 0^{\circ}, \sigma = 1$ a) Flapwise displacement time response, b) Torsional deformation time response, c) Flapwise displacement phase portrait, d) Torsional deformation phase portrait, e) Poincare map, f) PSD.

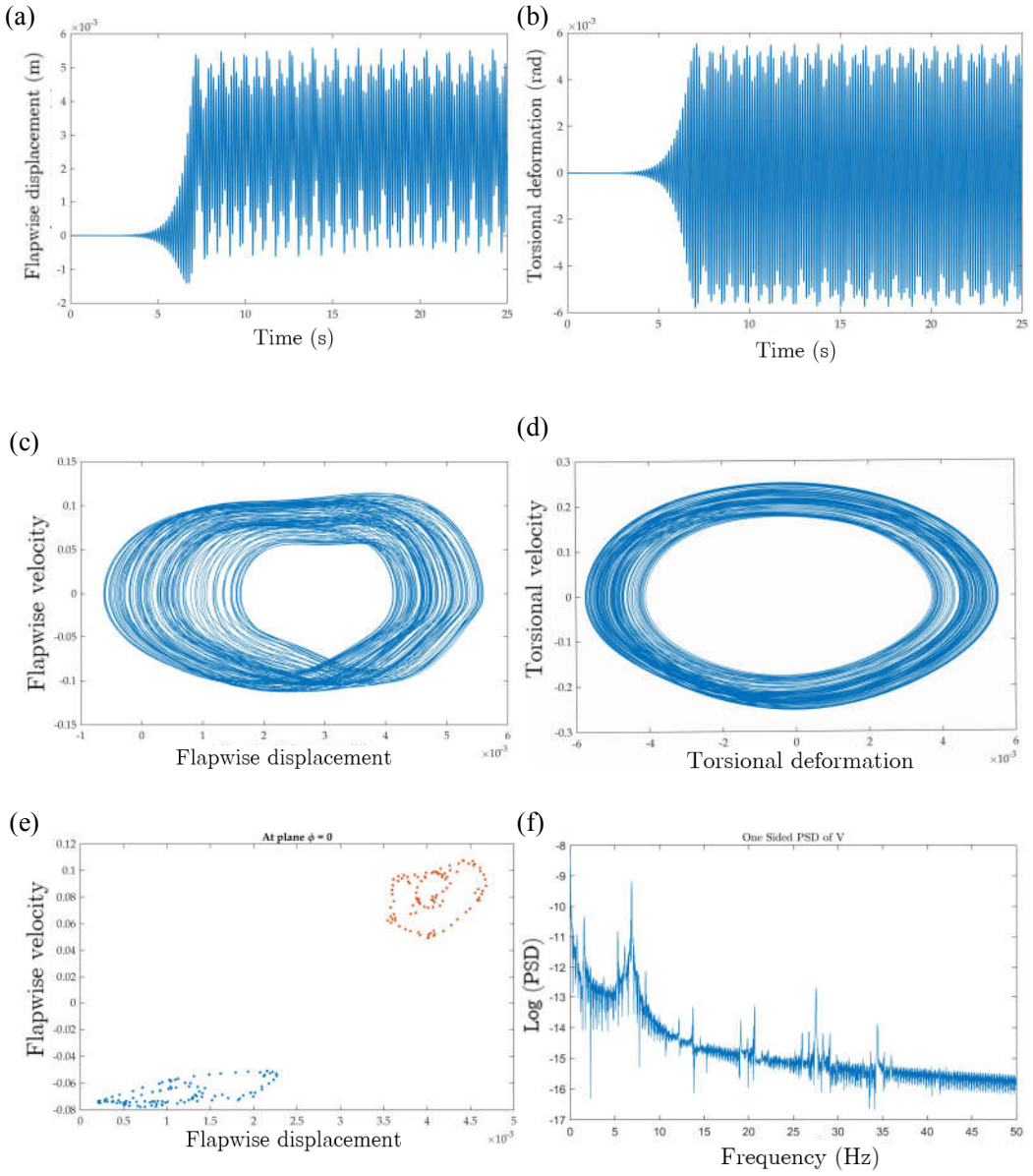

Figure 4-19 Response qualification at $\theta = -45^{\circ}, U = 118\frac{m}{s}, a = 0.3, \beta_0 = 0^{\circ}, \sigma = 1$ a) Flapwise displacement time response, b) Torsional deformation time response, c) Flapwise displacement phase portrait, d) Torsional deformation phase portrait, e) Poincare map, f) PSD.

4.2.2.3.2 Effect of Pretwist Angle on the Nonlinear Aeroelastic Response

The effect of pretwist angle of the wing on the nonlinear aeroelastic response of the composite wing is studied for a rectangular wing with the CAS configuration TWB structural model having -75° fiber angle. For a wing with zero pretwist angle $(\beta_0 = 0^{\circ})$ and for a wing with linearly varying twist along the wing span with a tip twist of $(\beta_0 = 5^{\circ})$. Figure 4-20 shows the bifurcation diagram of the torsional deformation (ϕ) and the flapwise bending deflection (v_0) degrees of freedom at the wing tip. Bifurcation diagram given in Figure 4-20 confirms the results of the linear aeroelastic analyses given in Figure 4-5 and Table 2-7. The delay of the onset of flutter with the introduction of pretwist is clear in Figure 4-20. It is seen that the bifurcation angle of the wing with 5° pretwist is slightly larger than the bifurcation angle of the wing with no pretwist, hence for the wing with pretwist, the LCO is almost close to the wing without pretwist. The effect of pretwist causes the flutter speed to increase but at the same time nonlinearity remains almost identical.

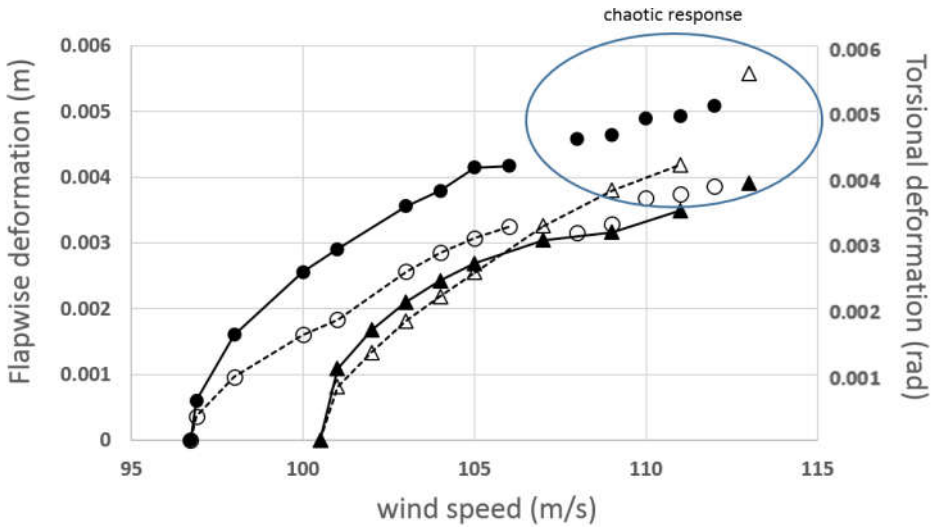

Figure 4-20 Bifurcation diagram of the flapwise bending (solid symbols) and torsional deformation (empty symbols) degrees of freedom for different taper ratios; circle: $\beta_0 = 0$, triangle: $\beta_0 = 5$ deg.

For the wing with 5° pretwist angle, Figure 4-21, Figure 4-22 and Figure 4-23 give the phase portraits, Poincare maps and one-sided power spectrum density (PSD) plots at the post-flutter speeds of 101 m/s, 109 m/s and 113 m/s, respectively. For the wing with 5° pretwist angle, flutter speed is 100.5 m/s. To see the effect of pretwist on the post-flutter response of the composite wing, these plots can be compared with the corresponding plots for the wing with no pretwist for the −75° fiber angle case given in Figure 4-11, Figure 4-12 and Figure 4-13. For the slightly higher post-flutter speed of 101 m/s, Figure 4-21a-b show that the phase trajectories are narrow closed orbits and Poincare map (Figure 4-21c) shows two distinct points representing entrance and exit from the corresponding Poincare section. At this air speed, the nonlinear aeroelastic response is clearly periodic which is also evident in the PSD plot given in Figure 4-21d. At the higher post-flutter speed of 109 m/s, Figure 4-22a-b show that amplitude of the oscillations increase, phase portraits thicken and the two sided Poincare map has more two dots, all of which are typical indications of quasi-periodic response. At the higher post-flutter speed of 113 m/s, as phase portraits and the Poincare map given in Figure 4-23 depict, the nonlinear aeroelastic response is chaotic.

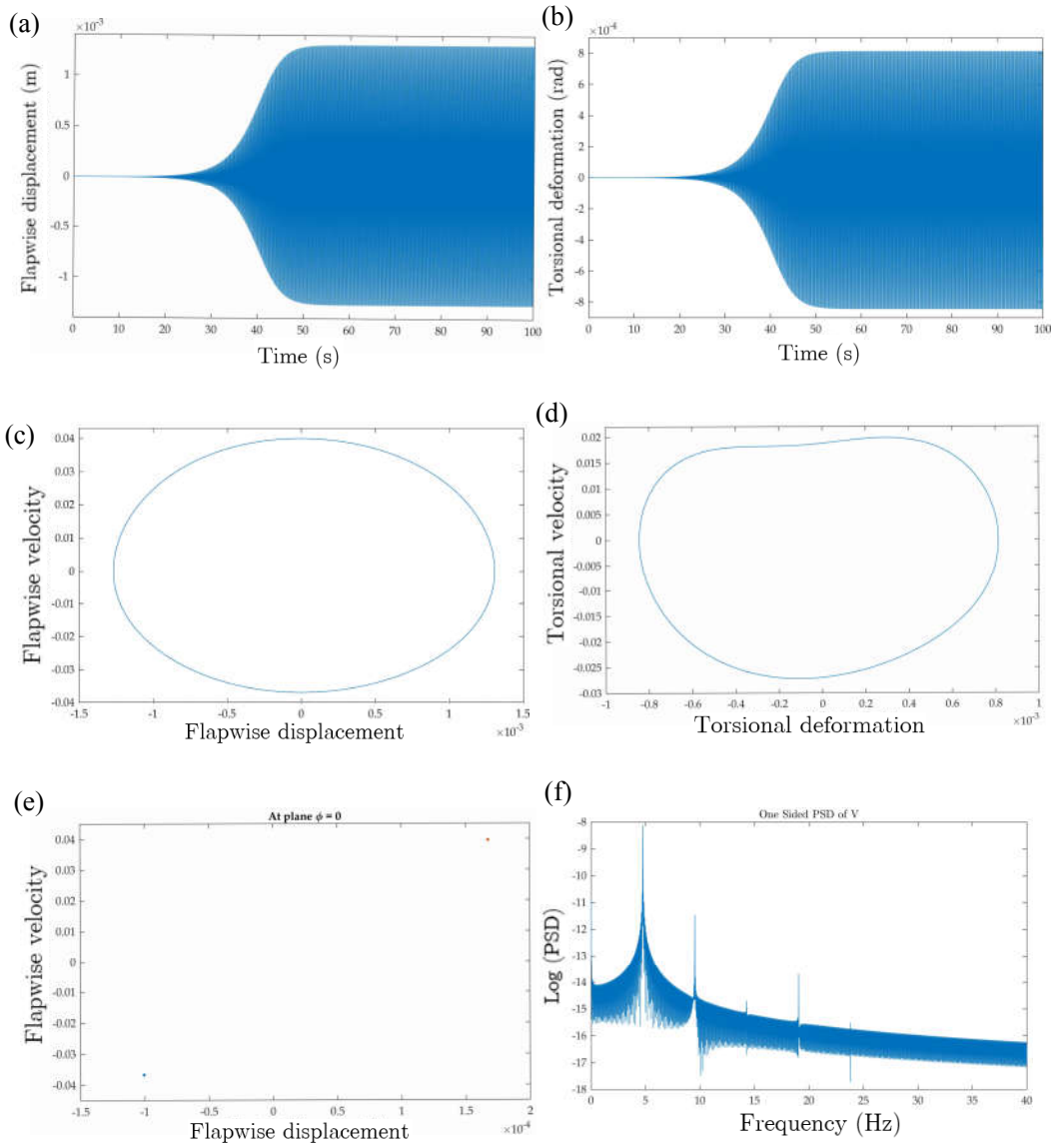

Figure 4-21 Response qualification at $\theta = -75^{\circ}, U = 101\frac{m}{s}, a = 0.3, \beta_0 = 5^{\circ}, \sigma = 1$ a) Flapwise displacement time response, b) Torsional deformation time response, c) Flapwise displacement phase portrait, d) Torsional deformation phase portrait, e) Poincare map, f) PSD.

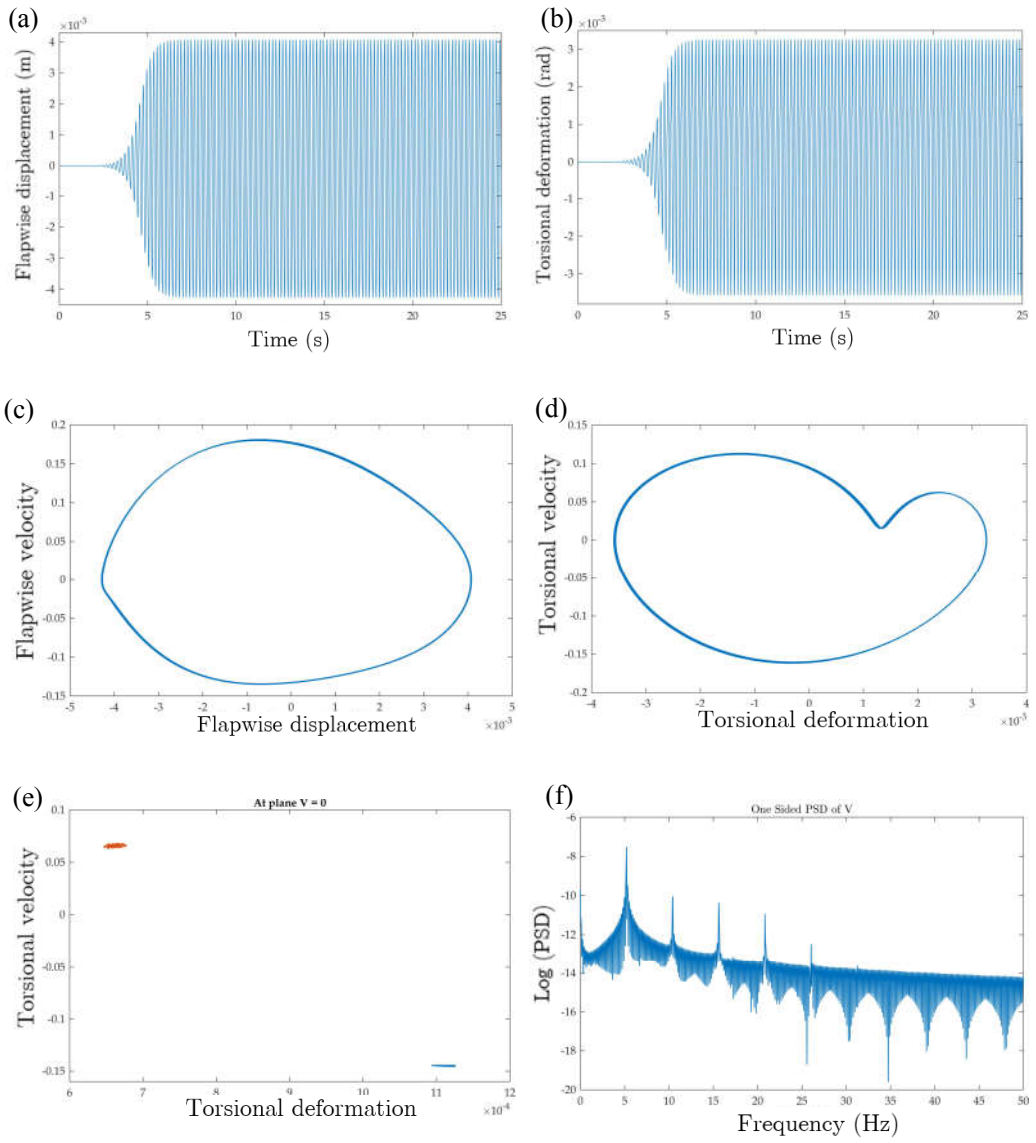

Figure 4-22 Response qualification at $\theta = -75^{\circ}, U = 107\frac{m}{s}, a = 0.3, \beta_0 = 5^{\circ}, \sigma = 1$ a) Flapwise displacement time response, b) Torsional deformation time response, c) Flapwise phase portrait, d) Torsional deformation phase portrait, e) Poincare map, f) PSD.

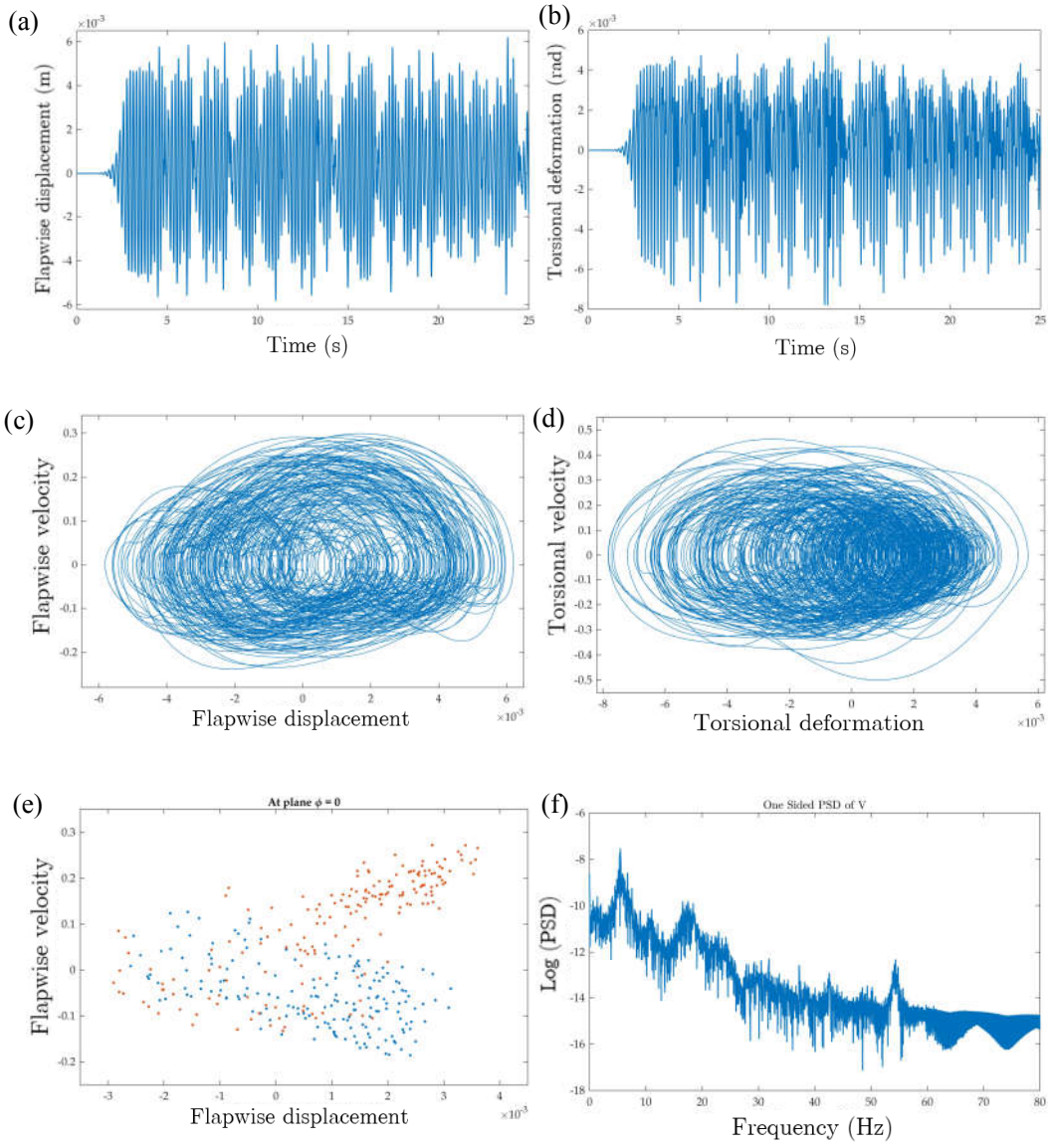

Figure 4-23 Response qualification at $\theta = -75^{\circ}, U = 113\frac{m}{s}, a = 0.3, \beta_0 = 5^{\circ}, \sigma = 1$ a) Flapwise displacement time response, b) Torsional deformation time response, c) Flapwise displacement phase portrait, d) Torsional deformation phase portrait, e) Poincare map, f) PSD.

4.2.2.3.3 Effect of Taper Ratio on the Nonlinear Aeroelastic Response

Having assessed the effects of twist and fiber angle on the nonlinear dynamic aeroelastic response of composite wings structurally modeled as TWBs, the effect of wing taper on the nonlinear dynamic aeroelastic response is studied with an example. To this aim, an untwisted $(\beta_0 = 0^\circ)$ TWB with the fiber angle of $\theta = -75^\circ$ is taken into account. In a first analysis, the bifurcation diagram is obtained in Figure 4-24, which shows the maximum values of torsional deformation and flapwise displacement degrees of freedom. As deduced from the bifurcation diagram, untapered wing structures have smaller critical speeds. It should be noted that in the present study, the steady aerodynamic load for a trimmed flight condition is not considered and only the dynamic motion about the zero deformed state is taken into account. Therefore, the tapered wing has lower aerodynamic loading than the rectangular wing. It is deemed that the combined effect of lower aerodynamic loading, lower mass and lower stiffness of the tapered wing compared to the rectangular wing is such that the tapered wing is prone to aeroelastic instability at higher air speed than the rectangular wing.

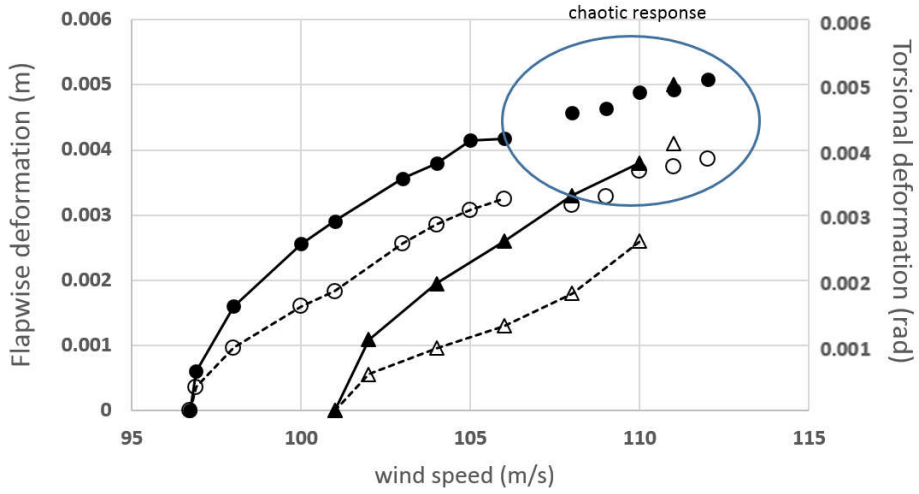

Figure 4-24 Bifurcation diagram of the flapwise bending (solid symbols) and torsional deformation (empty symbols) degrees of freedom for different taper ratios; circle: $\sigma = 1$, triangle: $\sigma = 0.6$.

The first sets of results are then reported for the taper ratio $\sigma = 0.6$ in Figure 4-25, Figure 4-26 and Figure 4-27 for airspeeds $U = 102,108,111$ m/s, respectively. The flutter speed for the taper ratio $\sigma = 0.6$ is 101 m/s. At the airspeed of 102 m/s, which is almost the initiation of the supercritical region, a purely periodic motion is detected (Figure 4-25). Time history plots are smooth, phase planes depict a narrow and closed orbit, PSD plot shows one dominant frequency and the Poincare map gives a single dot in the Poincare section of $\phi = 0^{\circ}$. As the airspeed increases to 108 m/s, time history plots, phase planes, PSD and Poincare map indicate a quasi-periodic motion. The character of motion remains the same at the extreme supercritical value airspeed of 111 m/s. In Figure 4-27, time history plots depict regularly varying amplitudes with several frequency content and several dominant frequencies are seen in the PSD plot. Phase plots show thick and closed orbits and the Poincare map depicts a finite number of points intersecting with the Poincare section of $\phi = 0$. It is clear that as the airspeed is increased, nonlinear response degenerates and approaches chaotic motion.

For a larger taper ratio of $\sigma = 0.8$ the same sets of results are obtained and reported in Figure 4-28, Figure 4-29 and Figure 4-30. The flutter speed for wing with taper ratio $\sigma = 0.8$ is 99 m/s. In this case, a periodic motion is observed at 100 m/s in Figure 4-28 followed by quasi-periodic response in 110 m/s in Figure 4-29 and a chaotic motion at the airspeed of 115 m/s in Figure 4-30. It is observed that for smaller taper ratios (larger σ values), chaotic motion may be encountered at lower airspeeds,and for higher taper ratios (smaller σ values), chaotic motion is encountered at higher airspeeds and for a wide range of airspeeds nonlinear aeroelastic response is quasi-periodic.

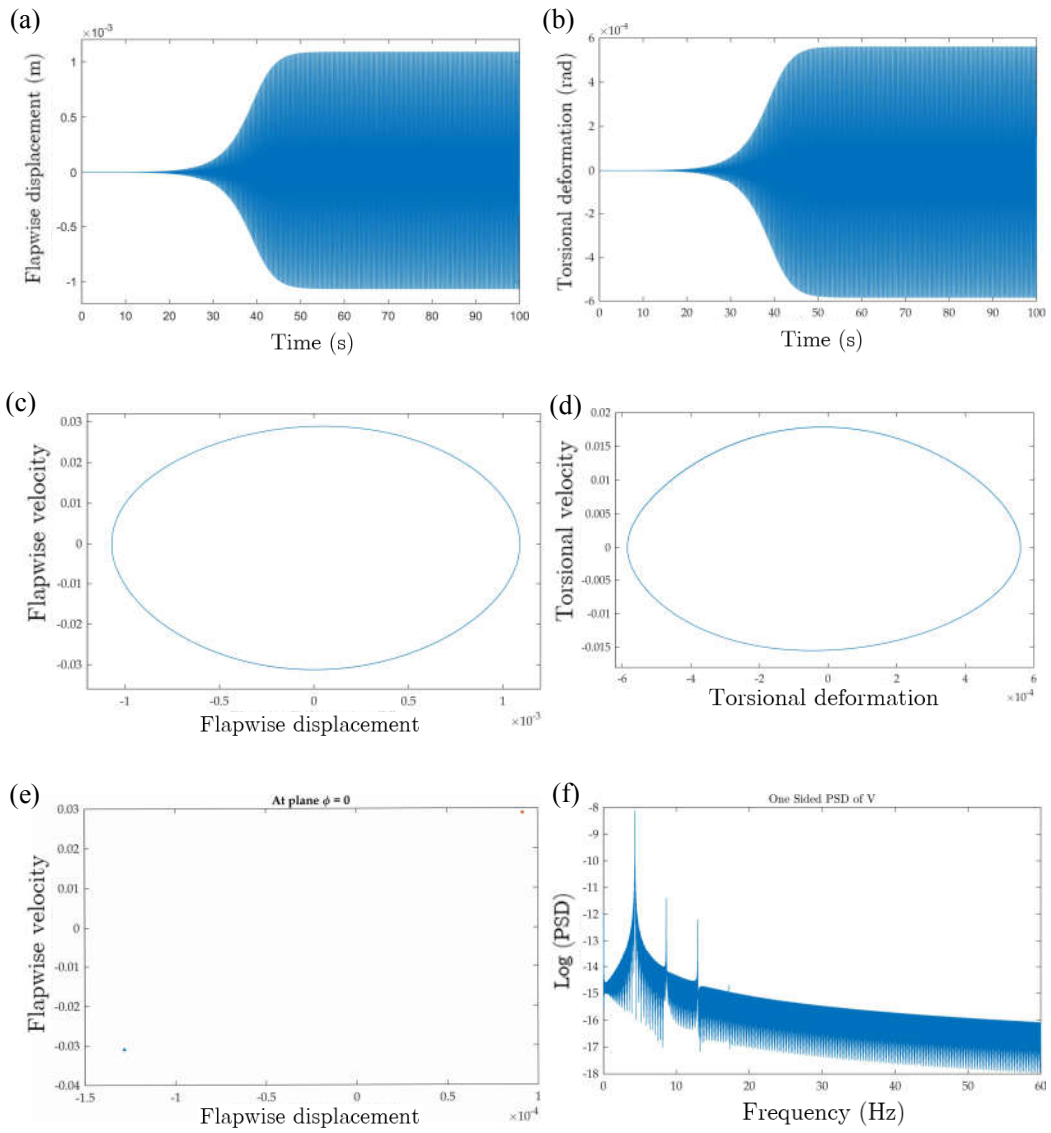

Figure 4-25 Response qualification at $\theta = -75^{\circ}, U = 102\frac{m}{s}, a = 0.3, \beta_0 = 0^{\circ}, \sigma = 0.6$, (a)Flapwise displacement time response, (b)Torsional deformation time response, (c)Flapwise displacement phase portrait, (d)Torsional deformation phase portrait, (e)Poincare map, (f)PSD.

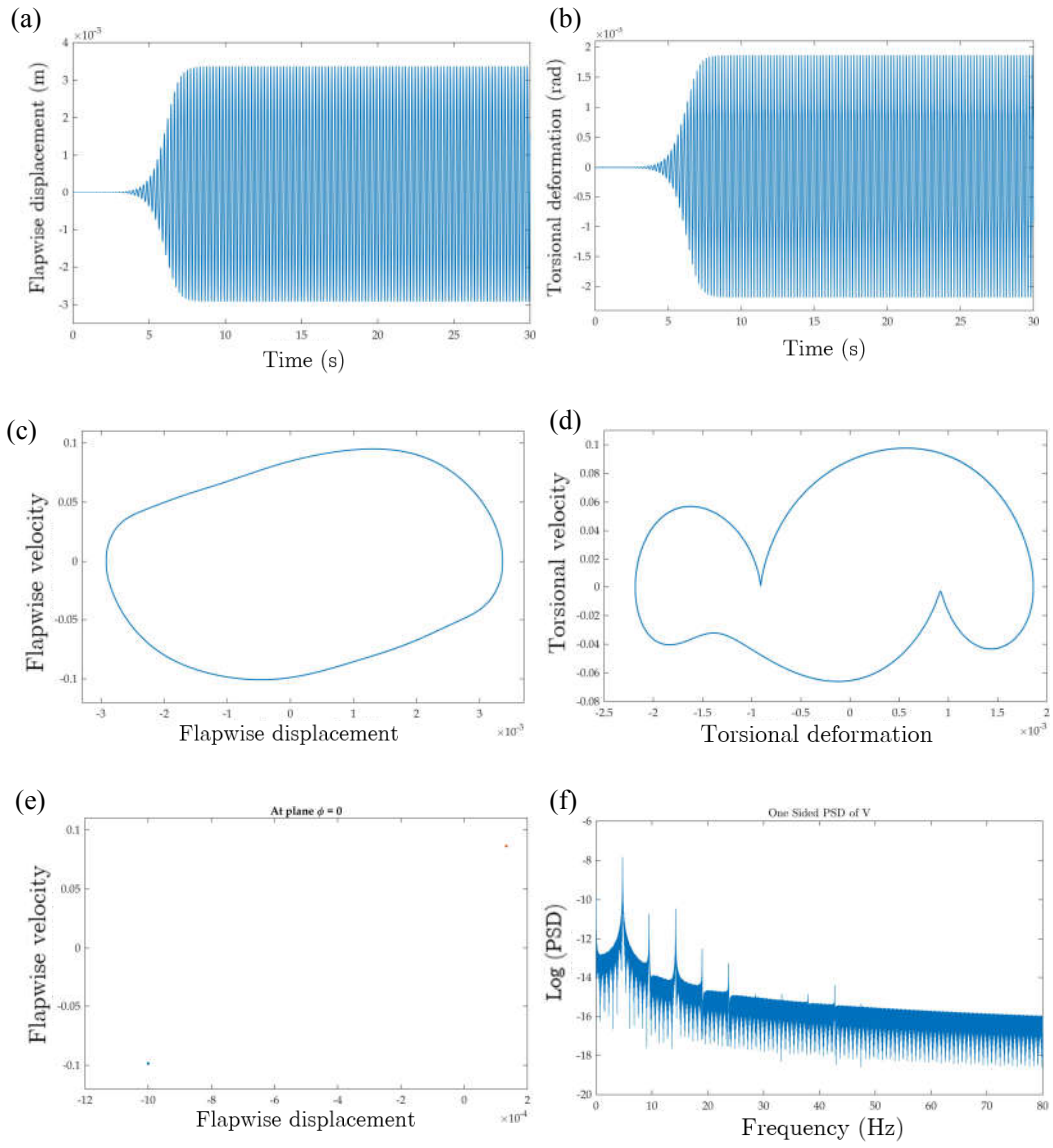

Figure 4-26 Response qualification at $\theta = -75^{\circ}, U = 108\frac{m}{s}, a = 0.3, \beta_0 = 0^{\circ}, \sigma = 0.6$, (a)Flapwise displacement time response, (b)Torsional deformation time response, (c) Flapwise displacement phase portrait, (d) Torsional deformation phase portrait, (e)Poincare map, (f)PSD.

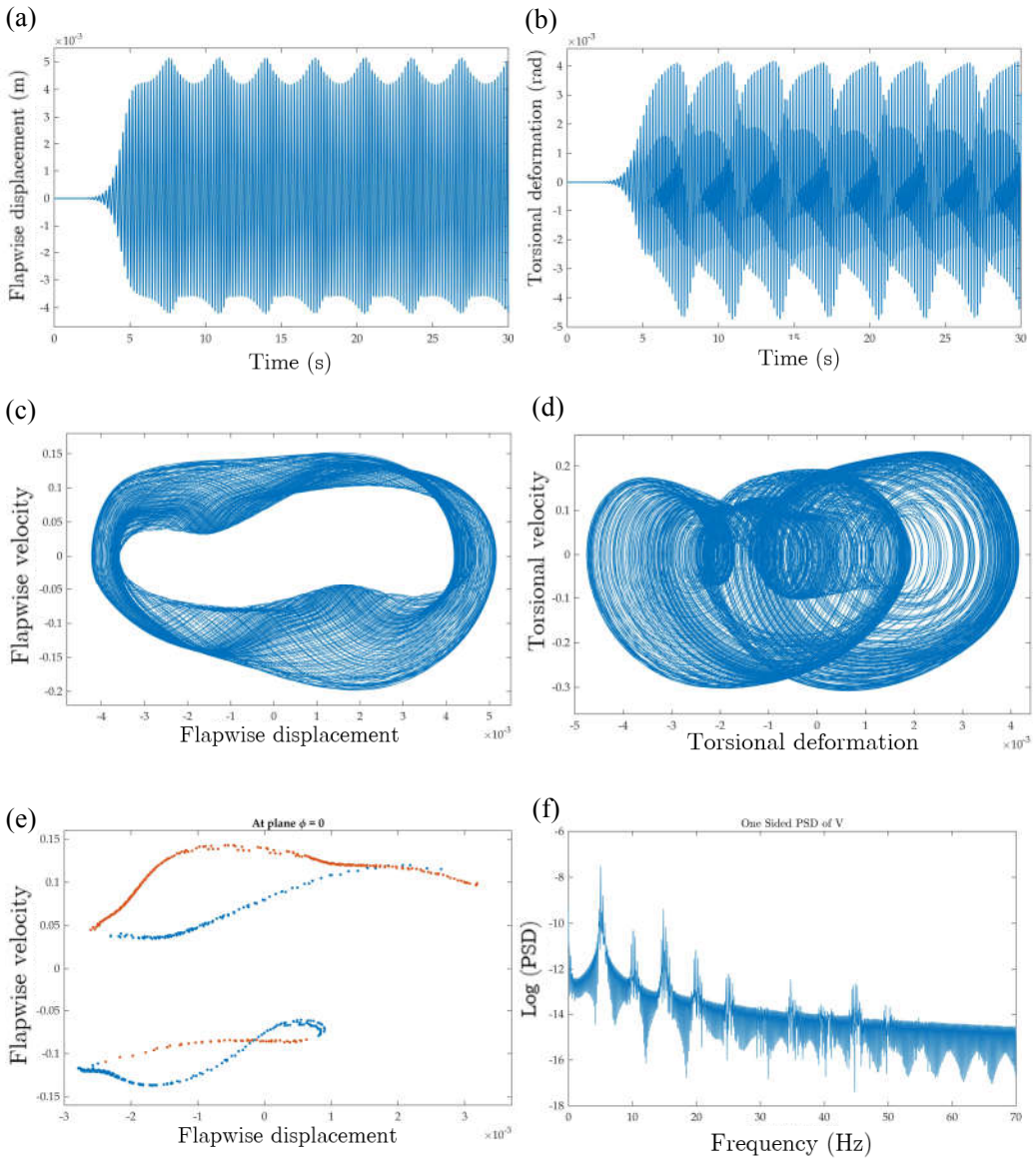

Figure 4-27 Response qualification at $\theta = -75^{\circ}, U = 111\frac{m}{s}, a = 0.3, \beta_0 = 0^{\circ}, \sigma = 0.6$, (a)Flapwise displacement time response, (b)Torsional deformation time response, (c)Flapwise displacement phase portrait, (d)Torsional deformation phase portrait, (e)Poincare map, (f)PSD.

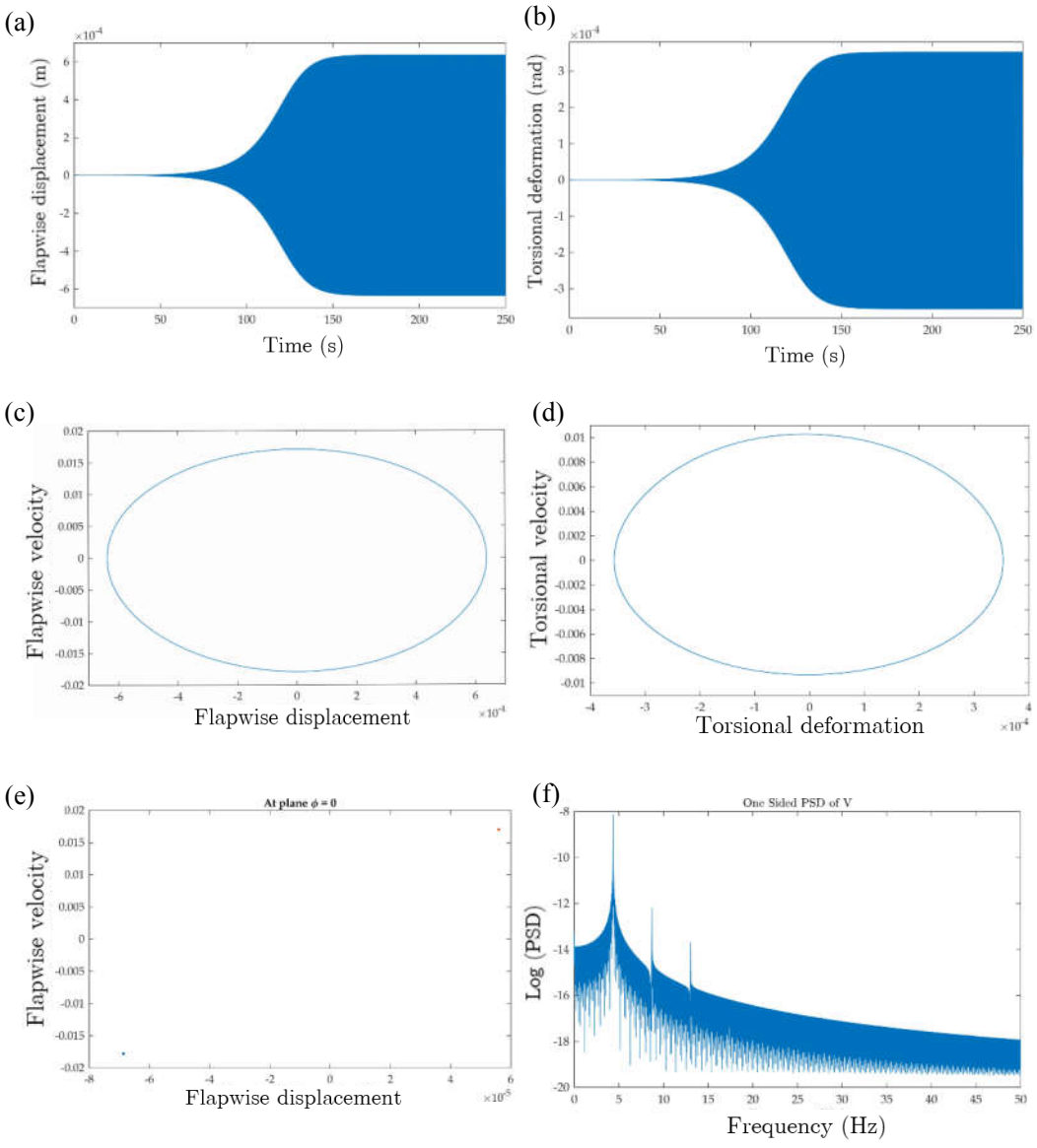

Figure 4-28 Response qualification at $\theta = -75^{\circ}, U = 100\frac{m}{s}, a = 0.3, \beta_0 = 0^{\circ}, \sigma = 0.8$, a)Flapwise displacement time response, b)Torsional deformation time response, c)Flapwise displacement phase portrait, d)Torsional deformation phase portrait, e)Poincare map, f)PSD.

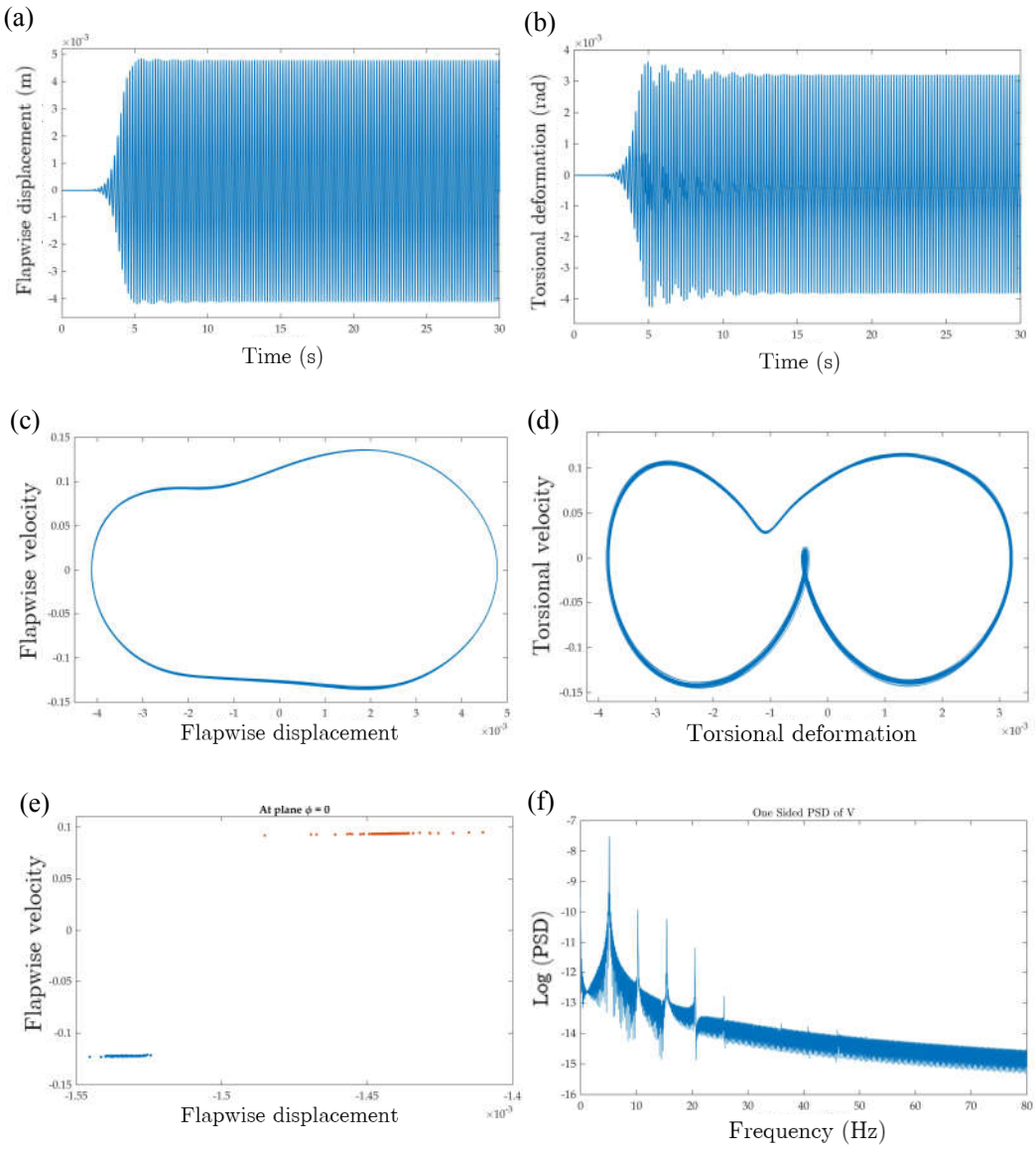

Figure 4-29 Response qualification at $\theta = -75^{\circ}, U = 110\frac{m}{s}, a = 0.3, \beta_0 = 0^{\circ}, \sigma = 0.8$, a)Flapwise displacement time response, b)Torsional deformation time response, c)Flapwise displacement phase portrait, d)Torsional deformation phase portrait, e)Poincare map, f)PSD.

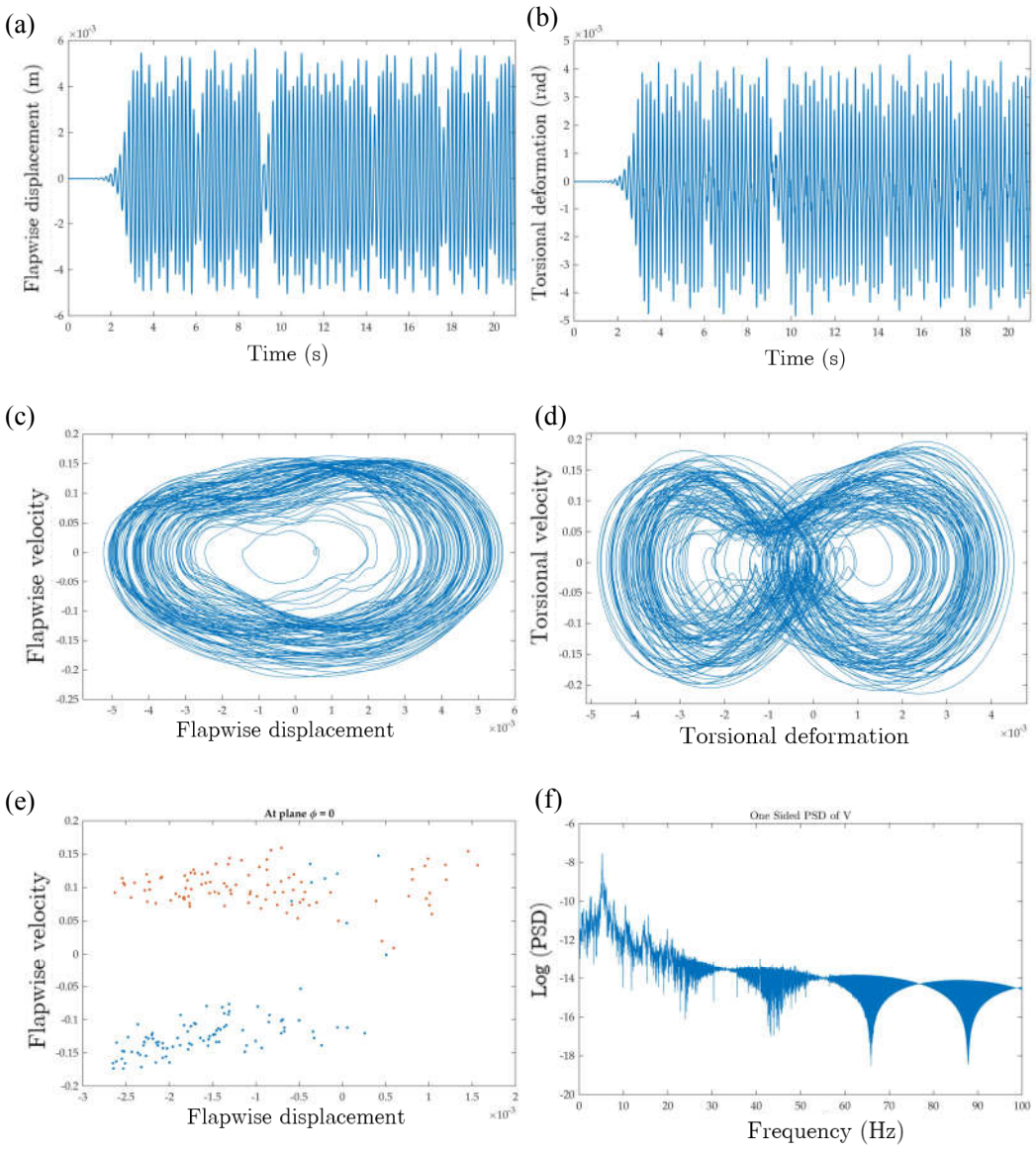

Figure 4-30 Response qualification at $\theta = -75^{\circ}, U = 115\frac{m}{s}, a = 0.3, \beta_0 = 0^{\circ}, \sigma = 0.8$, a)Flapwise displacement time response, b)Torsional deformation time response, c)Flapwise displacement phase portrait, d)Torsional deformation phase portrait, e)Poincare map, f)PSD.

A comprehensive study of the geometrically nonlinear aeroelastic behavior of pretwisted composite wings structurally modeled as TWB is performed. The structural equations of motion are obtained for the CAS configuration TWB in the most general form by including second order nonlinear strain displacement relations, nonuniform geometric features such as wing taper, pretwist, and warping restraint and transverse shear effects are taken into account.

For nonrotating composite wings structurally modeled as TWBs, the following items stand out as major conclusions of the study on the linear and nonlinear aeroelastic response under incompressible unsteady aerodynamics.

- Flutter speeds determined by the linear aeroelastic analysis of the composite wings via the frequency domain solution agree very well with the bifurcation speeds obtained by the time domain solutions of the nonlinear aeroelastic system of equations of the composite wing structurally modeled as TWB.
- Fiber angle of the CAS configuration TWB is a very influential parameter on the instability speed of the composite wing. For positive fiber angles, fibers are oriented towards the trailing edge of the wing resulting in additional increase in the effective angle of attack due to the elastic twist of the wing caused by bending-twisting coupling. Therefore, instability occurs in the form of divergence. For negative fiber angles, the form of instability is flutter because fibers are oriented towards the leading edge and divergence instability is deferred.
- Besides the flutter speed, the fiber angle of the CAS configuration TWB has a significant effect on the post-flutter LCO behavior of the composite wing. Post-flutter responses of composite wings with three different off-axis fiber angles (-75°, -60°, -45°) showed that although the flutter speed of the composite wing with -45° off-axis fiber angle is higher than the flutter speed of the -60° fiber angle case, from post-flutter response point of view, -60° fiber angle is preferable, since the well behaved post-flutter range is wide and the amplitudes of the LCOs are low compared to the -75° fiber angle case. For the -45° fiber angle case, bifurcation speed is highest but flapwise bending displacement and

torsional deformation amplitude curves are nearly vertical. Such a post-flutter behavior is a sign of weak nonlinearity and undesirable nonlinear aeroelastic response. From a design perspective, -60° fiber angle would be more preferable since the nonlinearity is very strong and the amplitude of the post-flutter LCO is contained in a band for air speeds, way beyond the bifurcation speed of the -45° fiber angle case. When both the flutter speed and the post-flutter response is considered, -60° fiber angle would be preferable since for the -45° fiber angle case, LCO amplitude curves are nearly vertical.

- The effect of pretwist causes the flutter speed to increase, but at the same time nonlinearity becomes slightly weaker. Comparison of the bifurcation diagrams, phase planes and Poincare maps at three post-flutter speeds for the composite wing with no pretwist and 5° pretwist at the wing tip, reveals that for small pretwist angles post-flutter responses are similar, hence bifurcation speed can be taken as the main design driver.
- For composite wings with different fiber angles and pretwist, post-flutter response of the tip of the composite wing is studied in more detail by preparing phase portraits, Poincare maps and PSD plots at three post-flutter speeds. Results reveal that while the response is periodic at speeds slightly over the flutter speed, as the air speed is increased, periodic responses get distorted and quasi-periodic and eventually chaotic responses are encountered.
- Wing taper ratio has a stabilizing effect on the stability margins of the wing. For untapered wings the flutter speed decreases and the wing is more prone to flutter instability at smaller speeds compared to a tapered wing. It should be noted that tapered wing analysis has been performed for the same span wings. Normally, for an aircraft structure an untapered wing and tapered wing must have different spans to have similar aircraft performances. Such a case has not been investigated in this study. For the same wing span, tapered wings have slightly higher flutter speeds and more well behaved post-flutter response.

4.3 Nonlinear Aeroelastic Analysis of the Composite rotating TWB-Blade Using Incompressible Unsteady Aerodynamic

This section focuses on rotating blade by considering the effect of angular velocity $(\Omega \neq 0)$ in Equations (4-16)-(4-48). In this part, nonlinear aeroelasticity of the *rotating large scale wind turbine* made up from composite rotating TWB with CAS configuration in the incompressible flow regime is investigated. Figure 4-31 shows the schematic description of rotating wind turbine blade with load carrying thin wall box beam and aerodynamic surface. The structural and aerodynamic coordinates are shown by (x, y, z) and (x_{ae}, z_{ae}).

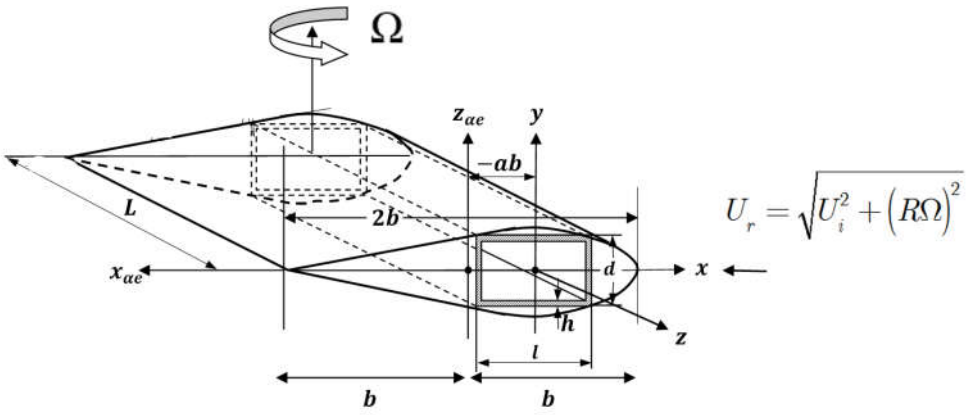

Figure 4-31 Aerodynamic and Structural Coordinates of the Symbolic Rotor blade with the "Thin-Walled Composite Box Beam" Configuration

Where, the relative velocity U_r is normal to the leading edge given in Equation (4-80).

$$U_r = \sqrt{U_i^2 + (R\Omega)^2}, \qquad \tan\psi = \frac{U_i}{R\Omega} \tag{4-80}$$

Where, U_i and $R\ \Omega$ are inflow velocity and angular velocity while, R are a spanwise position and ψ is the relative wind angle, respectively.

Table 4-8 gives the geometric and material properties of the 5 MW NREL wind turbine blade modelled as rotating box beam composed of glass/epoxy.

Table 4-8 Geometric and material properties of the glass/epoxy composite blade.

Material properties		**Geometric properties**	
$E_1\ (GPa)$	39.14e9	$L\ (m)$	60
$E_2\ (GPa)$	13.219e9	$l_{root}(m), \sigma_l$	0.591, 0.95
$E_3\ (GPa)$	13.219e9	$d_{root}(m), \sigma_d$	1.412, 0.25
$G_{12}\ (GPa)$	3.937e9	$h\ (m)$	0.056
$G_{13}\ (GPa)$	3.937e9	$\beta\ (deg.),$	0
$G_{23}\ (GPa)$	3.937e9	$\theta\ (deg.)$	-90,-85,-80,-75
$\vartheta_{12} = \vartheta_{23}$	0.3	$\rho\ (kg/m^3)$	2001
ϑ_{13}	0.8	$R_0\ (m)$	$0.1L$

Before the nonlinear aeroelastic analysis of composite wings, linear aeroelastic analyses have been performed to predict the flutter and divergence speeds in order to better evaluate the results of nonlinear aeroelastic analysis. As discussed before, Ritz-based methodology described for the nonlinear aeroelastic analysis is also followed in the linear aeroelastic analysis of the CAS configuration composite wings, and nine trial functions $(N = 9)$ are used in the series given in Equation (4-52) for the six degrees of freedom of the TWB and first nine $(m = 9)$ eigenfunctions are used for the modal reduction. For the composite TWB structure, geometric and material properties given in Table 4-8 are used and the nondimensional offset between the shear center and the mid chord is taken as $a = -0.1$, implying that the shear center is in front of the mid chord. Moreover, the spanwise and chordwise taper ratios are assumed to be $\sigma_l = 0.95, \sigma_d = 0.25$. Table 4-9 gives the variation of the aeroelastic instability rotation speed and associated frequency of the tapered composite blade with the fiber angle of the CAS configuration for an inflow speed of 10 m/s. Results are presented for an

untwisted blade. It is noted that for fiber angle -90°, flutter frequency is zero and the instability mode is divergence.

Table 4-9 flutter rotational speed and frequency at a vriety of lamination angles.

Fiber angle θ (Degree)	Flutter rotational speed Ω (rad/sec)	Flutter Frequency (rad/sec)
-90	2.85	0
-85	3	13.8
-80	3.15	9.87
-75	3.26	9.25

As given in Table 4-9, the maximum flutter rotational speed corresponds to a fiber angle of $-75°$ while the minimum flutter rotational speed occurs at a lamination angle of -90°. The nonlinear aeroelastic system of equations is verified by comparing the time domain solution obtained with the linear aeroelastic solution for the untwisted wing which has a $-75°$ fiber angle in the CAS configuration given in Table 4-9. For this configuration, from Table 4-9, it is seen that the flutter rotational speed is 3.26 rad/sec. Figure 4-32 shows the time history plots of the flapwise displacement of the rotating blade tip obtained by the time domain solution of the nonlinear system of Equation (4-78) for the subcritical rotation speed of 3.255 rad/sec, for the critical rotational speed of 3.26 rad/sec and for the supercritical rotational speed of 3.265 rad/sec. It is seen that at the critical speed, LCO is observed in the nonlinear aeroelastic solution. For rotational speed less than the critical speed, disturbance generated by the initial conditions imposed, attenuate due to the aerodynamic damping (Figure 4-32a). With the increase in the rotating speed, an exchange of energy between the blade structure and the aerodynamic flow commences at the bifurcation rotating speed which corresponds to the flutter rotational speed obtained by the linear aeroelastic analysis, and LCO starts (Figure 4-32b). In the supercritical region, amplitude of the LCO increases substantially and as Figure 4-32c shows the magnitude of oscillation of the flapwise deflection is much higher than the magnitude of the oscillations at the critical rotational speed.

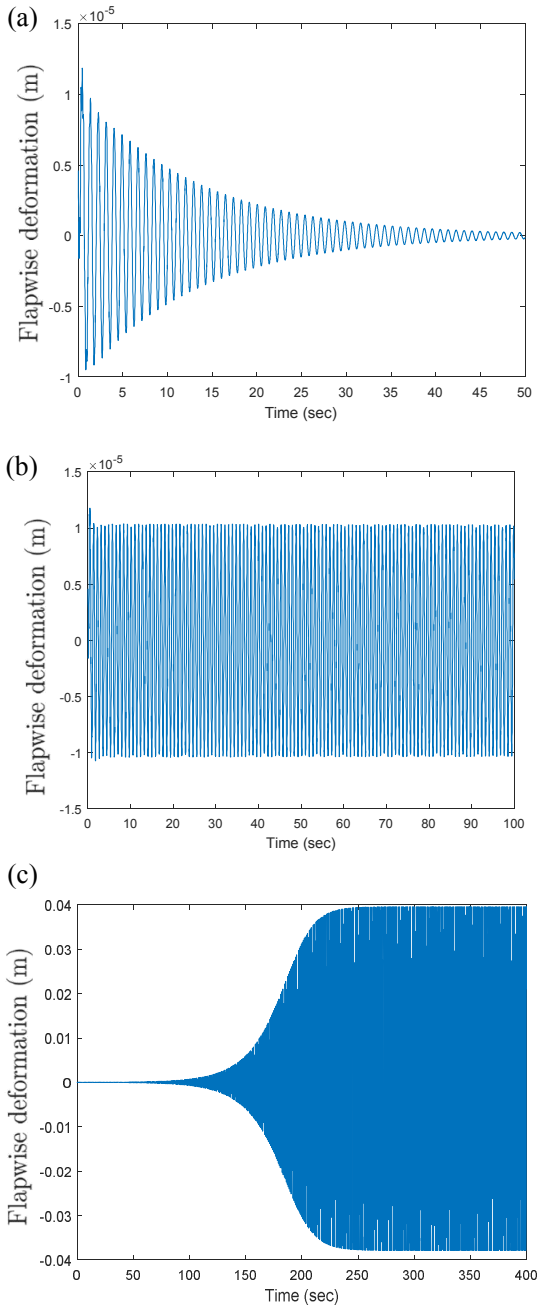

Figure 4-32 Nonlinear time history plots for three rotational speeds (a) Subcritical ($\Omega = 3.255\ rad/sec$) (b) Critical ($\Omega = 3.26\ rad/sec$) and (c) Supercritical ($\Omega = 3.265\ rad/sec$)

For the fiber angle of$\theta = -75^{\circ}$, Figure 4-33 gives the time history plots and associated phase portraits, at the post-flutter rotational speed of $3.265\ rad/sec$.

Figure 4-33 depicts that time history plots of the flapwise displacement and the torsional deformation at the blade tip are well smooth and phase portraits have closed narrow circuits representing periodic response.

At the higher post-flutter rotational speed of $3.28\ rad/sec$, as seen in Figure 4-34, amplitude of the oscillations increase and higher frequency content of the response is evident in the FFT plots of the flapwise bending displacement and torsional deformation. At this speed, it is clear that the response shows signs of degeneration and phase plane plots do not have narrow circuits, as shown in Figure 4-34,

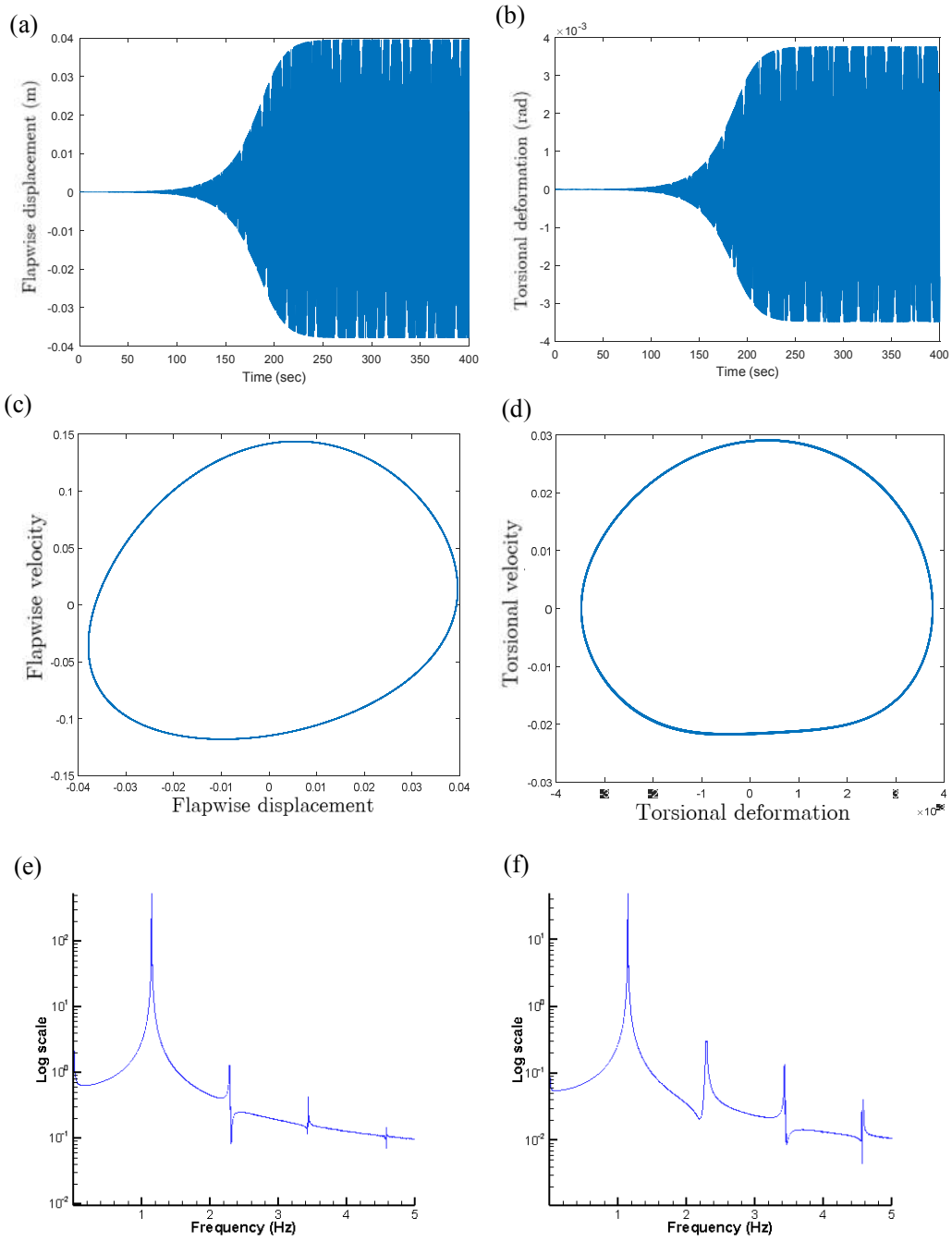

Figure 4-33 Response qualification at $\theta = -75^{\circ}, \Omega = 3.265\ rad/sec$, a)Flapwise displacement time response, b)Torsional deformation time response, c)Flapwise displacement phase portrait, d)Torsional deformation phase portrait, e) FFT flapwise deformation, f) FFT torsion deformation

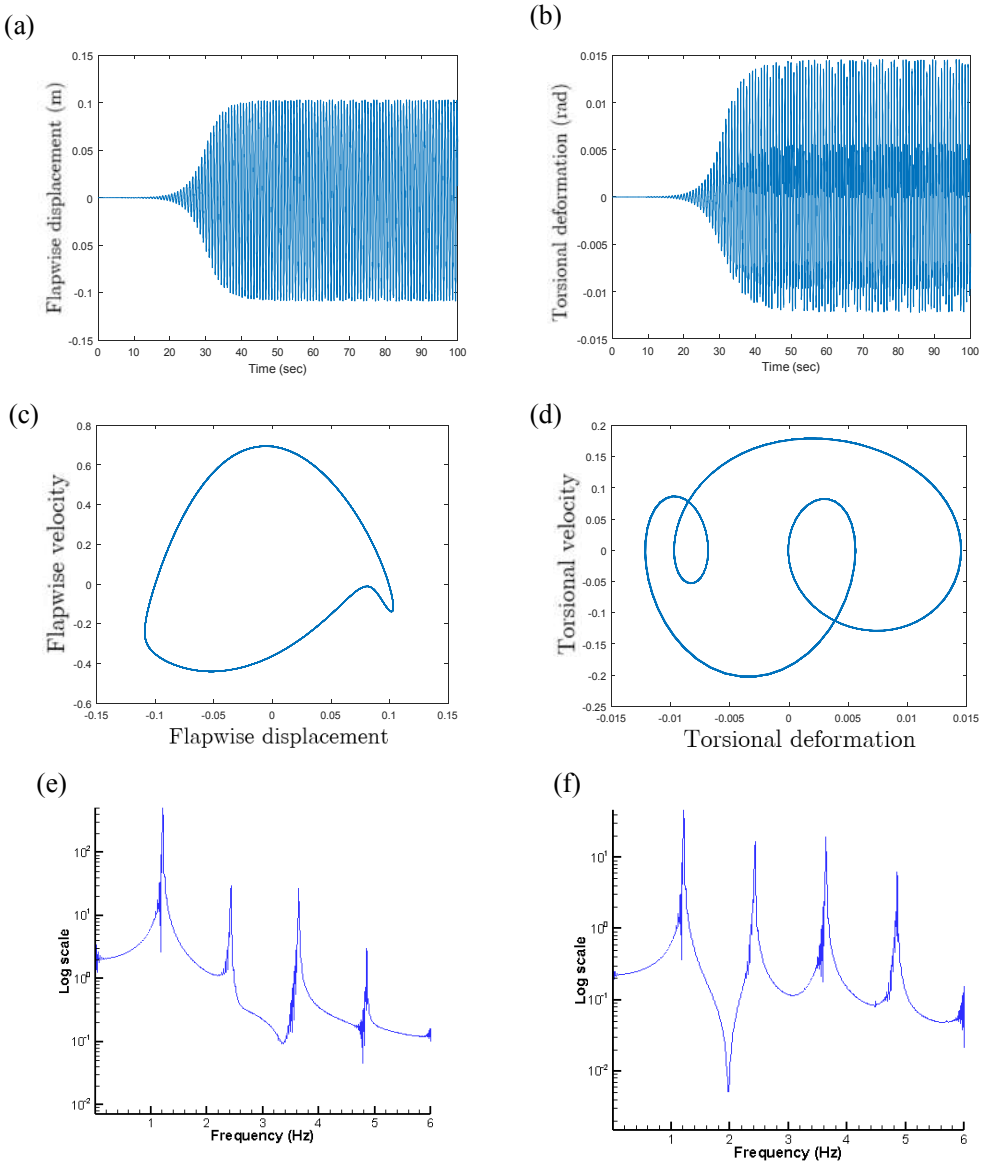

Figure 4-34 Response qualification at $\theta = -75^{\circ}, \Omega = 3.28 \frac{rad}{sec}$ a) Flapwise displacement time response, b) Torsional deformation time response, c) Flapwise displacement phase portrait, d) Torsional deformation phase portrait, e) FFT flapwise displacement, f) FFT torsional deformation

4.4 Nonlinear Aeroelastic Analysis of the Composite TWB-Wing Using Compressible Unsteady Indicial Aerodynamics

By neglecting rotating speed $(\Omega = 0)$ in Equations (4-16)-(4-48), Nonlinear aeroelastic behavior of swept *composite fix wing* shown in Figure 4-35 modeled as TWB and CAS configuration in the compressible flow regime is studied in this section.

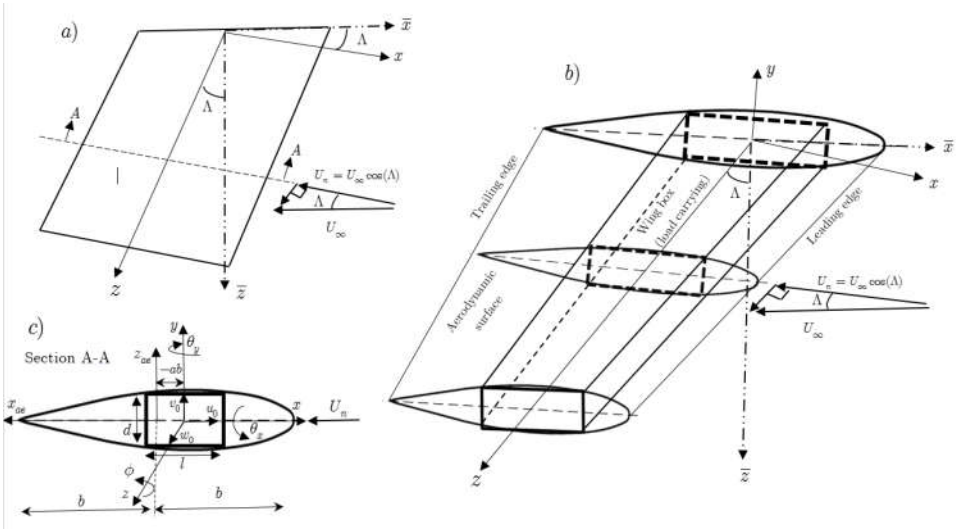

Figure 4-35 Schematic description of a swept wing modeled as a TWB with associated CAS layup configuration.

4.4.1 Nonlinear Integral Equation of Motion of the Composite Wing

For the compressible unsteady aerodynamics, only the work done by the external forces change. The last expression in the Hamilton's principle is the variation of work done by the external aerodynamic loading. For the compressible unsteady aerodynamics, variation of the external aerodynamic loading can be written as,

$$\delta W = \int_0^L \left(L_{ae\_c}(z,t)\delta v_0(z) + M_{ae\_c}(z,t)\delta\phi(z) \right) dz \tag{4-81}$$

where, $L_{ae\_c}(z,t)$ and $M_{ae\_c}(z,t)$ are the unsteady aerodynamic lift and pitching moment about the reference axis, respectively. The extended derivation of the unsteady compressible aerodynamic lift and pitching moment was explained in Chapter 3. Here, the summary of the procedure is described for swept wing model.

In the present study, explicit expressions for the unsteady aerodynamic loading $L_{ae\_c}(z,t)$ and $M_{ae\_c}(z,t)$ in the subsonic compressible flow regime in time domain, are obtained using indicial aerodynamics.

For arbitrary small motions of the thin airfoil in subsonic flow, with respect to the reference axis placed at the leading edge of the airfoil, downwash velocity corresponding to pitching and plunging motions can be expressed as,

$$w_a(x,z,t) = \hat{w}_a(z,t) - x\hat{\phi}_a(z,t) \tag{4-82}$$

where plunging and pitching motions $\hat{w}_a$ and $\hat{\phi}_a$ are given by,

$$\hat{w}_a(z,t) = \dot{v}_0 - U\cos\Lambda\phi + \frac{\partial v_0}{\partial z}U\sin\Lambda \tag{4-83}$$

$$\hat{\phi}_a(z,t) = \dot{\phi} + \frac{\partial \phi}{\partial z}U\sin\Lambda \tag{4-84}$$

It should be noted that Equations (4-83) and (4-84) are written for a swept wing configuration with the wing sweep angle Λ. Also, for the sake of brevity the free stream fluid velocity U_∞ is represented by U hereinafter.

The unsteady aerodynamic lift $L_{ae\_c}(z,t)$ and pitching moment $M_{ae\_c}(z,t)$ in the so called Theodorsen's coordinate, which is located at a distance $b(a+1)$ behind the leading edge, are then defined by Equations (4-85) and (4-86) which are obtained by employing the general law for transferring the axis of a moment of leading edge to the so called Theodorsen's axis.

$$L_{ae\_c}(z,t) = 2C_{L\phi}\rho U\cos\Lambda b^2\left[\hat{\phi}_a(z,0)\overline{\phi}_{cq}(t) + D_2(z,t)\right] - C_{L\phi}\rho U\cos\Lambda b\left[\hat{w}_a(z,0)\overline{\phi}_c(t) + D_1(z,t)\right] \tag{4-85}$$

$$M_{ae\_c}(z,t) = 4C_{L\phi}\rho U\cos\Lambda b^3\left[\hat{\phi}_a(z,0)\overline{\phi}_{cMq}(t) + D_4(z,t)\right] - 2C_{L\phi}\rho U\cos\Lambda b^2\left[\hat{w}_a(z,0)\overline{\phi}_{cM}(t) + D_3(z,t)\right] \tag{4-86}$$

where, $D_i; i = 1..4$ are defined as,

$$D_1(z,t) = \int_0^t \frac{d\hat{w}_a(z,\tau)}{d\tau}\overline{\phi}_c(t-\tau)d\tau \tag{4-87}$$

$$D_2(z,t) = \int_0^t \frac{d\hat{\phi}_a(z,\tau)}{d\tau}\overline{\phi}_{cq}(t-\tau)d\tau \tag{4-88}$$

$$D_3(z,t) = \int_0^t \frac{d\hat{w}_a(z,\tau)}{d\tau}\overline{\phi}_{cM}(t-\tau)d\tau \tag{4-89}$$

$$D_4(z,t) = \int_0^t \frac{d\hat{\phi}_a(z,\tau)}{d\tau}\overline{\phi}_{cMq}(t-\tau)d\tau \tag{4-90}$$

where, the aerodynamic indicial functions given in Equation (4-91) are defined in the reference coordinate in terms of indicial functions obtained in the leading edge.

$$\begin{aligned}
&\overline{\phi}_c(t) = \phi_c(t),\\
&\overline{\phi}_{cM}(t) = \phi_{cM}(t) + \left(\frac{a}{2}+\frac{1}{2}\right)\phi_c(t),\\
&\overline{\phi}_{cq}(t) = \phi_{cq}(t) - \left(\frac{a}{2}+\frac{1}{2}\right)\phi_c(t),\\
&\overline{\phi}_{cMq}(t) = \phi_{cMq}(t) + \left(\frac{a}{2}+\frac{1}{2}\right)\left(\phi_{cq}(t) - \phi_{cM}(t)\right) - \left(\frac{a}{2}+\frac{1}{2}\right)^2\phi_c(t).
\end{aligned} \tag{4-91}$$

where, the coefficients of the exponential representations of the indicial functions defined in leading edge are obtained as,

$$\phi_{c,cq,cM,cMq}(M,\tau) = \left[\alpha_{0c,0cq,0cM,0cMq}(M) - \sum_{i=1}^{3}\alpha_{ic,icq,icM,icMq}(M)\exp(-\beta_i\tau)\right]H(\tau) \tag{4-92}$$

where, $i = 1,2,3$

Once the Mach dependent base coefficients $(\alpha_{ic}, \alpha_{icM}, \alpha_{icq}, \alpha_{icMq}(M), i = 0,1,2,3)$ of the lift and the moment compressible indicial functions for the plunging and pitching motion with respect to the coordinate system established at the leading edge of the airfoil are determined using method introduced in Chapter 3 for any Mach number, base coefficients with respect to the axis located at $b(a+1)$ behind the leading edge can be determined utilizing the relations given by Equation (4-93) .

$$\begin{aligned}
\overline{\alpha}_{ic} &= \alpha_{ic}, \\
\overline{\alpha}_{icM} &= \alpha_{icM} + \left(\frac{a}{2} + \frac{1}{2}\right)\alpha_{ic}, \\
\overline{\alpha}_{icq} &= \alpha_{icq} - \left(\frac{a}{2} + \frac{1}{2}\right)\alpha_{ic}, \\
\overline{\alpha}_{icMq} &= \alpha_{icMq} + \left(\frac{a}{2} + \frac{1}{2}\right)\left(\alpha_{icq} - \alpha_{icM}\right) - \left(\frac{a}{2} + \frac{1}{2}\right)^2 \alpha_{ic}.
\end{aligned} \tag{4-93}$$

The integral expressions Equations (4-87)-(4-90) which appear in the lift and moment expressions, are expressed again by substituting the coefficients of the indicial functions Equation (4-93) into Equations (4-87)-(4-90),

$$D_1(z,t) = \overline{\alpha}_{0c}\hat{w}_a(z,t) - \sum_{i=1}^{3}\overline{\alpha}_{ic}(M)B_{ic}(z,t) \tag{4-94}$$

$$D_2(z,t) = \overline{\alpha}_{0cq}\hat{\phi}_a(z,t) - \sum_{i=1}^{3}\overline{\alpha}_{icq}(M)B_{icq}(z,t) \tag{4-95}$$

$$D_3(z,t) = \overline{\alpha}_{0cM}\hat{w}_a(z,t) - \sum_{i=1}^{3}\overline{\alpha}_{icM}(M)B_{icM}(z,t) \tag{4-96}$$

$$D_4(z,t) = \overline{\alpha}_{0cMq}\hat{\phi}_a(z,t) - \sum_{i=1}^{3}\overline{\alpha}_{icMq}(M)B_{icMq}(z,t) \tag{4-97}$$

When the Leibniz integral rule is applied to the integrals involving the exponential terms, it can be shown that the aerodynamic lag terms $B_{ic,icq,icM,icMq}(z,t)$ are defined by Equations .

$$\dot{B}_{ic}\left(z,t\right)+(\beta_i\frac{U\cos\Lambda}{b})B_{ic}\left(z,t\right)=\frac{d\hat{w}_a\left(z,t\right)}{dt};i=1,2,3 \tag{4-98}$$

$$\dot{B}_{icq}\left(z,t\right)+(\beta_i\frac{U\cos\Lambda}{b})B_{icq}\left(z,t\right)=\frac{d\hat{\phi}_a\left(z,t\right)}{dt};i=1,2,3 \tag{4-99}$$

$$\dot{B}_{icM}\left(z,t\right)+(\beta_i\frac{U\cos\Lambda}{b})B_{icM}\left(z,t\right)=\frac{d\hat{w}_a\left(z,t\right)}{dt};i=1,2,3 \tag{4-100}$$

$$\dot{B}_{icMq}\left(z,t\right)+(\beta_i\frac{U\cos\Lambda}{b})B_{icMq}\left(z,t\right)=\frac{d\hat{\phi}_a\left(z,t\right)}{dt};i=1,2,3 \tag{4-101}$$

Finally, assuming that the wing is at rest initially, the explicit expressions of the unsteady lift and moment in compressible flow regime are given by Equations (4-102) and (4-103).

$$\begin{aligned}L_{ae\_c}(z,t)=2C_{L\phi}\rho U\cos\Lambda b^2\left[\overline{\alpha}_{0cq}\hat{\phi}_a\left(z,t\right)-\sum_{i=1}^{3}\overline{\alpha}_{icq}B_{icq}\left(z,t\right)\right]-\\ C_{L\phi}\rho U\cos\Lambda b\left[\overline{\alpha}_{0c}\hat{w}_a\left(z,t\right)-\sum_{i=1}^{3}\overline{\alpha}_{ic}B_{ic}\left(z,t\right)\right]\end{aligned} \tag{4-102}$$

$$\begin{aligned}M_{ae\_c}(z,t)=4C_{L\phi}\rho U\cos\Lambda b^3\left[\overline{\alpha}_{0cMq}\hat{\phi}_a\left(z,t\right)-\sum_{i=1}^{3}\overline{\alpha}_{icMq}B_{icMq}\left(z,t\right)\right]-\\ 2C_{L\phi}\rho U\cos\Lambda b^2\left[\overline{\alpha}_{0cM}\hat{w}_a\left(z,t\right)-\sum_{i=1}^{3}\overline{\alpha}_{icM}B_{icM}\left(z,t\right)\right]\end{aligned} \tag{4-103}$$

The integral equation of motion for the CAS configuration with square and cubic nonlinearity is obtained after a rather cumbersome manipulation as in the given in Equation (4-16). To include 3D effects of the finite span swept wing, lift curve slope is obtained from the Diederich general formula as [38],

$$C_{L\phi}=\frac{c_{l\phi}\cos\Lambda_e}{\sqrt{1-M^2}}\frac{AR\sqrt{1-M^2}}{AR\sqrt{1-M^2}\sqrt{1+\left(\frac{c_{l\phi}\cos\Lambda_e}{\pi AR\sqrt{1-M^2}}\right)^2}+\frac{c_{l\phi}\cos\Lambda_e}{\pi}} \tag{4-104}$$

where,

$$\cos\Lambda_e = \frac{\sqrt{1-M^2}}{\sqrt{1-M^2\cos^2\Lambda}}\cos\Lambda \tag{4-105}$$

4.4.2 Nonlinear Aeroelastic Analysis of the Composite Wing Using Compressible Indicial Function

Nonlinear aeroelastic analysis is conducted by means of a Ritz based solution methodology utilizing the mode shapes of the linear structural system to approximate the spatial variation of the degrees of freedom of the thin walled beam. It should be noted that, determination of the mode shapes of the linear system is exactly same as defined in the incompressible case explained in Section 4.2.1.1. Equation (4-106) gives the reduced modal matrix $\boldsymbol{R}$, which is extracted from the eigenvalue analysis performed in 4.2.1.1, for the dominant m right eigenvectors corresponding to the translational and rotational degrees of freedom of the linear system.

$$R_{6N\times m} = \begin{bmatrix} R^{u^T}_{m\times N} & R^{v^T}_{m\times N} & R^{w^T}_{m\times N} & R^{x^T}_{m\times N} & R^{y^T}_{m\times N} & R^{\phi^T}_{m\times N} \end{bmatrix} \tag{4-106}$$

One can then construct a reduced order model by expressing any of the six degrees freedom $\Delta \in \{u_0, v_0, w_0, \theta_x, \theta_y, \phi\}$ in terms of the relevant trial function ψ^{Δ}, relevant reduced modal matrix $\boldsymbol{R}^{\Delta}$ which is composed of dominant m right eigenvectors and the modal coordinates as,

$$\Delta(z,t) = \psi^{\Delta^T} R^{\Delta}\vartheta(t) \tag{4-107}$$

Where $\vartheta(t)$ is the generalized modal coordinate vector of dimension of $m\times 1$, $\boldsymbol{R}^{\Delta}$ is the reduced modal matrix of dimension $N\times m$ composed of dominant m right eigenvectors corresponding to any of the degrees of freedom Δ, and ψ^{Δ} is the vector of trial functions, of dimension $N\times 1$, corresponding to any of the degrees of freedom Δ.

For the nonlinear system, the test functions for any of the degrees of freedom, which are the variations of the degrees of freedom, are defined by the premultiplication of the the vector of the trial functions ψ^{Δ} by the reduced modal matrix $\boldsymbol{L}^{\Delta T}$ which is composed of dominant m left eigenvectors corresponding to the translational and rotational degrees of freedom.

$$\delta\Delta(z) = L^{\Delta^T}\psi^{\Delta} \tag{4-108}$$

Modal expansions of the degrees of freedom of the TWB (Equation (4-107)) and the variations of the degrees of freedom (Equation (4-108)) are substituted into the integral form of the governing equations of motion Equation (4-16) , resulting in the reduced order system of nonlinear equations,

$$\boldsymbol{M}_{tc}\ddot{\vartheta}(t) + \boldsymbol{C}_{tc}\dot{\vartheta}(t) + \boldsymbol{K}_{tc}\vartheta(t) - Z_c(t) + \bar{H}^{NL}(t) = 0 \tag{4-109}$$

Where $\boldsymbol{M}_{tc}, \boldsymbol{C}_{tc}, \boldsymbol{K}_{tc}$ are the reduced order mass, aerodynamic damping and stiffness matrices of dimension $m \times m$, and Z_c and $\bar{H}_{NL}$ are the reduced order vectors of dimension $m \times 1$ and they include the aerodynamic lag states and the nonlinear terms, respectively. In the resulting reduced order system of equations, if the modal matrices composed of the left $(\boldsymbol{L}^T)$ and the right eigenvectors $(\boldsymbol{R})$ are factored out, reduced order mass, damping and stiffness matrices in Equation (4-109) are defined by,

$$\begin{aligned} \boldsymbol{M}_{tc} &= L^T(\boldsymbol{M}_s + \boldsymbol{M}_{ae\_c})R \\ \boldsymbol{C}_{tc} &= L^T\boldsymbol{C}_{ae-c}R \\ \boldsymbol{K}_{tc} &= L^T(\boldsymbol{K}_s + \boldsymbol{K}_{ae\_c})R \end{aligned} \tag{4-110}$$

where the structural mass $(\boldsymbol{M}_s)$ and stiffness $(\boldsymbol{K}_s)$ and the aerodynamic mass $(\boldsymbol{M}_{ae\_c})$, stiffness $(\boldsymbol{K}_{ae\_c})$ and damping $(\boldsymbol{C}_{ae\_c})$ matrices of dimension $6N \times 6N$ are defined in Appendix D. It should be noted that the aerodynamic damping matrix $\boldsymbol{C}_{ae\_c}$ in Equation (4-110) does not include the aerodynamic lag terms defined in Equations

(4-102) and (4-103), and these terms are collected in the aerodynamic lag vector Z_c. Aerodynamic lag vector Z_c is derived from the virtual work done by the aerodynamic lag states $(B_{ic}, B_{icq}, B_{icM}, B_{icMq})$ in the unsteady lift and moment expressions in Equations (4-102) and (4-103). In the integral equation of motion Equation (2-16), virtual work done by the unsteady lift and moment due to aerodynamic lag states is given by,

$$\int_0^L \left\{ \left[(L_{ae\_c})_{c\_Lag} + (L_{ae\_c})_{cq\_Lag} \right] \delta v_0 + \left[(M_{ae\_c})_{cM\_Lag} + (M_{ae\_c})_{cMq\_Lag} \right] \delta\phi \right\} dz \quad (4\text{-}111)$$

where the unsteady lift and moment due to aerodynamic lag states are given by Equations (4-112)-(4-115).

$$(L_{ae\_c})_{c\_Lag}(z,t) = -C_{L\phi}\rho U \cos\Lambda b \left(\bar{\alpha}_{1c} B_{1c}(z,t) + \bar{\alpha}_{2c} B_{2c}(z,t) + \bar{\alpha}_{3c} B_{3c}(z,t) \right) \quad (4\text{-}112)$$

$$(L_{ae\_c})_{cq\_Lag}(z,t) = 2C_{L\phi}\rho U \cos\Lambda b^2 \left(\bar{\alpha}_{1cq} B_{1cq}(z,t) + \bar{\alpha}_{2cq} B_{2cq}(z,t) + \bar{\alpha}_{3cq} B_{3cq}(z,t) \right) \quad (4\text{-}113)$$

$$(M_{ae\_c})_{cM\_Lag}(z,t) = 2C_{L\phi}\rho U \cos\Lambda b^2 \left(\bar{\alpha}_{1cM} B_{1cM}(z,t) + \bar{\alpha}_{2cM} B_{2cM}(z,t) + \bar{\alpha}_{3cM} B_{3cM}(z,t) \right) \quad (4\text{-}114)$$

$$(M_{ae\_c})_{cMq\_Lag}(z,t) = 4C_{L\phi}\rho U \cos\Lambda b^3 \left(\bar{\alpha}_{1cMq} B_{1cMq}(z,t) + \bar{\alpha}_{2cM} B_{2cMq}(z,t) + \bar{\alpha}_{3cMq} B_{3cMq}(z,t) \right) \quad (4\text{-}115)$$

Following the substitution of the unsteady lift and moment due to aerodynamic lag states in Equation (4-111), and expressing the variations δv_0 and $\delta\phi$ by Equation (4-108), after manipulations aerodynamic lag vector Z_c is obtained as,

$$Z_c(t) =$$

$$\begin{bmatrix} \overline{\alpha}_{1c}I & \overline{\alpha}_{2c}I & \overline{\alpha}_{3c}I & \overline{\alpha}_{1cq}I & \overline{\alpha}_{2cq}I & \overline{\alpha}_{3cq}I & \cdots \\ \cdots & \overline{\alpha}_{1cM}I & \overline{\alpha}_{2cM}I & \overline{\alpha}_{3cM}I & \overline{\alpha}_{1cMq}I & \overline{\alpha}_{2cMq}I & \overline{\alpha}_{3cMq}I \end{bmatrix} \begin{Bmatrix} \hat{B}_{1c}(t) \\ \hat{B}_{2c}(t) \\ \hat{B}_{3c}(t) \\ \vdots \\ \hat{B}_{1cMq}(t) \\ \hat{B}_{2cMq}(t) \\ \hat{B}_{3cMq}(t) \end{Bmatrix} \tag{4-116}$$

Where $\boldsymbol{I}$ is the identity matrix of order $m \times m$ and $\hat{B}_{ic}, \hat{B}_{icq}, \hat{B}_{icM}, \hat{B}_{icMq}, i = 1,2,3$ are vectors of order $m \times 1$ defined by,

$$\hat{B}_{ic}(t) = \left\{ \int_0^L C_{L\phi} \rho U \cos\Lambda b \left(L^{v^T} \psi^v \right) B_{ic}(z,t) dz \right\}, \qquad i = 1,2,3 \tag{4-117}$$

$$\hat{B}_{icq}(t) = \left\{ \int_0^L 2C_{L\phi} \rho U \cos\Lambda b^2 \left(L^{v^T} \psi^v \right) B_{icq}(z,t) dz \right\}, \qquad i = 1,2,3 \tag{4-118}$$

$$\hat{B}_{icM}(t) = \left\{ \int_0^L 2C_{L\phi} \rho U \cos\Lambda b^2 \left(L^{\phi^T} \psi^\phi \right) B_{icM}(z,t) dz \right\}, \qquad i = 1,2,3 \tag{4-119}$$

$$\hat{B}_{icMq}(t) = \left\{ \int_0^L 4C_{L\phi} \rho U \cos\Lambda b^3 \left(L^{\phi^T} \psi^\phi \right) B_{icMq}(z,t) dz \right\}, \qquad i = 1,2,3 \tag{4-120}$$

where the terms inside the curly brackets are vectors of dimension $m \times 1$, so they are the transformed aerodynamic lag state vectors $\hat{B}_{ic}, \hat{B}_{icq}, \hat{B}_{icM}, \hat{B}_{icMq}, i = 1,2,3$.

The reduced order vector of nonlinear terms $\overline{H}^{NL}$ in Equation (4-109) are defined by Equation Equation (4-70). With the introduction of the aerodynamic lag states, there are $12m$ number of additional unknowns in Equation (4-109), and to perform the nonlinear aeroelastic analysis of the composite wing, additional $12m$ number of additional equations are needed. To this end, the system of nonlinear equations Equation (4-109) is augmented by the differential equations that the aerodynamic lag states $B_{ic}(z,t), B_{icq}(z,t), B_{icM}(z,t), B_{icMq}(z,t), i = 1,2,3$ must satisfy (Equation (4-98)-

(4-101)). Since in the system of nonlinear equations, given by Equation (4-109), aerodynamic lag states are defined by the transformed aerodynamic lag state vectors $\hat{B}_{ic}(t), \hat{B}_{icq}(t), \hat{B}_{icM}(t), \hat{B}_{icMq}(t), i = 1,2,3$, Equations (4-98)-(4-101) are manipulated such that it is also expressed in terms of the the transformed vectors $\hat{B}_{ic}(t), \hat{B}_{icq}(t), \hat{B}_{icM}(t), \hat{B}_{icMq}(t), i = 1,2,3$. For this purpose, both sides of Equation (4-98)-(4-101) are multiplied by the expressions given in Equation (4-121)-(4-124),

$$C_{L\phi}\rho U \cos\Lambda b\left(\delta v_0\right) \tag{4-121}$$

$$2C_{L\phi}\rho U \cos\Lambda b^2\left(\delta v_0\right) \tag{4-122}$$

$$2C_{L\phi}\rho U \cos\Lambda b^2\left(\delta\phi\right) \tag{4-123}$$

$$4C_{L\phi}\rho U \cos\Lambda b^3\left(\delta\phi\right) \tag{4-124}$$

the variations δv_0 and $\delta\phi$ are expressed by Equation (4-108), modal expansions of the degrees of freedom (Equation (4-107)) which appear in the right hand side of Equations (4-98)-(4-101) are substituted, and both sides of Equations (4-98)-(4-101) are integrated along the span of the wing as shown in Equations (4-125)-(4-128).

$$\int_0^L C_{L\phi}\rho U \cos\Lambda b\left(L^{v^T}\psi^v\right)\left(\dot{B}_{ic}(z,t) + \beta_i \frac{U\cos\Lambda}{b} B_{ic}(z,t)\right)dz = RHS_c \qquad i = 1,2,3 \tag{4-125}$$

$$\int_0^L 2C_{L\phi}\rho U \cos\Lambda b^2\left(L^{v^T}\psi^v\right)\left(\dot{B}_{icq}(z,t) + \beta_i \frac{U\cos\Lambda}{b} B_{icq}(z,t)\right)dz = RHS_{cq} \qquad i = 1,2,3 \tag{4-126}$$

$$\int_0^L 2C_{L\phi}\rho U \cos\Lambda b^2\left(L^{\phi^T}\psi^\phi\right)\left(\dot{B}_{icM}(z,t) + \beta_i \frac{U\cos\Lambda}{b} B_{icM}(z,t)\right)dz = RHS_{cM} \qquad i = 1,2,3 \tag{4-127}$$

$$\int_0^L 4C_{L\phi}\rho U\cos\Lambda b^3\left(L^{\phi^T}\psi^{\phi}\right)\left(\dot{B}_{icMq}(z,t)+\beta_i\frac{U\cos\Lambda}{b}B_{icMq}(z,t)\right)dz = RHS_{cMq} \qquad (4\text{-}128)$$
$$i=1,2,3$$

After manipulations the right hand side RHS in Equations (4-125)-(4-128) can be brought into the form given by,

$$RHS_c = D_{1c}\dot{\vartheta}(t) + D_{2c}\ddot{\vartheta}(t) \qquad (4\text{-}129)$$

$$RHS_{cq} = D_{1cq}\dot{\vartheta}(t) + D_{2cq}\ddot{\vartheta}(t) \qquad (4\text{-}130)$$

$$RHS_{cM} = D_{1cM}\dot{\vartheta}(t) + D_{2cM}\ddot{\vartheta}(t) \qquad (4\text{-}131)$$

$$RHS_{cMq} = D_{1cMq}\dot{\vartheta}(t) + D_{2cMq}\ddot{\vartheta}(t) \qquad (4\text{-}132)$$

Where $\boldsymbol{D}_{1c},\boldsymbol{D}_{2c},\boldsymbol{D}_{1cq},\boldsymbol{D}_{2cq},\boldsymbol{D}_{1cM},\boldsymbol{D}_{2cM},\boldsymbol{D}_{1cMq},\boldsymbol{D}_{2cMq}$ are the $m\times m$ coefficient matrices defined by,

$$\begin{aligned}\left[\boldsymbol{D}_{1c}\right] &= \int_0^L C_{L\phi}\rho\left(U\cos\Lambda\right)^2 b\left[L^{v^T}\psi^v\psi^{\phi^T}R^{\phi} - \tan(\Lambda)L^{v^T}\psi^v\psi'^{\phi^T}R^{\phi}\right]dz\\ \left[\boldsymbol{D}_{2c}\right] &= -\int_0^L C_{L\phi}\rho U\cos\Lambda b\left[L^{v^T}\psi^v\psi^{v^T}R^{v}\right]dz\end{aligned} \qquad (4\text{-}133)$$

$$\begin{aligned}\left[\boldsymbol{D}_{1cq}\right] &= \int_0^L 2C_{L\phi}\rho(U\cos\Lambda)^2 b^2\left[\tan(\Lambda)L^{v^T}\psi^v\psi'^{\phi^T}R^{\phi}\right]dz\\ \left[\boldsymbol{D}_{2cq}\right] &= \int_0^L 2C_{L\phi}\rho U\cos\Lambda b^2\left[L^{v^T}\psi^v\psi'^{\phi^T}R^{\phi}\right]dz\end{aligned} \qquad (4\text{-}134)$$

$$\begin{aligned}\left[\boldsymbol{D}_{1cM}\right] &= \int_0^L 2C_{L\phi}\rho\left(U\cos\Lambda\right)^2 b^2\left[L^{\phi^T}\psi^{\phi}\psi^{\phi^T}R^{\phi} - \tan(\Lambda)L^{\phi^T}\psi^{\phi}\psi'^{v^T}R^{v}\right]dz\\ \left[\boldsymbol{D}_{2cM}\right] &= -\int_0^L 2C_{L\phi}\rho U\cos\Lambda b^2\left[L^{\phi^T}\psi^{\phi}\psi^{v^T}R^{v}\right]dz\end{aligned} \qquad (4\text{-}135)$$

$$\left[\boldsymbol{D}_{1cMq}\right] = \int_0^L 4C_{L\phi}\rho\left(U\cos\Lambda\right)^2 b^3\left[\tan(\Lambda)L^{\phi^T}\psi^{\phi}\psi'^{\phi^T}R^{\phi}\right]dz$$
$$\left[\boldsymbol{D}_{2cMq}\right] = \int_0^L 4C_{L\phi}\rho U\cos\Lambda b^3\left[L^{\phi^T}\psi^{\phi}\psi'^{\phi^T}R^{\phi}\right]dz \quad (4\text{-}136)$$

Comparing Equations (4-117)-(4-120) and Equations (4-125)-(4-128), it is evident that since the terms multipying the time derivative of the aerodynamic lag state $B_{ic}(z,t), B_{icq}(z,t), B_{icM}(z,t), B_{icMq}(z,t), i = 1,2,3$ in Equations (4-117)-(4-120) do not depend on time, Equations (4-125)-(4-128) can be written as,

$$\dot{\hat{B}}_{ic}(t) + \beta_i \frac{U\cos\Lambda}{b}\hat{B}_{ic}(t) = D_{1c}\dot{\vartheta}(t) + D_{2c}\ddot{\vartheta}(t) \qquad i = 1,2,3 \qquad (4\text{-}137)$$

$$\dot{\hat{B}}_{icq}(t) + \beta_i \frac{U\cos\Lambda}{b}\hat{B}_{icq}(t) = D_{1cq}\dot{\vartheta}(t) + D_{2cq}\ddot{\vartheta}(t) \qquad i = 1,2,3 \qquad (4\text{-}138)$$

$$\dot{\hat{B}}_{icM}(t) + \beta_i \frac{U\cos\Lambda}{b}\hat{B}_{icM}(t) = D_{1cM}\dot{\vartheta}(t) + D_{2cM}\ddot{\vartheta}(t) \qquad i = 1,2,3 \qquad (4\text{-}139)$$

$$\dot{\hat{B}}_{icMq}(t) + \beta_i \frac{U\cos\Lambda}{b}\hat{B}_{icMq}(t) = D_{1cMq}\dot{\vartheta}(t) + D_{2cMq}\ddot{\vartheta}(t) \qquad i = 1,2,3 \qquad (4\text{-}140)$$

where $\hat{B}_{ic}(t), \hat{B}_{icq}(t), \hat{B}_{icM}(t), \hat{B}_{icMq}(t), i = 1,2,3$ are the transformed aerodynamic lag state vector of dimension $m \times 1$ defined by Equations (4-117)-(4-120). It should be noted that in passing from Equations (4-125)-(4-128) to Equations (4-137)-(4-140), it is assumed that the semi-chord length b in the U/b term is constant along the span of the wing, which is so for rectangular wings. For tapered wings, it suffices to use the mean semi-chord length only in the U/b term in Equations (4-137)-(4-140).

By augmenting Equation (4-109) with Equations (4-137)-(4-140), the final form of the nonlinear aeroelastic system of equations of the CAS configuration composite wing modeled as TWB, compressible aerodynamics is obtained in state space representation as shown in Equation (4-141),

$$\begin{bmatrix} D_{CM} & 0 \\ D_d & -I \end{bmatrix}_{14m\times 14m} \frac{d}{dt}\begin{Bmatrix} \tilde{\vartheta} \\ \tilde{B} \end{Bmatrix}_{14m\times 1} + \begin{bmatrix} D_K & D_\alpha \\ 0 & D_\beta \end{bmatrix}_{14m\times 14m} \begin{Bmatrix} \tilde{\vartheta} \\ \tilde{B} \end{Bmatrix}_{14m\times 1} + \begin{Bmatrix} \bar{H}_{NL} \\ 0 \end{Bmatrix}_{14m\times 1} = 0 \quad (4\text{-}141)$$

where,

$$\left\{\tilde{\vartheta}\right\}_{2m\times 1} = \begin{Bmatrix} \vartheta \\ \dot{\vartheta} \end{Bmatrix}, \qquad \left\{\tilde{B}\right\}_{12m\times 1} = \begin{Bmatrix} \hat{B}_{1c} \\ \vdots \\ \hat{B}_{3cMq} \end{Bmatrix} \quad (4\text{-}142)$$

$$\left[D_{CM}\right] = \begin{bmatrix} C_t & M_t \\ I & 0 \end{bmatrix}_{2m\times 2m}, \qquad \left[D_K\right] = \begin{bmatrix} K_t & 0 \\ 0 & -I \end{bmatrix}_{2m\times 2m} \quad (4\text{-}143)$$

$$\left[D_d\right]_{12m\times 2m} = \begin{bmatrix} \begin{bmatrix} I_{m\times m} \\ \vdots \\ I_{m\times m} \end{bmatrix}_{3m\times m} & \left[D_{1c} \quad D_{2c}\right]_{m\times 2m} \\ \begin{bmatrix} I_{m\times m} \\ \vdots \\ I_{m\times m} \end{bmatrix}_{3m\times m} & \left[D_{1cq} \quad D_{2cq}\right]_{m\times 2m} \\ \begin{bmatrix} I_{m\times m} \\ \vdots \\ I_{m\times m} \end{bmatrix}_{3m\times m} & \left[D_{1cM} \quad D_{2cM}\right]_{m\times 2m} \\ \begin{bmatrix} I_{m\times m} \\ \vdots \\ I_{m\times m} \end{bmatrix}_{3m\times m} & \left[D_{1cMq} \quad D_{2cMq}\right]_{m\times 2m} \end{bmatrix} \quad (4\text{-}144)$$

$$\left[\bar{D}_\beta\right]_{3m\times 3m} = \begin{bmatrix} \left(-\beta_1 U_n/b\right) I_{m\times m} & 0 & 0 \\ 0 & \left(-\beta_2 U_n/b\right) I_{m\times m} & 0 \\ 0 & 0 & \left(-\beta_3 U_n/b\right) I_{m\times m} \end{bmatrix}, \quad (4\text{-}145)$$

$$\left[D_\beta\right]_{12m\times 12m} = \begin{bmatrix} \bar{D}_\beta & 0 & 0 & 0 \\ 0 & \bar{D}_\beta & 0 & 0 \\ 0 & 0 & \bar{D}_\beta & 0 \\ 0 & 0 & 0 & \bar{D}_\beta \end{bmatrix}$$

$$\left[D_{\alpha}\right]_{2m\times 12m} = \begin{bmatrix} \left[\alpha_{1c} I_{m\times m} \quad \cdots \quad \alpha_{3cMq} I_{m\times m}\right]_{m\times 12m} \\ \left[0\right]_{m\times 12m} \end{bmatrix} \tag{4-146}$$

In more compact form, Equation (4-141) is in the form,

$$A\dot{q} + Bq + F^{NL} = 0 \tag{4-147}$$

Where q is the state vector of dimension $14m \times 1, F^{NL}$ is the vector of nonlinear terms of dimension $14m \times 1$, and $\boldsymbol{A}$ and $\boldsymbol{B}$ are $14m \times 14m$ coefficient matrices defined in Equation (4-141).

Nonlinear aeroelastic respose of the composite wing modeled as TWB is performed in time domain by the direct integration of Equation (4-147) by the Runge-Kutta method for the prescribed initial conditions. Time history plots are then processed for nonlinear aeroelastic stability analysis.

4.4.3 Numerical Results and Discussions

In this section, structural and unsteady aerodynamics models described are utilized along with the Ritz based solution methodology to obtain various results. As the first case, numerical verification studies are conducted to show the validity of the whole model and then linear and nonlinear results are presented for different TWB configurations.

4.4.3.1 Validation Studies

The structural TWB linear model has already been verified in Chapter 2 by comparing the natural frequencies of the stationary CAS configuration TWB with those determined by the finite element solution performed by MSC Nastran.

Unsteady aerodynamics model based on the representation of the lift and the moment by the compressible indicial functions approximated by the aerodynamic lag states is verified by the well-known experimental study of Barmby et al. [125]. The experimental flutter speed and flutter frequency results obtained for the aluminum alloy wing of NACA 16-1010 profile in the subsonic compressible flow regime are compared with the predictions of the present study. In the model used in the verification study, structural model is based on geometrically linear equations and exactly the same Ritz based methodology described for the nonlinear aeroelastic analysis of the composite wing is used. In this respect, seven trial functions $(N = 7)$ are used in the series given in Equation (4-52) for the bending (v_0) and torsional (ϕ) degrees of freedom and first seven $(m = 7)$ eigenfunctions are used for the modal reduction of the nonlinear system. Flutter speed and frequency comparisons are made for the wing models given in Table 4-10. In order to adapt the present TWB structural model to the wing models of Barmby et al. [125], degrees of freedom are restricted to the flapwise bending deflection (v_0) and the elastic twist (ϕ) and the assignments given by Equation (4-79) are made for the stiffness and mass properties. It should be noted that the "*a"* parameter in Table 4-10 specifies the nondimensional offset between the shear center and the mid-chord, as shown in Figure 4-35. A negative value of the "*a"* parameter indicates that the shear center is forward of the mid chord. Table 4-11 compares the wind tunnel results of flutter Mach numbers and flutter frequencies with the proposed compressible indicial aerodynamics formulation. Results given in Table 4-11 show that present linear aeroelastic analysis results are in good agreement with the experimental results of Barmby et al. [125] for all variants of the TWB models including the effect of the wing sweep angle Λ.

Table 4-10 Geometric and material properties of the wings used for the validation study [125]

Model	$EI(Nm^2)$	$GJ(Nm^2)$	$L(m)$	$b(m)$	a	$I_\alpha(Kgm^2)$	$m_l(Kg\ /\ m)$	$\Lambda(\deg)$
40A	15	10.15	0.63	0.0509	-0.2	0.00024	0.339	0
40A	15	10.15	0.63	0.0509	-0.2	0.00024	0.338	0
40D	14.5	9.55	0.63	0.0509	-0.21	0.00023	0.322	15
-	94.6	26.5	0.574	0.0713	-0.08	0.00054	0.464	45
73	16.8	15.6	0.66	0.0509	-0.12	0.00022	0.476	30
72	22.4	11.7	0.66	0.0509	-0.12	0.00024	0.524	15
25A	18.5	5.6	0.813	0.0509	-0.2	0.00013	0.138	60
15	54.7	13	0.813	0.0509	-0.08	0.00017	0.289	60
12	156.8	41.3	0.422	0.0978	-0.07	0.00014	0.637	15
15	54.7	13	0.813	0.0509	-0.08	0.00017	0.289	60
13	152.4	31.82	0.462	0.0713	-0.08	0.00051	0.439	30
14	94.62	26.49	0.574	0.0713	-0.08	0.00054	0.461	45
24	30.96	8.06	0.553	0.0719	-0.02	0.00038	0.238	45

Table 4-11 Critical Mach numbers and frequencies of different wing models.

Model	**Flutter Mach Number**		**Flutter Frequency**	
	Experimental	Present	Experimental	Present
40A	0.5	0.526	61	63
40A	0.45	0.475	56	59
40D	0.51	0.482	62	59
-	0.81	0.788	37	41
73	0.69	0.708	24	27
72	0.59	0.61	30	34
25A	0.79	0.766	29	26
15	0.51	0.537	37	41
12	0.79	0.812	55	59
15	0.62	0.637	36	40
13	0.68	0.704	61	63
14	0.56	0.577	54	57
24	0.54	0.556	49	53

4.4.3.2 Linear Aeroelastic Analysis of Composite Wings

Prior to the nonlinear aeroelastic simulations of composite wings, linear aeroelastic analyses are performed to predict the stability margins for a better evaluation of nonlinear aeroelastic simulation results. The Ritz-based methodology is followed in the linear aeroelastic analysis of CAS TWBs configuration. Nine trial functions $(N = 9)$ are used in the expansions given in Equation (4-52) for the all six degrees of freedom. For the modal reduction, the number of mode shapes to be included is found to be 7 $(m = 7)$ for a reasonable convergence. Setting the nonlinear vector $F^{NL} = 0$ in Equation (4-147), linear aeroelastic system of equations is obtained. Considering $q = q_0 e^{\lambda t}$ where λ is the complex valued eigenvalue of the aeroelastic system, one obtains the standard form of the generalized eigenvalue problem. Geometric and material properties of thin walled beams studied, are given in Table 4-12.

Table 4-12 Geometric and material properties of composite wings used in aeroelastic numerical studies.

Material properties		**Geometric properties**	
$E_1\ (GPa)$	206.8e9	$L\ (m)$	10
$E_2\ (GPa)$	5.17e9	$l\ (m)$	0.757
$E_3\ (GPa)$	5.17e9	$d\ (m)$	0.12
$G_{12}\ (GPa)$	3.1e9	$h\ (m)$	0.03
$G_{13}\ (GPa)$	3.1e9	$\Lambda\ (deg.)$	15,30,45
$G_{23}\ (GPa)$	2.55e9	$\theta\ (deg.)$	-75, - 45
$\vartheta_{12} = \vartheta_{23}$	0.25	$\rho\ (kg/m^3)$	1528
ϑ_{13}	0.25	a	-0.3

To see the effect of compressibility on the aeroelastic instability margins, linear aeroelastic analysis of the composite wings has also been performed by incompressible indicial unsteady aerodynamics utilizing approximation of the Wagner's function by two aerodynamic lag terms and also by compressible indicial unsteady aerodynamics utilizing approximation of the indicial functions by a total of twelve aerodynamic lag terms. Table 4-13 presents the critical Mach numbers and corresponding critical frequencies for unswept wings ($\Lambda = 0$) for four different fiber angles of the CAS

configuration TWB. From the results given in Table 4-13, it is evident that compressibility accounts for reduction in aeroelastic instability speeds. Actually, instability speeds obtained by incompressible unsteady aerodynamics are not conservative. From Table 4-13, it is also seen that fiber angle of the CAS configuration TWB has a significant effect on the aeroelastic instability speed. For fiber angles other than -90°, the aeroelastic instability type is flutter and as the absolute value of the fiber angle increases, flutter Mach number decreases and for the -90° fiber angle case, critical frequency becomes zero indicating divergence instability. For the wing with no sweep, fiber angle of -45° results in the highest critical Mach number. It is to be noted that as Figure 4-35 shows, fiber angle is measured from the chordwise axis and when the fiber angle is $\pm 90^{\circ}$, fibers are aligned along the wing axis. Moreover, for negative fiber angles, fibers are aligned towards the leading edge, hence leading edge side of the wing is stiffer than the trailing edge side. Therefore, for TWBs with negative fiber angles other than -90°, flutter instability occurs at higher airspeeds compared to the TWBs with positive fiber angles. As a matter of fact, for positive fiber angles, critical Mach numbers are less than 0.3, consequently incompressible unsteady aerodynamics model is sufficient to study the aeroelastic instability characteristics. In the present study, results of composite wings with positive fiber angles are not presented since the main scope of the article is to investigate the aeroelastic stability of wings in the subsonic compressible flow regime.

Table 4-13 Critical Mach number and frequencies of composite CAS configuration wings obtained by compressible and incompressible indicial unsteady aerodynamics.

Fiber angle	Critical Mach number			Critical Frequency (rad/sec)		
	compressible	incompressible	Diff. (%)	compressible	incompressible	Diff. (%)
-45	0.73	0.87	16.3	34.56	38.5	10.2
-60	0.67	0.8	16.5	41.82	46.5	10.1
-75	0.67	0.75	10.2	66.31	69.3	4.31
-90	0.57	0.65	11.8	0	0	0

Figure 4-36 and Figure 4-37 show the effect of sweep angle on the critical Mach number and critical aeroelastic instability frequency for four different fiber angles of the CAS configuration TWB and for the range of the sweep angle $-45^\circ \leq \Lambda \leq 45^\circ$. In Figure 4-36 and Figure 4-37, positive sweep angle implies backward-swept wing and negative sweep angle implies forward-swept wing. Critical Mach number results are presented in the range $0.3 \leq M \leq 0.85$ since the unsteady aerodynamic model based on compressible indicial functions is valid in this range. For the fiber angle of -90°, fibers are aligned along the wing axis and bending-twisting coupling effect due to the material anisotropy is non-existent. For this configuration, Figure 4-36 and Figure 4-37 show that for forward-swept wings with negative sweep angle, divergence instability occurs and as the sweep angle is increased such that it becomes positive and the wing becomes backward-swept, critical Mach number increases and aeroelastic instability switches to flutter type. This is the typical effect of the wing sweep on the aeroelastic stability characteristics of wings which have no material coupling. It is seen that for fiber angles other than -90°, extreme forward-swept wings also have low critical Mach numbers with divergence instability. However, for moderate forward sweep angles, critical Mach number can be increased significantly with the use of fiber angles other than -90° with the -45° fiber angle being the most effective in increasing the critical Mach number. For the wing with zero sweep angle, the highest critical Mach number occurs for the fiber angle of -45°. For moderate backward-swept wings, off-axis fiber angles cause reduction of the critical Mach number.

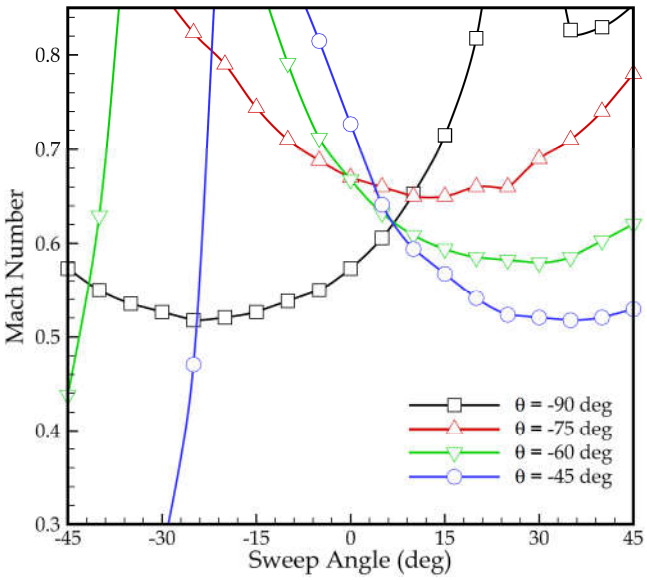

Figure 4-36 Effect of sweep and fiber angles on the stability margins of composite wings using the compressible indicial aerodynamic model / Critical Mach number versus the sweep angle

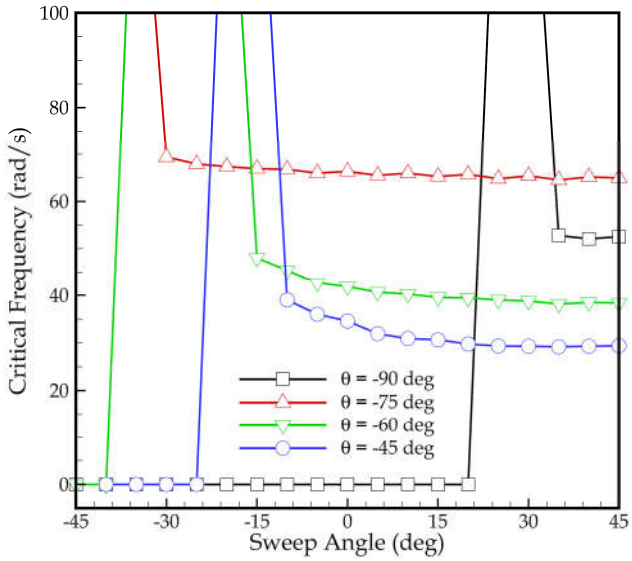

Figure 4-37 Effect of sweep and fiber angles on the stability margins of composite wings using the compressible indicial aerodynamic model / Critical frequency versus the sweep angle.

4.4.3.3 Nonlinear Aeroelastic Analysis of Composite Wings

For the CAS configuration composite wings which are structurally modeled as TWBs, nonlinear aeroelastic analyses have been performed in time domain through the fourth order Runge-Kutta direct integration of the governing nonlinear aeroelastic system of equations given by Equation (4-147). In the numerical simulations performed, it is assumed that the composite wing is initially at rest and the wing is given an initial disturbance by assigning an initial value of 1.0e−06 to all modal coordinates. As it was discussed before, with the very low initial conditions given to the modal coordinates, it is aimed to start self-excited oscillations and depending on the intrinsic character of the aeroelastic system, the response of the system may attenuate or increase. In the following, time history plots and the associated phase plots, Poincare and Power Spectrum Density (PSD) diagrams are given for the response of the wing tip $(z = L)$. Material and geometric properties of the composite wing used in the simulations are given in Table 4-12. Initially, the nonlinear aeroelastic system of equations is verified by comparing the time domain solution obtained with the linear aeroelastic solution for a rectangular wing with no seep and for the fiber angle of -75° in the CAS configuration. Referring to Table 4-13, it is seen that the predicted flutter Mach number is 0.67 according to the linear structural analysis. Figure 4-38 gives the time history plots of the flapwise wing tip deflection at the subcritical, critical and supercritical Mach numbers. As it is shown in Figure 4-38a, in a nonlinear analysis for Mach values less than 0.67, disturbance generated by the initial conditions imposed, attenuate due to the aerodynamic damping. With the increase in the Mach values, an exchange of energy between the wing structure and the aerodynamic flow commences at the bifurcation speed which corresponds to the flutter Mach number obtained by the linear aeroelastic analysis and LCO starts, as shown in Figure 4-38b, beyond the critical Mach number, in the supercritical region, amplitude of LCO increases substantially and as seen in Figure 4-38c, the magnitude of oscillations of the flapwise deflection is much higher than the magnitude of the oscillations at the critical condition.

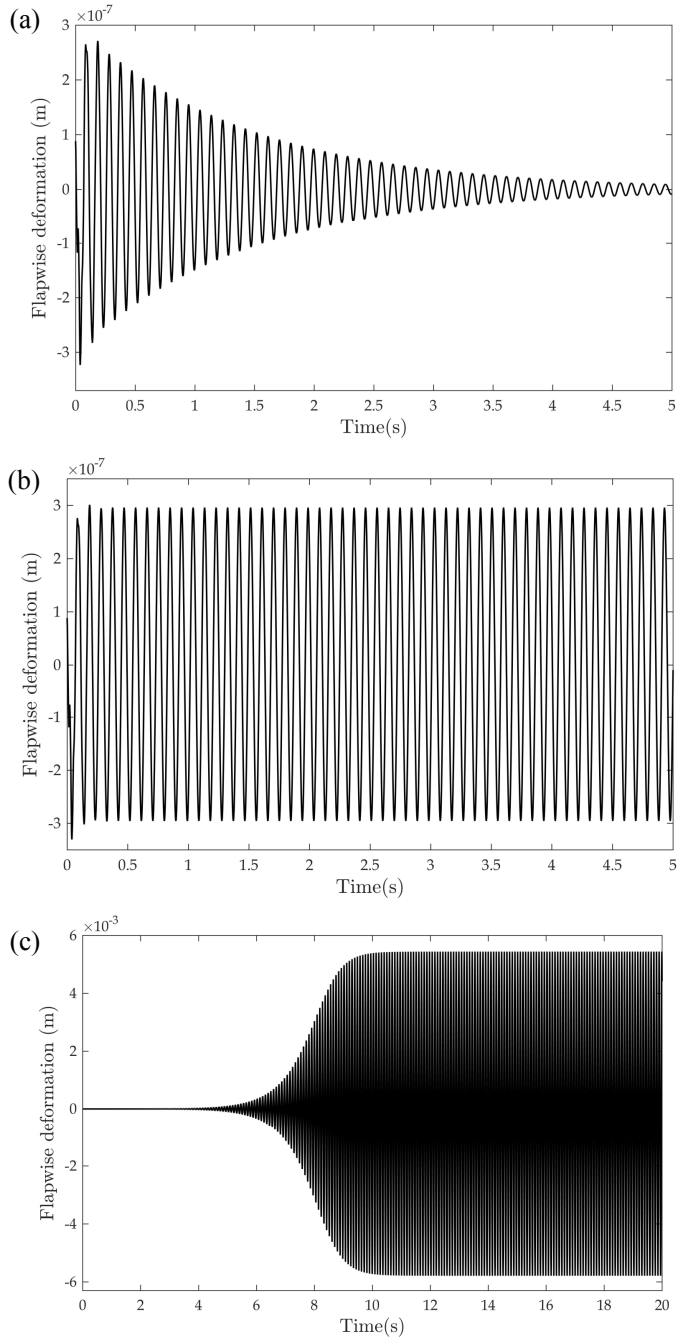

Figure 4-38 Nonlinear time history plots for three air speeds being (a) Subcritical ($M = 0.99\ M_f$) (b) Critical ($M = M_f$) and (c) Supercritical ($M = 1.01\ M_f$)

Bifurcation diagram of the unswept composite wing with the CAS configuration TWB structural model is presented in Figure 4-39 for fiber angles of -75° and -45°. Bifurcation points in Figure 4-39 refer to the Mach number above which LCOs of the wing tip deflection and wing tip twist occur and below the bifurcation point oscillations die out. For the CAS configuration TWB with fiber angles of -75° and -45°, bifurcation points are at Mach numbers 0.67 and 0.73, respectively. Bifurcation points identified by the nonlinear aeroelastic analysis coincide with the flutter Mach numbers determined by the linear aeroelastic analysis given in Table 4-13. Figure 4-39 shows that for the -45° fiber angle case, not only the instability occurs at a higher Mach number, but post-flutter LCO amplitudes of the flapwise and torsional deformation of the wing tip are also lower than the -75° fiber angle case. This observation clearly shows that post-flutter response of the composite wing with fiber angle of -45° is also more well behaved compared to the -75° fiber angle case. It should be noted at Mach numbers sufficiently higher than the critical Mach number, nonlinear aeroelastic response becomes either quasi-periodic or chaotic, and for these responses, maximum amplitude of flapwise wing tip deflection and maximum wing twist angle are plotted in the bifurcation diagram shown in Figure 4-39.

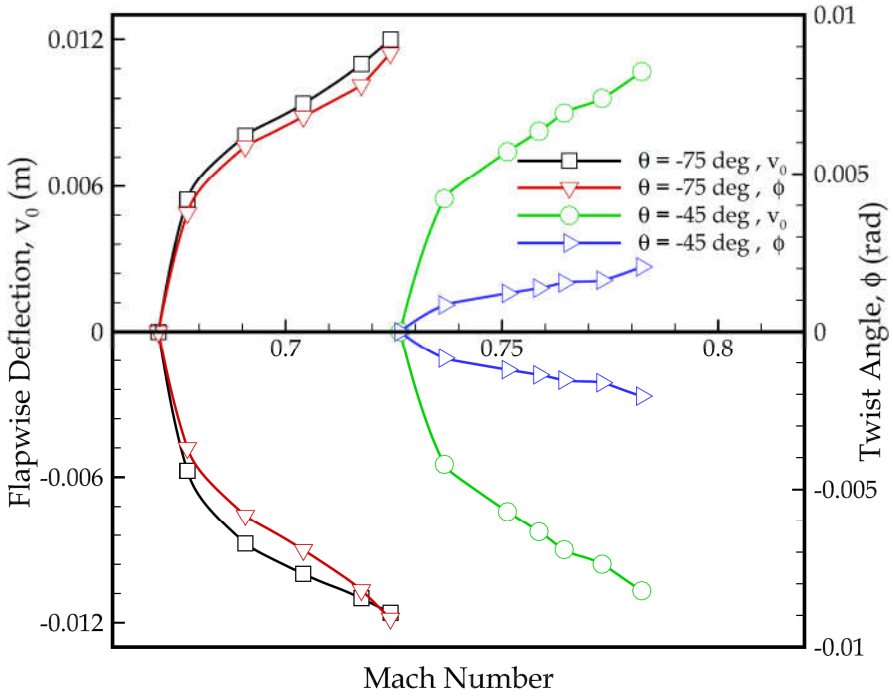

Figure 4-39 The effect of fiber angle on the bifurcation diagram of the composite wing with zero sweep angle

For the unswept wing with the CAS configuration fiber angle of -75°, Figure 4-40, Figure 4-41 and Figure 4-42 give the time histories of the flapwise wing tip displacement and wing tip twist and their respective power spectral density functions (PSDs) at post-flutter Mach numbers, $M/M_{\text{critical}} = 1.01, 1.05, 1.09$. From Figure 4-40, it is seen that for the low post-critical Mach number ($M/M_{\text{critical}} = 1.01$), aeroelastic response is purely periodic. At the post-flutter Mach ratio of 1.05, Figure 4-41 shows that oscillation amplitudes increase and response is quasi-periodic and responses are composed of more than one dominant frequency. Finally, as seen in Figure 4-42, at the post-flutter Mach ratio of 1.09, nonlinear aeroelastic response becomes chaotic and PSD plots show that broadband range of dominant frequencies exist in the responses.

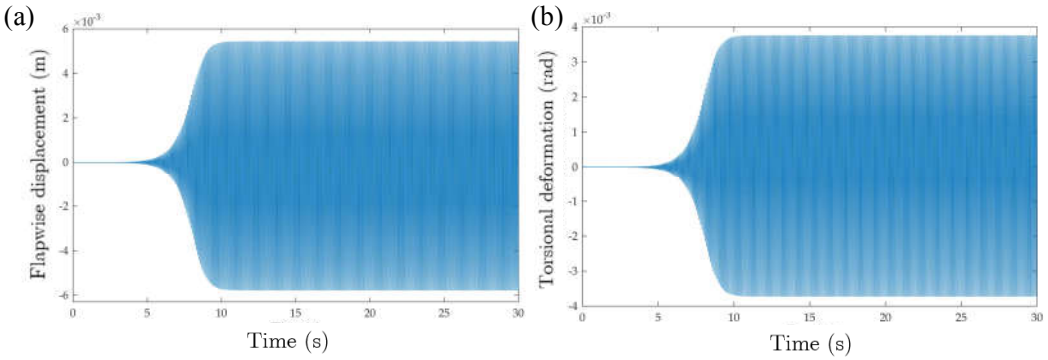

Figure 4-40 Response qualification of the composite wing with $\theta = -75^{\circ}$ and zero sweep angle at $M/M_{\text{critical}} = 1.01$ (a) Flapwise displacement (b) Torsional deformation.

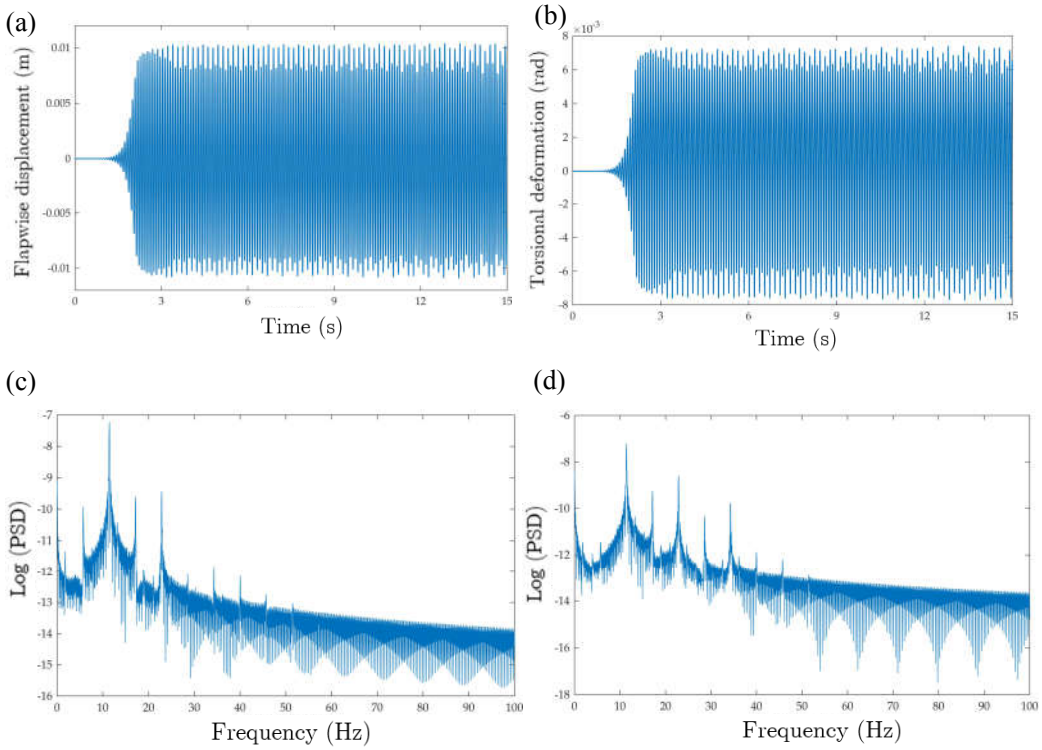

Figure 4-41 Response qualification of the composite wing with $\theta = -75^{\circ}$ and zero sweep angle at $M/M_{critical} = 1.05$, (a) Flapwise displacement (b) Torsional deformation (c) PSD of flapwise displacement (d) PSD of torsional deformation.

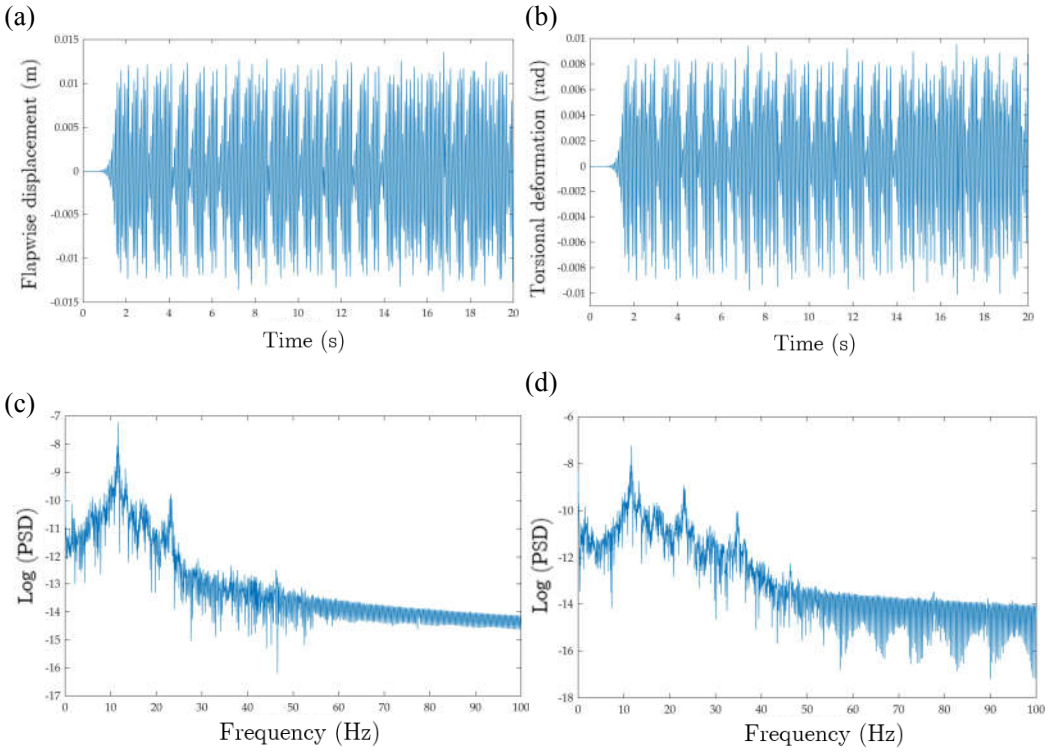

Figure 4-42 Response qualification of the composite wing with θ = −75° and zero sweep angle at $M/M_{critical}$ = 1.09, (a) Flapwise displacement (b) Torsional deformation (c) PSD of flapwise displacement (d) PSD of torsional deformation.

For the composite wing with the CAS configuration fiber angle of −75°, Figure 4-43 gives the bifurcation diagram which shows the effect of the sweep angle on the nonlinear aeroelastic response of the wing. Figure 4-43 compares the oscillation amplitudes of the flapwise tip deflection and tip twist of the unswept (Λ = 0°) and backward-swept wing (Λ = 30°). For the backward-swept wing, critical Mach number determined by the nonlinear aeroelastic analysis is 0.692 and this result agrees with the linear aeroelastic analysis results depicted in Figure 4-36. As seen in Figure 4-43, for the −75° fiber angle configuration, with the introduction of the wing sweep, critical

Mach number increases and amplitudes of oscillations reduce compared to the unswept wing at the same post-critical Mach number.

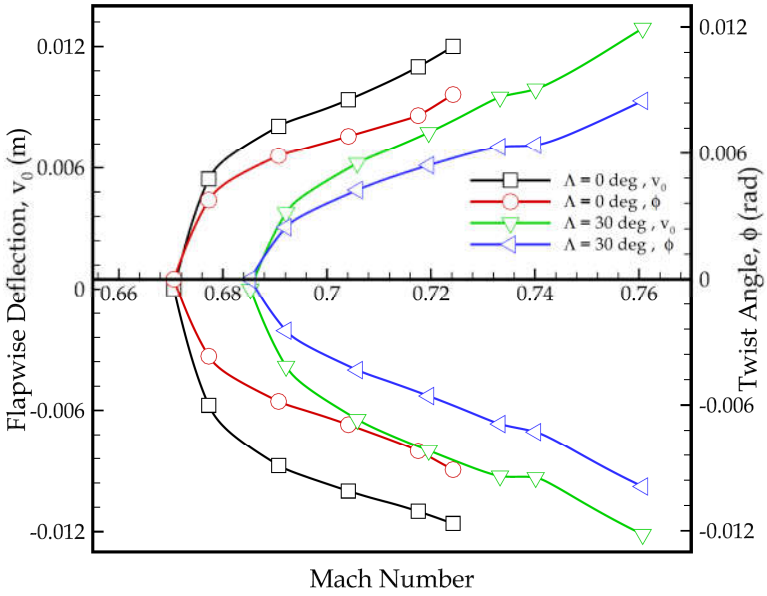

Figure 4-43 The effect of sweep angle on the bifurcation diagram of the composite wing with fiber angle $\theta = -75^{\circ}$

To aid the interpretation of the nonlinear aeroelastic response of the composite wing with the -75° fiber angle configuration, phase plots, and Poincare maps at the plane $\phi = 0$ are prepared for the unswept wing and backward-swept wings with the sweep angles $\Lambda = 15^{\circ}, 30^{\circ}, 45^{\circ}$. Figure 4-44, Figure 4-45 and Figure 4-46 present the phase portraits for the flapwise bending motion of the wing tip for the Mach ratios of 1.01, 1.05 and 1.09, respectively. As Figure 4-44 shows, at the low post-critical Mach ratio ($M/M_{\text{critical}} = 1.01$), nonlinear aeroelastic response of the wing is purely periodic with narrow closed orbits in the phase plot for all sweep angles. For the post-critical Mach ratio of 1.05, Figure 4-45 shows that nonlinear aeroelastic responses of wings with low sweep angles show quasi-periodic behavior which appears as closed thicker circuits in the phase plane. For the unswept wing, in the phase plane, there are two main thicker loops and as the sweep angle is increased, response of the wing becomes periodic again. Finally, for the higher post-critical Mach ratio of 1.09, phase plots given in

Figure 4-46 shows that nonlinear aeroelastic responses of the unswept wing and the wing with the sweep angle of 15° are chaotic which is evident from the numerous intermittent circuits. However, as the sweep angle is increased, nonlinear aeroelastic response of the wing tip becomes quasi-periodic again. Phase plots given in Figure 4-44, Figure 4-45 and Figure 4-46 all show that for the −75° fiber angle configuration, by increasing the backward sweep angle, nonlinear response of the wing becomes more well-behaved and the amplitude of oscillations of the flapwise bending motion of the wing tip reduces.

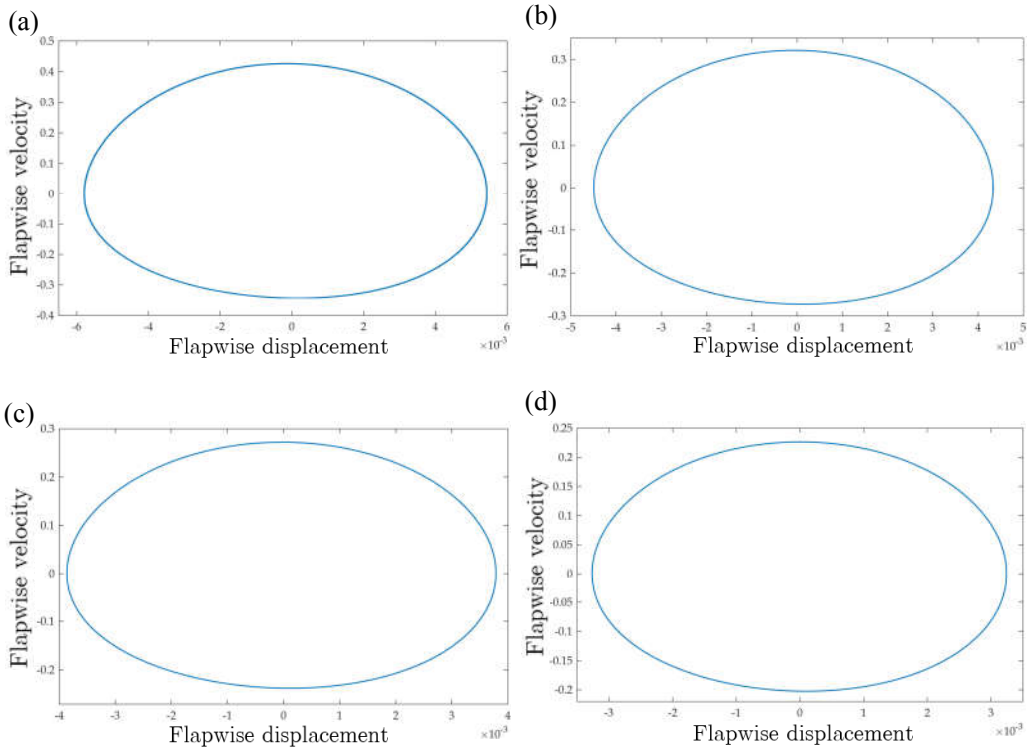

Figure 4-44 Phase plane plots of the flapwise bending motion for different sweep angles at $M/M_{\text{critical}} = 1.01$ and $\theta = -75°$, (a) $\Lambda = 0°$ (b) $\Lambda = 15°$ (c) $\Lambda = 30°$ (d) $\Lambda = 45°$

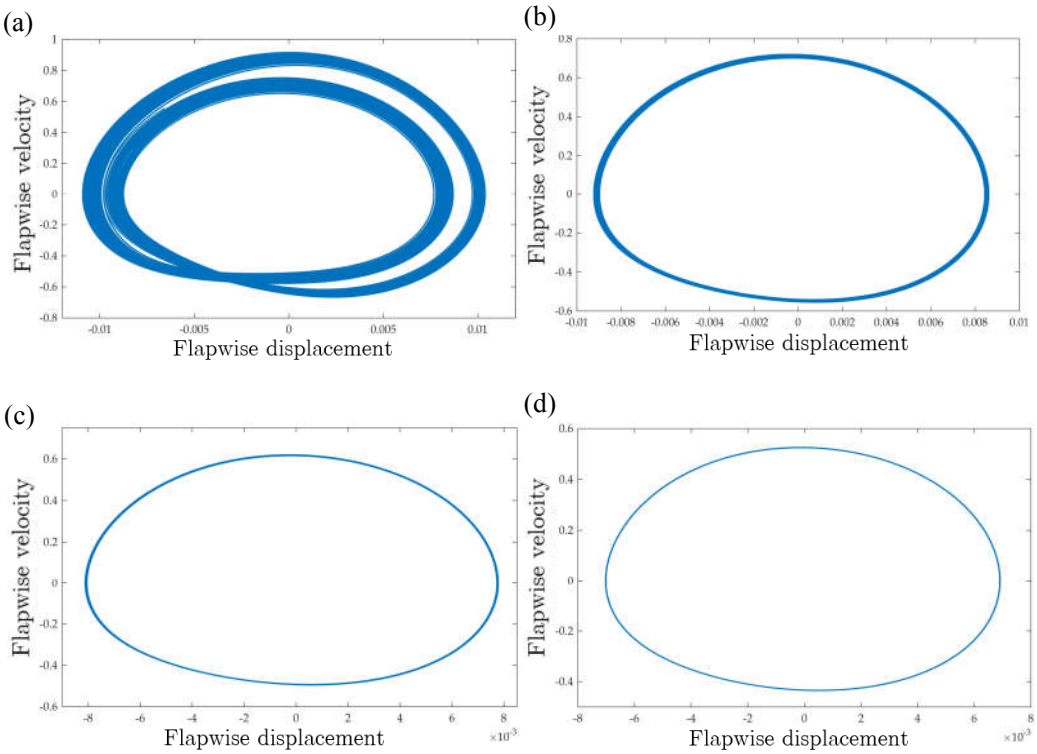

Figure 4-45 Phase plane plots of the flapwise bending motion for different sweep angles at $M/M_{\text{critical}} = 1.05$ and $\theta = -75^{\circ}$, (a) $\Lambda = 0^{\circ}$ (b) $\Lambda = 15^{\circ}$ (c) $\Lambda = 30^{\circ}$ (d) $\Lambda = 45^{\circ}$.

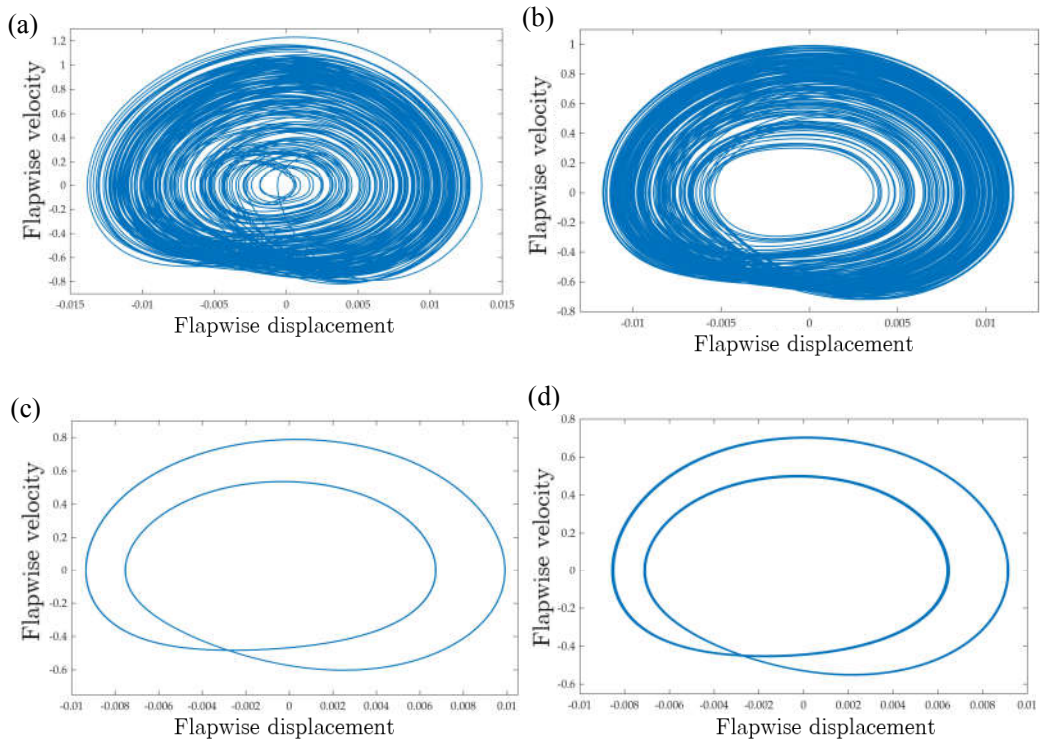

Figure 4-46 Phase plane plots of the flapwise bending motion for different sweep angles at $M/M_{\text{critical}} = 1.09$ and $\theta = -75^{\circ}$, (a) $\Lambda = 0^{\circ}$ (b) $\Lambda = 15^{\circ}$ (c) $\Lambda = 30^{\circ}$ (d) $\Lambda = 45^{\circ}$.

Figure 4-47, Figure 4-48 and Figure 4-49 show the Poincare plots which are constructed for the flapwise bending degree of freedom of the wing tip (v_0) at the section $\phi = 0^{\circ}$ by plotting crossings in both directions. At the low post-critical Mach ratio ($M/M_{\text{critical}} = 1.01$), Figure 4-47 shows that for all sweep angles, there are single dots which are indicative of the periodic response. For the post-critical Mach ratio of 1.05, Figure 4-48 shows that for the unswept wing, there are finite number of dots indicating quasi-periodic response. As the sweep angle is increased, number of dots in the Poincare maps decreases, and for the sweep angle of 45°, there is again single dot which indicates purely periodic response which agrees with the last phase plot given in Figure 4-44. For the post-critical Mach ratio of 1.09, Poincare maps, given by the first two plots in Figure 4-49, for the unswept wing and the wing with the sweep angle

of 15° have numerous dots indicating chaotic response. It is seen that for the thicker orbits in the phase plane, the number of dots emerging in the Poincare plots is also high.

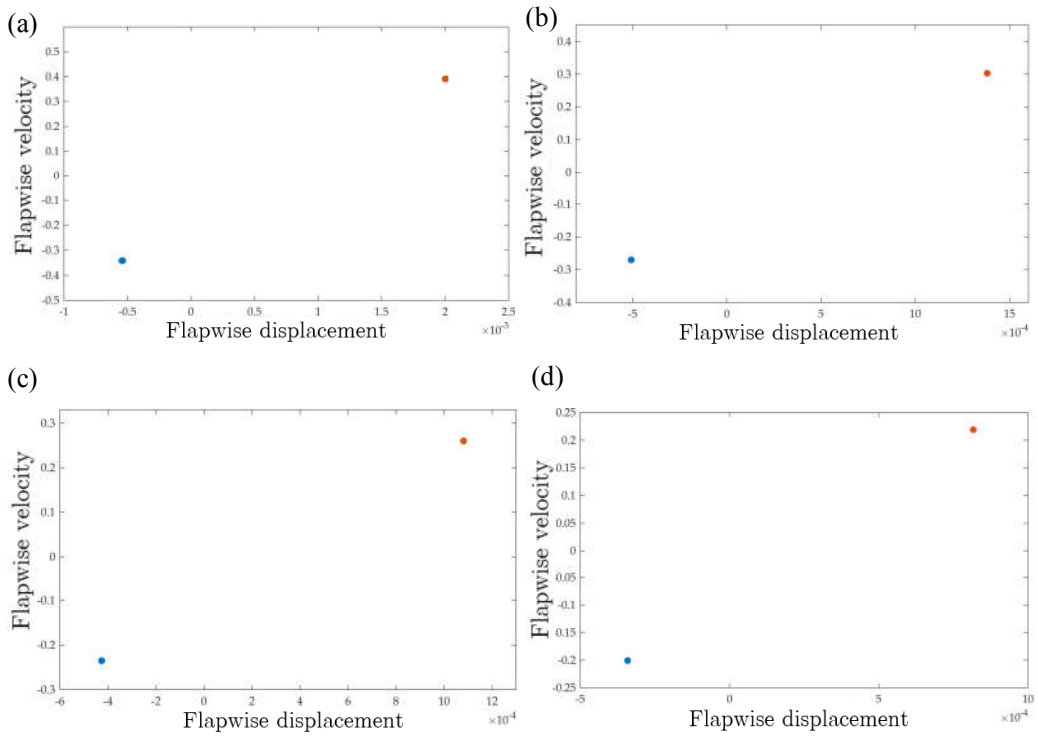

Figure 4-47 Poincare plots for different sweep angles at the plane of $\phi = 0^{\circ}$, $M/M_{\text{critical}} = 1.01$ and $\theta = -75^{\circ}$, (a) $\Lambda = 0^{\circ}$ (b) $\Lambda = 15^{\circ}$ (c) $\Lambda = 30^{\circ}$ (d) $\Lambda = 45^{\circ}$

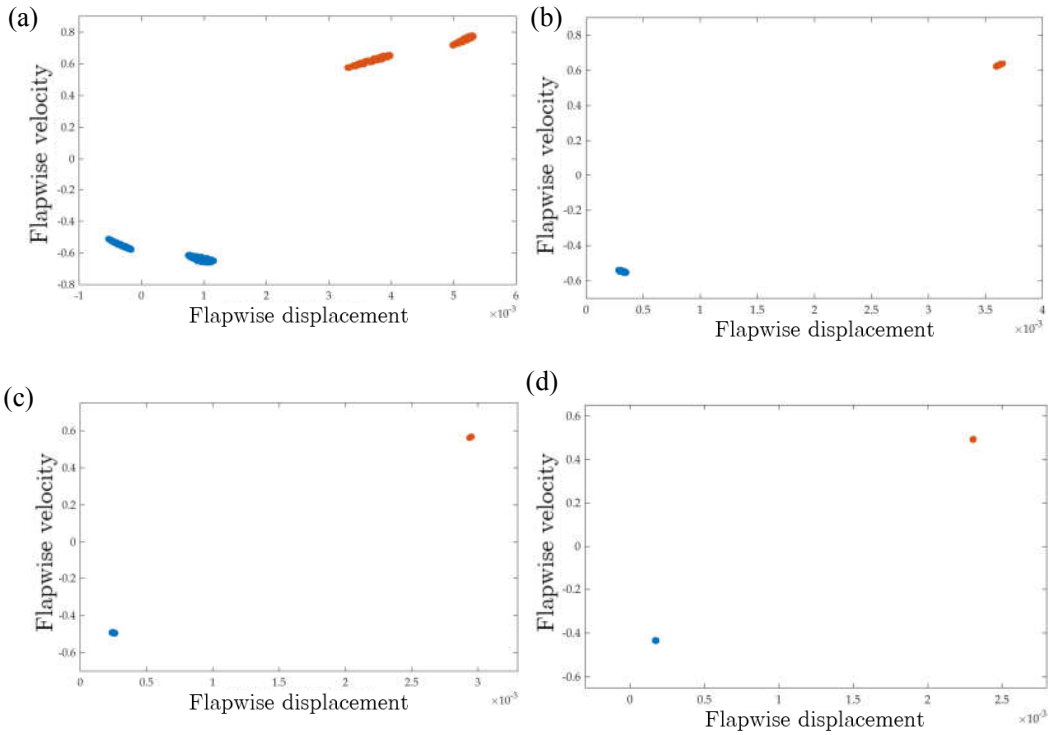

Figure 4-48 Poincare plots for different sweep angles at the plane of $\phi = 0^{\circ}$, $M/M_{\text{critical}} = 1.05$ and $\theta = -75^{\circ}$, (a) $\Lambda = 0^{\circ}$ (b) $\Lambda = 15^{\circ}$ (c) $\Lambda = 30^{\circ}$ (d) $\Lambda = 45^{\circ}$.

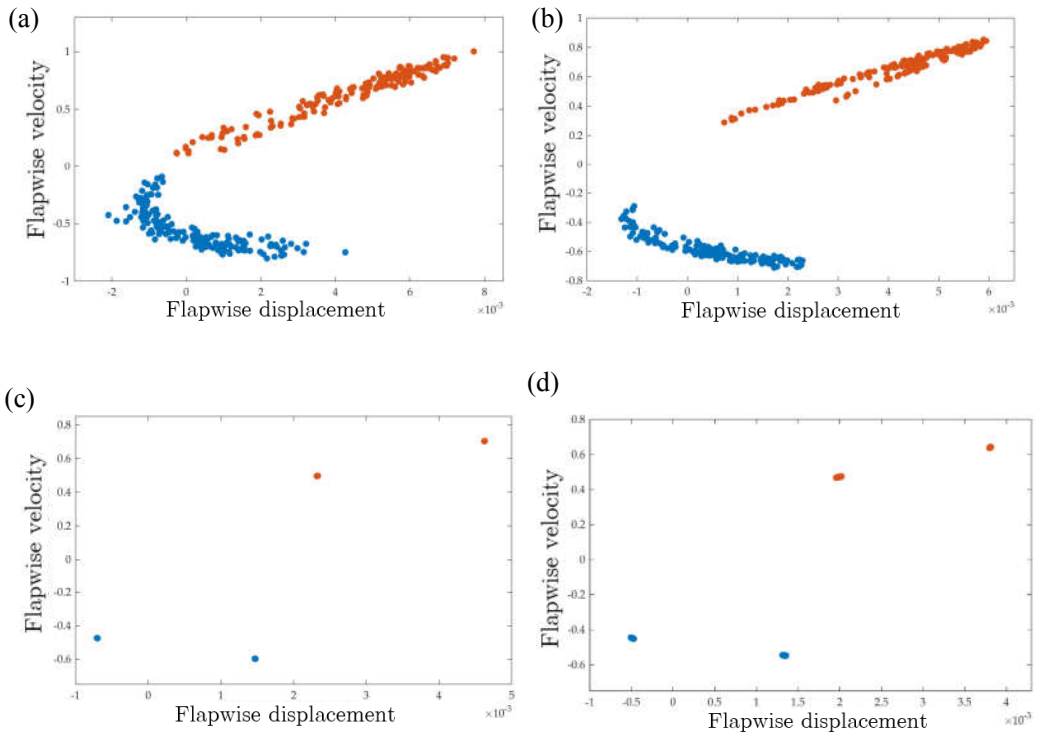

Figure 4-49 Poincare plots for different sweep angles at the plane of $\phi = 0^{\circ}$, $M/M_{\text{critical}} = 1.09$ and $\theta = -75^{\circ}$, (a) $\Lambda = 0^{\circ}$ (b) $\Lambda = 15^{\circ}$ (c) $\Lambda = 30^{\circ}$ (d) $\Lambda = 45^{\circ}$.

A comprehensive study of the geometrically nonlinear aeroelastic behavior of swept composite wings structurally modeled as thin walled beams (TWB) is performed. The structural equations of motion are obtained for the CAS configuration TWB by including up to third order nonlinear terms. The unsteady compressible aerodynamics model is constructed in the time domain by using a novel indicial approximation, which allows the calculation of compressible indicial functions at any Mach number up to 0.85, by incorporating twelve aerodynamic lag states. To construct the nonlinear coupled-field system of equations, twelve auxiliary equations governing the aerodynamic lag states are included in the formulation. The nonlinear aeroelastic system of equations of the composite wing is solved by means of a Ritz based solution methodology utilizing the mode shapes of the geometrically linear TWB model to approximate the spatial variation of the degrees of freedom of the TWB. Time response

of the nonlinear aeroelastic system is obtained via the Runge-Kutta direct integration algorithm. The effects of lamination angle and sweep angle of the CAS configuration TWB on the post-critical response of the composite wing are studied in depth by providing bifurcation diagrams, phase portraits, Poincare maps and one side Power Spectral Density (PSD) plots.

For composite wings structurally modeled as TWBs, the following items stand out as major conclusions of the study on the linear and nonlinear aeroelastic response under compressible unsteady aerodynamics.

- Results show that critical speeds determined by the linear aeroelastic analysis of the composite wings via the frequency domain solution agree very well with the bifurcation speeds obtained by the time domain solutions of the nonlinear aeroelastic system of equations of the composite wing structurally modeled as TWB.
- Compressibility accounts for reduction in aeroelastic instability speeds and instability speeds obtained by incompressible unsteady aerodynamics are not conservative.
- For the composite wing with the CAS configuration TWB structural model, fiber angle is seen to be a very influential parameter on the instability speed of the composite wing. For negative fiber angles, the form of instability is of flutter type because fibers are oriented towards the leading edge and divergence instability is deferred and flutter instability occurs at higher airspeeds where the compressibility effect is not negligible compared to the TWBs with positive fiber angles.
- Furthermore, it is shown that combination of the fiber angle of the CAS configuration and the sweep angle of the wing has significant effect on the critical speeds as well as the post-critical nonlinear aeroelastic response of the composite wing. For the low off-axis fiber angle of -75°, it seen that aeroelastic response of forward swept wings can be improved significantly. Moreover, it is also shown in the article that as the backward sweep angle of wing is

increased, post-critical aeroelastic response of the wing becomes more well behaved compared to wings with low backward sweep angles.

- It is evident that compressibility accounts for reduction in aeroelastic instability speeds especially at higher Mach numbers. Actually, instability speeds obtained by incompressible unsteady aerodynamics are not conservative.

CHAPTER 5

FLUTTER CHARACTERISTICS OF COMPOSITE WIND TURBINE BLADES WITH BENDING TWISTING COUPLING

Bending-twisting coupling is used in composite wind turbine blades to alleviate loads in the high power output wind turbine systems with long blades. Increased bending and torsional flexibility of long wind turbine blades may cause flutter instability at lower wind speeds. For long blades, at the flutter condition, relative velocities at blade sections away from the hub centre are usually in the subsonic compressible range. In this chapter, the effect of the compressibility on the flutter characteristics of bend-twist coupled (BTC) composite blades has been investigated. Flutter analyses have been performed for the baseline blade and the BTC blades designed for the 5MW wind turbine of NREL. Beam model of the blade has been developed by making analogy with the structural model of the prewisted rotating TWB and utilizing the variational asymptotic beam section (VABS) method for the calculation of sectional properties of the wind turbine blades. To investigate the effect of compressibility on the flutter characteristics of the blades, aeroelastic analyses have been performed both in frequency and time domain utilizing unsteady aerodynamics via incompressible and compressible indicial functions and comparisons are made with the results of a multibody wind turbine simulation program.

In this chapter, for the purpose of studying the effect of compressibility on the flutter characteristics, classical flutter analyses of composite wind turbine blades have been performed both in frequency and time domain utilizing unsteady aerodynamics via incompressible and compressible indicial functions. It is to be noted that, as explained

in detail in Chapter 3, in the literature exponential representations of compressible indicial functions are available only for certain Mach numbers. For the sections of the blade, which are in the compressible flow regime, to perform continuous calculation of the compressible indicial functions in the course of frequency domain solution of aeroelastic instability, approximation methodology which is presented for the calculation of compressible indicial functions at any Mach number in Chapter 3 has also been used in this chapter. Structural model of wind turbine blades is based on beam models which have been developed by making analogy with the rotating TWB and utilizing the VABS method for the calculation of sectional properties of the wind turbine blades. For the inboard blade sections, which are in the incompressible flow regime, structural blade model is integrated with the incompressible unsteady aerodynamics model utilizing Wagner's function, and for the outboard blade sections, which are in the compressible flow regime, structural blade model is integrated with the compressible unsteady aerodynamics model based on compressible indicial functions. Aeroelastic system of equations are solved by the extended Galerkin method both for blades with no pretwist and with the prescribed pretwist of the NREL blade. The proposed approach allows for frequency domain solution of aeroelastic instability of wind turbine blades whose sections are both in incompressible and compressible flow regime.

5.1 Wind Turbine Blade Model

NREL's 5 MW wind turbine blade is inversely designed with 17 sections along the spanwise direction [127]. Inverse design process of the blade is described in the flowchart given in Figure 5-1.

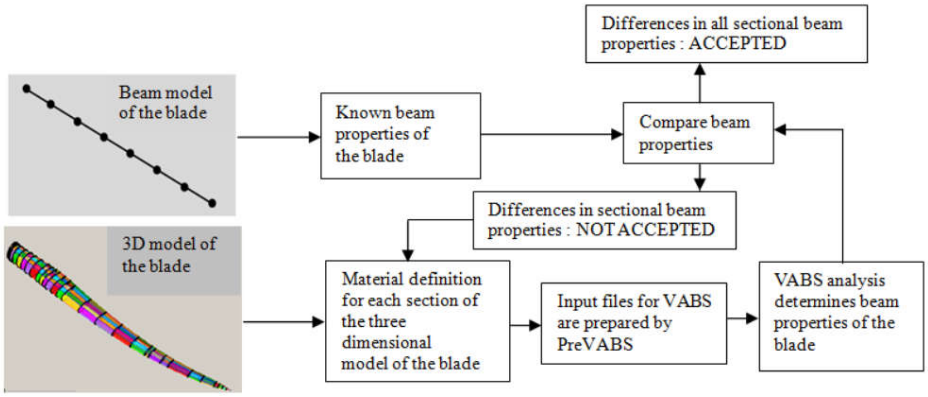

Figure 5-1 Inverse design loop of a wind turbine blade with known cross-sectional beam properties

The geometric properties of the inversely designed blade are taken from NREL's report [128]. However, the transition region near the blade root is undefined in the NREL's report. Therefore, the transition region of the blade is generated so that a smooth transition is achieved through the axis of the blade. The 3D reference blade design is shown in Figure 5-2.

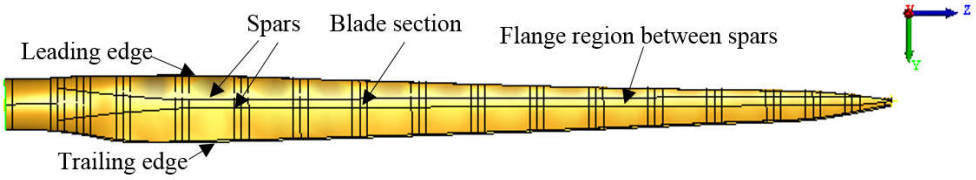

Figure 5-2 Three dimensional inversely designed reference blade [1]

The chord lengths of the sections and the name of the airfoils are presented in Table 5-1. Front and rear spars are placed such that the thickest section of the airfoils is bounded by the shear webs. The blade pitch axis passes through the center of the circular cross-section of the root and the middle of the spars, and the sections of the blades are arranged accordingly to pitch axis. The inversely designed blade is fully composed of GFRP material. The skins between the leading edge and front spar, and rear spar and trailing edge portions as well as two spars are made of ±45° biaxial

lamina. Furthermore, circular root blade section is composed of 0° and 90° UD GFRP plies placed with respect to the blade axis. Flange regions between the two shear webs on the pressure and suction side are shaded in dark brown in Figure 5-3 and are composed of 0° UD GFRP plies.

Table 5-1 Geometrical properties of NREL's 5 MW turbine blade

Section Starting Point (m)	Chord Length of Section (m)	Airfoil Name
0	3.542	Circular
3.644	3.711	Transition
5.467	4.050	Transition
8.200	4.557	DU40_A17
12.300	4.652	DU35_A17
16.400	4.458	DU35_A17
20.500	4.249	DU30_A17
24.600	4.007	DU25_A17
28.700	3.748	DU25_A17
32.800	3.502	DU21_A19
36.900	3.256	DU21_A20
41.000	3.010	NACA643-618
45.100	2.764	NACA643-618
49.200	2.518	NACA643-618
53.300	2.313	NACA643-618
56.033	2.086	NACA643-618
58.767	1.419	NACA643-618
61.500	0.500	NACA643-618

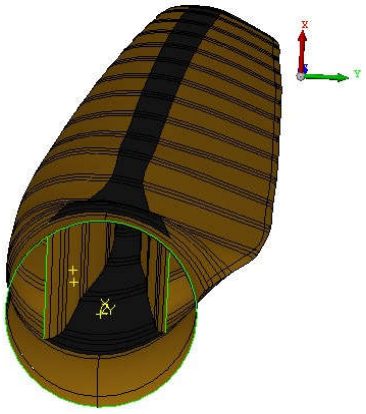

Figure 5-3 Flange region between the spars on pressure and suction sides [1]

For the design process, sectional edgewise, flapwise and torsional stiffness properties of inversely designed blade are closely matched to that of NREL's 5 MW turbine blade by modifying the number of plies in each section by utilizing VABS through which the sectional properties of the beam-blade are calculated [129]. Utmost importance is given in the inverse design phase of the blade since the turbine blade ought to have comparable properties with the NREL's blade in order to represent the loads on the turbine and power production correctly.

Blade is divided into 17 sections, for each section of blade, appropriate laminate definitions are made for the upper and lower surfaces of the blade box blade between the already designed spar caps. The finite element models of the cross section profile are set up in PreVABS commercial code [130]. VABS code is used to process of the output of PreVABS model. The VABS code is capable of calculating the airfoil shape cross sectional beam properties of the blade which are highly comparable with the beam section properties of the known NREL's 5 MW blade structure. The schematic description of the sections of the blade with distinct airfoil profiles is shown in Figure 5-4.

In Figure 5-4, (x, y, z) coordinate system is the rotating structural coordinate system established at the blade root and the conventional Theodorsen's aerodynamic coordinate system (x_{ae}, z_{ze}) for a blade section is also shown together with the structural coordinate system (x, y, z). In a blade section, u_p, v_p, w_p are the translations of the shear center of the TWB wind turbine blade model in the (x, y, z) directions, respectively and $\theta_x(z,t), \theta_y(z,t), \phi(z,t)$ are the rotations about the (x, y, z) axes.

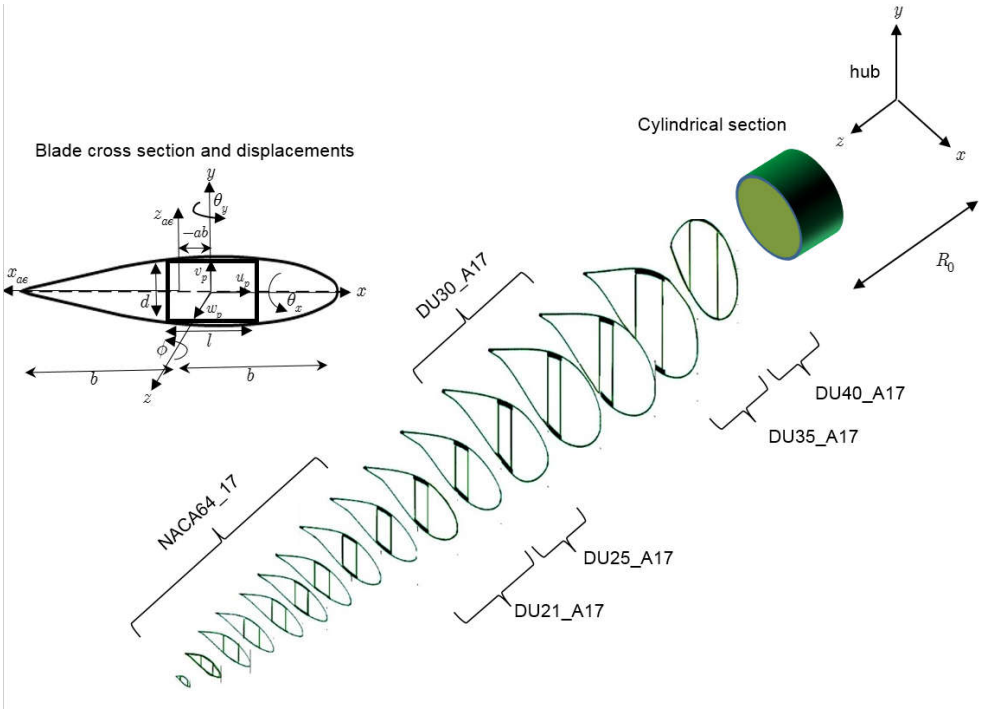

Figure 5-4 schematic description of the blade sections with distinct airfoil profiles

Following design of the baseline blade, the number of composite layers in certain sections of the blade have been modified to have gradual thickness drops along the span of the blade. Figure 5-5 and Figure 5-6 compare the sectional flatwise bending stiffness and torsional stiffness of the inversely designed baseline blade and the NREL five-megawatt turbine blade. It is seen that the baseline turbine blade represents the sectional flatwise and torsional stiffness of the 5MW wind turbine blade of NREL reasonably well. It should be noted that the baseline blade design is not a detailed design and not a production blade. With the inverse design method, it is aimed to define a baseline blade that has a similar mass and stiffness distribution along the blade span as the blade of the NREL five-megawatt wind turbine.

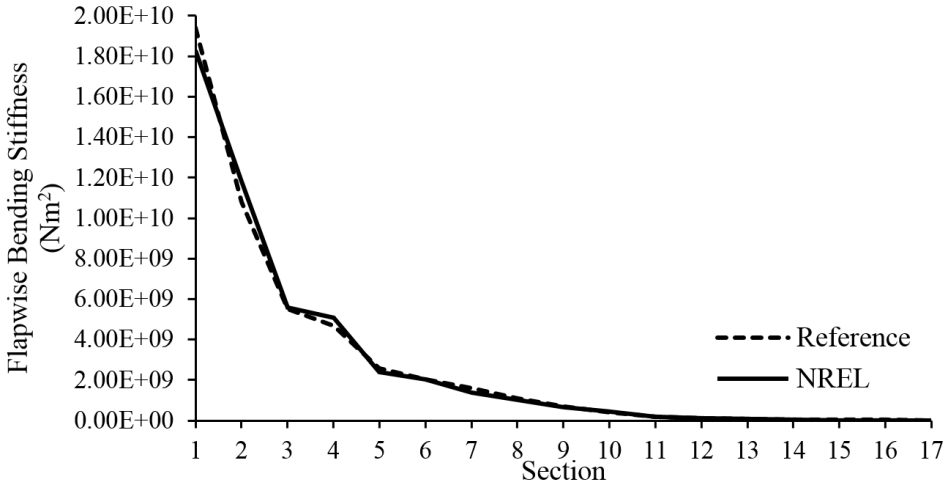

Figure 5-5 Sectional flapwise bending stiffness of the reference and NREL's 5MW wind turbine blade

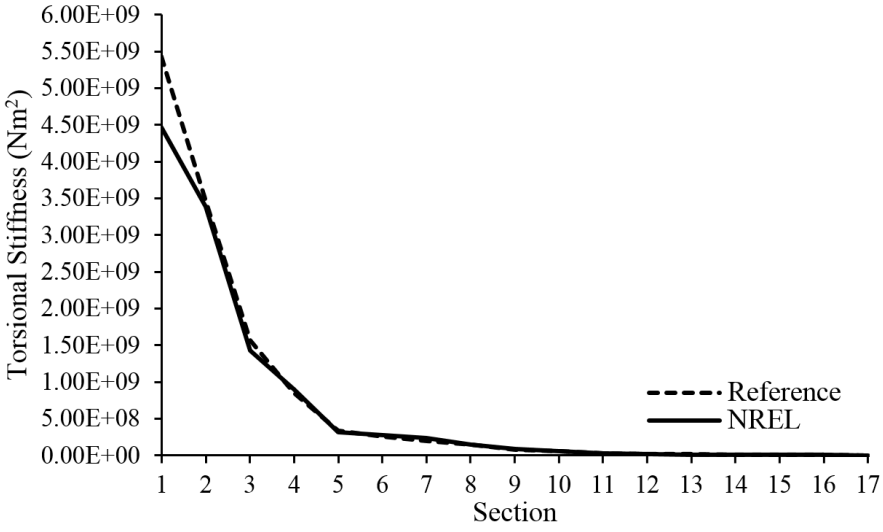

Figure 5-6 Sectional torsional bending stiffness of the reference and NREL's 5MW wind turbine blade

Blades with bending-twisting coupling are created by modifying the spar cap plies at the outboard section of the blade. Note that the reference blade is an uncoupled blade that consists of on-axis GFRP plies in the flange region between the front and the rear webs. GFRP material are used in the spar cap plies in the design process of the blades.

The baseline blade, which is the inversely designed wind turbine blade having sectional stiffness properties matched to that of NREL's 5 MW wind turbine blade, has full-GFRP material with 0° fiber angle configuration in the spar caps. Based on the outcome of the study by Sener [1] in the bend-twist coupled wind turbine blades off-axis fiber angle range is decided to be 10º and 20º. Bend-twist coupling effect is exploited by utilizing GFRP material in spar cap plies oriented at 10º and 20º with respect to the blade axis. For all blade configurations, inboard 31.5 meter portion comprise of 0° GFRP plies. The outboard 30 meter portion of the blade is where the modifications take place by retaining GFRP plies with 10º and 20º fiber angles in the spar caps as depicted in Figure 5-7.

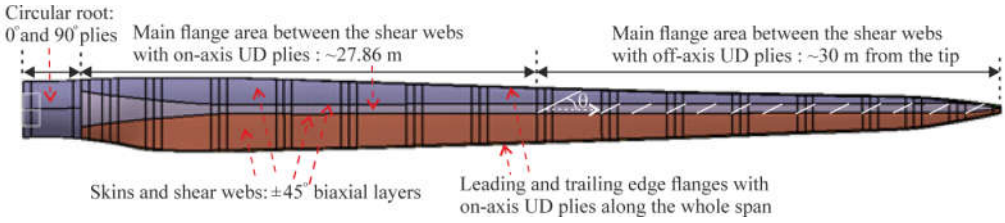

Figure 5-7 Spar cap region with fiber angles of the spar cap plies oriented with respect to the blade axis

In the present study, full GFRP bend-twist coupled blades are designed by modifying the baseline blade. Off-axis ply angle in the BTC sections of the BTC blades is taken as 10º and 20º and off-axis pressure and suction side spar cap plies are placed in the outboard 30 m of the blade. BTC blades are designed by rotating the unidirectional plies in the pressure and the suction side spar caps of the outboard 30 m of the baseline blade towards the leading edge by the fiber angle θ. Table 5-2 describes the baseline and the BTC blade designs made. Since the same number of plies in the outboard 30 m of the BTC blades (BTC_10 and BTC_20) is used as in the baseline blade, BTC blades have lower flatwise bending stiffness compared to the baseline blade in the bend-twist sections.

Table 5-2 Blade configurations studied

Blades	Description
baseline	Baseline GFRP blade with pressure/suction side GFRP spar cap plies along the blade axis (0 deg.) in the bend-twist sections of the blade.
BTC_10	0 deg. plies in the bend-twist sections of GFRP_1 blade are made 10º.
BTC_20	0 deg. plies in the bend-twist sections of GFRP_1 blade are made 20º.

5.2 Governing Aeroelastic Equations of the Rotating Beam-Blade Model

In this section aeroelastic equations of the beam-blade are derived. In this respect, to generate the parametric expressions of the stiffness, mass and inertia terms associated with the sections of the blade, governing equations are derived assuming that the blade is structurally composed of a single cell box beam. Once the governing equations are obtained in parametric form, stiffness, mass and inertia terms which appear in the governing equations are replaced by the stiffness, mass and inertia properties of the blade sections determined by VABS for the real blade structure. In this respect, single cell box beam serves as a tool to come up with the constitutive equation relating the general beam stress-resultants and the generalized strain counterparts and also the mass and the inertia terms. The resulting beam-blade model is coupled with both incompressible and compressible unsteady aerodynamic models based on the incompressible and compressible indicial functions to come up with the aeroelastic system of equations.

5.2.1 Basic Assumptions and Kinematic Relations Employed in the TWB Structural Model

Figure 5-8 shows the wind turbine blade cross section in undeformed and deformed planes and the structural rotating coordinate system. Rotating coordinate system (x, y, z) is placed at the root of the TWB blade and the local coordinate system (n, s, z)

is defined at the mid plane of the cross section of the TWB such that s is the axis tangent to the middle surface and n is the axis perpendicular to the s axis. The displacements u and v of any point on the beam cross section in the x and y directions can be defined in terms of the displacements of shear center P and the rotation $\phi(z,t)$ of the cross section about the shear center P, as shown in Figure 5-8. In the following, thin walled beam kinematics is based on the geometrically linear theory and cross-sectional warping is neglected.

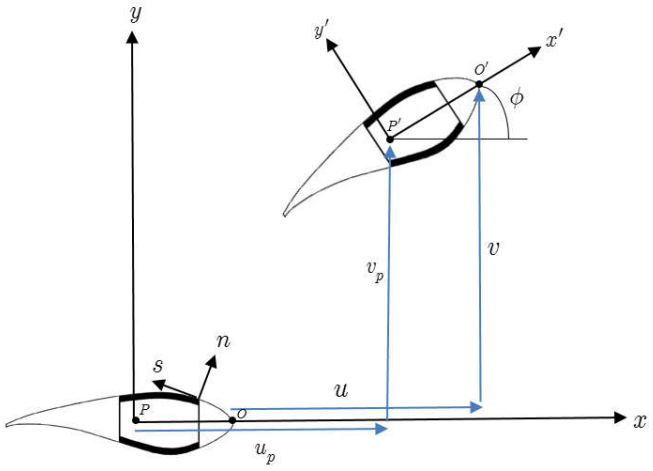

Figure 5-8 Blade cross-section before and after deformation

For the geometrically linear thin walled beam kinematics, neglecting the cross-sectional warping, the 3-D displacements $(u(x,y,z,t), v(x,y,z,t), w(x,y,z,t))$ are described in terms of the displacements $u_p(z,t), v_p(z,t), w_p(z,t)$ of the shear center and the twist angle $\phi(z,t)$ as [92],

$$\begin{aligned} u &= u_p - \left(y - n\frac{dx}{ds}\right)\phi \\ v &= v_p + \left(x + n\frac{dy}{ds}\right)\phi \\ w &= w_p + \left(x + n\frac{dy}{ds}\right)\theta_y + \left(y - n\frac{dx}{ds}\right)\theta_x \end{aligned} \tag{5-1}$$

where, u_p, v_p, w_p are the translations of the shear center of the thin walled wind turbine blade in the x, y, z directions, respectively and $\theta_x(z,t), \theta_y(z,t), \phi(z,t)$ are the rotations about the x, y, z axes. It should be noted that displacements given by Equation (5-1) are explicitly valid for a single cell box beam. In the following, governing equations are derived assuming that the blade is structurally composed of a single cell box beam. The approximation of the linear strain tensor is adopted to derive the strain-displacement relations. The nonzero components of the strain are defined by,

$$\varepsilon_{zz} = \frac{\partial w}{\partial z} \tag{5-2}$$

$$\gamma_{sz} = \gamma_{xz}\frac{dx}{ds} + \gamma_{yz}\frac{dy}{ds} + 2n\phi' \tag{5-3}$$

$$\gamma_{nz} = \gamma_{xz}\frac{dy}{ds} - \gamma_{yz}\frac{dx}{ds} \tag{5-4}$$

where $()'$ corresponds to differentiation with respect to the z coordinate.

By substituting displacement components in Equation (5-1) into the axial strain expression given by Equation (5-2), the nonzero axial strain can be rewritten as given in Equation (5-5),

$$\varepsilon_{zz} = \varepsilon^0_{zz} + n\varepsilon^1_{zz} \tag{5-5}$$

where the strain components $\varepsilon^0_{zz}, \varepsilon^1_{zz}$ all include linear terms and their explicit expressions are given as,

$$\varepsilon^0_{zz} = \theta'_y x + \theta'_x y + w'_p \tag{5-6}$$

$$\varepsilon^1_{zz} = \frac{dy}{ds}\theta'_y - \frac{dx}{ds}\theta'_x \tag{5-7}$$

In order to determine the expressions for the shear strains γ_{sz} and γ_{nz}, local shear strains in the yz plane γ_{yz} and xz plane γ_{xz} given by Equations (5-8) and (5-9) are substituted into Equations (5-3) and (5-4).

$$\gamma_{yz} = \theta_x + v_0' \tag{5-8}$$

$$\gamma_{xz} = \theta_y + u_0' \tag{5-9}$$

Following the substitution, the transverse shear strains γ_{sz} and γ_{nz} can be expressed as,

$$\gamma_{sz} = \gamma_{sz}^0 + n\gamma_{sz}^1 \tag{5-10}$$

$$\gamma_{nz} = \gamma_{nz}^0 \tag{5-11}$$

where the explicit expressions of the shear strain components $\gamma_{sz}^0, \gamma_{sz}^1, \gamma_{nz}^0$ are given as,

$$\gamma_{sz}^0 = \theta_y \frac{dx}{ds} + \theta_x \frac{dy}{ds} \tag{5-12}$$

$$\gamma_{sz}^1 = 2\phi' \tag{5-13}$$

$$\gamma_{nz}^0 = \theta_y \frac{dy}{ds} - \theta_x \frac{dx}{ds} \tag{5-14}$$

5.2.2 Constitutive relations

The relationship between the stresses and strains in a layer in contracted form can be expressed in terms of the reduced stiffness coefficients $\bar{Q}_{ij}$ of the composite blade by Equation (5-15).

$$\begin{Bmatrix} \sigma_{ss} \\ \sigma_{zz} \\ \sigma_{nz} \\ \sigma_{sn} \\ \sigma_{sz} \end{Bmatrix}_k = \begin{bmatrix} \bar{Q}_{11} & \bar{Q}_{12} & 0 & 0 & \bar{Q}_{16} \\ \bar{Q}_{21} & \bar{Q}_{22} & 0 & 0 & \bar{Q}_{26} \\ 0 & 0 & \bar{Q}_{44} & \bar{Q}_{45} & 0 \\ 0 & 0 & \bar{Q}_{54} & \bar{Q}_{55} & 0 \\ \bar{Q}_{61} & \bar{Q}_{62} & 0 & 0 & \bar{Q}_{66} \end{bmatrix}_k \begin{Bmatrix} \varepsilon_{ss} \\ \varepsilon_{zz} \\ \gamma_{nz} \\ \gamma_{sn} \\ \gamma_{sz} \end{Bmatrix}_k \tag{5-15}$$

The explicit expressions of the reduced stiffness coefficients $\bar{Q}_{ij}$ are given in APPENDIX A.

5.2.3 Energy Expressions

The governing equation of motion can be analytically derived using the Hamilton's principle in the absence surface shear forces, and thermal loadings as,

$$\begin{aligned} &\int_{t_1}^{t_2} (\delta T - \delta\left(V + V_{cf}\right) + \delta W)dt = 0 \\ &at \quad t = t_1, t_2\,, \\ &\delta u_0 = \delta v_0 = \delta w_0 = \delta\theta_x = \delta\theta_y = \delta\phi = 0 \end{aligned} \tag{5-16}$$

where, T, V, V_{cf} and W are the kinetic energy, strain energy due to large strains, strain energy due to the centrifugal force and the work done by external loads, respectively.

In the thin walled beam theory employed, it is assumed that the cross section of the TWB does not distort and geometrical dimensions stay invariant in its plane, implying that $\varepsilon_{xx} = \varepsilon_{yy} = \gamma_{xy} = 0$. In addition, shell force and moment resultants due to the tangential normal stress σ_{ss} and the in-plane shear stress τ_{ns} are assumed to be small

and omitted [92]. Under these assumptions, the strain energy in terms of the nonzero 3D stress and strain components can be expressed as,

$$V = \frac{1}{2}\int_0^L \int_s \int_n \left[\sigma_{zz}\varepsilon_{zz} + \sigma_{sz}\varepsilon_{sz} + \sigma_{nz}\varepsilon_{nz}\right] dnds dz = \frac{1}{2}\int_0^L \int_s \int_n \left[\sigma_{zz}\left(\varepsilon_{zz}^0 + n\varepsilon_{zz}^1\right) + \sigma_{sz}\left(\gamma_{sz}^0 + n\gamma_{sz}^1\right) + \sigma_{nz}\gamma_{nz}^0\right] dnds dz \tag{5-17}$$

where the integral is taken over the whole cross-section of the blade and it is assumed that the blade has a length of L. Utilizing the strain displacement relations defined by Equations (5-6), (5-7) and Equations (5-12)-(5-14) and taking the integral along the wall thickness and along the contour of the cross-section of the thin walled blade, the strain energy due to the deformation of the blade caused by the external forces excluding the centrifugal force can be expressed as,

$$V = \frac{1}{2}\int_0^L \left[T_z w_0' + Q_x(\theta_y + u_0') + Q_y(\theta_x + v_0') + M_y\theta_y' + M_x\theta_x' + M_z\phi'\right] dz \tag{5-18}$$

where, T_z is the axial force, Q_x, Q_y correspond to the chord-wise and flap-wise shear forces, M_x, M_y are associated with the flap-wise bending moment (moment about x direction) and chord-wise bending moment (moment about y direction), M_z corresponds to the Saint –Venant twist moment.

As described in Chapter 2, one dimensional beam stress and moment resultants and their generalized strain counterparts given in Equation (5-18) are related to each other through Equation (5-19).

$$\{F\} = [A]\{D\} \tag{5-19}$$

where the F, A, D are the one dimensional beam stresses and moment results For the geometrically linear TWB and neglecting warping, the resulting stiffness matrix A becomes 6×6 Explicitly, one dimensional beam stress and moment resultants and

their generalized strain counterparts given in Equation (5-18) are related to each other through Equation (5-19). Explicitly, Equation (5-19) can be expressed as,

$$\begin{Bmatrix} T_z \\ Q_x \\ Q_y \\ M_y \\ M_x \\ M_z \end{Bmatrix} = \begin{bmatrix} a_{11} & a_{12} & a_{13} & a_{14} & a_{15} & a_{16} \\ & a_{22} & a_{23} & a_{24} & a_{25} & a_{26} \\ & & a_{33} & a_{34} & a_{35} & a_{36} \\ & & & a_{44} & a_{45} & a_{46} \\ & & & & a_{55} & a_{56} \\ sym & & & & & a_{66} \end{bmatrix} \begin{Bmatrix} w_0' \\ \theta_y \\ \theta_x \\ \theta_y' \\ \theta_x' \\ \phi' \end{Bmatrix} \tag{5-20}$$

For a single cell thin walled beam, stiffness coefficients a_{ij} are given by the contour integral of the stiffness coefficients A_{ij}, B_{ij}, D_{ij} as shown in Chapter 2.3. For a wind turbine blade with airfoil shape, and multi-cell configuration, calculation of the stiffness coefficients through integration over the cross-section of the blade is a tedious work. The 6×6 stiffness matrix of the cross-section (A) of the thin walled blade can also be calculated using a separate, two-dimensional linear FEM analysis of an arbitrarily shaped composite cross section which is decoupled from the one-dimensional global analysis for the beam. In this study, an improved finite element cross-sectional analysis code (VABS) is used to extract the beam sectional properties of the blade sections using the Timoshenko model for the stiffness matrix, as shown in Equation (5-20). In classical flutter, the critical flutter mode is the flapwise bending-torsion coupling. For this reason, in the present study a further simplification is made in the degrees of freedom included in the governing equations and only the flapwise bending displacement (v_0), flapwise bending rotation (θ_x) and torsional rotation (ϕ) are retained in the governing equations. Moreover, to study the effect of bending-twisting coupling on the flutter characteristics of wind turbine blades, only the bending-twisting coupling coefficient a_{56} is retained in the constitutive equation. With these simplifications, Equation (5-20) reduces to Equation (5-21).

$$\begin{Bmatrix} Q_y \\ M_x \\ M_z \end{Bmatrix} = \begin{bmatrix} a_{33} & 0 & 0 \\ & a_{55} & a_{56} \\ sym & & a_{66} \end{bmatrix} \begin{Bmatrix} \theta_x + v_0' \\ \theta_x' \\ \phi' \end{Bmatrix} \tag{5-21}$$

For the baseline and the bend-twist coupled blade configurations given in Table 5-2, Figure 5-9, Figure 5-10, Figure 5-11 and Figure 5-12 show the sectional flapwise bending (a_{55}), flapwise transverse shear (a_{33}), torsional stiffness (a_{66}) and flapwise bending-torsion coupling stiffness (a_{56}) of the inversely designed baseline blade and bend-twist coupled blades BTC 10 and BTC 20 described in Table 5-2. Sectional stiffnesses are presented only for the bend-twist coupled sections of the blade in the outboard 30 m of the blade.

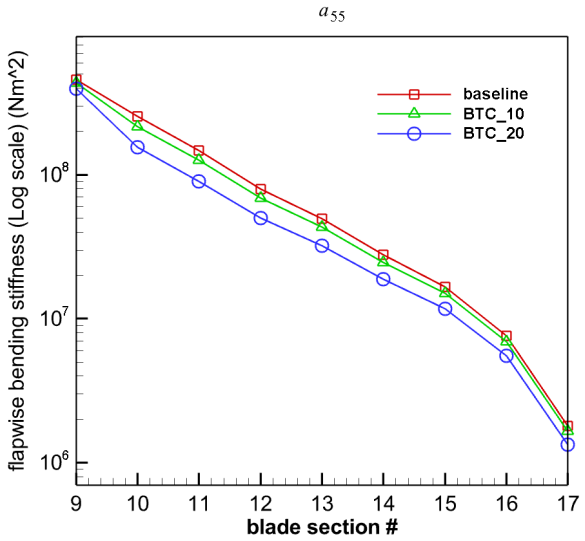

Figure 5-9 Sectional flapwise bending stiffness (a_{55}) of the blades

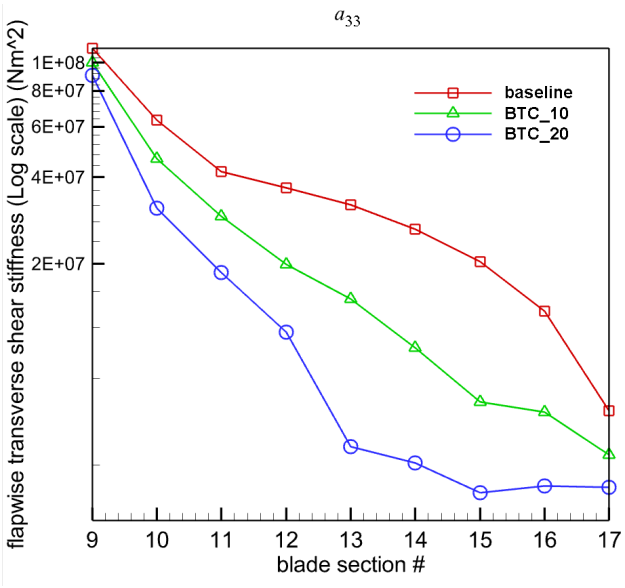

Figure 5-10 Sectional flapwise transverse shear stiffness (a_{33})of the blades

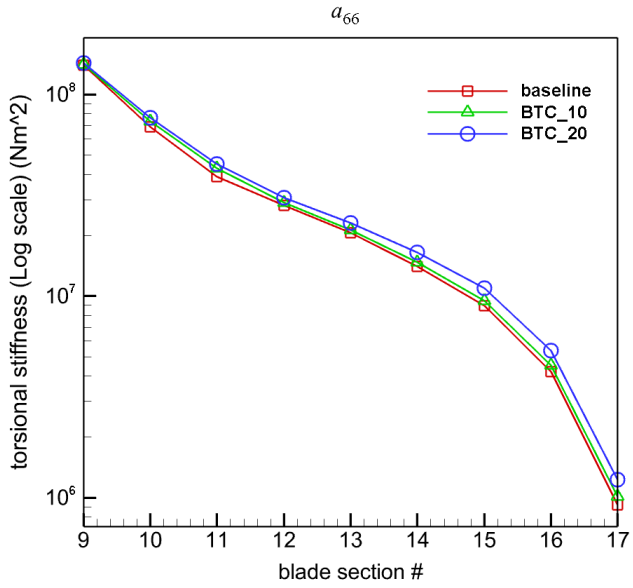

Figure 5-11 Sectional torsion stiffness (a_{66}) of the blades

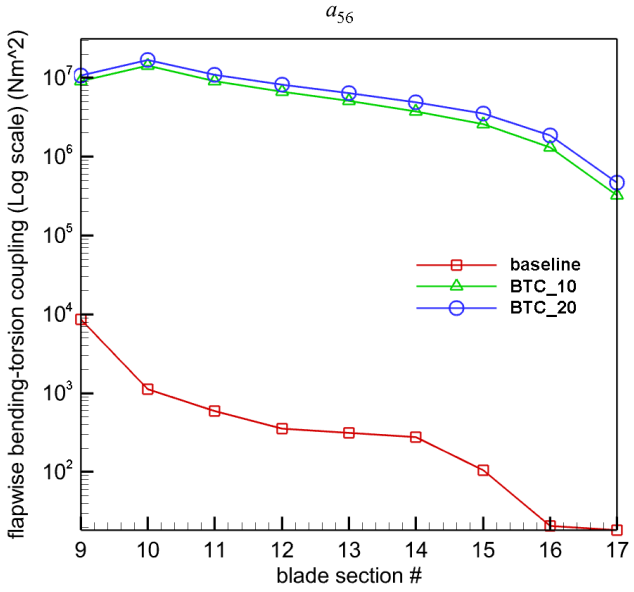

Figure 5-12 Sectional flapwise bending –torsion coupling stiffness (a_{56}) of the blades

Utilizing the simplified constitutive equation given by Equation (5-21), Equation (5-18) can be expressed as in Equation (5-22).

$$V = \frac{1}{2}\int_0^L \left[a_{33}(\theta_x + v_0')^2 + a_{55}\theta_x'^2 + 2a_{56}\left(\theta_x'\phi'\right) + a_{66}\phi'^2 \right] dz \tag{5-22}$$

In the process of the derivation of the equations of motion of the blade, one needs to express the variation of the kinetic energy. Equation (5-23) gives the variation of the kinetic energy of the blade,

$$T = \frac{1}{2}\iiint \rho \dot{R}^2 \quad dndsdz \tag{5-23}$$

$$\delta T = \iiint \rho \dot{R}\delta\dot{R} \quad dndsdz = \iiint \rho \ddot{R}\delta R \quad dndsdz$$

where ρ is the average mass density of the composite laminate of the walls of the blade and the position vector R of an arbitrary point in the deformed rotating blade with respect to the center of the hub is given by,

$$R = (x+u)\hat{i} + (y+v)\hat{j} + (z+w+R_0)\hat{k} \tag{5-24}$$

where the displacements components u, v, w are given by Equation and R_0 is the distance from the hub center to the blade root. For a blade rotating at an angular velocity Ω about the y axis shown in Figure 5-4, the acceleration of an arbitrary point $(\ddot{R})$ in the deformed rotating TWB can be expressed as,

$$\ddot{R} = a_x\hat{i} + a_y\hat{j} + a_z\hat{k} \tag{5-25}$$

where,

$$a_x = \left[\ddot{u} + \underbrace{2\dot{w}\Omega}_{Coriolis} - \underbrace{(x+u)\Omega^2}_{Centrifugal}\right], \qquad a_y = \ddot{v}, \tag{5-26}$$

$$a_z = \left[\ddot{w} - \underbrace{2\dot{u}\Omega}_{Coriolis} - \underbrace{\left(z+w+R_0\right)\Omega^2}_{Centrifugal}\right]$$

In Equation (5-26), the effects of the Coriolis and centrifugal terms induced by angular velocity are clearly identified. The variation of the kinetic energy can then be expressed as,

$$\delta T = -\int \left[b_1\ddot{v}_0\delta v_0 + b_4\left(\ddot{\theta}_x - \Omega^2\theta_x\right)\delta\theta_x + \left(b_5 - b_4\right)\left(\ddot{\phi} + \Omega^2\phi\right)\delta\phi\right]dz \tag{5-27}$$

where, the distribution of non-vanishing inertia terms, mass per unit length (b_1) and mass moment of inertia about the x, y axes (b_4, b_5) along the blade span are defined in Chapter 2, and in log scale variation of the mass and inertia terms are presented in Figure 5-13.

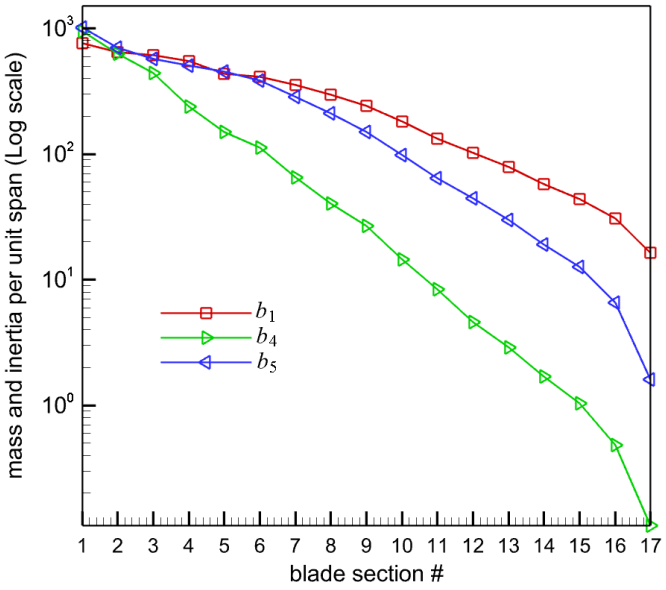

Figure 5-13 variation of the mass per unit span (b_1) and mass moment of inertia (b_4, b_5) along the blade span

Rotary blades are subjected to centrifugal forces and in the present study the effect of centrifugal forces is also taken into account. The centrifugal force acting on the rotating beam at a spanwise location z can be expressed as,

$$F_c = \int_z^L \rho\Omega^2 \left(R_0 + z\right) dz = \rho\Omega^2 R\left(z\right) \tag{5-28}$$

where, ρ is the density of the TWB and $R(z)$ is defined as,

$$R\left(z\right) = \left[R_0\left(L - z\right) + \frac{1}{2}\left(L^2 - z^2\right)\right] \tag{5-29}$$

The contribution of the centrifugal force to the strain energy in the TWB can be expressed as,

$$V_{cf} = \frac{1}{2}\int_0^L \int_s \int_n F_c \left[\left(u'\right)^2 + \left(v'\right)^2\right] dnds dz \tag{5-30}$$

where, u, v are the 3-D displacements in the edgewise and flapwise directions, respectively and F_c is the centrifugal force. By substituting the displacements defined by Equation (5-1) and the centrifugal force defined by Equation (5-28) into Equation (5-30), the variation of the strain energy due to centrifugal force is obtained in explicit form as in Equation (5-31).

$$\begin{aligned}\delta V_{cf} = -\int \begin{bmatrix} b_1\Omega^2\left(R(z)v_0'' + R'(z)v_0'\right)\delta v_0 + \\ \left(b_4 + b_5\right)\Omega^2\left(R(z)\phi'' + R'(z)\phi'\right)\delta\phi \end{bmatrix} dz + \\ \left[b_1\Omega^2\left(R(z)v_0'\right)\delta v_0 + \left(b_4 + b_5\right)\Omega^2\left(R(z)\phi'\right)\delta\phi\right]_0^L\end{aligned} \tag{5-31}$$

5.2.4 Unsteady aerodynamics models

The last portion of the Hamiltonian in Equation (5-16) is the variation of work done by the external loadings. The only loading considered in this study is the one due to the unsteady aerodynamics. Hence, one can write δW as,

$$\delta W = \int_0^L \left(L_{ae}(z,t)\delta v_0(z) + M_{ae}(z,t)\delta\phi(z)\right) dz \tag{5-32}$$

Where L_{ae} and M_{ae} are the unsteady aerodynamic lift and pitching moment.

For a large wind turbine blade, the aerodynamics for a single blade is similar to that of a fixed wing but with a free stream velocity that varies linearly from the root to the tip. It is also assumed that the shed wake of the preceding blade dies out sufficiently fast so that the oncoming blade essentially encounters still air. In the following, both the incompressible and compressible unsteady aerodynamics models based on indicial functions are introduced by referencing Chapter 3. In the present study, the static deformation of the blade and the mean steady aerodynamic loads are not considered, and the flutter occurrence is investigated with respect to the undeformed blade. One common assumption in both models is the attached flow assumption since the aerodynamic models are based on small disturbance theory. Thus, intrinsic flutter

characteristics of the wind turbine blade has been investigated for small deformation of the blade about a static deformation state utilizing linear unsteady aerodynamics. However, the current model can be improved by including stall aerodynamics using models such as ONERA stall aerodynamics as a future study.

5.2.4.1 Incompressible unsteady aerodynamics based on Wagner's function

By referencing Chapter 3, the general form of the unsteady incompressible aerodynamic lift L_{ae}^{inc} and pitching moment M_{ae}^{inc} expressed in terms of Wagner's function are given by Equations (5-33) and (5-34).

$$L_{ae}^{inc}(z,t) = -\pi\rho b^2 \dot{w}_{0.5c}(z,t) - C_{L\phi}\rho U_r b\left\{ w_{0.75c}(z,0)\phi_W(\frac{U_r}{b}t) + \int_0^t \left[\frac{dw_{0.75c}(z,\tau)}{d\tau}\phi_W\left(\frac{U_r}{b}(t-\tau)\right)\right] d\tau \right\} \quad (5\text{-}33)$$

$$M_{ae}^{inc}(z,t) = -\pi\rho b^3\left[\frac{U_r}{2}\dot{\phi} - U_r a\dot{\phi} + a\ddot{v}_0 + b\left(\frac{1}{8}+a^2\right)\ddot{\phi}\right] - C_{L\phi}\rho U_r b^2\left(\frac{1}{2}+a\right)\left\{ w_{0.75}(z,0)\,\phi_W(\frac{U_r}{b}t) + \int_0^t \left[\frac{dw_{0.75c}(z,\tau)}{d\tau}\phi_W\left(\frac{U_r}{b}(t-\tau)\right)\right] d\tau \right\} \quad (5\text{-}34)$$

where ρ, b U_r, $C_{L\phi}$, a are the air density, semi-chord length of the blade, relative wind speed, lift curve slope and the nondimensional offset between the shear center and the mid-chord, respectively. ϕ_W is the incompressible indicial function, Wagner's function, and $w_{0.5c}(z,t)$, $w_{0.75c}(z,t)$ are the downwash terms at the mid-chord and three-quarter chord of the blade and the are given by Equations (3-9). A negative value of the a parameter indicates that the shear center is forward of the mid chord. For a wind turbine blade rotating at an angular velocity of Ω , the relative velocity U_r at blade section z measured from the hub center is given by Equation (5-35).

$$U_r = \sqrt{U_i^2 + (\Omega z)^2} \tag{5-35}$$

As discussed in Chapter 3, the integrals appearing in Equations (5-33) and (5-34) are handled by using the approximate representation of the Wagner's function given by,

$$\phi_W(\frac{U_r}{b}t) = 1 - \sum_{i=1}^{2} \alpha_i e^{-\beta_i \frac{U_r}{b}t} \tag{5-36}$$

where $H(t)$ represents the step function and α_1 =0.165, α_2 =0.335 , β_1 =0.335, β_2 = 0.3. Substituting the approximation of the Wagner's function into the integral expressions in Equations (5-33) and (5-34), one can express the integrals in terms of aerodynamic lag terms $B_i(z,t)$ as,

$$\int_0^t \frac{dw_{0.75c}(z,\tau)}{d\tau} \phi_W\left(\frac{U_r}{b}(t-\tau)\right) d\tau = w_{0.75c}(z,t) - \sum_{i=1}^{n} \alpha_i B_i(z,t) \tag{5-37}$$

where, by making use of the Leibniz integral rule, it can be shown that the aerodynamic lag terms $B_i(z,t)$ have to satisfy Equation (5-38).

$$\dot{B}_i + (\beta_i \frac{U_r}{b}) B_i = \dot{w}_{0.75c}(z,t); \qquad i = 1,2 \tag{5-38}$$

For 3-D blades with finite span, to reflect the 3-D effects, lift curve slope and the position of the three-quarter chord position, where the downwash is calculated, are modified according to Equation (5-39) only in the circulatory lift and moment expressions in Equations (5-33) and (5-34).

$$C_{L\phi} = \frac{AR}{AR\sqrt{1+\left(\frac{2}{AR}\right)^2}+2} c_{l\phi} \tag{5-39}$$

where, AR is the aspect ratio.

Substituting the approximation of the integral in Equation (5-37) and the downwash at the mid-chord and three-quarter chord into the unsteady lift and moment expressions, Equations (5-33) and (5-34), the final form of the unsteady lift and moment are obtained as given by Equation (5-40) and (4-41).

$$\begin{aligned} L_{ae}^{inc}(z,t) = & -\pi\rho_\infty b^2[\ddot{v}_0 - U_r\dot{\phi} + ba\ddot{\phi}] - \\ & C_{L\phi}\rho_\infty U_r b\left[\dot{v}_0 - U_r\phi + ba\dot{\phi} - \frac{b}{2}(\frac{C_{L\phi}}{\pi}-1)\dot{\phi} - \sum_{i=1}^{2}\alpha_i B_i(z,t)\right] \end{aligned} \tag{5-40}$$

$$\begin{aligned} M_{ae}^{inc}(z,t) = & -\pi\rho_\infty b^3\left[\frac{1}{2}(\frac{C_{L\phi}}{\pi}-1)U_r\dot{\phi} - U_r a\dot{\phi} + a\ddot{v}_0 + b(\frac{1}{8}+a^2)\ddot{\phi}\right] \\ & - C_{L\phi}\rho_\infty U_r b^2\left(\frac{1}{2}+a\right)\left[\dot{v}_0 - U_r\phi + ba\dot{\phi} - \frac{b}{2}(\frac{C_{L\phi}}{\pi}-1)\dot{\phi} - \sum_{i=1}^{2}\alpha_i B_i(z,t)\right] \end{aligned} \tag{5-41}$$

5.2.4.2 Compressible Unsteady Aerodynamics Based on Compressible Indicial Functions

In the present study, to study the effect of compressibility on the flutter characteristics of wind turbine blades, explicit expressions for the unsteady aerodynamic loading in the subsonic compressible flow regime in time domain are obtained using indicial aerodynamics. For arbitrary small motions of the thin airfoil in the subsonic flow, with respect to the baseline axis placed at the leading edge of the airfoil, downwash velocity corresponding to pitching and plunging motions can be expressed as,

$$w_a(x,z,t) = \underbrace{\left[\dot{v}_0(z,t) - U_r\phi(z,t)\right]}_{w_v(z,t)} - x\,\underbrace{\dot{\phi}(z,t)}_{w_\phi(z,t)} \tag{5-42}$$

where the downwash velocity is divided into two parts; $w_v = \dot{v}_0 - U_r\phi$ indicates the plunging motion and $w_\phi = \dot{\phi}$ is the pitching motion of the airfoil.

Compressible aerodynamic loads in the Theodorsen's coordinate which is located at a distance $b(a+1)$ behind the leading edge are defined in terms of the indicial functions as;

$$L^c_{ae}\left(z,t\right) = -C_{L\phi}\rho U_r b\left[w_v(z,0)\,\bar{\phi}_c(\frac{U_r}{b}t) + \int_0^t \frac{dw_v(z,\tau)}{d\tau}\bar{\phi}_c\left(\frac{U_r}{b}(t-\tau)\right)d\tau\right] + \tag{5-43}$$
$$2C_{L\phi}\rho U_r b^2\left[w_\phi(z,0)\bar{\phi}_{cq}(\frac{U_r}{b}t) + \int_0^t \frac{dw_\phi\left(z,\tau\right)}{d\tau}\bar{\phi}_{cq}\left(\frac{U_r}{b}(t-\tau)\right)d\tau\right]$$

$$M^c_{ae}\left(z,t\right) = -2C_{L\phi}\rho U_r b^2\left[w_v(z,0)\,\bar{\phi}_{cM}(\frac{U_r}{b}t) + \int_0^t \frac{dw_v(z,\tau)}{d\tau}\bar{\phi}_c\left(\frac{U_r}{b}(t-\tau)\right)dt_0\right] + \tag{5-44}$$
$$4C_{L\phi}\rho U_r b^3\left[w_\phi(z,0)\bar{\phi}_{cMq}(\frac{U_r}{b}t) + \int_0^t \frac{dw_\phi\left(z,\tau\right)}{d\tau}\bar{\phi}_{cMq}\left(\frac{U_r}{b}(t-\tau)\right)dt_0\right]$$

where the set of aerodynamic indicial functions in the Theodorsen's coordinate $(\bar{\phi}_c, \bar{\phi}_{cM}, \bar{\phi}_{cq}, \bar{\phi}_{cMq})$ are related to the indicial functions defined with respect to the axis located at the leading edge of the airfoil as,

$$\begin{aligned}
&\bar{\phi}_c\left(M,\frac{U_r}{b}t\right) = \phi_c\left(M,\frac{U_r}{b}t\right)\\
&\bar{\phi}_{cM}\left(M,\frac{U_r}{b}t\right) = \phi_{cM}\left(M,\frac{U_r}{b}t\right) + \left(\frac{a}{2}+\frac{1}{2}\right)\phi_c\left(M,\frac{U_r}{b}t\right)\\
&\bar{\phi}_{cq}\left(M,\frac{U_r}{b}t\right) = \phi_{cq}\left(M,\frac{U_r}{b}t\right) - \left(\frac{a}{2}+\frac{1}{2}\right)\phi_c\left(M,\frac{U_r}{b}t\right)\\
&\bar{\phi}_{cMq}\left(M,\frac{U_r}{b}t\right) = \phi_{cMq}\left(M,\frac{U_r}{b}t\right) + \left(\frac{a}{2}+\frac{1}{2}\right)\left(\phi_{cq}\left(M,\frac{U_r}{b}t\right) - \phi_{cM}\left(M,\frac{U_r}{b}t\right)\right) -\\
&\quad \left(\frac{a}{2}+\frac{1}{2}\right)^2\phi_c\left(M,\frac{U_r}{b}t\right)
\end{aligned} \tag{5-45}$$

where, ϕ_c and ϕ_{cM} are the indicial lift and pitching moment functions due to the unit step change of the plunging motion (w_v) and ϕ_{cq} and ϕ_{cMq} are the indicial lift and pitching moment functions due to the unit step change of the pitching motion (w_ϕ)

about the coordinate located at the leading edge of the airfoil. It should be noted that to simplify the writing, Mach dependency of the indicial functions is not shown in the lift and pitching moment expressions given by Equations (5-43) and (5-44).

Similar to the incompressible case, approximate representations of the Mach number dependent compressible indicial functions, defined with respect to the leading edge of the airfoil, may be utilized to handle the integrals appearing given in the unsteady lift and moment expressions in Equations (5-43) and (5-44). Equation

(5-46) gives the approximate representations of the compressible indicial functions which are used in the present study. It should be noted that in the literature, coefficients of the exponential representations of the indicial functions are obtained numerically for a limited number of Mach numbers $(M = 0.5, 0.6, 0.7, 0.8)$. For the frequency domain solution of the flutter in the compressible flow regime, compressible indicial functions have to be calculated for any Mach number. For this purpose, as described in detail in Chapter 3 a methodology is used to extract the coefficients of the approximate representations of the compressible indicial functions for any Mach number less than 0.8.

$$\begin{aligned}
\phi_c\left(M, \frac{U_r}{b}t\right) &= \alpha_{0c}(M) - \sum_{i=1}^{3} \alpha_{ic}(M)\, \mathrm{e}^{-\beta_i \frac{U_r}{b}t} \\
\phi_{cM}\left(M, \frac{U_r}{b}t\right) &= \alpha_{0cM}(M) - \sum_{i=1}^{3} \alpha_{icM}(M)\, \mathrm{e}^{-\beta_i \frac{U_r}{b}t} \\
\phi_{cq}\left(M, \frac{U_r}{b}t\right) &= \alpha_{0cq}(M) - \sum_{i=1}^{3} \alpha_{icq}(M)\, \mathrm{e}^{-\beta_i \frac{U_r}{b}t} \\
\phi_{cMq}\left(M, \frac{U_r}{b}t\right) &= \alpha_{0cMq}(M) - \sum_{i=1}^{3} \alpha_{icMq}(M)\, \mathrm{e}^{-\beta_i \frac{U_r}{b}t}
\end{aligned} \tag{5-46}$$

Based on method comprehensively explained in Chapter 2, once the Mach dependent base coefficients $(\alpha_{ic,icM,icq,icMq}(M), i = 1,2,3)$ of the lift and the moment compressible indicial functions for the plunging and pitching motion with respect to the coordinate

system established at the leading edge of the airfoil are determined for any Mach number, base coefficients with respect to the axis located at $b(a+1)$ aft of the leading edge can be determined utilizing the relations given by Equation (5-47),

$$
\begin{aligned}
&\bar{\alpha}_{ic}(M) = \alpha_{ic}(M) \\
&\bar{\alpha}_{icM}(M) = \alpha_{icM}(M) + \left(\frac{a}{2}+\frac{1}{2}\right)\alpha_{ic}(M) \\
&\bar{\alpha}_{icq}(M) = \alpha_{icq}(M) - \left(\frac{a}{2}+\frac{1}{2}\right)\alpha_{ic}(M) \\
&\bar{\alpha}_{icMq}(M) = \alpha_{icMq}(M) + \left(\frac{a}{2}+\frac{1}{2}\right)\left(\alpha_{icq}(M) - \alpha_{icM}(M)\right) - \left(\frac{a}{2}+\frac{1}{2}\right)^2 \alpha_{ic}(M)
\end{aligned}
\tag{5-47}
$$

Where $i = 1,2,3$. It should be noted that these relations are the same as those given by Equations (5-45) for the indicial functions themselves owing to the fact that, the approximate exponential representation of the four indicial functions are defined with the same Mach-independent power coefficients $(\beta_i, i = 1,2,3)$.

The integrals in the lift and moment expressions in Equations (5-43) and (5-44) are re-expressed by substituting the exponential representations of the indicial functions, defined with respect to the axis located at $b(a+1)$ aft of the leading edge, in the integrals as shown in Equation (5-48).

$$
\begin{aligned}
D_1(z,t) &= \int_0^t \frac{dw_v(z,\tau)}{d\tau}\bar{\phi}_c\left(\frac{U_r}{b}(t-\tau)\right)d\tau = \int_0^t \frac{dw_v(z,\tau)}{d\tau}\left(\bar{\alpha}_{0c}(M) - \sum_{i=1}^{3}\bar{\alpha}_{ic}(M)\,\mathrm{e}^{-\beta_i\frac{U_r}{b}(t-\tau)}\right)d\tau \\
D_2(z,t) &= \int_0^t \frac{dw_\phi(z,\tau)}{d\tau}\bar{\phi}_{cq}\left(\frac{U_r}{b}(t-\tau)\right)d\tau = \int_0^t \frac{dw_\phi(z,\tau)}{d\tau}\left(\bar{\alpha}_{0cq}(M) - \sum_{i=1}^{3}\bar{\alpha}_{icq}(M)\,\mathrm{e}^{-\beta_i\frac{U_r}{b}(t-\tau)}\right)d\tau \\
D_3(z,t) &= \int_0^t \frac{dw_v(z,\tau)}{d\tau}\bar{\phi}_{cM}\left(\frac{U_r}{b}(t-\tau)\right)d\tau = \int_0^t \frac{dw_v(z,\tau)}{d\tau}\left(\bar{\alpha}_{0cM}(M) - \sum_{i=1}^{3}\bar{\alpha}_{icM}(M)\,\mathrm{e}^{-\beta_i\frac{U_r}{b}(t-\tau)}\right)d\tau \\
D_4(z,t) &= \int_0^t \frac{dw_\phi(z,\tau)}{d\tau}\bar{\phi}_{cqM}\left(\frac{U_r}{b}(t-\tau)\right)d\tau = \int_0^t \frac{dw_\phi(z,\tau)}{d\tau}\left(\bar{\alpha}_{0cqM}(M) - \sum_{i=1}^{3}\bar{\alpha}_{icqM}(M)\,\mathrm{e}^{-\beta_i\frac{U_r}{b}(t-\tau)}\right)d\tau
\end{aligned}
\tag{5-48}
$$

By defining the integrals involving the exponential terms in Equation (5-48) as the aerodynamic lag terms $B_{ic,icq,icM,icMq}(z,t)$, assuming that the wing is initially at rest (

$w_v(z,0) = w_\phi(z,0) = 0$) and making use of the Leibniz integral rule, Equation (5-48) is transformed into Equation (5-49).

$$
\begin{aligned}
D_1\left(z,t\right) &= \overline{\alpha}_{0_c} w_v(z,t) - \sum_{i=1}^{3} \overline{\alpha}_{ic} B_{ic}\left(z,t\right) \\
D_2\left(z,t\right) &= \overline{\alpha}_{0_{cq}} w_\phi(z,t) - \sum_{i=1}^{3} \overline{\alpha}_{icq} B_{icq}\left(z,t\right) \\
D_3\left(z,t\right) &= \overline{\alpha}_{0_{cM}} w_v(z,t) - \sum_{i=1}^{3} \overline{\alpha}_{icM} B_{icM}\left(z,t\right) \\
D_4\left(z,t\right) &= \overline{\alpha}_{0_{cMq}} w_\phi(z,t) - \sum_{i=1}^{3} \overline{\alpha}_{icMq} B_{icMq}\left(z,t\right)
\end{aligned}
\tag{5-49}
$$

When the Leibniz integral rule is applied to the integrals involving the exponential terms in Equation (5-49), it can be shown that the aerodynamic lag terms $B_{ic,icq,icM,icMq}\left(z,t\right)$ are defined by Equation (5-50),

$$
\begin{aligned}
\dot{B}_{ic}\left(z,t\right) + (\beta_i \frac{U_r}{b}) B_{ic}\left(z,t\right) &= \frac{dw_v\left(z,t\right)}{dt} \\
\dot{B}_{icq}\left(z,t\right) + (\beta_i \frac{U_r}{b}) B_{icq}\left(z,t\right) &= \frac{dw_\phi\left(z,t\right)}{dt} \\
\dot{B}_{icM}\left(z,t\right) + (\beta_i \frac{U_r}{b}) B_{icM}\left(z,t\right) &= \frac{dw_v\left(z,t\right)}{dt} \\
\dot{B}_{icMq}\left(z,t\right) + (\beta_i \frac{U_r}{b}) B_{icMq}\left(z,t\right) &= \frac{dw_\phi\left(z,t\right)}{dt}
\end{aligned}
\tag{5-50}
$$

It should be noted that three aerodynamic lag terms are used for each indicial function so a total number of twelve aerodynamic lag terms would exist in the description of the 3D unsteady aerodynamic loads in the subsonic compressible flow. Finally, unsteady compressible aerodynamic lift $L^c_{ae}(z,t)$ and pitching moment $M^c_{ae}(z,t)$ about the Theodorsen's coordinate in terms of indicial functions are expressed as,

$$L_{ae}^{c}(z,t) = -C_{L\phi}\rho U_r b\left[\overline{\alpha}_{0c}(M)w_v\left(z,t\right) - \sum_{i=1}^{3}\overline{\alpha}_{ic}(M)B_{ic}\left(z,t\right)\right] + 2C_{L\phi}\rho U_r b^2\left[\overline{\alpha}_{0cq}(M)w_\phi\left(z,t\right) - \sum_{i=1}^{3}\overline{\alpha}_{icq}(M)B_{icq}\left(z,t\right)\right] \tag{5-51}$$

$$M_{ae}^{c}(z,t) = -2C_{L\phi}\rho U_r b^2\left[\overline{\alpha}_{0cM}(M)w_v\left(z,t\right) - \sum_{i=1}^{3}\overline{\alpha}_{icM}(M)B_{icM}\left(z,t\right)\right] + 4C_{L\phi}\rho U_r b^3\left[\overline{\alpha}_{0cMq}(M)w_\phi\left(z,t\right) - \sum_{i=1}^{3}\overline{\alpha}_{icMq}(M)B_{icMq}\left(z,t\right)\right] \tag{5-52}$$

To include 3-D effects of the finite span wing, lift curve slope $C_{L\phi}$ is obtained from Diederich general formula as [100],

$$C_{L\phi} = \frac{ARc_{l\phi}}{AR\sqrt{1-M^2}\sqrt{1+\left(\frac{c_{l\phi}}{\pi AR\sqrt{1-M^2}}\right)^2}+\frac{c_{l\phi}}{\pi}} \tag{5-53}$$

Where M is the Mach number and $c_{l\phi}$ is the 2D lift curve slope.

5.2.5 Governing Equation of Motion of the Beam-Blade Model

The geometrically linear form of aeroelastic governing equations of motion have been derived through the Hamilton's principle, by including the expressions for the variations of the strain energy due to deformation, strain energy due to centrifugal force and the kinetic energy in Equation (5-16). As it is mentioned previously, to study the classical flutter phenomenon in a simplified way, in the governing equations, and only the flapwise bending displacement (v_0), flapwise bending rotation (θ_x) and the torsional rotation (ϕ) are retained in the governing equations. Moreover, to study the effect of bending-twisting coupling on the flutter characteristics of wind turbine blades, only the bending-twisting coupling is retained in the constitutive equation given by Equation (5-21).

Application of the Hamilton's principle yields Equations (5-54)-(5-56) as the governing aeroelastic equations of motion for the beam-blade. In Equations (5-54)-(5-56), if the compressibility effect is neglected, then unsteady aerodynamic lift and moment expressions $L_{ae}(z,t)$ and $M_{ae}(z,t)$ are equal to their incompressible counterparts given by Equations (5-40) and (5-41). On the other hand, if the compressibility effect is included, then for the sections of the blade which are in the incompressible flow regime, $L_{ae}(z,t)$ and $M_{ae}(z,t)$ are again equal to their incompressible counterparts given by Equations (5-40) and (5-41), and for the sections of the blade which are in the compressible flow regime, $L_{ae}(z,t)$ and $M_{ae}(z,t)$ are equal to their compressible counterparts given by Equations (5-51) and (5-52).

$$\delta v_0 : a_{33}(v_0'' + \theta_x') - b_1\left(\ddot{v}_0 - \Omega^2\left[v_0'' R(z) + R'(z)v_0'\right]\right) + L_{ae}(z,t) = 0 \tag{5-54}$$

$$\delta\theta_x : -a_{33}\left(v_0' + \theta_x\right) + a_{55}\theta_x'' + a_{56}\phi'' - b_4\left(\ddot{\theta}_x - \Omega^2\theta_x\right) = 0 \tag{5-55}$$

$$\delta\phi : a_{56}\theta_x'' + a_{66}\phi'' + \left(b_4 + b_5\right)\Omega^2\left(R(z)\phi'' + R'(z)\phi'\right) - \left(b_4 - b_5\right)\left(\ddot{\phi} + \Omega^2\phi\right) + M_{ae}(z,t) = 0 \tag{5-56}$$

5.2.6 Solution methodology

5.2.6.1 Solution of the Aeroelastic System of Equations of the Beam-Blade Neglecting Compressibility Effects

When the compressibility effects are neglected, unsteady lift and moment expressions given by Equations (5-40) and (5-41) are used in the aeroelastic system of Equations (5-54)-(5-56), and the Extended Galerkin`s Method (EGM) is employed for the solution of aeroelastic instability speed and frequency. For the incompressible unsteady aerodynamics, structural degree of freedom vector, which is composed of the

flapwise bending deflection (v_0), flapwise bending rotation (θ_x) and the torsional deformation (ϕ), is augmented with the aerodynamic variables which are the aerodynamic lag states B_1 and B_2. The variables of the aeroelastic system are denoted by the symbol Δ as shown in Equation (5-57).

$$\Delta \in \left(v_o, \theta_x, \phi, B_1, B_2 \right) \tag{5-57}$$

For the incompressible aerodynamics, governing aeroelastic system of equations comprise of Equations (5-54)-(5-56), and Equation (5-38) for the two aerodynamic lag states B_1, B_2.

In order to employ the EGM, structural and aerodynamic variables are separated spatially and temporally as,

$$\Delta(z,t) = \left\{ \Psi_\Delta(z) \right\}^T \left\{ q_\Delta(t) \right\} \tag{5-58}$$

where,

$$\begin{aligned} \left\{ \Psi_\Delta(z) \right\} &= \left\{ \Psi_{\Delta,1}(z)\ \Psi_{\Delta,2}(z) \ldots \Psi_{\Delta,N}(z) \right\}^T \\ \left\{ q_\Delta(t) \right\} &= \left\{ q_{\Delta,1}(t)\ q_{\Delta,2}(t) \ldots\ q_{\Delta,N}(t) \right\}^T \end{aligned} \tag{5-59}$$

where, $\Psi_{\Delta,i}$ is the polynomial shape function of degree *i* which satisfies the essential boundary conditions and *N* is the highest degree of the polynomial that is retained in the shape function vector $\left\{ \Psi_\Delta(z) \right\}$. In the present study, to achieve convergence for flutter solutions, polynomials up to 9th degree (*N* =9) are taken as the shape functions ($\left\{ \Psi_\Delta(z) \right\} = z^i\ ;\ i = 1 \ldots 9$). The state vector of the generalized time dependent variables of the aeroelastic system is defined by Equation (5-60).

$$\{q(t)\} = \left\{ \underbrace{\{q_v(t)\}^T \quad \{q_{\theta_x}(t)\}^T \quad \{q_\phi(t)\}^T}_{q_{str}} \quad \{q_{B_1}(t)\}^T \quad \{q_{B_2}(t)\}^T \right\}^T \tag{5-60}$$

In the governing aeroelastic system of equations given by Equations (5-54)-(5-56) and Equation (5-38), the structural variables (v_0, θ_x, ϕ) and incompressible aerodynamic variables (B_1, B_2) are substituted by their spatially and temporally separated forms given by Equation (5-58). Then, in the implementation of the EGM, Equation (5-54) is multiplied by Ψ_v, Equation (5-55) is multiplied by Ψ_{θ_x}, Equation (5-56) is multiplied by Ψ_ϕ, for *i*=1 Equation (5-38) is multiplied by Ψ_{B_1} and for *i*=2 Equation (5-38) is multiplied by Ψ_{B_2} and the resulting equations are integrated along the blade span with respect to *z*. As a result of implementing EGM, the general aeroelastic system of equations are obtained as,

$$\begin{aligned} \left[\boldsymbol{M}_s + \boldsymbol{M}_a^{inc} \right]_{5N \times 3N} \{\ddot{q}_{str}\} + \left[\boldsymbol{C}_a^{inc} \right]_{5N \times 5N} \{\dot{q}\} + \\ \left[\boldsymbol{K}_s + \boldsymbol{K}_a^{inc} \right]_{5N \times 5N} \{q\} = \{0\} \end{aligned} \tag{5-61}$$

where, $\boldsymbol{M}_s$ and $\boldsymbol{M}_a^{inc}$ are the structural and the incompressible aerodynamic mass matrices, $\boldsymbol{C}_a^{inc}$ is the incompressible aerodynamic damping matrix, and $\boldsymbol{K}_s$ and $\boldsymbol{K}_a^{inc}$ are the structural and the incompressible aerodynamic stiffness matrices. Explicit definitions of the matrices are given in Appendix G.

Equation (5-61) is expressed in state space form by augmenting the state vector of the generalized time dependent variables $\{q(t)\}$ by the time derivatives of the generalized time dependent structural variables, as shown in Equation (5-62).

$$\{X(t)\}_{8NX1} = \left\{ \{q(t)\}^T \quad \{\dot{q}_{v_0}(t)\}^T \quad \{\dot{q}_{\theta_x}(t)\}^T \quad \{\dot{q}_\phi(t)\}^T \right\}^T \tag{5-62}$$

With the definition of the augmented the state vector of the generalized time dependent variables, Equation (5-61) is transformed into Equation (5-63).

$$\begin{bmatrix} \boldsymbol{C}_a^{inc} & \left(\boldsymbol{M}_s + \boldsymbol{M}_a^{inc}\right) \\ \boldsymbol{I} & \boldsymbol{0} \end{bmatrix}_{8N\times 8N} \{\dot{X}\} + \begin{bmatrix} \left(\boldsymbol{K}_s + \boldsymbol{K}_a^{inc}\right) & \boldsymbol{0} \\ \boldsymbol{0} & -\boldsymbol{I} \end{bmatrix}_{8N\times 8N} \{X\} = \{0\} \quad (5\text{-}63)$$

where $\boldsymbol{I}$ is the identity matrix of order $3N\times 5N$ and $\boldsymbol{0}$ is the zero matrix of order $3N\times 3N$ Equation (5-63) can then be re-written in a more compact state space form as,

$$\{\dot{X}\} = [\boldsymbol{A}]\{X\} \quad (5\text{-}64)$$

where the coefficient matrix $\boldsymbol{A}$ is given by Equation (5-65).

$$[\boldsymbol{A}] = \begin{bmatrix} \boldsymbol{C}_a^{inc} & \left(\boldsymbol{M}_s + \boldsymbol{M}_a^{inc}\right) \\ \boldsymbol{I} & \boldsymbol{0} \end{bmatrix}^{-1} \begin{bmatrix} \left(\boldsymbol{K}_s + \boldsymbol{K}_a^{inc}\right) & \boldsymbol{0} \\ \boldsymbol{0} & -\boldsymbol{I} \end{bmatrix} \quad (5\text{-}65)$$

The solution to Equation (5-64) is assumed to be in the form of,

$$\{X(t)\} = \{X_0\} e^{\lambda t} \quad (5\text{-}66)$$

where $\{X_0\}$ is an amplitude vector and λ is the eigenvalue, both of which can be complex quantities, in general. After inserting Equation (5-66) into Equation (5-64), the eigenvalue problem is obtained as in Equation (5-67).

$$\{A\}\{\boldsymbol{X}_0\} = \lambda\{\boldsymbol{X}_0\} \quad (5\text{-}67)$$

Solution of (5-67) yields the eigenvalues λ_r and the corresponding eigenvectors $\{X_0\}_r$ $(r = 1,2,...8N)$. The real part of the eigenvalue λ_r is the measure of the damping of the *r*th mode and the imaginary part of the eigenvalue λ_r is the *r*th frequency of the damped oscillation of the beam-blade. To predict the onset of aeroelasic instability, for varying relative wind speeds, eigenvalue solutions are performed until the aerodynamic damping, which is the real part of the eigenvalue λ_r , becomes zero. Relative wind speed corresponding to the zero aerodynamic damping is the aeroelastic instability speed. At this speed, the imaginary part of the eigenvalue gives the frequency associated with the aeroelastic instability. If the frequency comes out as zero, then aeroelastic instability is divergence instability and if the frequency is

non-zero, aeroelastic instability is flutter instability. With this approach, frequency domain solution of the aeroelastic instability speed and frequency of the beam-blade can be obtained very fast. It should be noted that for a rotating wind turbine blade, relative wind velocity depends on both the inflow wind speed and the rotational speed of the blade. Hence, one needs to perform aeroelastic instability analysis either at a fixed wind speed and determine the flutter rotational speed, or determine the flutter wind speed corresponding to a specified rotational speed of the rotor.

Moreover, time domain solution of Equation (5-64) gives the time response of the aeroelastic system for a prescribed initial condition. With the time domain solution approach, aeroelastic instability speed and frequency can also be identified by performing solutions at different relative wind speeds (U_r) until diverging oscillations are obtained.

5.2.6.2 Solution of the Aeroelastic System of Equations of the Beam-Blade Including Compressibility Effects

In the present study, the compressibility effects are included into the solution process by switching from incompressible unsteady aerodynamics to compressible unsteady aerodynamics for blade sections away from the blade root. Compressibility effects are included starting from the blade section at which the relative velocity becomes higher than Mach 0.3. Figure G1 in Appendix G2 gives the schematic of the wind turbine blade whose sections are both in the incompressible and compressible flow regime.

In the compressible flow regime, the solution process for the aeroelastic instability speed and frequency by the EGM is essentially the same as the process described for the incompressible unsteady aerodynamics case. For the blade sections which are in the compressible flow regime, structural degree of freedom vector, which is composed of the flapwise bending deflection (v_0), flapwise bending rotation (θ_x) and the torsional deformation (ϕ), is augmented with the twelve the aerodynamic lag states defined for the compressible lift and pitching moment indicial functions corresponding

to the plunging and pitching motions, respectively. Hence, for the compressible unsteady aerodynamics case, variables of the aeroelastic system are given by Equation (5-68).

$$\Delta \in \begin{pmatrix} v_o, \theta_x, \phi, B_{1c}, B_{2c}, B_{3c}, B_{1cq}, B_{2cq}, B_{3cq}, B_{1cM}, \\ B_{2cM}, B_{3cM}, B_{1cMq}, B_{2cMq}, B_{3cMq} \end{pmatrix} \tag{5-68}$$

Similar to the incompressible case, in the governing aeroelastic system of equations given by Equations (5-54)-(5-56) and Equation (5-50), the structural variables (v_0, θ_x, ϕ) and compressible aerodynamic variables $(B_{ic}, B_{icq}, B_{icM}, B_{icMq},\ i = 1,2,3)$ are substituted by their spatially and temporally separated forms given by Equation (5-58) where $\{q_\Delta(t)\}$ is now defined using the variables of the aeroelastic system involving compressible aerodynamics given by Equation (5-68). Extended Galerkin Method is applied in the same way as in the incompressible case by multiplying each equation by the polynomial shape function $\Psi_\Delta(z)$ corresponding to the relevant structural and aerodynamic variable and integrating over the span of the beam-blade with respect to *z*. As in the incompressible case, to achieve convergence for flutter solutions, polynomials up to 9th degree (*N* =9) are taken as the shape functions $(\{\Psi_\Delta(z)\} = z^i;\ i = 1...9)$. As described in Appendix G2, at relative wind speeds near the onset of flutter, it is assumed that for a length of l_a from the blade root, the blade is in the incompressible flow regime, and the outboard portion of the blade is in the compressible flow regime. In the inboard sections of the blade where the incompressible aerodynamics is applicable, governing system of equations comprise of 5 equations (Equations (5-54)-(5-56) and Equation (5-38), *i*=1, 2) with 5*N* number of generalized time dependent variables $q_\Delta(t)$ in discretized form. Whereas, in the outboard sections of the blade where the compressible aerodynamics is applicable, the governing system of equations comprise of 15 equations (Equations (5-54)-(5-56) and Equation (5-50), *i*=1,2,3) with 15*N* number of generalized time dependent variables

$q_\Delta(t)$ in discretized form. To apply the EGM in a unified way, same size aerodynamic mass, aerodynamic damping and aerodynamic stiffness matrices are needed in the incompressible and the compressible regions. To achieve this, incompressible aerodynamic mass, aerodynamic damping and aerodynamic stiffness matrices are augmented by adding zero elements to equate the sizes of the matrices with the compressible counterparts. In the compressible flow regime, the generalized time dependent variable vector is defined by Equation (5-69).

$$\{q(t)\} = \left\{ \underbrace{\{q_v(t)\}^T \quad \{q_{\theta_x}(t)\}^T \quad \{q_\phi(t)\}^T}_{\{q_{str}(t)\}} \quad \{q_{B_{1c}}(t)\}^T \quad \{q_{B_{2c}}(t)\}^T \quad \dots \quad \{q_{B_{3cMq}}(t)\}^T \right\}^T \tag{5-69}$$

In the incompressible range, the same generalized time dependent variable vector is kept, but zero elements are placed in the relevant positions of the aerodynamic mass, damping and stiffness matrices, and the expressions for the incompressible unsteady lift and pitching moment given by Equations (5-40) and (5-41) along with the auxiliary equations defining aerodynamic lag states, Equation (5-38), are utilized when applying the EGM. In this respect, $\{q_{B_{1c}}(t)\}$ is replaced by $\{q_{B_1}(t)\}$ and $\{q_{B_{2c}}(t)\}$ is replaced by $\{q_{B_2}(t)\}$. In the compressible range, unsteady compressible lift and pitching moment given by Equations (5-51) and (5-52) along with the auxiliary equations defining aerodynamic lag states, Equation (5-50) , are utilized when applying EGM. Finally, with application of the EGM, unified aeroelastic system of equations is obtained as,

$$\begin{gathered} \left[\boldsymbol{M}_s + \boldsymbol{M}_a^{total}\right]_{15N\times 3N} \{\ddot{q}_{str}\} + \left[\boldsymbol{C}_a^{total}\right]_{15N\times 15N} \{\dot{q}\} + \\ \left[\boldsymbol{K}_s + \boldsymbol{K}_a^{total}\right]_{15N\times 15N} \{q\} = \{0\} \end{gathered} \tag{5-70}$$

where $\boldsymbol{M}_a^{total}$, $\boldsymbol{C}_a^{total}$ and $\boldsymbol{K}_a^{total}$ are the overall aerodynamic mass, damping and stiffness matrices obtained by merging the corresponding incompressible and compressible aerodynamic mass, damping and stiffness matrices. Explicit expressions

for the overall aerodynamic mass, damping and stiffness matrices for the blade whose inboard sections are in the incompressible flow regime and outboard sections are in the compressible flow regime are given in Appendix G2. Similar to the incompressible case, Equation (5-70) is expressed in state space form by augmenting the state vector of the generalized time dependent variables (Equation (5-69)) by the time derivatives of the generalized time dependent structural variables, as shown in Equation (5-71).

$$\left\{X(t)\right\}_{18N\times 1} = \left\{ \left\{q(t)\right\}^T \quad \left\{\dot{q}_{v_0}(t)\right\}^T \quad \left\{\dot{q}_{\theta_x}(t)\right\}^T \quad \left\{\dot{q}_{\phi}(t)\right\}^T \right\}^T \tag{5-71}$$

With the definition of the augmented the state vector of the generalized time dependent variables given by Equation (5-71), Equation (5-70) is transformed into Equation (5-72).

$$\begin{bmatrix} \boldsymbol{C}_a^{total} & \left(\boldsymbol{M}_s + \boldsymbol{M}_a^{total}\right) \\ \boldsymbol{I} & \boldsymbol{0} \end{bmatrix}_{18N\times 18N} \left\{\dot{X}\right\}_{18N\times 1} + \begin{bmatrix} \left(\boldsymbol{K}_s + \boldsymbol{K}_a^{inc}\right) & \boldsymbol{0} \\ \boldsymbol{0} & -\boldsymbol{I} \end{bmatrix}_{18N\times 18N} \left\{X\right\}_{18N\times 1} = \left\{0\right\} \tag{5-72}$$

where $\boldsymbol{I}$ is the identity matrix of order $3N\times 15N$ and $\boldsymbol{0}$ is the zero matrix of order $3N\times 3N$. Equation (5-72) can be re-written in more compact form as,

$$\left\{\dot{X}\right\} = \left[\boldsymbol{A}\right]\left\{X\right\} \tag{5-73}$$

where the coefficient matrix $\boldsymbol{A}$ is given by Equation (5-74) and the solution for the eigenvalues and the eigenvectors is performed similarly as described for the incompressible case.

$$\left[\boldsymbol{A}\right] = \begin{bmatrix} \boldsymbol{C}_a^{total} & \left(\boldsymbol{M}_s + \boldsymbol{M}_a^{total}\right) \\ \boldsymbol{I} & \boldsymbol{0} \end{bmatrix}^{-1} \begin{bmatrix} \left(\boldsymbol{K}_s + \boldsymbol{K}_a^{total}\right) & \boldsymbol{0} \\ \boldsymbol{0} & -\boldsymbol{I} \end{bmatrix} \tag{5-74}$$

5.3 Time Domain Flutter Analysis of Wind Turbine Blades by the Multibody Simulation of the Wind Turbine

To compare the aeroelastic instability results obtained by the present methodology, for the incompressible unsteady aerodynamics case, aeroelastic instability of the wind turbine blade is also studied by performing time domain analysis of the multibody model of the wind turbine system. For this purpose, time domain flutter analysis has been performed by the wind turbine multibody simulation program PHATAS [131] for validation purposes. Table 5-3 gives main wind turbine properties used in the multibody simulation of the wind turbine system in PHATAS. For the baseline wind turbine system, certain properties of NREL's wind turbine are modified, but in essence both turbine definitions are similar.

Table 5-3 Main properties of the reference the wind turbine system established in PHATAS

Wind turbine properties	Baseline wind turbine definition in PHATAS
Nominal power	5 MW
Number of blades	3
Number of blade elements used	17
Blade prebent at the tip	0 m
Demanded rated generator torque	37880 Nm
Gearbox ratio	105
Blade length	61.5 m
Rotor conicity	0^o
Rotor tilt angle	0^o
Hub height	100 m
Hub mass	50,000 kg
Hub inertia	100000 kgm^2

To study the effectiveness of bending twisting coupling induced in composite blades on the aeroelastic stability characteristics of wind turbine blades, a realistic reference wind turbine model is needed to perform aeroelastic time marching multibody

simulations. In the present study, the reference wind turbine and blade designs are established utilizing some of the known properties of NREL's 5 MW turbine [128].

Figure 5-14 Drive train model in PHATAS shows the components of the drive train of the multibody model of the 5 MW turbine generated in PHATAS.

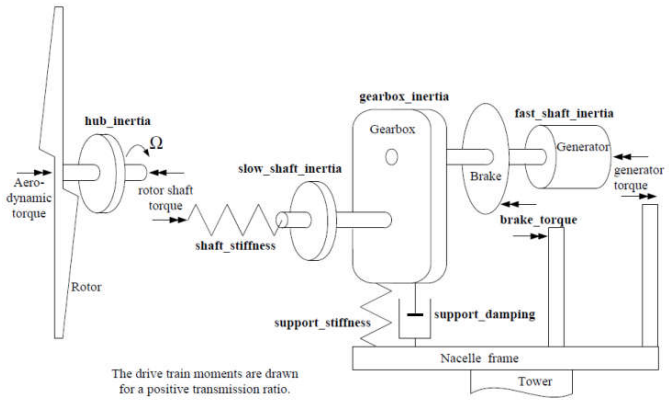

Figure 5-14 Drive train model in PHATAS

In PHATAS, blade is modeled as a coupled non-linear beam. Geometric non-linearity is taken into account during the calculation of the displacements when the curvature is integrated twice along the deformed blade axis. In the beam formulation, warping is neglected and the same form of the constitutive equation relating the flapwise shear force, flapwise bending moment and the torsional moment to the respective deformation measures given in Equation (5-21) is used in the simulation performed by PHATAS. In the beam-blade model generated in PHATAS, blade is again defined by the sectional beam properties calculated by VABS.

5.4 Free Vibration Analysis of the Blades

Before performing time domain flutter simulation by the wind turbine multibody simulation tool PHATAS, free vibration analysis results of a single rotor blade obtained by the present methodology are compared with the results obtained by the

BLADEMODE [132] which is a companion code of PHATAS. The same beam-blade model used in the wind turbine system set up in PHATAS is used in the BLADEMODE. BLADEMODE considers small vibrations about an equilibrium state and with the linearized equations of motion, frequency domain based analysis can be performed making it possible to find the natural frequencies for increasing wind or rotor speeds. In the present study, natural frequencies are compared for the stationary blade under no load to ensure that the structural dynamic models of the blades used in the present study and the beam-blade models used by PHATAS are similar.

In the current methodology, by excluding the aerodynamic mass, damping and stiffness matrices from Equation (5-63) and assuming harmonic motion $\left(\{X\} = \{X_0 e^{iwt}\}\right)$, one obtains the standard form of a generalized free vibration eigenvalue problem and the eigenvalues w can be calculated.

For the baseline blade and bend-twist coupled blades defined in Table 5-2, Table 5-4 gives the comparison of the first six natural frequencies of the baseline blade and the bend-twist coupled blades calculated by the present model and the BLADEMODE. For the three blades and the six modes, the natural frequencies determined by the present solution method and BLADEMODE agree with each other within 5% on the average. More importantly, both solution methods predict the same trend for the variation of the natural frequency with the off axis fiber angle. Table 5-4 shows that lowest four modes are flapwise bending modes and with an increase in the fiber angle, flapwise bending frequencies of the first four modes decrease.

Table 5-4 Comparison of first six natural frequencies of the baseline blade and bend-twist coupled blades calculated by the present model and the BLADEMODE

Mode	Solution Method	Base line (Hz)	BTC_10 (Hz)	BTC_20 (Hz)
1	Present	0.8 (1st F[1])	0.78 (1st F)	0.7 (1st F)
	FOCUS	0.76 (1st F)	0.73 (1st F)	0.66 (1st F)
2	Present	2.11 (2nd F)	1.96 (2nd F)	1.77 (2nd F)
	FOCUS	1.99 (2nd F)	1.86 (2nd F)	1.67 (2nd F)
3	Present	4.31 (3rd F)	4.07 (3rd F)	3.68 (3rd F)
	FOCUS	4.07 (3rd F)	3.86 (3rd F)	3.46 (3rd F)
4	Present	7.49 (4th F)	6.85 (4th F)	6.22 (4th F)
	FOCUS	7.05 (4th F)	6.54 (4th F)	5.95 (4th F)
5	Present	9.54 (**1st T**)	9.76 (**1st T**)	9.21 (5th F)
	FOCUS	9.22 (**1st T**)	9.3 (**1st T**)	8.7 (5th F)
6	Present	11 (5th F)	10.26 (5th F)	9.89 (**1st T**)
	FOCUS	10.33 (5th F)	9.73 (5th F)	9.5 (**1st T**)

[1] " F " and " T " indicate flapwise bending and torsion modes

5.5 Time Domain Flutter Analysis by PHATAS

In order to investigate the aeroelastic stability of wind turbine blades presented in Table 5-2, overspeed analyses are performed with PHATAS utilizing the 5 MW reference wind turbine system defined in Table 5-3. Overspeed analysis simulates the idling rotor with a fixed blade pitch angle in response to a gradually increasing wind speed. Overspeed analysis is performed without using any blade control and applying slowly increasing wind velocity. In the overspeed analysis, rotor blades are given an initial rotational speed, rotor is disconnected from the generator, blade pitch angles are set to a fixed angle and pitch controller is not turned on. Far field wind speed is slowly increased, resulting in an increase of the rotational speed without any bound since the pitch controller is not turned on. Using this loadcase, the required output signals for investigating the onset of flutter are obtained for increasing wind and rotor speed. The time domain analysis results are monitored for output parameters relevant to the flutter analysis. Flapwise and torsional blade tip displacements and rotational speed of the rotor are the main monitored parameters.

In order to make the PHATAS model as similar as possible to the present aeroelastic model used for the classical flutter analysis, lagging flag is turned off and only the flapping flag and blade torsion flags are turned on. Moreover, tower and yaw dynamics are turned off and the blade pitch angle is set to a very small value since the present model assumes that the blade does not have an initial pitch angle. Likewise, geometric twist is also taken as zero for all blade sections. In the aerodynamic model, sectional incompressible aerodynamic coefficients are taken as specified for the NREL blade [128] and dynamic stall model is turned off since the present numerical model does not also have stall aerodynamics. Initial rotor speed is taken as 4 RPM and vertical wind shear is not considered. Detailed procedure of obtaining the flutter wind and rotational speeds from the time responses of the rotational speed of the rotor, flapwise and torsional deformation of the blade tip and angle of attack and lift coefficient of the blade sections using overspeed analysis of the PHATAS code is comprehensively studied previously by authors [133] [134]. The presence of the aeroelastic instability is identified by plotting the time responses obtained by the overspeed analysis for increasing wind speed. For the bend-twist coupled blade BTC_20 defined in Table 5-2, Figure 5-15 presents the gradually increasing wind speed at the hub height and the corresponding rotational speed of the rotor.

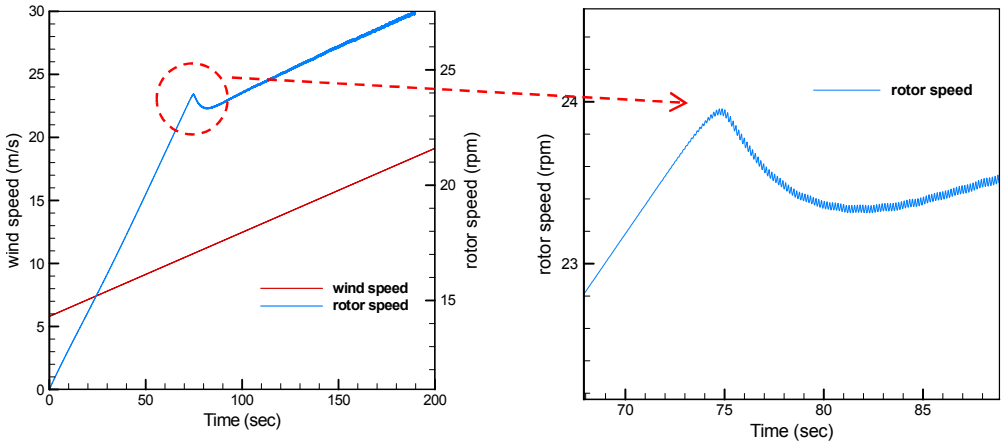

Figure 5-15 Gradually increasing wind speed at the hub height and the corresponding rotational speed of the rotor / Bend-twist coupled blade BTC_20

In Figure 5-15, it is seen that the oscillation of the rotor speed starts at about 72 seconds followed by the slight drop in the rotational speed. After the slight drop, rotational speed continues to increase gradually while the amplitude of the oscillation of the rotational speed grows, as shown in the zoomed figure.

Figure 5-16 shows the time responses of the flapwise bending displacement and the torsional rotation of the blade tip for the bend-twist coupled blade BTC_20. Diverging oscillations of the flapwise blade tip displacement and the torsional rotation occur more or less at about the same time as the expansion seen in the response of the rotor speed. Diverging oscillations indicate the occurrence of classical flutter. From the flapwise bending displacement and torsional rotation responses of the blade tip shown in Figure 5-16, it can be deduced that the onset of flutter occurs at about 73 seconds. At this time, from Figure 5-15, the wind speed is about 10.7 m/s and the corresponding rotational speed is about 23.8 RPM.

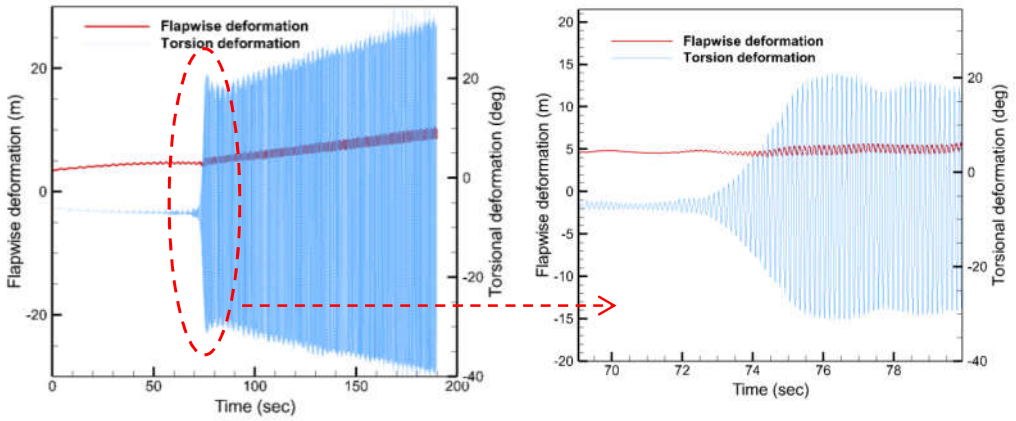

Figure 5-16 Time responses of the flapwise deflection and torsional rotation of the blade tip / Bend-twist coupled blade BTC_20

In Figure 5-17 and Figure 5-18, it is seen that expansion of the rotor speed occurs at about 80 and 66.26 seconds for the baseline and the BTC_10, respectively. Diverging

oscillations of the flapwise blade tip displacement and the torsional deformation occur a little earlier than the expansion seen in the response of the rotor speed. From the rotor speed responses, it can be deduced that the suspected flutter rotational speed is about 23.54 RPM. Figure 5-17 and Figure 5-18 also show that expansion in the torsional deformation takes place before the kink in the flapwise deformation.

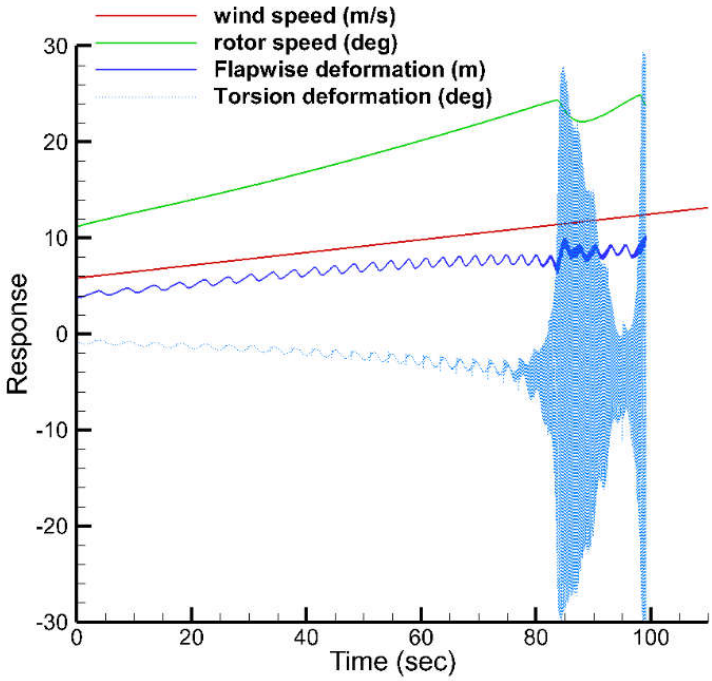

Figure 5-17 Torsional deformation (Deg.), flapwise displacement (m) of the blade tip, rotor speed (RPM) and wind speed (m/s) for the baseline blade obtained by the overspeed analysis

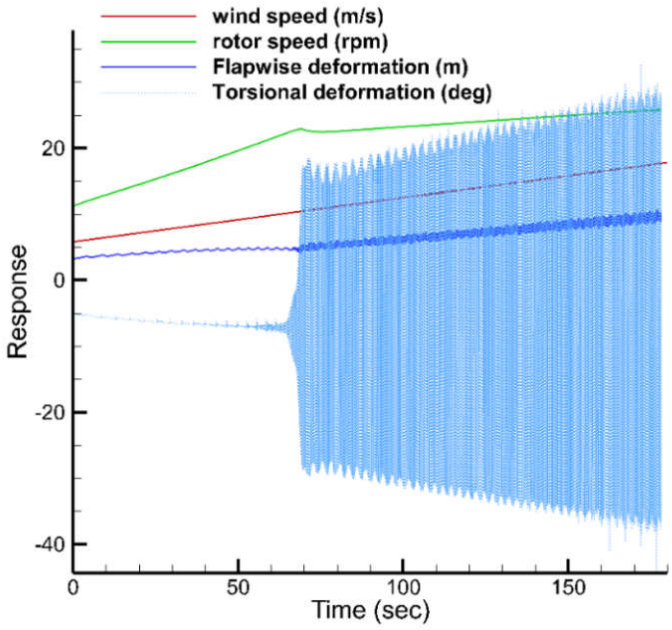

Figure 5-18 Torsional deformation (Deg.), flapwise displacement (m) of the blade tip, rotor speed (RPM) and wind speed (m/s) for the BTC_10 blade obtained by the overspeed analysis

Figure 5-19, Figure 5-20 and Figure 5-21 show the FFT (Logarithmic scale) of the flapwise displacement and torsional deformation time responses of the baseline, BTC_10 and BTC_20 at the tip section of the blades, respectively. Frequency response plots show that the flutter frequencies of the flapwise displacement and the torsional deformation are close to each other. The flutter frequencies for baseline, BTC_10 and BTC_20 are 6.51, 7.6 and 7.31, respectively.

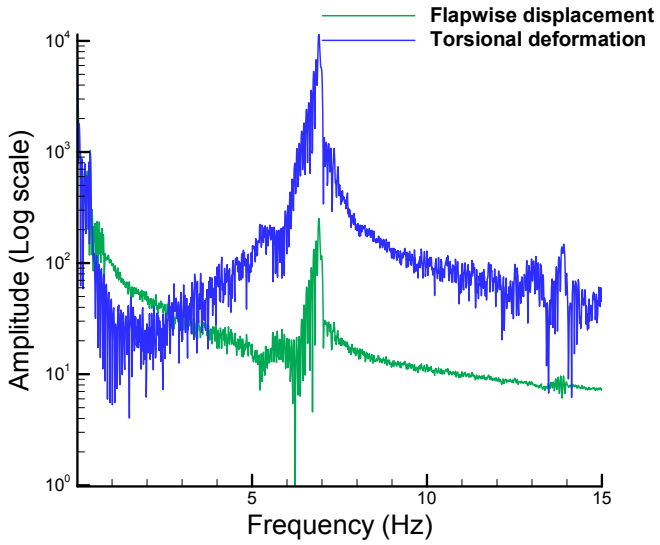

Figure 5-19 Frequency response plots of the time history of the flapwise (green line) and the torsional deformations (blue line) of the blade tip of the baseline blade

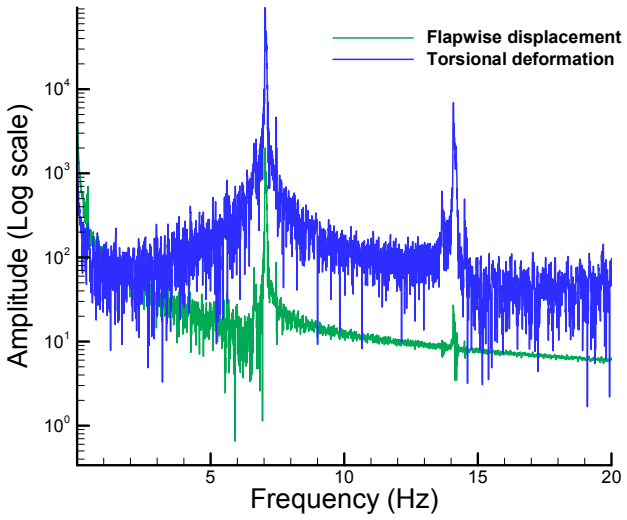

Figure 5-20 Frequency response plots of the time history of the flapwise (green line) and the torsional deformations (blue line) of the blade tip of the BTC_10 blade

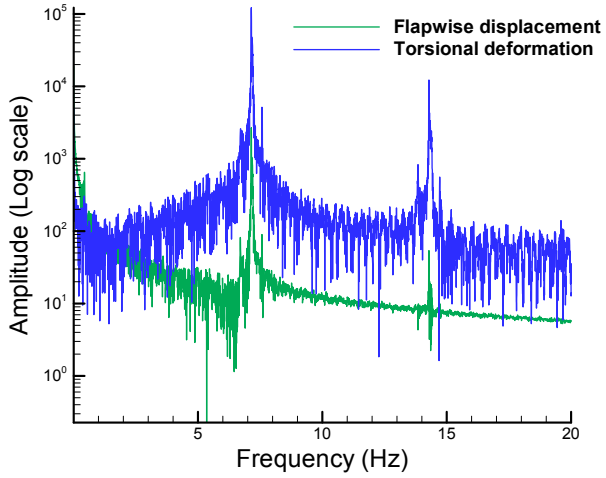

Figure 5-21 Frequency response plots of the time history of the flapwise (green line) and the torsional deformations (blue line) of the blade tip of the BTC_20 blade

5.6 Comparison of Time Domain Flutter Analysis Results of PHATAS and the Present Frequency Domain Flutter Results for Incompressible Aerodynamics and Blades with no Pretwist

In the overspeed analysis performed by PHATAS, both the rotational speed and the wind speed vary. Wind speed is increased gradually and given as input. The flutter instability is decided by monitoring the oscillations in the rotational speed and the flapwise bending displacement and the torsional rotation of the blade tip. In the present numerical model developed, one can specify the inflow wind speed as input, and the related flutter rotational speed is then calculated for different blade configurations. Or, alternatively the rotor speed can be specified as input and the flutter wind speed can be determined. In the comparison study performed with the numerical model developed and PHATAS, flutter rotational speeds are compared. In order to compare the flutter rotational speeds obtained from the time domain responses predicted by PHATAS and the present frequency domain solution method, the wind speed at the time when the blade first starts to have diverging oscillations in PHATAS is given as

the input wind speed to the present model. Thus, the flutter rotational speeds calculated by the present model and PHATAS can be directly compared with each other. For instance, for the bend-twist coupled blade BTC_20, as explained in Section 5.5, the flutter rotational speed obtained by PHATAS is about 23.8 RPM and the corresponding wind speed is about 10.7 m/s. Hence, in the present model input wind speed is specified as 10.7 m/s and the flutter rotational speed is calculated as 25.7 RPM. Table 5-5 compares the flutter rotational speeds and frequencies of the untwisted blades calculated with the present model and PHATAS for the baseline blade and for the bend-twist coupled blades BTC_10 and BTC_20. It should be noted that in the present frequency domain solution, flutter frequency is directly obtained. For the PHATAS simulation, flutter frequencies are determined through the fast Fourier transform analysis of the time response of the deformation mode that enters into the flutter first. It is noted that for the three blades, flutter rotational speeds determined by the present solution method and the PHATAS agree with each other within 6.5% on the average. Moreover, similar to the natural frequency results, both solution methods predict the same trend for the variation of the flutter rotational speed with the off axis fiber angle of the bend-twist coupled blades.

Table 5-5 Comparison of flutter rotational speeds and frequencies of without pretwist calculated by present model and PHATAS

Aeodynamic model		Baseline	BTC_10	BTC_20
	Wind speed (m/sec)	11	10.2	10.7
Present model Incompressible Indicial aerodynamics	Flutter rotational speed (rad/s)	2.63	2.55	2.69
	Flutter frequency (Hz)	6.4	6.65	6.7
PHATAS Incompressible unsteady BEM aerodynamics	Flutter rotational speed (rad/s)	2.465	2.4	2.492
	Flutter frequency (Hz)	6.51	7.6	7.31

Bend-twist coupled blades BTC_10 and BTC_20 have lower flapwise bending stiffness than the baseline blade but they also have higher torsional stiffness compared to the baseline blade. On the other hand, bend-twist flexibility of the bend-twist sections of the BTC blades is substantially higher than the baseline blade. Higher bend-twist flexibility has a lowering effect on the flutter rotational speed. In the BTC blades, as seen in Figure 5-7, fibers are oriented towards the leading edge in the main spar caps. Hence, bending-twisting coupling works toward decreasing the effective angle of attack of the blade sections and has positive effect on lowering the loads. All these effects should be considered together in comparing the flutter characteristics of the baseline and the BTC blades. From Table 5-5, it is seen that for the BTC blade with 10^{o} off-axis fiber angle (BTC_10), flutter rotational speed decreases compared to the flutter rotational speed of the baseline blade, and for the BTC blade with 20^{o} off-axis fiber angle (BTC_20) flutter rotational speed slightly increases compared to the flutter rotational speed of the baseline blade. It is deduced that the combined effect of the reduction in the flapwise bending stiffness and increase in the bending-twisting flexibility are the main reasons for the drop in the flutter rotational speed of the BTC_10 blade compared to the flutter rotational speed of the baseline blade. The increase of the torsional stiffness and the load reduction due to the off-axis fiber angle of the BTC_10 blade do not compensate the effects of the lower flapwise bending stiffness and increased bending-twisting flexibility of the BTC_10 blade, and consequently the flutter rotational speed of the BTC_10 blade decreases slightly compared to the flutter rotational speed of the baseline blade. On the other hand, for the BTC_20 blade, increase in the off-axis fiber angle accounts for increased torsional stiffness as well as higher load reduction and these effects dominate such that the flutter rotational speed of the BTC_20 blade increases compared to the flutter rotational speed of the baseline blade.

5.7 Comparison of Time Domain Flutter Analysis Results of PHATAS and the Present Frequency Domain Flutter Results for Incompressible Aerodynamics and Blades with Pretwist

The next comparison is performed for the blades with pretwist. In the present study, as discussed previously in Chapter 2, the pretwist model of Librescu [92] is adopted, and the pretwist is applied before any deformation takes place. In this model, the inertia and stiffness quantities are determined in the rotated coordinate system (x_t, y_t, z_t). The transformation between the fixed coordinate system (x, y, z) and the rotated coordinate system (x_t, y_t, z_t) is given by,

$$\begin{aligned} x &= x_t \cos\Big(\beta(z)\Big) - y_t \sin\Big(\beta(z)\Big) \\ y &= x_t \sin\Big(\beta(z)\Big) + y_t(s) \cos\Big(\beta(z)\Big) \\ z &= z_t \end{aligned} \tag{5-75}$$

where, $\beta(z)$ is the pretwist angle and in Figure 5-8 pretwist $\beta(z)$ could replace the elastic twist ϕ. Due to the pretwist, stiffness and the inertia terms of the thin walled beam-blade become a function of the pretwist angle $\beta(z)$. Following the application of the transformation given by Equation (5-75), stiffness (a_{ij}) and inertia terms (b_i) become a function of the pretwist angle $\beta(z)$. Appendix C gives the transformed stiffness (a_{ij}) and inertia terms (b_i) obtained after applying the transformation given by Equation (5-75). It should be noted that in the present model which is based on the small disturbance theory, since the static deformation of the blade and the mean steady aerodynamic loads are not considered for the unsteady aeroelastic instability analysis, pretwist does not affect the steady aerodynamic loads. However, in the unsteady blade element momentum aerodynamics model used in PHATAS, pretwist affects the steady loads.

Figure 5-22 shows the variation of the pretwist in wind turbine blade sections. Pretwist distribution in Figure 5-22 is same as the pretwist of the NREL 5MW wind turbine blade.

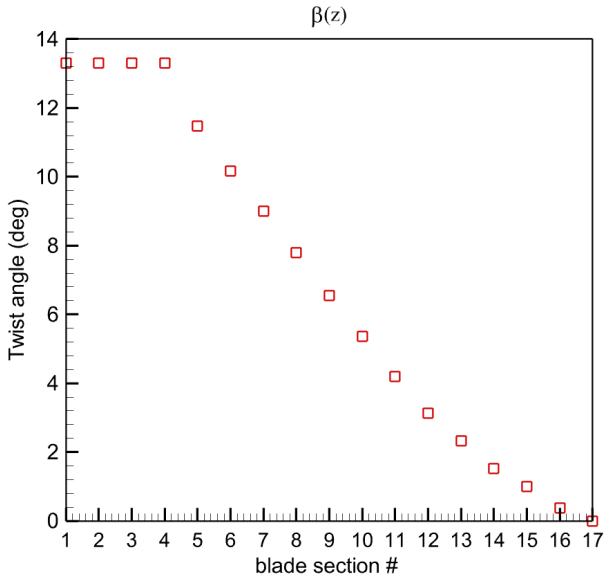

Figure 5-22 Pretwist distribution along blade span

Table 5-6 compares the flutter rotational speeds and frequencies of the blades with pretwist calculated with the present model and PHATAS for the baseline blade and for the bend-twist coupled blades BTC_10 and BTC_20. It is noted that for the three blades, flutter rotational speeds determined by the present solution method and PHATAS again agree with each other within 6% on the average. Both solution methods predict the same trend for the variation of the flutter rotational speed with the off axis fiber angle of the bend-twist coupled blades. Moreover, comparison of Table 5-5 and Table 5-6 reveal that for the baseline blade and the BTC_10 blade, flutter rotational speeds slightly decrease when pretwist is included, and for the BTC_20 blade, flutter rotational speed slightly increases for the blade with pretwist. Both the present model and PHATAS predict the same trend for the variation of the flutter rotational speeds with the pretwist for the three blades.

The comparison study showed that the present method captures variations of the flutter rotational speed with the off-axis fiber angle and the pretwist reasonably well when compared to the results of the wind turbine multibody simulation program PHATAS.

Table 5-6 Comparison of flutter rotational speeds and frequencies of blades with pretwist calculated by the present model and PHATAS

Aerodynamic model	Blades	Baseline	BTC_10	BTC_20
	Wind speed (m/sec)	10.6	9.9	10.8
Present model Incompressible indicial aerodynamics	Flutter rotational speed (rad/s)	2.55	2.535	2.73
	Flutter frequency (Hz)	6	6.6	6.8
PHATAS Incompressible unsteady BEM aerodynamics	Flutter rotational speed (rad/s)	2.42	2.38	2.533
	Flutter frequency (Hz)	6.38	7.44	7.34

5.8 Effect of compressibility on the flutter rotational speed of composite blades

The effect of compressibility on the rotational speed of the composite blades has been investigated by performing aeroelastic analysis using incompressible and compressible aerodynamics based on incompressible and compressible indicial functions. Utilizing the results of the flutter solutions performed using incompressible aerodynamics, incompressible range from the blade root is decided based on the relative velocity information at the flutter condition for the baseline and BTC blades. It is assumed that the blade is in the incompressible flow regime for Mach numbers less than or equal to 0.3 which is calculated using the relative velocity. As defined in Appendix G, it is assumed that for a length of l_a from the blade root, the blade is in the incompressible flow regime, and in the outboard portion of the blade, blade is in the compressible flow regime. It should be noted that the overspeed analysis performed with PHATAS showed that the flutter wind speeds are between 10-11 m/s. In the

present approach, for studying the effect of compressibility on the flutter characteristics of composite blades, the wind speed is taken as 10 m/s for the three blades and flutter rotational speeds are calculated for the same wind speed condition. For the constant wind speed of 10 m/s, at the flutter condition the incompressible range from the blade root (l_a) for the baseline and BTC (BTC_10 and BTC_20) blades are calculated as 38 m, 39.5 m and 37.5 m, respectively. Based on these lengths, the number of sections which are in the incompressible flow regime for the baseline, BTC_10 and BTC_20 blades is taken as 10 ($N_e^{inc} = 10$) and the rest of the blade sections are assumed to be in the compressible flow regime.

Table 5-7 compares the flutter rotational speeds and frequencies of the untwisted baseline blade and BTC blades calculated by implementing the incompressible and the combined incompressible-compressible unsteady aerodynamic models based on indicial functions. It is evident from the results that compressibility has a decreasing effect on the flutter rotational speed. Flutter rotational speeds calculated by using the combined incompressible-compressible unsteady aerodynamic model are 6.44%, 6.64% and 7.8% lower than the flutter rotational speeds obtained by neglecting compressibility for the baseline, BTC_10 and BTC_20 blades, respectively. Lowering of the flutter rotational speed due to the compressibility is in accordance with the findings in the [135] [136]. Table 5-8 compares the flutter rotational speeds and frequencies of the baseline blade and BTC blades with pretwist. As in the untwisted blade case, flutter rotational speeds calculated by using the combined incompressible-compressible unsteady aerodynamic model based on indicial functions are lower than the flutter rotational speeds obtained by neglecting compressibility. It is noted that the incompressible flutter results are not conservative, hence in the aeroelastic stability study of long wind turbine blades, compressibility effects must be taken into consideration.

Table 5-7 Comparison of flutter rotational speeds and frequencies of blades without pretwist calculated by the present model using incompressible and combined incompressible-compressible aerodynamics / Wind speed=10m/s

Aerodynamic model	Blades	Baseline	BTC_10	BTC_20
Incompressible indicial aerodynamics	Flutter rotational speed (rad/sec)	2.64	2.56	2.7
	Flutter frequency (Hz)	6.4	6.65	6.7
Combined Incompressible-Compressible indicial aerodynamics	Flutter rotational speed (rad/sec)	2.468	2.393	2.489
	Flutter frequency (Hz)	6.02	6.29	6.34

Table 5-8 Comparison of flutter rotational speeds and frequencies of blades with pretwist calculated by the present model using incompressible and combined incompressible-compressible aerodynamics / Wind speed=10m/s

Aerodynamic model	Blades	Baseline	BTC_10	BTC_20
Incompressible indicial aerodynamics	Flutter rotational speed (rad/sec)	2.555	2.535	2.74
	Flutter frequency (Hz)	6	6.6	6.8
Combined Incompressible-Compressible indicial aerodynamics	Flutter rotational speed (rad/sec)	2.416	2.383	2.554
	Flutter frequency (Hz)	5.64	6.27	6.4

For the untwisted baseline blade, Figure 5-23 shows the time responses of the flapwise displacement of the blade tip obtained by the time domain solution of the linear aeroelastic system of equations (Equation (5-73)) utilizing the combined incompressible-compressible unsteady aerodynamics based on indicial functions for three different rotational speeds. Runge-Kutta integration method has been used for the time domain solution. Specifically, time responses are presented for the subcritical rotational speed of 2.46 rad/sec, for the flutter rotational speed of 2.468 rad/sec and for the supercritical rotational speed of 2.48 rad/sec at the constant wind speed of 10 m/s.

For rotational speeds less than the critical speed, disturbance, generated by the initial conditions imposed, attenuate due to the aerodynamic damping, as seen in Figure 5-23a. With the increase in the rotational speed, amplitude of the oscillations grows and the response becomes undamped at the instability speed which corresponds to the flutter rotational speed (Figure 5-23b). For the rotational speed higher than the flutter rotational speed, in the supercritical region, amplitude of the oscillations increases exponentially as shown in Figure 5-23c. It should be noted that for the impending blade flutter, linear aeroelastic analysis suffices, since the flapwise bending displacement and the torsional rotation of the blade tip are small in the initial phase of the blade flutter.

For the subcritical rotational speed of 2.3 rad/s, time domain solution of Equation (5-73) corresponding to a disturbance of 0.01 velocity initial conditions for flapwise bending displacement and zero displacement initial conditions has been performed for the untwisted blades utilizing the combined incompressible-compressible unsteady aerodynamics based on indicial functions. It is to be noted that the subcritical rotational speed of 2.3 rad/s is closest to the flutter rotational speed of the BTC_10 blade without pretwist, and it is expected that the response of the BTC_10 blade takes the longest time to damp out. Figure 5-24 gives the flapwise bending displacement and the torsional rotation responses of the blade tip for the baseline, BTC_10 and the BTC_20 blades. Time responses given in Figure 5-24 show that for the BTC_10 blade, the flapwise bending displacement and the torsional rotation responses of the blade tip damp out in a longer time compared to the corresponding responses of the baseline and the BTC_20 blades. This observation is in accordance with the frequency domain flutter results given in Table 5-7 since the rotational speed of 2.3 rad/s is closest to the flutter rotational speed of the BTC_10 blade.

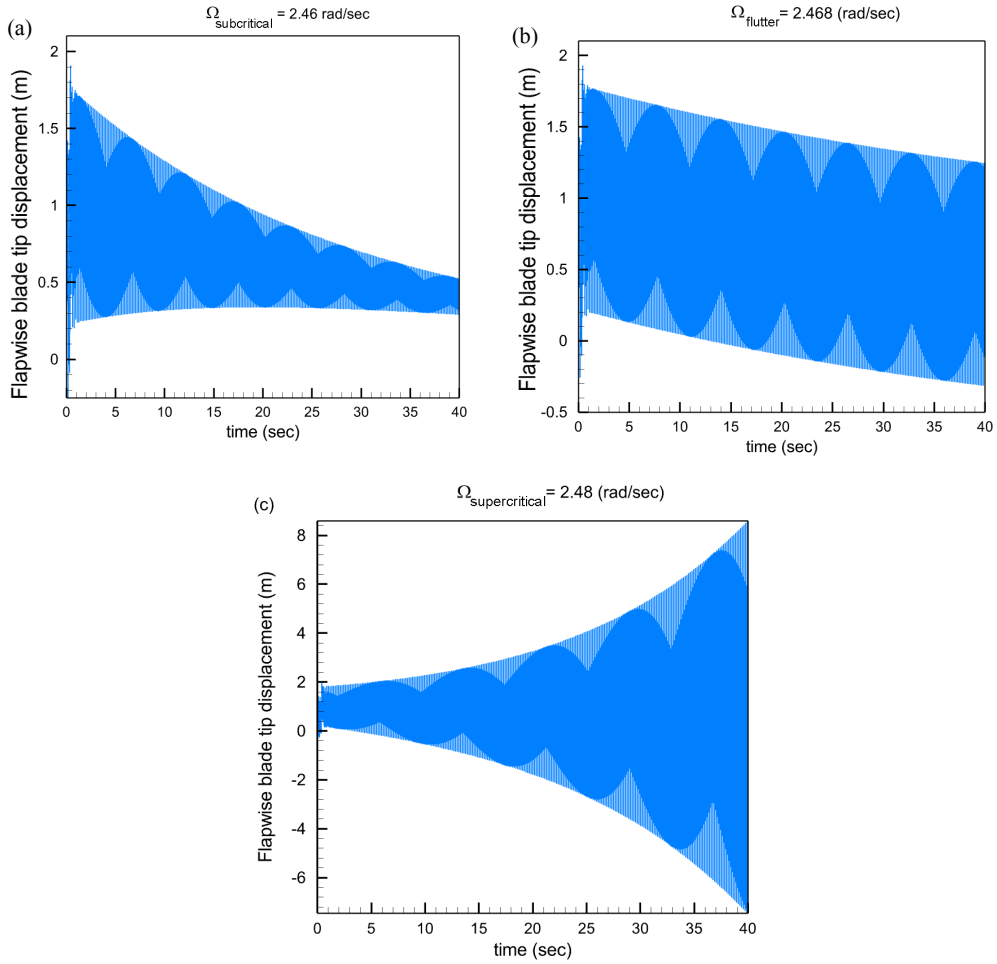

Figure 5-23 Time responses of the flapwise blade tip displacement for the baseline blade and for three rotational speeds (a) Subcritical ($\Omega = 2.46$ rad/s) (b) Flutter ($\Omega = 2.468$ rad/s) and (c) Supercritical ($\Omega = 2.48$ rad/s)

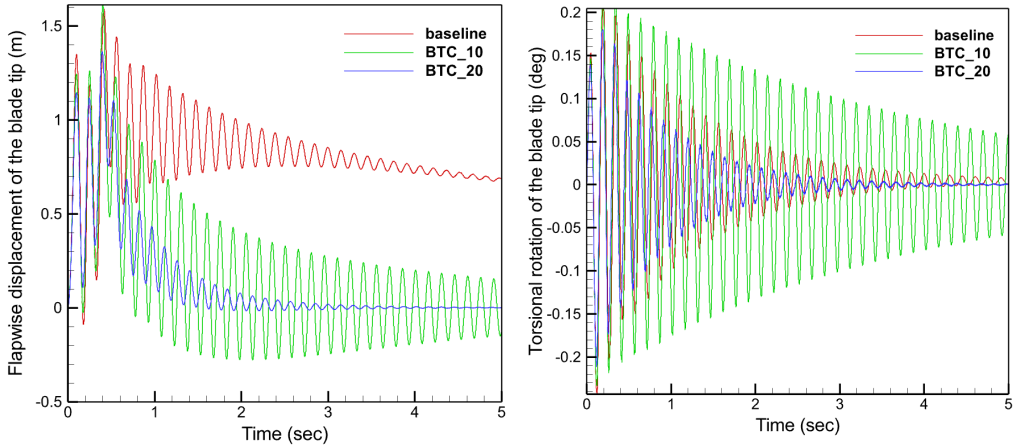

Figure 5-24 Flapwise bending displacement and torsional rotation responses of the blade tip for the baseline, BTC_10 and the BTC_20 blades at the subcritical rotational speed $\Omega = 2.3$ rad/s

In this chapter, a frequency domain solution methodology of the classical flutter phenomenon of composite wind turbine blades has been presented by including the effect of the compressibility. Flutter analyses have been performed for the baseline blade and the BTC blades designed for the 5MW wind turbine of NREL. Beam model of the blade has been developed by making analogy with the structural model of the prewisted rotating thin walled beam introduced in Chapter 2 and utilizing the VABS method for the calculation of the sectional properties of the wind turbine blades. The effect of compressibility has been incorporated into the unsteady aerodynamics model using the compressible indicial functions. The linear aeroelastic system of equations of the composite wind turbine blade has been solved by implementing the extended Galerkin method.

Compressibility has been included into the unsteady aerodynamic model only for the outboard blade sections which are in the compressible flow regime exceeding Mach 0.3. For the sections of the blade, which are in the compressible flow regime, to perform continuous calculation of the compressible indicial functions in the course of frequency domain solution of aeroelastic instability, an approximation methodology is presented for the calculation of compressible indicial functions at any Mach number.

Inboard sections of the blade which are exposed to relative velocities less than Mach 0.3 are assumed to be in the incompressible flow regime. Incompressible and compressible regions of the blade are seamlessly integrated utilizing the Extended Galerkin Method of solution to come up with the eigenvalue problem for the determination of the flutter rotational speed and flutter frequency.

For the incompressible unsteady aerodynamics case, the present solution methodology has been compared with the time domain aeroelastic instability analysis of the wind turbine blades by the multibody simulation program PHATAS. The comparison study showed that the present method captures variations of the flutter rotational speed with the off-axis fiber angle and the pretwist reasonably well when compared to the results of the wind turbine multibody simulation program PHATAS.

Aeroelastic instability analysis results of the untwisted blades and the blades with pretwist showed that compressibility has a decreasing effect on the flutter rotational speed, and that the incompressible flutter results are not conservative. The present frequency domain approach for the aeroelastic stability analysis of long wind turbine blades is deemed to be very advantageous compared to other approaches which usually require time domain solutions, such as coupled CFD and structural FE methods. Especially, in the initial design phase of wind turbine blades, the effect of frequent design changes on the aeroelastic stability characteristics of composite wind turbine blades can be assessed very effectively in terms of model preparation and solution time with the approach presented in this study. This study shows that with use of compressible indicial functions, the effect of compressibility can also be taken into account in the frequency domain aeroelastic stability analysis of long wind turbine blades whose outboard sections are inevitably in the compressible flow regime at the onset of flutter.

CONCLUSION

In the present study, an efficient aeroelastic model based on an analytical composite thin walled beam model including geometrical nonlinearity and the indicial functions approach for modeling the unsteady aerodynamics has been studied and formulated. To the best of author's knowledge, the comprehensive treatment of nonlinear aeroelasticity of aircraft wings and wind turbine blades structurally modeled as nonlinear anisotropic thin walled beams incorporating the effect of the compressibility in the unsteady aerodynamic model is addressed for the first time in literature. The methodology developed in this work enables the systematic examination of divergence (static instability), flutter (dynamic instability), and qualification of post-flutter dynamic response utilizing the aeroelastic tailoring concept.

Specifically, the major conclusions of this thesis study include:

- In the structure part, a composite rotating thin walled beam model including geometrical nonlinearity based on an existing linear thin walled beam model has been developed. The linear model has been validated against the FE software. Improved structural models are specifically developed for the CAS and the CUS layup TWBs to exploit the flapwise bending-torsion, extension-chordwise bending coupling in the CAS-TWB and extension-torsion, flapwise bending-chordwise bending coupling in the CUS-TWB. It is shown that for both CAS and CUS TWBs, in general, natural frequencies increase with rotational speed which is a sign of centrifugal stiffening effect. Results showed that as the rotational speed increases, mode switching from flapwise to chordwise bending and vice versa, and from torsional mode to flapwise bending mode. Pretwist causes stiffening effect at higher fiber angles and at low angular velocities for both CAS and CUS configurations, and it is mostly effective on the torsional mode. In the frequency range studied, the main difference between the CAS and the CUS configurations is the higher torsional

frequency of the CAS configuration for higher fiber angles ($-30° < \theta < -90°$) compared to the CUS configuration. CAS configuration TWB offers a more separate bending-torsion frequency range and might have a higher flutter speed than the CUS configuration.

- In the aerodynamic part, the unsteady Mach dependent compressible aerodynamics model is constructed in the time domain by using a novel indicial approximation, which allows to perform direct stability analysis of compressible indicial functions at any Mach number up to 0.85, by incorporating twelve aerodynamic lag states.
- In the aeroelastic part, a comprehensive study of the geometrically nonlinear aeroelastic behavior of pretwisted, tapered and swept composite wings structurally modeled as thin walled beams (TWB) subjected to incompressible and compressible unsteady aerodynamics is performed. The aeroelastic equations of motion are obtained for the CAS configuration TWB in the most general form by including second order nonlinear strain displacement relations, nonuniform geometric features such as wing taper, pretwist, and warping restraint and transverse shear effects are taken into account. Flutter speeds determined by the linear aeroelastic analysis of composite structures via frequency domain solution. Nonlinear aeroelastic respose of the composite wing modeled as TWB is performed in time domain by the direct integration of aeroelastic governing equation of motion by the Runge-Kutta method for the prescribed initial conditions. Post flutter bahavior of the composite structures has been studied using bifurcation diagram, phase portrait, PSD, FFT and Poincaro map. It is shown that, Fiber angle of the CAS configuration TWB is a very influential parameter on the flutter speed of the composite wing. For the positive fiber angles the instability is in the form of divergence and for negative fiber angle is in the form of flutter. Besides the flutter speed, the fiber angle of the CAS configuration TWB has a significant effect on the post-flutter LCO behavior of the composite wing. Besides the flutter speed, the fiber angle of the CAS configuration TWB has a significant effect on the post-flutter LCO behavior of the composite wing. Post-flutter responses of composite wings

with three different off-axis fiber angles (-75°, -60°, -45°) showed that although the flutter speed of the composite wing with -45° off-axis fiber angle is higher than the flutter speed of the -60° fiber angle case, from post-flutter response point of view, -60° fiber angle is preferable, since the well behaved post-flutter range is wide and the amplitudes of the LCOs are low compared to the -75° fiber angle case. For the -45° fiber angle case, bifurcation speed is highest but flapwise bending displacement and torsional deformation amplitude curves are nearly vertical. The effect of pretwist causes the flutter speed to increase, but at the same time nonlinearity becomes slightly weaker. Wing taper ratio has a stabilizing effect on the stability margins of the wing. For untapered wings the flutter speed decreases and the wing is more prone to flutter instability at smaller speeds compared to a tapered wing. For the low off-axis fiber angle of -75°, it seen that aeroelastic response of forward swept wings can be improved significantly. Moreover, it is also shown in the study that as the backward sweep angle of wing is increased, post-critical aeroelastic response of the wing becomes more well behaved compared to wings with low backward sweep angles. It is evident that compressibility accounts for reduction in aeroelastic instability speeds especially at higher Mach numbers. Actually, instability speeds obtained by incompressible unsteady aerodynamics are not conservative.

- In the last chapter, a frequency domain solution methodology of the classical flutter phenomenon of composite wind turbine blades has been presented by including the effect of the compressibility. Flutter analyses have been performed for the baseline blade and the BTC blades designed for the 5MW wind turbine of NREL. Aeroelastic instability analysis results of the untwisted blades and the blades with pretwist showed that compressibility has a decreasing effect on the flutter rotational speed, and that the incompressible flutter results are not conservative

FUTURE WORK

The emergence of new structural geometries and materials generates major challenges to the aeroelastic discipline. Aeroelastic analysis of high aspect ratio aircraft wing and wind turbine blade made of from composite materials subjected to unsteady aerodynamics including geometrical non-uniformity and nonlinearity was the main scope of the present study. The following are some of the studies that which are recommended as future work.

- Coupling of nonlinear aerodynamic models with current nonlinear structure model to investigate flutter speeds and post-flutter behaviors. The proposed aerodynamic models are;
- ✓ Dynamic stall aerodynamics for modeling separated flow at high torsion angles like ONERA or Beddoes-Leishman type dynamic stall aerodynamics
- ✓ Higher order nonlinear piston theory for extending current aeroelastic model to cover supersonic flight regime.
- Utilizing variable stiffness concept for the improvement of structural dynamic and aeroelastic characteristics of thin walled composite beams.
- Development of geometrically exact beam model for fixed and rotary wings and coupling with the proposed incompressible and compressible unsteady aerodynamics models based on indicial functions.
- Multicell TWB configuration as structural model to investigate more realistic airfoil shape of cross section with wing double or more boxes.
- Extension of the six degree of freedom beam-blade model to cover all of normal, shear and coupling stiffnesses in the most general form of governing equations.
- Modeling of structural damping in the composite aircraft wings and turbine blades and its influence on the aeroelastic instability and response.

REFERENCES

[1] Ö. Şener, "Determination of the bending twisting coupling potential of composite materials via digital image correlation and its implementation in wind turbine blades," Middle East Technical University, MS.c thesis, Ankara, 2017.

[2] J. Locke and U. Valencia, "Design Studies for Twist-Coupled Wind Turbine Blades, Sandia National Laboratories," Report No. SAND2004-0522, 2004.

[3] M. Capellaro, "Design Limits of Bend Twist Coupled Wind Turbine Blades," in *53rd AIAA/ASME/ASCE/AHS/ASC Structures, Structural Dynamics and Materials Conference*, Honolulu, Hawaii, 2012.

[4] C. Bottasso, F. Campagnolo, A. Croce and C. Tibaldi, "ptimization-based study of bend–twist coupled rotor blades for passive and integrated passive/active load alleviation," *Wind Energy,* vol. 16, p. 1149–1166, 2013.

[5] M. O. Gözcü, M. N. Olgun and A. Kayran, "Investigation of the Effect of Off-Axis Spar Cap Plies on Damage Equivalent Loads in Wind Turbines with Superelement Blade Definition," in *AIAA Science and Technology Forum and Exposition 2014, AIAA 2014-1223*, National Harbor, MD, 2014.

[6] K. Hayat and S. K. Ha, "Load mitigation of wind turbine blade by aero-elastic tailoring via unbalanced laminates composites," *Composite Structures,* vol. 128, p. 122–133, 2015.

[7] M. Gözcü, T. Farsadi, Ö. Şener and A. Kayran, "Assessment of the Effect of Hybrid GFRP-CFRP Usage in Wind Turbine Blades on the Reduction of Fatigue Damage Equivalent Loads in the Wind Turbine System," in *AIAA Science and Technology Forum and Exposition, 33rd Wind Energy Symposium*, Florida, 2015.

[8] "wikimedia Commons," 20 May 2015. [Online]. Available: https://commons.wikimedia.org/.

[9] M. H. Hansen, "Aeroelastic instability problems for wind turbines," *wind energy,* vol. 10, no. 6, 2007.

[10] M. O. L. Hansen, N. J. Sørensen, S. Voutsinas, N. Sørensen and H. A. Madsen, "State of the art in wind turbine aerodynamics and aeroelasticity," *Progress in aerospace sciences,* vol. 42, no. 2, pp. 285-330, 2006.

[11] L. Leishman and J. Gordon, "Challenges in modeling the unsteady aerodynamics of wind turbines," in *ASME-IMECE, Wind Energy Symposium*, 2002.

[12] D. Lobitz and P. Veers, "Aeroelastic behavior of twist-coupled HAWT blades," in *ASME-IMECE Wind Energy Symposium*, 1998.

[13] D. Lobitz, "Aeroelastic stability predictions for a MW-sized blade," *Wind Energy,* vol. 7, no. 3, pp. 211-224, 2004.

[14] B. C. Owens, D. T. Griffith, B. R. Resor and J. E. Hurtado, "Impact of modeling approach on flutter predictions for very large wind turbine blade designs," in *merican Helicopter Society 69th Annual Forum*, Phoenix, 2013.

[15] B. C. Owens and D. T. Griffith, "Aeroelastic stability investigations for large-scale vertical axis wind turbines," *Journal of Physics: Conference Series, IOP Publishing,* vol. 524, no. 1, 2014.

[16] A. R. Stäblein, M. H. Hansen and G. Pirrung, "Fundamental aeroelastic properties of a bend–twist coupled blade section," *Journal of Fluids and Structures,* vol. 68, pp. 72-89, 2017.

[17] P. Pourazarm, Y. Modarres-Sadeghi and M. Lackner, "A parametric study of coupled-mode flutter for MW-size wind turbine blades," *Wind Energy,* vol. 19, no. 3, pp. 497-514, 2015.

[18] P. Pourazarm, L. Caracoglia, M. Lackner and Y. Modarres-Sadeghi, "Stochastic analysis of flow-induced dynamic instabilities of wind turbine blades," *Journal of Wind Engineering and Industrial Aerodynamics,* vol. 137, pp. 37-45, 2015.

[19] M.-S. Jeong, S.-J. Y. I. Lee and K.-C. Park, "Torsional stiffness effects on the dynamic stability of a horizontal axis wind turbine blade," *Energies,* vol. 6, no. 4, pp. 2242-2261, 2013.

[20] T. Buhl, H. Markou, H. Hansen, K. Thomsen and F. Rasmussen, "Aeroelastic Stability Analysis and Passive Instability Suppression," in *European Wind Energy Conference and Exhibition*, Athens, 2006.

[21] D. C. Janetzke and R. V. Krishna, "Whirl flutter analysis of a horizontal-axis wind turbine with a two-bladed teetering rotor," *Solar Energy,* vol. 31, no. 2, pp. 173-182, 1983.

[22] H. J. T. Kooijman, "Bending-torsion coupling of a wind turbine rotor blade," Energy Research Foundation ECN, Netherlands, 1996.

[23] D. W. Lobitz, P. S. Veers, G. R. Eisler, D. J. Laino, P. G. Migliore and G. Bir, "The use of twist-coupled blades to enhance the performance of horizontal axis wind turbines," Sandia National Laboratories, SAND2001-1003, Albuquerque, 2001.

[24] P. K. Chaviaropoulos, N. N. Soerensen, M. O. L. Hansen, I. G. Nikolaou, K. A. Aggelis, J. Johansen and M. Gaunaa, "Viscous and aeroelastic effects on wind turbine blades. The VISCEL project. Part II: Aeroelastic stability investigations," *Wind Energy,* vol. 6, no. 4, pp. 387-403, 2003.

[25] K. Hayat, A. G. d. Lecea, C. D. Moriones and S. K. Ha, "Flutter performance of bend–twist coupled large-scale wind turbine blades," *Journal of Sound and Vibration,* vol. 370, pp. 149-162, 2016.

[26] K. Hayat and K. Sung, "Flutter performance of large-scale wind turbine blade with shallow-angled skins," *Composite Structures,* vol. 132, pp. 575-583, 2015.

[27] S. R. Vatne, "Aeroelastic instability and flutter for a 10 MW wind turbine," Master thesis, Norwegian University of Science and Technology, 2011.

[28] L. Shruti and Y. Modarres-Sadeghi, "Supercritical and subcritical dynamic flow-induced instabilities of a small-scale wind turbine blade placed in uniform flow," *Journal of Fluids and Structures,* vol. 54, pp. 936-946, 2015.

[29] T. Liu, Y. Ren and X. Yang, "Nonlinear aeroelastic stability analysis of wind turbine blade with bending–bending–twist coupling," *Journal of Fluids and Structures,* vol. 42, pp. 488-502, 2013.

[30] D. O. Yu and O. J. Kwon, "Predicting wind turbine blade loads and aeroelastic response using a coupled CFD–CSD method," *Renewable Energy,* vol. 70, pp. 184-196, 2014.

[31] C. A. Baxevanou, P. Chaviaropoulos, S. G. Voutsinas and N. S. Vlachos, "Evaluation study of a Navier–Stokes CFD aeroelastic model of wind turbine airfoils in classical flutter," *Journal of wind engineering and industrial aerodynamics,* vol. 96, no. 8, pp. 1425-1443, 2008.

[32] C. Arakawa, O. Fleig, M. Iida and M. Shimooka, "Numerical approach for noise reduction of wind turbine blade tip with earth simulator," *Journal of the Earth Simulator,* vol. 2, no. 3, pp. 11-33, 2005.

[33] J. N. Sørensen, "Viscous effects on wind turbine blades," ET-AFM-9902, Department of Energy Engineering, Technical University of Denmark, 1999.

[34] P. K. Chaviaropoulos, I. G. Nikolaou, K. Aggelis, N. N. Sørensen, B. Montgomerie and H. V. Geyr, "Viscous and aeroelastic effects on wind turbine blades: the Viscel Project," in *European wind energy conference*, Copenhagen, 2001.

[35] G. Xu and L. N. Sankar, "Computational study of horizontal axis wind turbines," *Journal of Solar Energy Engineering transactions of ASME,* vol. 122, no. 1, pp. 35-39, 2000.

[36] M. O. L. Hansen, J. N. Sørensen, S. Voutsinas, N. Sørensen and H. A. Madsen, "State of the art in wind turbine aerodynamics and aeroelasticity," *Progress in aerospace sciences,* vol. 42, no. 4, pp. 285-330, 2006.

[37] Z. Qin, "Vibration and Aeroelasticity of Advanced Aircraft Wings Modeled as Thin-Walled Beams--Dynamics, Stability and Control," Doctoral dissertation, virginia technical university, 2001.

[38] S. A. Sina, T. Farsadi and H. Haddadpour, "Aeroelastic Stability and Response of Composite Swept Wings in Subsonic Flow Using Indicial Aerodynamics," *Journal of Vibration and Acoustics,* vol. 135, no. 5, pp. 051019-1-14, 2013.

[39] T. Farsadi and J. Javanshir, "Expansion of Indicial Function Approximations for 2-D Subsonic Compressible Aerodynamic Loads," in *SME International Mechanical Engineering Congress and Exposition* , 2012.

[40] E. Bruhn, Analysis and design of flight vehicle structures, S.R. Jacobs, 1973.

[41] X. Cai, P. Pan, J. Zhu and R. Gu, "The Analysis of the Aerodynamic Character and Structural Response of Large-Scale Wind Turbine Blades," *Energies,* vol. 6, no. 7, pp. 3134-3148, 2013.

[42] M. J. Patil, D. H. Hodges and C. E. S. Cesnik, "Nonlinear aeroelastic analysis of complete aircraft in subsonic flow," *Journal of aircraft,* vol. 37, no. 5, pp. 753-760, 2000.

[43] V. Vlasov, Thin-walled elastic beams, National Technical Information Service, 1984.

[44] S. Timoshenko, Vibration Problems in Engineering, New York: D.Van Nostrand Company INC., 1937.

[45] S. Timoshenko, "Theory of bending, torsion and buckling of thin-walled members of open cross section," *Journal of the Franklin Institute,* vol. 239, no. 4, pp. 249-268, 1945.

[46] A. Gjelsvik, The theory of thin walled bars, Wiley, 1981.

[47] O. Bauchau, "A beam theory for anisotropic materials," *journal of applied mechanics,* vol. 52, no. 2, pp. 416-422, 1985.

[48] O. Bauchau, B. Coffenberry and L. Rehfield, "Composite box beam analysis: Theory and experiments," *Journal of Reinforced plastic and composites,* vol. 6, no. 1, pp. 25-35, 1987.

[49] J. N. R. B. and L.-S. T., "A vlasov theory for fiber reinforced beams with thin walled open cross sections," *International journal of solids and structures,* vol. 20, no. 3, pp. 277-297, 1984.

[50] E. Mansfield and A. Sobey, "The fibre composite helicopter blade: Part i: Stiffness properties: Part ii: Prospects for aeroelastic," *Aeronautical Quarterly,* vol. 30, no. 2, pp. 413-449, 1979.

[51] L. C. Bank, "Shear coefficients for thin-walled composite beams," *Composite Structures,* vol. 8, no. 1, pp. 47-61, 1987.

[52] L. C. Bank and T. P. Melehan, "Shear coefficients for multicelled thin-walled composite beams," *Composite Structures ,* vol. 11, no. 4, pp. 259-276, 1989.

[53] J. K. Suresh and V. T. Nagaraj, "Higher-order shear deformation theory for thin-walled composite beams," *Journal of Aircraft,* vol. 33, no. 5, pp. 978-986, 1996.

[54] Z. Qin and L. Librescu, "Static and dynamic validations of a refined thin-walled composite beam model," *AIAA journal,* vol. 39, no. 12, pp. 2422-2424, 2001.

[55] Z. Qin and L. Librescu, "On a shear-deformable theory of anisotropic thin-walled beams: further contribution and validations," *Composite Structures,* vol. 56, no. 4, pp. 345-358, 2002.

[56] L. Librescu and O. Song, Thin-walled composite beams: theory and application, Springer, 2006.

[57] D. Moore, "A non-linear theory for the behaviour of thin-walled sections subject to combined bending and torsion," *Thin Walled Structures,* vol. 4, no. 6, pp. 449-466, 1986.

[58] M. M. Attard, "Nonlinear theory of non-uniform torsion of thin-walled open beams," *Thin-Walled Structures,* vol. 4, no. 2, pp. 101-134, 1986.

[59] G. v. Erp, C. Menken and F. Veldpaus, "The non-linear flexural-torsional behaviour of straight slender elastic beams with arbitrary cross sections," *Thin-Walled Structures,* vol. 6, no. 5, pp. 285-404, 1988.

[60] K. Bhaskar and L. Librescu, "A geometrically non-linear theory for laminated anisotropic thin-walled beams," *International Journal of Engineering Science,* vol. 33, no. 9, pp. 1331-1344, 1995.

[61] X. Wang and Z. Qin, "Nonlinear modal interactions in composite thin-walled beam structures with simultaneous 1: 2 internal and 1: 1 external resonances," *Nonlinear Dynamics,* vol. 86, no. 2, pp. 1381-1405, 2016.

[62] C. S. A. Petre and L. Librescu, "Aeroelastic divergence of multicell wings taking their fixing restraints into account," *Revue de Mecanique Appliquee,* vol. 19, no. 6, pp. 689-698, 1961.

[63] L. Librescu and S. Thangjitham, "The warping restraint effect in the critical and subcritical static aeroelastic behavior of swept forward composite wing structures," *SAE Technical Paper,* 1989.

[64] L. Librescu and O. Song, "Static aeroelastic tailoring of composite aircraft swept wings modelled as thin-walled beam structures," in *Fifth Japan-U.S. Conference on Composite Materials*, TOKYO.

[65] O. Song and L. Librescu, "Free vibration and aeroelastic divergence of aircraft wings modelledas composite thin-walled beams," in *32nd Structures, Structural Dynamics, and Materials Conference*, 1991.

[66] L. Librescu and O. Song, "On the static aeroelastic tailoring of composite aircraft swept wings modelled as thin-walled beam structures," *Composites Engineering,* vol. 2, no. 5-7, pp. 497-512, 1992.

[67] C.-H. Hong and I. Chopra, "Aeroelastic stability analysis of a composite rotor blade," *Journal of the American Helicopter,* vol. 30, no. 2, pp. 57-67, 1985.

[68] D. H. C. Cesnik and M. Patil, "Aeroelastic analysis of composite wings," in *37th Structure, Structural Dynamics and Materials*, Salt Lake City, 1996.

[69] Z. Qin and L. Librescu, "Aeroelastic instability of aircraft wings modelled as anisotropic composite thin-walled beams in incompressible flow," *Journal of fluids and structures ,* vol. 18, no. 1, pp. 43-61, 2003.

[70] Z. Qin and L. Librescu, "Dynamic aeroelastic response of aircraft wings modeled as anisotropic thin-walled beams," *Journal of aircraft,* vol. 40, no. 3, pp. 532-543, 2003.

[71] H. Haddadpour, M. Kouchakzadeh and F. Shadmehri, "Aeroelastic instability of aircraft composite wings in an incompressible flow," *Composite Structures,* vol. 83, no. 1, pp. 93-99, 2008.

[72] S. Na, J.-S. Song, J.-H. Choo and Z. Qin, "Dynamic aeroelastic response and active control of composite thin-walled beam structures in compressible flow," *Journal of Sound and Vibration,* vol. 330, no. 21, pp. 4998-5013, 2011.

[73] L. Li, V. V. Volovoi and D. Hodges, "Cross-Sectional Design of Composite Rotor Blades," *Journal of the American Helicopter Society,* vol. 53, no. 3, pp. 240-251, 2008.

[74] U. K. Chakravarty, "On the modeling of composite beam cross-sections," *Composites Part B: Engineering,* vol. 42, no. 4, pp. 982-991, 2011.

[75] N.-L. R. F., T. S. R. and B. S. W., "Application of Bend- Twist Coupled Blades for Horizontal Axis Tidal Turbines," *Renewable Energy,* vol. 50, pp. 541-550, 2013.

[76] R. Bunton and C. Denegri, "Limit cycle oscillation characteristics of fighter aircraft,," *Journal of Aircraft ,* vol. 37, p. 916, 2000.

[77] Z. Yang and L. Zhao, "Analysis of limit cycle flutter of an airfoil in incompressible flow," *Journal of Sound and Vibration,* vol. 123, no. 1, 1988.

[78] M. Conner, D. Tang, E. Dowell and L. Virgin, "Nonlinear behavior of a typical airfoil section with control surface freeplay: A numerical and experimental study," *Journal of Fluids and Structures,* vol. 11, no. 89, 1997.

[79] B. Lee and P. LeBlanc, "Flutter Analysis of a Two-Dimensional Airfoil with Cubic Non-linear Restoring Force," Tech. Rep. NRC No. 25438,aeronautical Note NAE-AN-36, Canada, 1986.

[80] T. Liu, "nonliear aeroelastic response analysis of rotor blade modeled as composite thin-walled structure," *Taiyangneng Xuebao/Acta Energiae Solaris Sinica,* vol. 33, no. 1, pp. 105-112, 2012.

[81] A. v. Rooij, "AEROELASTIC LIMIT-CYCLE OSCILLATIONS RESULTING FROM AERODYNAMIC NON-LINEARITIES," Technische Universiteit Delft, PhD thesis, Netherlands, 2017.

[82] E. Dowell, J. Edwards and T. Strganac, "Nonlinear aeroelasticity," *Journal of aircraft,* vol. 40, no. 5, pp. 857-874, 2003.

[83] L. Liu, Y. Wong and B. Lee, "Application of the centre manifold theory in non-linear aeroelasticity," *Journal of Sound and vibration,* vol. 234, no. 4, pp. 641-659, 2000.

[84] S. Preidikman and D. Mook, "Time-domain simulations of linear and nonlinear aeroelastic behavior," *Journal of Vibration and Control,* vol. 6, no. 8, pp. 1135-1175, 2000.

[85] B. D. Hall, D. T. Mook, A. H. Nayfeh and S. Preidikman, "Novel strategy for suppressing the flutter oscillations of aircraft wings," *AIAA journal,* vol. 39, no. 10, pp. 1843-1850, 2001.

[86] D. S. Woolston, "An investigation of effects of certain types of structural nonlnearities on wing and control surface flutter," *Journal of the Aeronautical Sciences,* vol. 24, no. 1, pp. 57-63, 1957.

[87] B. Lee and J. Desrochers, "Flutter analysis of a two-dimensional airfoil containing structural nonlinearities," Technical report, National Aaeronautical Establishment Ottawa, Ontario, 1987.

[88] S. Price, B. Lee and H. Alighanbari, "Postinstability behavior of a two-dimensional airfoil with a structural nonlinearity," *Journal of Aircraft,* vol. 31, no. 6, pp. 1395-1401, 1994.

[89] K. Kim, "Nonlinear aeroelastic analysis of aircraft wing-with-store configurations," Ph.D. thesis, Texas A&M University, 2004.

[90] D. Tang and E. Dowell, "Effects of geometric structural nonlinearity on flutter and limit cycle oscillations of high-aspect-ratio wings," *Journal of fluids and structures ,* vol. 19, no. 3, pp. 291-306, 2004.

[91] M. J. Patil, D. H. Hodges and C. E. Cesnik, "Limit-cycle oscillations in high-aspect-ratio wings," *Journal of fluids and structures,* vol. 15, no. 1, pp. 107-132, 2001.

[92] L. Librescu and O. Song, Thin walled composite beams: theory and application, Netherlands: Springer, 2006.

[93] L. W. Rehfield and A. R. Atilgan, "Toward understanding the tailoring mechanisms for thin walled composite tubular beam," in *Symp. on mechanics of composite materials, ASME* , NY, USA, 1989.

[94] O. Song, L. Librescu and S. Y. Oh, "Vibration of pre-twisted adaptive rotating blades modeled as anisotropic thin-walled beams," *AIAA Journal,* vol. 39, no. 2, pp. 285-295, 2001.

[95] L. L. L. Meirovitch and S. S. Na, "Control of Cantilever Vibration via Structural Tailoring and Adaptive Materials," *AIAA Journal,* vol. 35, no. 8, pp. 1309-1315, 1997.

[96] T. Theodorsen, "General Theory of Aerodynamic Instability and the Mechanism of Flutter," NACA report, 1935.

[97] R. Loewy, "A Two-Dimensional Approximation to the Unsteady Aerodynamics of Rotary Wing," *Journal of the Aeronautical Sciences,* vol. 24, no. 2, pp. 81-92, 1957.

[98] J. M. Greenberg, "Airfoil in Sinusoidal Motion in a Pulsating Stream," NACA TN No. 1326, USA, 1947.

[99] H. Wagner, "Uber die Entstehung des dynamischen Auftriebes von Tragfl¨ugeln," pp. 17-35, February 1925.

[100] R. L. Bisplingho, H. Ashley and R. L. Halfman, aeroelasticity, New York: Dover publications, 1996.

[101] T. V. Karman and W. R. Sears, "Airfoil Theory for Non-Uniform Motion," *Journal of the aeronautical Sciences,* vol. 5, no. 10, pp. 379-390, 1938.

[102] R. L. Bisplinghoff, H. Ashley and R. L. Halfman, Aeroelasticity, Cambridge: Addison-Wesely publishing, 1962.

[103] H. Haddadpour and R. Firouz-Abadi, "Evaluation of quasi-steady aerodynamic modeling for flutter prediction of aircraft wings in incompressible flow," *Thin-walled structures,* vol. 44, no. 9, pp. 931-936, 2006.

[104] R. T. Jones, "The unsteady lift of a wing of finite aspect ratio," National Advisory Committee for Aeronautics. Langley Aeronautical Lab.

[105] M. Karpel, "Design for active flutter suppression and gust alleviation using state-space aeroelastic modeling," *journal of aircraft,* vol. 19, no. 3, pp. 221-227, 1982.

[106] E. Yates, "Calculation of Flutter Characteristics for Finite-span Swept Or Unswept Wings at Subsonic, Transonic, and Supersonic Speeds by a Modified Strip Analysis," Virginia Polytechnic Institute, PhD thesis, 1959.

[107] T. Murray, "On the use of the indicial-function concept in the analysis of unsteady motions of wings and wing-tail combinations," NACA Technical Report 1188, USA, 1954.

[108] H. Lomax, "Indicial aerodynamics," AGARD Manual of Aeroelasticit, Pt. II, chapter 6, 1960.

[109] G. J. Leishman, Principles of helicopter aerodynamics with CD extra, Cambridge university press, 2006.

[110] J. Leishman, "Indicial lift approximations for two-dimensional subsonic flow as obtained from oscillatory measurements," *Journal of Aircraft,* vol. 30, no. 3, pp. 340-351, 1993.

[111] B. Mazelsky, "Numerical determination of indicial lift of a two-dimensional sinking airfoil at subsonic Mach numbers from oscillatory lift coefficients with calculations for Mach number 0.7," NACA Technical Note, No. 2562, 1951.

[112] B. Mazelsky, "Determination of Indicial Lift and Moment of a Two Dimensional Pitching Airfoil at Subsonic Mach Numbers From Oscillatory Coefficients With Numerical Calculations for a Mach Number of 0.7," NACA Technical Note, No. 2613, 1952.

[113] B. Mazelsky and J. A. Drischler, "Numerical determination of indicial lift and moment functions for a two-dimensional sinking and pitching airfoil at Mach numbers 0.5 and 0.6," NACA Technical Note, No. 2739, 1952.

[114] J. G. Leishman, Principles of Helicopter aerodynamics, USA: cambridge university press, 2001.

[115] P. Marzocca, L. Librescu and G. Chiocchia, "Aeroelastic response of a 2-D airfoil in a compressible flow field and exposed to blast loading," *Aerospace Science and Technology,* vol. 6, no. 4, p. 259–272, 2002.

[116] W. F. Diederich, "A plan-form parameter for correlating certain aerodynamic characteristics of swept wings," NASA report- NACA-TN-2335 , USA, 1951.

[117] A. Arena, W. Lacarbonara and P. Marzocca, "Nonlinear aeroelastic formulation for flexible high-aspect ratio wings via geometrically exact approach," in

Proceedings of the 52nd AIAA/ASME/ASCE/AHS/ASC Structures, Structural Dynamics and Materials Conference, Colorado, USA, 2011.

[118] K. Eskandary, M. Dardel, M. Pashaei and A. Moosavi, "Nonlinear aeroelastic analysis of high-aspect-ratio wings in low subsonic flow," *Acta Astronaut,* vol. 70, pp. 6-22, 2012.

[119] S. Shams, M. Sadr and H. Haddadpour, "An efficient method for nonlinear aeroelasticity of slender wings," *Nonlinear Dynamics,* vol. 67, p. 659–681, 2012.

[120] M. Patil, D. Hodges and C. Cesnik, "Characterizing the effects of geometrical nonlinearities on aeroelastic behavior of high-aspect-ratio wings," in *Proceedings of the International Forum on Aeroelasticity and Structural Dynamics (IFASD 1999)*, Virginia, USA, 1999.

[121] S. Shams, M. S. Lahidjiani and H. Haddadpour, "Nonlinear aeroelastic response of slender wings based on wagner function," *Thin-Walled Structure,* vol. 46, p. 1192–1203, 2008.

[122] E. Jacobs and A. Sherman, "Airfoil section characteristics as affected by variations of the reynolds number," Tech. rep., NACA Report No. 586, USA.

[123] A. H. Nayfeh and D. T. Mook, Nonlinear oscillations, John Wiley & Sons, 2008.

[124] Z. Qin and L. Librescu, "On a shear-deformable theory of anisotropic thin-walled beams: further contribution and validations," *Composite Structures,* vol. 56, no. 4, pp. 345-358, 2002.

[125] J. G. Barmby, H. J. Cunningham and I. Garrick, "tudy of effects of sweep on the flutter of cantilever wings," NASA report, USA, 1950.

[126] D. Tang and E. H. Dowell, "Experimental and Theoretical Study on Aeroelastic Response of High-Aspect-Ratio Wings," *AIAA Journal,* vol. 39, no. 8, pp. 1430-1441, 2001.

[127] M. O. Gözcü and A. Kayran, "Investigation of the effect of bending twisting coupling on the loads in wind turbines with superelement blade definition," *Journal of physics: conference series,* vol. 524, no. 1, 2014.

[128] J. Jonkman, S. Butterfield, W. Musial and G. Scott, "Definition of a 5-MW Reference Wind Turbine Offshore System Development," National Renewable Energy Laboratory, NREL/TP-500-38060, 2009.

[129] Ö. Şener, T. Farsadi and A. Kayran, "Effect of Fiber Orientation of Bend-Twist Coupled Blades on the Structural Performance of the Wind Turbine System," in *35th Wind Energy Symposium, AIAA SciTech Forum* , Grapevine, TX, 2017.

[130] W. Yu, J. Ho and D. Hodges, "Variational Asymptotic Beam Sectional Analysis - An Updated Version," *International Journal of Engineering Science,* vol. 59, pp. 40-64, 2012.

[131] C. Lindenburg, "PHATAS Release “JAN-2012a” User’s Manual, Program for Horizontal Axis wind Turbine Analysis and Simulation," ECN-I--05-005 r10, 2012.

[132] L. C., "BLADEMODE Program for Rotor Blade Mode Analysis," ECN-C--02-050, Knowledge Center WMC, Wieringerweft, The Netherlands, 2003.

[133] T. Farsadi and A. Kayran, "Aeroelastic stability evaluation of bend-twist coupled composite wind turbine blades designed for load alleviation in wind turbine systems," in *34th Wind Energy Symposium, AIAA SciTech Forum*, FL, USA, 2016.

[134] F. T. and K. A., "Time domain flutter analysis of bend-twist coupled composite wind turbine blades and comparisons with the baseline blade," in *world*

congress on advances in civil, environmental and material research (ACEM16), Jeju Island, Korea, 2016.

[135] K. Jones and M. Platzer, "Airfoil Geometry and Flow Compressibility Effects on Wing and Blade Flutter," in *AIAA Paper No. 98-0517, 36th AIAA Aerospace Sciences Meeting*, Nevada, USA, 1998.

[136] F. P. and Y. C., "Effect of Modified Aerodynamic Strip Theories on Rotor Blade Aeroelastic Stability," *AIAA Journal,* vol. 15, no. 7, pp. 932-940, 1977.

[137] America's Climate Choices: Panel on Advancing the Science of Climate Change; National Research Council, Washington, D.C.: The National Academies Press, 2010.

[138] "America's Climate Choices: Panel on Advancing the Science of Climate Change," National Research Council : The National Academies Press, Washington, D.C., 2010.

[139] H. Haddadpour and R. Firouz-Abadi, "Evaluation of quasi-steady aerodynamic modeling for flutter prediction of aircraft wings in incompressible flow," *Thin-walled structures,* vol. 44, no. 9, pp. 931-936, 2006.

[140] M. Gözcü, T. Farsadi, Ö. Şener and A. Kayran, "Assessment of the Effect of Hybrid GFRP-CFRP Usage in Wind Turbine Blades on the Reduction of Fatigue Damage Equivalent Loads in the Wind Turbine System," in *AIAA SciTech, 33rd Wind Energy Symposium*, Kissimmee, FL, 2015.

[141] E. Voegele, "biomass," U.S. Energy Information Administration , 10 March 2015. [Online]. Available: biomassmagazine.com.

[142] J. Leishman, "Validation of approximate indicial aerodynamic functions for wo-dimensional subsonic flow," *Journal of Aircraft,* vol. 25, no. 10, pp. 914-922, 1988.

[143] T. Farsadi and A. Kayran, "Time domain flutter analysis of bend-twist coupled composite wind turbine blades and comparisons with the baseline blade," in *world congress on advances in civil, environmental and material research*, Jeju Island, Korea, 2016.

[144] T. Farsadi, O. Sener and A. Kayran, "Free vibration analysis of uniform and asymmetric composite pretwisted rotating thin walled beam," in *Proceedings of the ASME International Mechanical Engineering Congress and Exposition, Florida, USA*, IMECE2017-70531, 2017.

APPENDICES

A. CONSTITUTIVE EQUATIONS AND STIFFNESS COMPONENTS

The Constitutive Equations;

$$\bar{Q}_{11} = \bar{C}_{11} - \frac{\bar{C}_{13}^2}{\bar{C}_{33}} \tag{A.1}$$

$$\bar{Q}_{12} = \bar{C}_{12} - \frac{\bar{C}_{13}\bar{C}_{23}}{\bar{C}_{33}} \tag{A.2}$$

$$\bar{Q}_{16} = \bar{C}_{16} - \frac{\bar{C}_{13}\bar{C}_{36}}{\bar{C}_{33}} \tag{A.3}$$

$$\bar{Q}_{22} = \bar{C}_{22} - \frac{\bar{C}_{23}^2}{\bar{C}_{33}} \tag{A.4}$$

$$\bar{Q}_{26} = \bar{C}_{26} - \frac{\bar{C}_{23}\bar{C}_{36}}{\bar{C}_{33}} \tag{A.5}$$

$$\bar{Q}_{66} = \bar{C}_{66} - \frac{\bar{C}_{36}^2}{\bar{C}_{33}} \tag{A.6}$$

$$\bar{Q}_{44} = \bar{C}_{44}, \qquad \bar{Q}_{55} = \bar{C}_{55}, \qquad \bar{Q}_{45} = \bar{C}_{45} \tag{A.7}$$

Where,

$$\bar{C}_{11} = C_{11}\cos^4\theta + 2(C_{12} + 2C_{66})\cos^2\theta\sin^2\theta + C_{22}\sin^4\theta \tag{A.8}$$

$$\bar{C}_{12} = C_{12}\cos^4\theta + (C_{11} + C_{22} - 4C_{66})\cos^2\theta\sin^2\theta + C_{12}\sin^4\theta \tag{A.9}$$

$$\bar{C}_{13} = C_{13}\cos^2\theta + C_{23}\sin^2\theta \tag{A.10}$$

$$\bar{C}_{16} = \left(C_{11} - C_{12} - 2C_{66}\right)\cos^3\theta\sin\theta + (C_{12} + 2C_{66} - C_{22})\cos\theta\sin^3\theta \tag{A.11}$$

$$\bar{C}_{22} = C_{22}\cos^4\theta + 2(C_{12} + 2C_{66})\cos^2\theta\sin^2\theta + C_{11}\sin^4\theta \tag{A.12}$$

$$\bar{C}_{23} = C_{23}\cos^2\theta + C_{13}\sin^2\theta \tag{A.13}$$

$$\bar{C}_{26} = \left(C_{12} - C_{22} + 2C_{66}\right)\cos^3\theta\sin\theta + \left(C_{11} - C_{12} - 2C_{66}\right)\cos\theta\sin^3\theta \tag{A.14}$$

$$\bar{C}_{33} = C_{33} \tag{A.15}$$

$$\bar{C}_{36} = \left(C_{13} - C_{23}\right)\cos\theta\sin\theta \tag{A.16}$$

$$\bar{C}_{66} = \left(C_{11} + C_{22} - 2C_{12} - 2C_{66}\right)\cos^2\theta\sin^2\theta + C_{66}\cos^4\theta\sin^4\theta \tag{A.17}$$

$$\bar{C}_{44} = C_{44}\cos^2\theta + C_{55}\sin^2\theta \tag{A.18}$$

$$\bar{C}_{45} = \left(C_{55} - C_{44}\right)\cos\theta\sin\theta \tag{A.19}$$

$$\bar{C}_{55} = C_{55}\cos^2\theta + C_{44}\sin^2\theta \tag{A.20}$$

and where,

$$C_{11} = \frac{E_1\left(1 - v_{23}v_{32}\right)}{\Delta} \tag{A.21}$$

$$C_{12} = \frac{E_1\left(v_{21} + v_{31}v_{23}\right)}{\Delta} \tag{A.22}$$

$$C_{13} = \frac{E_1\left(v_{31} + v_{21}v_{32}\right)}{\Delta} \tag{A.23}$$

$$C_{22} = \frac{E_2\left(1 - v_{13}v_{31}\right)}{\Delta} \tag{A.24}$$

$$C_{23} = \frac{E_2\left(v_{32} + v_{12}v_{31}\right)}{\Delta} \tag{A.25}$$

$$C_{33} = \frac{E_3\left(1 - v_{12}v_{21}\right)}{\Delta} \tag{A.26}$$

$$C_{44} = G_{23}, \qquad C_{55} = G_{13}, \qquad C_{66} = G_{12} \tag{A.27}$$

$$\Delta = \left(1 - v_{12}v_{21} - v_{23}v_{32} - v_{31}v_{13} - 2v_{21}v_{32}v_{13}\right) \tag{A.28}$$

The components of the reduced stiffness matrix in Equation (2-1) are as follows,

$$K_{11} = A_{22} - \left(\frac{A_{21}^2 D_{11} + B_{21}^2 A_{11} - 2A_{21} B_{11} B_{21}}{A_{11} D_{11} - B_{11}^2} \right) \tag{A.29}$$

$$K_{12} = B_{22} - \left(\frac{B_{21} A_{21} D_{11} - B_{21}^2 B_{11} + B_{21} A_{11} D_{21} - A_{21} B_{11} D_{21}}{A_{11} D_{11} - B_{11}^2} \right) \tag{A.30}$$

$$K_{13} = D_{22} - \left(\frac{D_{21} A_{21} D_{11} - D_{21} B_{21} B_{11} + B_{21} A_{11} F_{21} - A_{21} B_{11} F_{21}}{A_{11} D_{11} - B_{11}^2} \right) \tag{A.31}$$

$$K_{14} = A_{26} - \left(\frac{A_{61} A_{21} D_{11} - A_{61} B_{21} B_{11} + B_{21} A_{11} B_{61} - A_{21} B_{11} B_{61}}{A_{11} D_{11} - B_{11}^2} \right) \tag{A.32}$$

$$K_{15} = B_{26} - \left(\frac{B_{61} A_{21} D_{11} - B_{61} B_{21} B_{11} + B_{21} A_{11} D_{61} - A_{21} B_{11} D_{61}}{A_{11} D_{11} - B_{11}^2} \right) \tag{A.33}$$

$$K_{22} = D_{22} - \left(\frac{B_{21}^2 D_{11} - B_{21} D_{21} B_{11} + D_{21}^2 A_{11} - D_{21} B_{21} B_{11}}{A_{11} D_{11} - B_{11}^2} \right) \tag{A.34}$$

$$K_{23} = F_{22} - \left(\frac{B_{21} D_{21} D_{11} - D_{21}^2 B_{11} + F_{21} D_{21} A_{11} - F_{21} B_{21} B_{11}}{A_{11} D_{11} - B_{11}^2} \right) \tag{A.35}$$

$$K_{24} = B_{26} - \left(\frac{A_{61} B_{21} D_{11} - A_{61} D_{21} B_{11} + B_{61} D_{21} A_{11} - B_{61} B_{21} B_{11}}{A_{11} D_{11} - B_{11}^2} \right) \tag{A.36}$$

$$K_{25} = D_{26} - \left(\frac{B_{61} B_{21} D_{11} - B_{61} D_{21} B_{11} + D_{61} D_{21} A_{11} - D_{61} B_{21} B_{11}}{A_{11} D_{11} - B_{11}^2} \right) \tag{A.37}$$

$$K_{33} = H_{22} - \left(\frac{D_{21}^2 D_{11} - D_{21} F_{21} B_{11} + F_{21}^2 A_{11} - F_{21} D_{21} B_{11}}{A_{11} D_{11} - B_{11}^2} \right) \tag{A.38}$$

$$K_{34} = D_{26} - \left(\frac{A_{61} D_{21} D_{11} - A_{61} F_{21} B_{11} + B_{61} F_{21} A_{11} - B_{61} D_{21} B_{11}}{A_{11} D_{11} - B_{11}^2} \right) \tag{A.39}$$

$$K_{35} = F_{26} - \left(\frac{B_{61} D_{21} D_{11} - B_{61} F_{21} B_{11} + D_{61} F_{21} A_{11} - D_{61} D_{21} B_{11}}{A_{11} D_{11} - B_{11}^2} \right) \tag{A.40}$$

$$K_{44} = A_{66} - \left(\frac{A_{61}^2 D_{11} - A_{61} B_{61} B_{11} + B_{61}^2 A_{11} - B_{61} A_{61} B_{11}}{A_{11} D_{11} - B_{11}^2} \right) \tag{A.41}$$

$$K_{45} = B_{66} - \left(\frac{B_{61} A_{61} D_{11} - B_{61}^2 B_{11} + D_{61} B_{61} A_{11} - D_{61} A_{61} B_{11}}{A_{11} D_{11} - B_{11}^2} \right) \tag{A.42}$$

$$K_{55} = D_{66} - \left(\frac{B_{61}^2 D_{11} - B_{61} D_{61} B_{11} + D_{61}^2 A_{11} - D_{61} B_{61} B_{11}}{A_{11} D_{11} - B_{11}^2} \right) \tag{A.43}$$

B. ELEMENTS OF THE STIFFNESS MATRIX

The following relations are explicit definitions of the 8 × 8 symmetric stiffness matrix, presented in Equation (4-108).

stiffness	Definition	Nature and/or coupling involved	Dimension
a_{11}	$\oint_C K_{11} ds$	Extensional	[F]
a_{12}	$\oint_C K_{14} \frac{dx}{ds} ds$	Extension – Chordwise shear	[F]
a_{13}	$\oint_C K_{14} \frac{dy}{ds} ds$	Extension – Flpawise shear	[F]
a_{14}	$\oint_C \left(K_{11} x + K_{12} \frac{dy}{ds} \right) ds$	Extension – Chordwise bending	[F.L]
a_{15}	$\oint_C \left(K_{11} y - K_{12} \frac{dx}{ds} \right) ds$	Extension – Flapwise bending	[F.L]
a_{16}	$\oint_C \left(K_{14} \Psi(s) + 2K_{15} \right) ds$	Extension – Torsion	[F.L]
a_{17}	$\oint_C \left(K_{11} F_w(s) + K_{12} a(s) \right) ds$	Extension – Warping	[F.L^2]
a_{18}	$\oint_C \left(K_{11} \left(x^2 + y^2 \right) + 2K_{12} r_n(s) + K_{13} \right) ds$	Extension – higher order coupling of Torsion	[F.L^2]
a_{22}	$\oint_C \left(K_{44} \left(\frac{dx}{ds} \right)^2 + \left(A_{44} - \frac{A_{45}^2}{A_{55}} \right) \left(\frac{dy}{ds} \right)^2 \right) ds$	Chordwise transverse shear	[F]
a_{23}	$\oint_C \frac{dx}{ds} \frac{dy}{ds} \left(K_{44} - \left(A_{44} - \frac{A_{45}^2}{A_{55}} \right) \right) ds$	Chordwise shear - Flpawise shear	[F]
a_{24}	$\oint_C \frac{dx}{ds} \left(K_{41} x + K_{42} \frac{dy}{ds} \right) ds$	Chordwise shear – Chordwise bending	[F.L]
a_{25}	$\oint_C \frac{dx}{ds} \left(K_{41} y - K_{42} \frac{dx}{ds} \right) ds$	Chordwise shear – Flapwise bending	[F.L]
a_{26}	$\oint_C \frac{dx}{ds} \left(K_{44} \Psi(s) + 2K_{45} \right) ds$	Chordwise shear – Torsion	[F.L]

a_{27}	$\oint_C \frac{dx}{ds}\left(K_{41}F_w\left(s\right)+K_{42}a\left(s\right)\right)ds$	Chordwise shear – Warping	[F.L^2]
a_{28}	$\oint_C \frac{dx}{ds}\left(K_{41}\left(x^2+y^2\right)+2K_{42}r_n\left(s\right)+K_{43}\right)ds$	Chordwise shear – higher order coupling of Torsion	[F.L^2]
a_{33}	$\oint_C \left(K_{44}\left(\frac{dy}{ds}\right)^2+\left(A_{44}-\frac{A_{45}^2}{A_{55}}\right)\left(\frac{dx}{ds}\right)^2\right)ds$	Flpawise transverse shear	[F]
a_{34}	$\oint_C \frac{dy}{ds}\left(K_{41}x+K_{42}\frac{dy}{ds}\right)ds$	Flpawise shear - Chordwise bending	[F.L]
a_{35}	$\oint_C \frac{dy}{ds}\left(K_{41}y-K_{42}\frac{dx}{ds}\right)ds$	Flpawise shear - Flapwise bending	[F.L]
a_{36}	$\oint_C \frac{dy}{ds}\left(K_{44}\Psi\left(s\right)+2K_{45}\right)ds$	Flpawise shear – Torsion	[F.L]
a_{37}	$\oint_C \frac{dy}{ds}\left(K_{41}F_w\left(s\right)+K_{42}a\left(s\right)\right)ds$	Flpawise shear - Warping	[F.L^2]
a_{38}	$\oint_C \frac{dy}{ds}\left(K_{41}\left(x^2+y^2\right)+2K_{42}r_n\left(s\right)+K_{43}\right)ds$	Flpawise shear - higher order coupling of Torsion	[F.L^2]
a_{44}	$\oint_C \left(K_{11}x^2+K_{21}x\frac{dy}{ds}+K_{12}x\frac{dy}{ds}+K_{22}\left(\frac{dy}{ds}\right)^2\right)ds$	Chordwise bending	[F.L]
a_{45}	$\oint_C \left(K_{11}yx+K_{21}y\frac{dy}{ds}-K_{12}x\frac{dx}{ds}-K_{22}\frac{dy}{ds}\frac{dx}{ds}\right)ds$	Chordwise bending - Flapwise bending	[F.L]
a_{46}	$\oint_C \left(\Psi\left(s\right)\left(K_{14}x+K_{24}\frac{dy}{ds}\right)+2\left(K_{15}x+K_{25}\frac{dy}{ds}\right)\right)ds$	Chordwise bending - Torsion	[F.L]
a_{47}	$\oint_C \left(F_w\left(s\right)\left(K_{11}x+K_{21}\frac{dy}{ds}\right)+a\left(s\right)\left(K_{12}x+K_{22}\frac{dy}{ds}\right)\right)ds$	Chordwise bending - Warping	[F.L^2]
a_{48}	$\oint_C \left(\begin{array}{l}\left(K_{11}x+K_{21}\frac{dy}{ds}\right)\left(x^2+y^2\right)+x\left(2K_{12}r_n\left(s\right)+K_{13}\right)+\\ \frac{dy}{ds}\left(2K_{22}r_n\left(s\right)+K_{23}\right)\end{array}\right)ds$	Chordwise bending – higher order coupling of Torsion	[F.L^2]

a_{55}	$\oint_C \left(y\left(K_{11}y - K_{21}\frac{dx}{ds} \right) - \frac{dx}{ds}\left(K_{12}y - K_{22}\frac{dx}{ds} \right) \right) ds$	Flapwise bending moment	[F.L]
a_{56}	$\oint_C \left(\Psi(s)\left(K_{14}y - K_{24}\frac{dx}{ds} \right) + 2\left(K_{15}y - K_{25}\frac{dx}{ds} \right) \right) ds$	Flapwise bending - Torsion	[F.L]
a_{57}	$\oint_C \left(F_w(s)\left(K_{11}y - K_{21}\frac{dx}{ds} \right) + a(s)\left(K_{12}y - K_{22}\frac{dx}{ds} \right) \right) ds$	Flapwise bending - Warping	[F.L^2]
a_{58}	$\oint_C \left(\begin{array}{l} \left(K_{11}y - K_{21}\frac{dx}{ds} \right)\left(x^2 + y^2 \right) + y\left(2K_{12}r_n(s) + K_{13} \right) - \\ \frac{dx}{ds}\left(2K_{22}r_n(s) + K_{23} \right) \end{array} \right) ds$	Flapwise bending - higher order coupling of Torsion	[F.L^2]
a_{66}	$\oint_C \left(\left(K_{44}\Psi + 2K_{54} + 2K_{45} \right)\Psi(s) + 4K_{55} \right) ds$	Torsion	[F.L]
a_{67}	$\oint_C \left(\left(K_{41}\Psi + 2K_{51} \right)F_w(s) + \left(K_{42}\Psi + 2K_{52} \right)a(s) \right) ds$	Torsion - Warping	[F.L^2]
a_{68}	$\oint_C \left(\begin{array}{l} \left(K_{41}\Psi + 2K_{51} \right)\left(x^2 + y^2 \right) + 2\left(K_{42}\Psi + 2K_{52} \right)r_n(s) + \\ \left(K_{43}\Psi + 2K_{53} \right) \end{array} \right) ds$	Torsion - higher order coupling of Torsion	[F.L^2]
a_{77}	$\oint_C \left(K_{11}F_w^2(s) + 2K_{21}a(s)F_w(s) + K_{22}a^2(s) \right) ds$	Warping	[F.L^2]
a_{78}	$\oint_C \left(\begin{array}{l} \left(K_{11}F_w(s) + K_{21}a(s) \right)\left(x^2 + y^2 \right) + \\ \left(2K_{12}F_w(s) + 2K_{22}a(s) \right)2r_n(s) + \\ \left(K_{13}F_w(s) + K_{23}a(s) \right) \end{array} \right) ds,$	Warping - higher order coupling of Torsion	[F.L^2]
a_{88}	$\oint_C \left(\begin{array}{l} \left(x^2 + y^2 \right)\left(\left(x^2 + y^2 \right)K_{11} + 2r_n(s)K_{21} + K_{31} \right) + \\ 2r_n(s)\left(\left(x^2 + y^2 \right)K_{12} + 2r_n(s)K_{22} + K_{32} \right) + \\ \left(\left(x^2 + y^2 \right)K_{13} + 2r_n(s)K_{23} + K_{33} \right) \end{array} \right) ds$	higher order coupling of Torsion	[F.L^2]

C. AXES AND STIFFNESS QUANTITIES AND TRANSFORMATIONS

a) Transformation of axes and their derivatives with pre-twist angle $\beta = \beta_0/L$

$$x = x^p \cos\beta - y^p \sin\beta \tag{C.1}$$

$$y = x^p \sin\beta + y^p \cos\beta \tag{C.2}$$

$$x^2 = x^{p2} \cos^2\beta - 2x^p y^p \cos\beta \sin\beta + y^{p2} \sin^2\beta \tag{C.3}$$

$$y^2 = x^{p2} \sin^2\beta + 2x^p y^p \cos\beta \sin\beta + y^{p2} \cos^2\beta \tag{C.4}$$

$$xy = \left(x^{p2} - y^{p2}\right)\cos\beta \sin\beta + x^p y^p \cos^2\beta - x^p y^p \sin^2\beta \tag{C.5}$$

$$\frac{dx}{ds} = \frac{dx^p}{ds}\cos\beta - \frac{dy^p}{ds}\sin\beta \tag{C.6}$$

$$\frac{dy}{ds} = \frac{dx^p}{ds}\sin\beta + \frac{dy^p}{ds}\cos\beta \tag{C.7}$$

$$x^2 + y^2 = \left(x^{p2} + y^{p2}\right) \tag{C.8}$$

$$\frac{dx}{ds}^2 = \frac{dx^p}{ds}^2 \cos^2\beta - 2\frac{dy^p}{ds}\frac{dx^p}{ds}\cos\beta \sin\beta + \frac{dy^p}{ds}^2 \sin^2\beta \tag{C.9}$$

$$\frac{dy}{ds}^2 = \frac{dx^p}{ds}^2 \sin^2\beta + 2\frac{dy^p}{ds}\frac{dx^p}{ds}\cos\beta \sin\beta + \frac{dy^p}{ds}^2 \cos^2\beta \tag{C.10}$$

$$\frac{dx}{ds}\frac{dy}{ds} = \frac{dx^p}{ds}\frac{dy^p}{ds}\cos^2\beta - \frac{dx^p}{ds}\frac{dy^p}{ds}\sin^2\beta + \left(\frac{dx^p}{ds}^2 - \frac{dy^p}{ds}^2\right)\cos\beta \sin\beta \tag{C.11}$$

$$x\frac{dx}{ds} = x^p \frac{dx^p}{ds}\cos^2\beta - \left(x^p \frac{dy^p}{ds} + y^p \frac{dx^p}{ds}\right)\cos\beta \sin\beta + y^p \frac{dy^p}{ds}\sin^2\beta \tag{C.12}$$

$$y\frac{dx}{ds} = \left(x^p \frac{dx^p}{ds} - y^p \frac{dy^p}{ds}\right)\cos\beta \sin\beta - x^p \frac{dy^p}{ds}\sin^2\beta + y^p \frac{dx^p}{ds}\cos^2\beta \tag{C.13}$$

$$y\frac{dy}{ds} = x^p \frac{dx^p}{ds}\sin^2\beta + \left(x^p \frac{dy^p}{ds} + y^p \frac{dx^p}{ds}\right)\cos\beta \sin\beta + y^p \frac{dy^p}{ds}\cos^2\beta \tag{C.14}$$

$$x\frac{dy}{ds}=\left(x^{p}\frac{dx^{p}}{ds}-y^{p}\frac{dy^{p}}{ds}\right)\cos\beta\sin\beta+x^{p}\frac{dy^{p}}{ds}\cos^{2}\beta-y^{p}\frac{dx^{p}}{ds}\sin^{2}\beta \tag{C.15}$$

$$a(s)=a^{p}(s) \tag{C.16}$$

$$r_{n}(s)=r_{n}^{p}(s) \tag{C.17}$$

$$F_{w}(s)=F_{w}^{p}(s) \tag{C.18}$$

b) Stiffness quantities in terms of principal axes (x^p, y^p)

a_{ij}	**Definition**
a_{11}	a_{11}^{p}
a_{12}	$a_{12}^{p}\cos\beta-a_{13}^{p}\sin\beta$
a_{13}	$a_{12}^{p}\sin\beta+a_{13}^{p}\cos\beta$
a_{14}	$a_{14}^{p}\cos\beta-a_{15}^{p}\sin\beta$
a_{15}	$a_{14}^{p}\sin\beta+a_{15}^{p}\cos\beta$
a_{16}	a_{16}^{p}
a_{17}	a_{17}^{p}
a_{18}	a_{18}^{p}
a_{22}	$a_{22}^{p}\cos^{2}\beta-2a_{32}^{p}\cos\beta\sin\beta+a_{33}^{p}\sin^{2}\beta$
a_{23}	$a_{23}^{p}\cos^{2}\beta-a_{23}^{p}\sin^{2}\beta+a_{22}^{p}\cos\beta\sin\beta-a_{33}^{p}\cos\beta\sin\beta$
a_{24}	$a_{24}^{p}\cos^{2}\beta-a_{34}^{p}\cos\beta\sin\beta-a_{25}^{p}\cos\beta\sin\beta+a_{35}^{p}\sin^{2}\beta$
a_{25}	$a_{24}^{p}\cos\beta\sin\beta-a_{34}^{p}\sin^{2}\beta+a_{25}^{p}\cos^{2}\beta-a_{35}^{p}\cos\beta\sin\beta$
a_{26}	$a_{26}^{p}\cos\beta-a_{36}^{p}\sin\beta$
a_{27}	$a_{27}^{p}\cos\beta-a_{37}^{p}\sin\beta$
a_{28}	$a_{28}^{p}\cos\beta-a_{38}^{p}\sin\beta$

$$a_{33} \quad a_{22}^{p} \sin^2 \beta + a_{23}^{p} \cos\beta \sin\beta + a_{33}^{p} \cos^2 \beta$$

$$a_{34} \quad a_{34}^{p} \cos^2 \beta + a_{24}^{p} \cos\beta \sin\beta - a_{25}^{p} \sin^2 \beta - a_{35}^{p} \cos\beta \sin\beta$$

$$a_{35} \quad a_{24}^{p} \sin^2 \beta + a_{34}^{p} \cos\beta \sin\beta + a_{25}^{p} \cos\beta \sin\beta + a_{35}^{p} \cos^2 \beta$$

$$a_{36} \quad a_{26}^{p} \sin\beta + a_{36}^{p} \cos\beta$$

$$a_{37} \quad a_{27}^{p} \sin\beta + a_{37}^{p} \cos\beta$$

$$a_{38} \quad a_{28}^{p} \sin\beta + a_{38}^{p} \cos\beta$$

$$a_{44} \quad a_{44}^{p} \cos^2 \beta - a_{45}^{p} \cos\beta \sin\beta - a_{54}^{p} \cos\beta \sin\beta + a_{55}^{p} \sin^2 \beta$$

$$a_{45} \quad a_{45}^{p} \cos^2 \beta + a_{44}^{p} \cos\beta \sin\beta - a_{54}^{p} \sin^2 \beta - a_{55}^{p} \cos\beta \sin\beta$$

$$a_{46} \quad a_{46}^{p} \cos\beta - a_{56}^{p} \sin\beta$$

$$a_{47} \quad a_{47}^{p} \cos\beta - a_{57}^{p} \sin\beta$$

$$a_{48} \quad a_{48}^{p} \cos\beta - a_{58}^{p} \sin\beta$$

$$a_{55} \quad a_{44}^{p} \sin^2 \beta + 2a_{45}^{p} \sin\beta \cos\beta + a_{55}^{p} \cos^2 \beta$$

$$a_{56} \quad a_{56}^{p} \cos\beta + a_{46}^{p} \sin\beta$$

$$a_{57} \quad a_{57}^{p} \cos\beta + a_{47}^{p} \sin\beta$$

$$a_{58} \quad a_{58}^{p} \cos\beta + a_{48}^{p} \sin\beta$$

$$a_{66} \quad a_{66}^{p}$$

$$a_{67} \quad a_{67}^{p}$$

$$a_{68} \quad a_{68}^{p}$$

$$a_{77} \quad a_{77}^{p}$$

$$a_{78} \quad a_{78}^{p}$$

$$a_{88} \quad a_{88}^{p}$$

D. STRUCTURAL AND AERODYNAMIC MATRICES

The stiffness and mass matrices of the structure models are given explicitly for $\boldsymbol{i, j = 1, 2, 3, \cdots, N}$ as the following.

CAS Configuration

$$\left[M_s\right]_{6N\times 6N} = \begin{bmatrix} M_{11}^s & 0 & 0 & 0 & 0 & 0 \\ 0 & M_{22}^s & 0 & 0 & 0 & 0 \\ 0 & 0 & M_{33}^s & 0 & 0 & 0 \\ 0 & 0 & 0 & M_{44}^s & 0 & 0 \\ 0 & 0 & 0 & 0 & M_{55}^s & 0 \\ 0 & 0 & 0 & 0 & 0 & M_{66}^s \end{bmatrix} \tag{D.1}$$

Where,

$$M_{11}^s(i,j) = \int_0^L b_1 \psi_i^u \psi_j^u dz \tag{D.2}$$

$$M_{22}^s(i,j) = \int_0^L b_1 \psi_i^v \psi_j^v dz \tag{D.3}$$

$$M_{33}^s(i,j) = \int_0^L b_1 \psi_i^w \psi_j^w dz \tag{D.4}$$

$$M_{44}^s(i,j) = \int_0^L \left(b_4 + b_{12}\right) \psi_i^x \psi_j^x dz \tag{D.5}$$

$$M_{55}^s(i,j) = \int_0^L \left(b_5 + b_{11}\right) \psi_i^y \psi_j^y dz \tag{D.6}$$

$$M_{66}^s(i,j) = \int_0^L \left(b_4 + b_{12}\right) \psi_i^\phi \psi_j^\phi dz + \int_0^L \left(b_5 + b_{11}\right) \psi_i^\phi \psi_j^\phi dz + \int_0^L b_{10} \left(\psi_i^\phi\right)' \left(\psi_j^\phi\right)' dz \tag{D.7}$$

$$\left[K_s\right]_{6N\times 6N} = \begin{bmatrix} K_{11}^s & 0 & K_{13}^s & 0 & K_{15}^s & 0 \\ 0 & K_{22}^s & 0 & K_{24}^s & 0 & K_{26}^s \\ K_{31}^s & 0 & K_{33}^s & 0 & K_{35}^s & 0 \\ 0 & K_{42}^s & 0 & K_{44}^s & 0 & K_{46}^s \\ K_{51}^s & 0 & K_{53}^s & 0 & K_{55}^s & 0 \\ 0 & K_{62}^s & 0 & K_{64}^s & 0 & K_{66}^s \end{bmatrix} \tag{D.8}$$

Where

$$K_{11}^s(i,j) = -\Omega^2 \int_0^L b_1 \psi_i^u \psi_j^u dz + \int_0^L a_{22} \left(\psi_i^u\right)' \left(\psi_j^u\right)' dz + A\Omega^2 \int_0^L R\left(z\right) b_1 \left(\psi_i^u\right)' \left(\psi_j^u\right)' dz \tag{D.9}$$

$$K_{13}^s(i,j) = \int_0^L a_{12} \left(\psi_i^w\right)' \left(\psi_j^u\right)' dz \tag{D.10}$$

$$K_{15}^s(i,j) = \int_0^L a_{22} \left(\psi_i^y\right)' \psi_j^u dz \tag{D.11}$$

$$K_{24}^s(i,j) = \int_0^L a_{33} \left(\psi_i^x\right)' \psi_j^v dz \tag{D.12}$$

$$K_{22}^s(i,j) = \int_0^L a_{33} \left(\psi_i^v\right)' \left(\psi_j^v\right)' dz + A\Omega^2 \int_0^L R\left(z\right) b_1 \left(\psi_i^v\right)' \left(\psi_j^v\right)' dz \tag{D.13}$$

$$K_{26}^s(i,j) = \int_0^L -a_{37} \left(\psi_i^\phi\right)' \left(\psi_j^v\right)'' dz \tag{D.14}$$

$$K_{33}^s(i,j) = -\Omega^2 \int_0^L b_1 \psi_i^w \psi_j^w dz + \int_0^L a_{11} \left(\psi_i^w\right)' \left(\psi_j^w\right)' dz \tag{D.15}$$

$$K_{31}^s(i,j) = \int_0^L a_{12} \left(\psi_i^u\right)' \left(\psi_j^w\right)' dz \tag{D.16}$$

$$K_{35}^{s}(i,j) = \int_0^L a_{12}\left(\psi_i^y\right)' \psi_j^w dz \tag{D.17}$$

$$K_{42}^{s}(i,j) = \int_0^L a_{33}\psi_i^v \left(\psi_j^x\right)' dz \tag{D.18}$$

$$K_{44}^{s}(i,j) = \int_0^L a_{33}\psi_i^x\psi_j^x dz - \Omega^2 \int_0^L \left(b_4 + b_{12}\right)\psi_i^x\psi_j^x dz + \int_0^L a_{55}\left(\psi_i^x\right)'\left(\psi_j^x\right)' dz \tag{D.19}$$

$$K_{46}^{s}(i,j) = \int_0^L -a_{37}\psi_i^\phi \left(\psi_j^x\right)'' dz + \int_0^L a_{56}\left(\psi_i^\phi\right)'\left(\psi_j^x\right)' dz \tag{D.20}$$

$$K_{53}^{s}(i,j) = \int_0^L a_{12}\left(\psi_i^w\right)' \psi_j^y dz \tag{D.21}$$

$$K_{51}^{s}(i,j) = \int_0^L a_{22}\psi_i^u \left(\psi_j^y\right)' dz \tag{D.22}$$

$$K_{55}^{s}(i,j) = \int_0^L a_{22}\psi_i^y\psi_j^y dz - \Omega^2 \int_0^L \left(b_5 + b_{11}\right)\psi_i^y\psi_j^y dz + \int_0^L a_{44}\left(\psi_i^y\right)'\left(\psi_j^y\right)' dz \tag{D.23}$$

$$\begin{aligned} K_{66}^{s}(i,j) = {} & -\Omega^2 \int_0^L \left(b_4 + b_{12}\right)\psi_i^\phi\psi_j^\phi dz + \Omega^2 \int_0^L \left(b_5 + b_{11}\right)\psi_i^\phi\psi_j^\phi dz + \\ & \int_0^L a_{66}\left(\psi_i^\phi\right)'\left(\psi_j^\phi\right)' dz + A\Omega^2 \int_0^L R\left(z\right)\left(b_4 + b_{12}\right)\left(\psi_i^\phi\right)'\left(\psi_j^\phi\right)' dz + \\ & A\Omega^2 \int_0^L R\left(z\right)\left(b_5 + b_{11}\right)\left(\psi_i^\phi\right)'\left(\psi_j^\phi\right)' dz - \\ & \Omega^2 \int_0^L b_{10}\left(\psi_i^\phi\right)'\left(\psi_j^\phi\right)' dz - \int_0^L a_{77}\left(\psi_i^\phi\right)''\left(\psi_j^\phi\right)'' dz \end{aligned} \tag{D.24}$$

$$K_{64}^{s}(i,j) = \int_0^L a_{56}\left(\psi_i^x\right)'\left(\psi_j^\phi\right)' dz - \int_0^L a_{37}\left(\psi_i^x\right)''\psi_j^\phi dz \tag{D.25}$$

$$K_{62}^{s}(i,j) = -\int_{0}^{L} a_{37}\left(\psi_{i}^{v}\right)''\left(\psi_{j}^{\phi}\right)' dz \tag{D.26}$$

CUS Configuration

$$\left[K_{s}\right]_{6N\times 6N} = \begin{bmatrix} K_{s11} & 0 & 0 & K_{s14} & K_{s15} & 0 \\ 0 & K_{s22} & 0 & K_{s24} & K_{s25} & 0 \\ 0 & 0 & K_{s33} & 0 & 0 & K_{s36} \\ K_{s41} & K_{s42} & 0 & K_{s44} & K_{s45} & 0 \\ K_{s51} & K_{s52} & 0 & K_{s54} & K_{s55} & 0 \\ 0 & 0 & K_{s63} & 0 & 0 & K_{s66} \end{bmatrix} \tag{D.27}$$

Where.

$$K_{11}^{s}(i,j) = -\Omega^{2}\int_{0}^{L} b_{1}\psi_{i}^{u}\psi_{j}^{u}dz + \int_{0}^{L} a_{22}\left(\psi_{i}^{u}\right)'\left(\psi_{j}^{u}\right)' dz + A\Omega^{2}\int_{0}^{L} R\left(z\right)b_{1}\left(\psi_{i}^{u}\right)'\left(\psi_{j}^{u}\right)' dz \tag{D.28}$$

$$K_{14}^{s}(i,j) = \int_{0}^{L} a_{25}\left(\psi_{j}^{u}\right)'\left(\psi_{i}^{x}\right)' dz \tag{D.29}$$

$$K_{15}^{s}(i,j) = \int_{0}^{L} a_{22}\left(\psi_{i}^{y}\right)'\psi_{j}^{u}dz \tag{D.30}$$

$$K_{24}^{s}(i,j) = \int_{0}^{L} a_{33}\left(\psi_{i}^{x}\right)'\psi_{j}^{v}dz \tag{D.31}$$

$$K_{22}^{s}(i,j) = \int_{0}^{L} a_{33}\left(\psi_{i}^{v}\right)'\left(\psi_{j}^{v}\right)' dz + A\Omega^{2}\int_{0}^{L} R\left(z\right)b_{1}\left(\psi_{i}^{v}\right)'\left(\psi_{j}^{v}\right)' dz \tag{D.32}$$

$$K_{25}^{s}(i,j) = \int_{0}^{L} a_{34}\left(\psi_{j}^{v}\right)'\left(\psi_{i}^{y}\right)' dz \tag{D.33}$$

$$K^s_{33}(i,j) = -\Omega^2 \int_0^L b_1 \psi_i^w \psi_j^w dz + \int_0^L a_{11} \left(\psi_i^w\right)' \left(\psi_j^w\right)' dz \tag{D.34}$$

$$K^s_{36}(i,j) = \int_0^L a_{16} \left(\psi_j^w\right)' \left(\psi_i^\phi\right)' dz \tag{D.35}$$

$$K^s_{42}(i,j) = \int_0^L a_{33} \psi_i^v \left(\psi_j^x\right)' dz \tag{D.36}$$

$$K^s_{44}(i,j) = \int_0^L a_{33} \psi_i^x \psi_j^x dz - \Omega^2 \int_0^L \left(b_4 + b_{12}\right) \psi_i^x \psi_j^x dz + \int_0^L a_{55} \left(\psi_i^x\right)' \left(\psi_j^x\right)' dz \tag{D.37}$$

$$K^s_{41}(i,j) = \int_0^L a_{25} \left(\psi_j^x\right)' \left(\psi_i^u\right)' dz \tag{D.38}$$

$$K^s_{45}(i,j) = \int_0^L a_{25} \psi_i^y \left(\psi_j^x\right)' dz + \int_0^L a_{34} \psi_j^x \left(\psi_i^y\right)' dz \tag{D.39}$$

$$K^s_{52}(i,j) = \int_0^L a_{34} \left(\psi_j^y\right)' \left(\psi_i^v\right)' dz \tag{D.40}$$

$$K^s_{54}(i,j) = \int_0^L a_{25} \left(\psi_j^x\right)' \psi_i^y dz + \int_0^L a_{34} \left(\psi_i^y\right)' \psi_j^x dz \tag{D.41}$$

$$K^s_{51}(i,j) = \int_0^L a_{22} \psi_j^u \left(\psi_i^y\right)' dz \tag{D.42}$$

$$K^s_{55}(i,j) = \int_0^L a_{22} \psi_i^y \psi_j^y dz - \Omega^2 \int_0^L \left(b_5 + b_{11}\right) \psi_i^y \psi_j^y dz + \int_0^L a_{44} \left(\psi_i^y\right)' \left(\psi_j^y\right)' dz \tag{D.43}$$

$$K_{66}^{s}(i,j) = -\Omega^2 \int_0^L \left(b_4 + b_{12}\right)\psi_i^{\phi}\psi_j^{\phi} dz + \Omega^2 \int_0^L \left(b_5 + b_{11}\right)\psi_i^{\phi}\psi_j^{\phi} dz +$$
$$\int_0^L a_{66}\left(\psi_i^{\phi}\right)'\left(\psi_j^{\phi}\right)' dz + A\Omega^2 \int_0^L R(z)\left(b_4 + b_{12}\right)\left(\psi_i^{\phi}\right)'\left(\psi_j^{\phi}\right)' dz + \quad \text{(D.44)}$$
$$A\Omega^2 \int_0^L R(z)\left(b_5 + b_{11}\right)\left(\psi_i^{\phi}\right)'\left(\psi_j^{\phi}\right)' dz -$$
$$\Omega^2 \int_0^L b_{10}\left(\psi_i^{\phi}\right)'\left(\psi_j^{\phi}\right)' dz + \int_0^L a_{77}\left(\psi_i^{\phi}\right)''\left(\psi_j^{\phi}\right)'' dz$$

$$K_{63}^{s}(i,j) = \int_0^L a_{16}\left(\psi_j^{\phi}\right)'\left(\psi_i^{w}\right)' dz \quad \text{(D.45)}$$

The mass, damping and stiffness matrices of the aerodynamic models are given explicitly for $\boldsymbol{i, j = 1, 2, 3, \cdots, N}$ as the following.

Incompressible unsteady aerodynamic (based on Wagner's Function)

Aerodynamic Mass Matrix

$$M_{ae} = \begin{bmatrix} 0 & 0 & 0 & 0 & 0 & 0 \\ 0 & M_{22}^{a} & 0 & 0 & 0 & M_{26}^{a} \\ 0 & 0 & 0 & 0 & 0 & 0 \\ 0 & 0 & 0 & 0 & 0 & 0 \\ 0 & 0 & 0 & 0 & 0 & 0 \\ 0 & M_{62}^{a} & 0 & 0 & 0 & M_{66}^{a} \end{bmatrix} \quad \text{(D.46)}$$

Where,

$$M_{22}^{a}(i,j) = \int_0^L \pi\rho U b^2 \psi_i^{v}\psi_j^{v^T} dz \quad \text{(D.47)}$$

$$M_{26}^{a}(i,j) = \int_{0}^{L} \pi\rho U a b^{3} \psi_{i}^{\phi} \psi_{j}^{v^{T}} dz \tag{D.48}$$

$$M_{62}^{a}(i,j) = \int_{0}^{L} \pi\rho a b^{3} \psi_{i}^{v} \psi_{j}^{\phi^{T}} dz \tag{D.49}$$

$$M_{66}^{a}(i,j) = \int_{0}^{L} \pi\rho \left(\frac{1}{8} + a^{2}\right) b^{4} \psi_{i}^{\phi} \psi_{j}^{\phi^{T}} dz \tag{D.50}$$

Aerodynamic damping Matrix

$$C_{ae} = \begin{bmatrix} 0 & 0 & 0 & 0 & 0 & 0 \\ 0 & C_{22}^{a} & 0 & 0 & 0 & C_{26}^{a} \\ 0 & 0 & 0 & 0 & 0 & 0 \\ 0 & 0 & 0 & 0 & 0 & 0 \\ 0 & 0 & 0 & 0 & 0 & 0 \\ 0 & C_{62}^{a} & 0 & 0 & 0 & C_{66}^{a} \end{bmatrix} \tag{D.51}$$

Where,

$$C_{22}^{a}(i,j) = \int_{0}^{L} C_{L\phi} \rho U b \psi_{i}^{v} \psi_{j}^{v^{T}} dz \tag{D.52}$$

$$C_{26}^{a}(i,j) = \int_{0}^{L} \rho U b^{2} \left(C_{L\phi} \left(a + \frac{1}{2} - \frac{C_{L\phi}}{2\pi} \right) - \pi U \right) \psi_{i}^{\phi} \psi_{j}^{v^{T}} dz \tag{D.53}$$

$$C_{62}^{a}(i,j) = \int_{0}^{L} C_{L\phi} \rho U b^{2} \left(a + \frac{1}{2} \right) \psi_{i}^{v} \psi_{j}^{\phi^{T}} dz \tag{D.54}$$

$$C_{66}^{a}(i,j) = \int_{0}^{L} \rho U b^{3} \left(C_{L\phi} \left(a + \frac{1}{2} \right) - \pi \right) \left(a + \frac{1}{2} - \frac{C_{L\phi}}{2\pi} \right) \psi_{i}^{\phi} \psi_{j}^{\phi^{T}} dz \tag{D.55}$$

Aerodynamic Stiffness Matrix

$$K_{ae} = \begin{bmatrix} 0 & 0 & 0 & 0 & 0 & 0 \\ 0 & 0 & 0 & 0 & 0 & K_{26}^{a} \\ 0 & 0 & 0 & 0 & 0 & 0 \\ 0 & 0 & 0 & 0 & 0 & 0 \\ 0 & 0 & 0 & 0 & 0 & 0 \\ 0 & 0 & 0 & 0 & 0 & K_{66}^{a} \end{bmatrix} \tag{D.56}$$

Where,

$$K_{26}^{a}(i,j) = -\int_{0}^{L} C_{L\phi}\rho U^2 b \psi_i^{\phi} \psi_j^{v^T} dz \tag{D.57}$$

$$K_{66}^{a}(i,j) = -\int_{0}^{L} C_{L\phi}\rho U^2 b^2 \left(a + \frac{1}{2}\right) \psi_i^{\phi} \psi_j^{\phi^T} dz \tag{D.58}$$

Compressible unsteady aerodynamic (based on Indicial Function)

Aerodynamic Damping Matrix

$$C_{ae\_c} = \begin{bmatrix} 0 & 0 & 0 & 0 & 0 & 0 \\ 0 & C_{22}^{a} & 0 & 0 & 0 & C_{26}^{a} \\ 0 & 0 & 0 & 0 & 0 & 0 \\ 0 & 0 & 0 & 0 & 0 & 0 \\ 0 & 0 & 0 & 0 & 0 & 0 \\ 0 & C_{62}^{a} & 0 & 0 & 0 & C_{66}^{a} \end{bmatrix} \tag{D.59}$$

Where,

$$C_{22}^{a}(i,j) = \int_{0}^{L} C_{L\phi}\rho U_{n} b\alpha_{0c}\psi_{i}^{v}\psi_{j}^{v^{T}}\,dz \tag{D.60}$$

$$C_{26}^{a}(i,j) = -\int_{0}^{L} 2C_{L\phi}\rho U_{n} b^{2}\alpha_{0cq}\psi_{i}^{\phi}\psi_{j}^{v^{T}}\,dz \tag{D.61}$$

$$C_{62}^{a}(i,j) = \int_{0}^{L} 2C_{L\phi}\rho U_{n} b^{2}\alpha_{0cM}\psi_{i}^{v}\psi_{j}^{\phi^{T}}\,dz \tag{D.62}$$

$$C_{66}^{a}(i,j) = -\int_{0}^{L} 4C_{L\phi}\rho U_{n} b^{3}\alpha_{0cMq}\psi_{i}^{\phi}\psi_{j}^{\phi^{T}}\,dz \tag{D.63}$$

Aerodynamic Stiffness Matrix

$$K_{ae\_c} = \begin{bmatrix} 0 & 0 & 0 & 0 & 0 & 0 \\ 0 & K_{22}^{a} & 0 & 0 & 0 & K_{26}^{a} \\ 0 & 0 & 0 & 0 & 0 & 0 \\ 0 & 0 & 0 & 0 & 0 & 0 \\ 0 & 0 & 0 & 0 & 0 & 0 \\ 0 & K_{62}^{a} & 0 & 0 & 0 & K_{66}^{a} \end{bmatrix} \tag{D.64}$$

Where,

$$K_{22}^{a}(i,j) = \int_{0}^{L} C_{L\phi}\rho U_{n}^{2} b\alpha_{0c}\tan(\Lambda)\psi_{i}^{v}\psi_{j}^{\prime v^{T}}\,dz \tag{D.65}$$

$$K_{26}^{a}(i,j) = -\int_{0}^{L} C_{L\phi}\rho U_{n}^{2} b\alpha_{0c}\psi_{i}^{\phi}\psi_{j}^{v^{T}}\,dz - \int_{0}^{L} 2C_{L\phi}\rho U_{n}^{2} b^{2}\alpha_{0cq}\tan(\Lambda)\psi_{i}^{v}\psi_{j}^{\prime\phi^{T}}\,dz \tag{D.66}$$

$$K_{62}^{a}(i,j) = \int_{0}^{L} 2C_{L\phi}\rho U_{n}^{2} b^{2}\alpha_{0cM}\tan(\Lambda)\psi_{i}^{\phi}\psi_{j}^{\prime v^{T}}\,dz \tag{D.67}$$

$$K_{66}^{a}(i,j) = -\int_{0}^{L} 2C_{L\phi}\rho U_{n}^{2} b^{2} \alpha_{0cM} \psi_{i}^{\phi} \psi_{j}^{\phi^{T}} dz - \int_{0}^{L} 4C_{L\phi}\rho U_{n}^{2} b^{3} \alpha_{0cMq} \tan(\Lambda) \psi_{i}^{\phi} \psi_{j}^{\prime\phi^{T}} dz \tag{D.68}$$

E. SIMPLIFIED NONLINEAR EXPRESSIONS

The following are the algebraic expressions obtained by substitution of Equation (4-60) into the nonlinear expressions defined in Equations (4-30)-(4-39) and (4-40)-(4-48).

Quadratic nonlinear terms

$$
\begin{aligned}
N_u^2 &= a_{22}\sum_{r=1}^{m}\sum_{s=1}^{m}\left(\psi^{v\prime T}R^v\right)_r\left(\psi^{\phi T}R^\phi\right)_s\vartheta_r\vartheta_s - \\
&a_{33}\left(\sum_{r=1}^{m}\sum_{s=1}^{m}\left(\psi^{xT}R^x\right)_r\left(\psi^{\phi T}R^\phi\right)_s\vartheta_r\vartheta_s + \left(\psi^{v\prime T}R^v\right)_r\left(\psi^{\phi T}R^\phi\right)_s\vartheta_r\vartheta_s\right) - \\
&a_{55}\sum_{r=1}^{m}\sum_{s=1}^{m}\left(\psi^{x\prime T}R^x\right)_r\left(\psi^{\phi\prime T}R^\phi\right)_s\vartheta_r\vartheta_s + \\
&a_{12}\left(\sum_{r=1}^{m}\sum_{s=1}^{m}\left(\frac{3}{2}\left(\psi^{u\prime T}R^u\right)_r\left(\psi^{u\prime T}R^u\right)_s\vartheta_r\vartheta_s + \frac{1}{2}\left(\psi^{v\prime T}R^v\right)_r\left(\psi^{v\prime T}R^v\right)_s\vartheta_r\vartheta_s + \right.\right. \\
&\left.\left.\left(\psi^{yT}R^y\right)_r\left(\psi^{u\prime T}R^u\right)_s\vartheta_r\vartheta_s\right)\right) + \\
&\frac{1}{2}a_{28}\sum_{r=1}^{m}\sum_{s=1}^{m}\left(\psi^{\phi\prime T}R^\phi\right)_r\left(\psi^{\phi\prime T}R^\phi\right)_s\vartheta_r\vartheta_s - a_{56}\sum_{r=1}^{m}\sum_{s=1}^{m}\left(\psi^{\phi\prime T}R^\phi\right)_r\left(\psi^{\phi\prime T}R^\phi\right)_s\vartheta_r\vartheta_s + \\
&a_{11}\sum_{r=1}^{m}\sum_{s=1}^{m}\left(\psi^{u\prime T}R^u\right)_r\left(\psi^{w\prime T}R^w\right)_s\vartheta_r\vartheta_s + a_{37}\sum_{r=1}^{m}\sum_{s=1}^{m}\left(\psi^{\phi\prime\prime T}R^\phi\right)_r\left(\psi^{\phi T}R^\phi\right)_s\vartheta_r\vartheta_s
\end{aligned}
\tag{E.1}
$$

$$
\begin{aligned}
N_v^2 &= a_{12}\left(\sum_{r=1}^{m}\sum_{s=1}^{m}\left(\left(\psi^{u\prime T}R^u\right)_r\left(\psi^{v\prime T}R^v\right)_s\vartheta_r\vartheta_s + \left(\psi^{v\prime T}R^v\right)_r\left(\psi^{yT}R^y\right)_s\vartheta_r\vartheta_s + \right.\right. \\
&\left.\left.\left(\psi^{w\prime T}R^w\right)_r\left(\psi^{\phi T}R^\phi\right)_s\vartheta_r\vartheta_s\right)\right) \\
&a_{22}\left(\sum_{r=1}^{m}\sum_{s=1}^{m}\left(\psi^{u\prime T}R^u\right)_r\left(\psi^{\phi T}R^\phi\right)_s\vartheta_r\vartheta_s + \left(\psi^{yT}R^y\right)_r\left(\psi^{\phi T}R^\phi\right)_s\vartheta_r\vartheta_s\right) - \\
&a_{33}\sum_{r=1}^{m}\sum_{s=1}^{m}\left(\psi^{u\prime T}R^u\right)_r\left(\psi^{\phi T}R^\phi\right)_s\vartheta_r\vartheta_s + a_{44}\sum_{r=1}^{m}\sum_{s=1}^{m}\left(\psi^{\phi\prime T}R^\phi\right)_r\left(\psi^{y\prime T}R^y\right)_s\vartheta_r\vartheta_s + \\
&a_{11}\sum_{r=1}^{m}\sum_{s=1}^{m}\left(\psi^{v\prime T}R^v\right)_r\left(\psi^{w\prime T}R^w\right)_s\vartheta_r\vartheta_s
\end{aligned}
\tag{E.2}
$$

$$
\begin{aligned}
N_w^2 &= \frac{1}{2}a_{11}\left(\sum_{r=1}^{m}\sum_{s=1}^{m}\left(\psi^{u\prime T}R^u\right)_r\left(\psi^{u\prime T}R^u\right)_s\vartheta_r\vartheta_s + \left(\psi^{v\prime T}R^v\right)_r\left(\psi^{v\prime T}R^v\right)_s\vartheta_r\vartheta_s\right) + \\
&a_{12}\sum_{r=1}^{m}\sum_{s=1}^{m}\left(\psi^{v\prime T}R^v\right)_r\left(\psi^{\phi T}R^\phi\right)_s\vartheta_r\vartheta_s + \frac{1}{2}a_{18}\sum_{r=1}^{m}\sum_{s=1}^{m}\left(\psi^{\phi\prime T}R^\phi\right)_r\left(\psi^{\phi\prime T}R^\phi\right)_s\vartheta_r\vartheta_s
\end{aligned}
\tag{E.3}
$$

$$
N_x^2\Big|_1 = -a_{33}\sum_{r=1}^{m}\sum_{s=1}^{m}\left(\psi^{u\prime T}R^u\right)_r\left(\psi^{\phi T}R^\phi\right)_s\vartheta_r\vartheta_s \tag{E.4}
$$

$$N_x^2\Big|_2 = -a_{55}\sum_{r=1}^{m}\sum_{s=1}^{m}\left(\psi^{u\prime T}R^u\right)_r\left(\psi^{\phi\prime T}R^\phi\right)_s\vartheta_r\vartheta_s \tag{E.5}$$

$$N_y^2\Big|_1 = \frac{1}{2}a_{12}\left(\sum_{r=1}^{m}\sum_{s=1}^{m}\left(\psi^{u\prime T}R^u\right)_r\left(\psi^{u\prime T}R^u\right)_s\vartheta_r\vartheta_s+\left(\psi^{v\prime T}R^v\right)_r\left(\psi^{v\prime T}R^v\right)_s\vartheta_r\vartheta_s\right)+ \tag{E.6}$$
$$a_{22}\sum_{r=1}^{m}\sum_{s=1}^{m}\left(\psi^{v\prime T}R^v\right)_r\left(\psi^{\phi T}R^\phi\right)_s\vartheta_r\vartheta_s+\frac{1}{2}a_{28}\sum_{r=1}^{m}\sum_{s=1}^{m}\left(\psi^{\phi\prime T}R^\phi\right)_r\left(\psi^{\phi\prime T}R^\phi\right)_s\vartheta_r\vartheta_s$$

$$N_y^2\Big|_2 = a_{44}\sum_{r=1}^{m}\sum_{s=1}^{m}\left(\psi^{v\prime T}R^v\right)_r\left(\psi^{\phi\prime T}R^\phi\right)_s\vartheta_r\vartheta_s \tag{E.7}$$

$$N_\phi^2\Big|_1 = a_{22}\left(\sum_{r=1}^{m}\sum_{s=1}^{m}\left(\psi^{u\prime T}R^u\right)_r\left(\psi^{v\prime T}R^v\right)_s\vartheta_r\vartheta_s+\left(\psi^{v\prime T}R^v\right)_r\left(\psi^{yT}R^y\right)_s\vartheta_r\vartheta_s\right)- \tag{E.8}$$
$$a_{33}\left(\sum_{r=1}^{m}\sum_{s=1}^{m}\left(\psi^{u\prime T}R^u\right)_r\left(\psi^{v\prime T}R^v\right)_s\vartheta_r\vartheta_s+\left(\psi^{u\prime T}R^u\right)_r\left(\psi^{xT}R^x\right)_s\vartheta_r\vartheta_s\right)+$$
$$a_{12}\sum_{r=1}^{m}\sum_{s=1}^{m}\left(\psi^{v\prime T}R^v\right)_r\left(\psi^{w\prime T}R^w\right)_s\vartheta_r\vartheta_s+a_{37}\sum_{r=1}^{m}\sum_{s=1}^{m}\left(\psi^{u\prime T}R^u\right)_r\left(\psi^{\phi\prime\prime T}R^\phi\right)_s\vartheta_r\vartheta_s$$

$$N_\phi^2\Big|_2 = a_{44}\sum_{r=1}^{m}\sum_{s=1}^{m}\left(\psi^{y\prime T}R^y\right)_r\left(\psi^{v\prime T}R^v\right)_s\vartheta_r\vartheta_s+$$
$$a_{28}\left(\sum_{r=1}^{m}\sum_{s=1}^{m}\left(\psi^{yT}R^y\right)_r\left(\psi^{\phi\prime T}R^\phi\right)_s\vartheta_r\vartheta_s+\left(\psi^{u\prime T}R^u\right)_r\left(\psi^{\phi\prime T}R^\phi\right)_s\vartheta_r\vartheta_s\right)- \tag{E.9}$$
$$2a_{56}\sum_{r=1}^{m}\sum_{s=1}^{m}\left(\psi^{\phi\prime T}R^\phi\right)_r\left(\psi^{u\prime T}R^u\right)_s\vartheta_r\vartheta_s-a_{55}\sum_{r=1}^{m}\sum_{s=1}^{m}\left(\psi^{x\prime T}R^x\right)_r\left(\psi^{u\prime T}R^u\right)_s\vartheta_r\vartheta_s+$$
$$a_{18}\sum_{r=1}^{m}\sum_{s=1}^{m}\left(\psi^{w\prime T}R^w\right)_r\left(\psi^{\phi\prime T}R^\phi\right)_s\vartheta_r\vartheta_s$$

$$N_\phi^2\Big|_3 = -a_{37}\sum_{r=1}^{m}\sum_{s=1}^{m}\left(\psi^{u\prime T}R^u\right)_r\left(\psi^{\phi T}R^\phi\right)_s\vartheta_r\vartheta_s \tag{E.10}$$

Cubic nonlinear terms

$$
\begin{aligned}
N_u^3 &= \left(a_{33}-a_{22}\right)\sum_{r=1}^{m}\sum_{s=1}^{m}\sum_{p=1}^{m}\left(\psi^{u\prime T}R^u\right)_r\left(\psi^{\phi T}R^\phi\right)_s\left(\psi^{\phi T}R^\phi\right)_p\vartheta_r\vartheta_s\vartheta_p - \\
&\frac{a_{22}}{2}\sum_{r=1}^{m}\sum_{s=1}^{m}\sum_{p=1}^{m}\left(\psi^{yT}R^y\right)_r\left(\psi^{\phi T}R^\phi\right)_s\left(\psi^{\phi T}R^\phi\right)_p\vartheta_r\vartheta_s\vartheta_p - \\
&\frac{a_{12}}{2}\sum_{r=1}^{m}\sum_{s=1}^{m}\sum_{p=1}^{m}\left(\psi^{w\prime T}R^w\right)_r\left(\psi^{\phi T}R^\phi\right)_s\left(\psi^{\phi T}R^\phi\right)_p\vartheta_r\vartheta_s\vartheta_p - \\
&a_{12}\sum_{r=1}^{m}\sum_{s=1}^{m}\sum_{p=1}^{m}\left(\psi^{u\prime T}R^u\right)_r\left(\psi^{v\prime T}R^v\right)_s\left(\psi^{\phi T}R^\phi\right)_p\vartheta_r\vartheta_s\vartheta_p + \\
&\frac{a_{11}}{2}\sum_{r=1}^{m}\sum_{s=1}^{m}\sum_{p=1}^{m}\left(\psi^{u\prime T}R^u\right)_r\left(\psi^{u\prime T}R^u\right)_s\left(\psi^{u\prime T}R^u\right)_p\vartheta_r\vartheta_s\vartheta_p + \\
&\frac{a_{11}}{2}\sum_{r=1}^{m}\sum_{s=1}^{m}\sum_{p=1}^{m}\left(\psi^{u\prime T}R^u\right)_r\left(\psi^{v\prime T}R^v\right)_s\left(\psi^{v\prime T}R^v\right)_p\vartheta_r\vartheta_s\vartheta_p - \\
&a_{44}\sum_{r=1}^{m}\sum_{s=1}^{m}\sum_{p=1}^{m}\left(\psi^{y\prime T}R^y\right)_r\left(\psi^{\phi\prime T}R^\phi\right)_s\left(\psi^{\phi T}R^\phi\right)_p\vartheta_r\vartheta_s\vartheta_p + \\
&\left(a_{55}+\frac{a_{18}}{2}\right)\sum_{r=1}^{m}\sum_{s=1}^{m}\sum_{p=1}^{m}\left(\psi^{u\prime T}R^u\right)_r\left(\psi^{\phi\prime T}R^\phi\right)_s\left(\psi^{\phi\prime T}R^\phi\right)_p\vartheta_r\vartheta_s\vartheta_p
\end{aligned}
\tag{E.11}
$$

$$
\begin{aligned}
N_v^3 &= \frac{a_{11}}{2}\sum_{r=1}^{m}\sum_{s=1}^{m}\sum_{p=1}^{m}\left(\psi^{v\prime T}R^v\right)_r\left(\psi^{u\prime T}R^u\right)_s\left(\psi^{u\prime T}R^u\right)_p\vartheta_r\vartheta_s\vartheta_p - \\
&\frac{3a_{12}}{2}\sum_{r=1}^{m}\sum_{s=1}^{m}\sum_{p=1}^{m}\left(\psi^{v\prime T}R^v\right)_r\left(\psi^{v\prime T}R^v\right)_s\left(\psi^{\phi T}R^\phi\right)_p\vartheta_r\vartheta_s\vartheta_p + \\
&\left(a_{22}-a_{33}\right)\sum_{r=1}^{m}\sum_{s=1}^{m}\sum_{p=1}^{m}\left(\psi^{v\prime T}R^v\right)_r\left(\psi^{\phi T}R^\phi\right)_s\left(\psi^{\phi T}R^\phi\right)_p\vartheta_r\vartheta_s\vartheta_p - \\
&\frac{a_{33}}{2}\sum_{r=1}^{m}\sum_{s=1}^{m}\sum_{p=1}^{m}\left(\psi^{xT}R^x\right)_r\left(\psi^{\phi T}R^\phi\right)_s\left(\psi^{\phi T}R^\phi\right)_p\vartheta_r\vartheta_s\vartheta_p + \\
&\left(\frac{a_{18}}{2}+a_{44}\right)\sum_{r=1}^{m}\sum_{s=1}^{m}\sum_{p=1}^{m}\left(\psi^{v\prime T}R^v\right)_r\left(\psi^{\phi\prime T}R^\phi\right)_s\left(\psi^{\phi\prime T}R^\phi\right)_p\vartheta_r\vartheta_s\vartheta_p - \\
&\frac{a_{12}}{2}\sum_{r=1}^{m}\sum_{s=1}^{m}\sum_{p=1}^{m}\left(\psi^{u\prime T}R^u\right)_r\left(\psi^{u\prime T}R^u\right)_s\left(\psi^{\phi T}R^\phi\right)_p\vartheta_r\vartheta_s\vartheta_p + \\
&\frac{a_{11}}{2}\sum_{r=1}^{m}\sum_{s=1}^{m}\sum_{p=1}^{m}\left(\psi^{v\prime T}R^v\right)_r\left(\psi^{v\prime T}R^v\right)_s\left(\psi^{v\prime T}R^v\right)_p\vartheta_r\vartheta_s\vartheta_p - \\
&a_{55}\sum_{r=1}^{m}\sum_{s=1}^{m}\sum_{p=1}^{m}\left(\psi^{x\prime T}R^x\right)_r\left(\psi^{\phi\prime T}R^\phi\right)_s\left(\psi^{\phi T}R^\phi\right)_p\vartheta_r\vartheta_s\vartheta_p - \\
&a_{56}\sum_{r=1}^{m}\sum_{s=1}^{m}\sum_{p=1}^{m}\left(\psi^{\phi\prime T}R^v\right)_r\left(\psi^{\phi\prime T}R^u\right)_s\left(\psi^{\phi T}R^\phi\right)_p\vartheta_r\vartheta_s\vartheta_p
\end{aligned}
\tag{E.12}
$$

$$N_w^3 = \frac{-a_{12}}{2}\sum_{r=1}^{m}\sum_{s=1}^{m}\sum_{p=1}^{m}\left(\psi^{u\prime T}R^u\right)_r\left(\psi^{\phi T}R^\phi\right)_s\left(\psi^{\phi T}R^\phi\right)_p\vartheta_r\vartheta_s\vartheta_p \tag{E.13}$$

$$N_x^3\Big|_1 = -\frac{a_{33}}{2}\sum_{r=1}^{m}\sum_{s=1}^{m}\sum_{p=1}^{m}\left(\psi^{v\prime T}R^v\right)_r\left(\psi^{\phi T}R^\phi\right)_s\left(\psi^{\phi T}R^\phi\right)_p\vartheta_r\vartheta_s\vartheta_p \tag{E.14}$$

$$N_x^3\Big|_2 = -a_{55}\sum_{r=1}^{m}\sum_{s=1}^{m}\sum_{p=1}^{m}\left(\psi^{v\prime T}R^v\right)_r\left(\psi^{\phi\prime T}R^\phi\right)_s\left(\psi^{\phi T}R^\phi\right)_p\vartheta_r\vartheta_s\vartheta_p \tag{E.15}$$

$$N_y^3\Big|_1 = \frac{a_{22}}{2}\sum_{r=1}^{m}\sum_{s=1}^{m}\sum_{p=1}^{m}\left(\psi^{u\prime T}R^u\right)_r\left(\psi^{\phi T}R^\phi\right)_s\left(\psi^{\phi T}R^\phi\right)_p\vartheta_r\vartheta_s\vartheta_p \tag{E.16}$$

$$N_y^3\Big|_2 = a_{44}\sum_{r=1}^{m}\sum_{s=1}^{m}\sum_{p=1}^{m}\left(\psi^{u\prime T}R^u\right)_r\left(\psi^{\phi\prime T}R^\phi\right)_s\left(\psi^{\phi T}R^\phi\right)_p\vartheta_r\vartheta_s\vartheta_p \tag{E.17}$$

$$\begin{aligned}
N_\phi^3\Big|_1 = &-a_{55}\sum_{r=1}^{m}\sum_{s=1}^{m}\sum_{p=1}^{m}\left(\psi^{v\prime T}R^v\right)_r\left(\psi^{\phi\prime T}R^\phi\right)_s\left(\psi^{\phi T}R^\phi\right)_p\vartheta_r\vartheta_s\vartheta_p - \\
&a_{56}\sum_{r=1}^{m}\sum_{s=1}^{m}\sum_{p=1}^{m}\left(\psi^{v\prime T}R^v\right)_r\left(\psi^{\phi\prime T}R^\phi\right)_s\left(\psi^{\phi\prime T}R^\phi\right)_p\vartheta_r\vartheta_s\vartheta_p - \\
&\frac{a_{12}}{2}\sum_{r=1}^{m}\sum_{s=1}^{m}\sum_{p=1}^{m}\left(\psi^{v\prime T}R^v\right)_r\left(\psi^{u\prime T}R^u\right)_s\left(\psi^{u\prime T}R^u\right)_p\vartheta_r\vartheta_s\vartheta_p - \\
&\frac{a_{12}}{2}\sum_{r=1}^{m}\sum_{s=1}^{m}\sum_{p=1}^{m}\left(\psi^{v\prime T}R^v\right)_r\left(\psi^{v\prime T}R^v\right)_s\left(\psi^{v\prime T}R^v\right)_p\vartheta_r\vartheta_s\vartheta_p - \\
&\frac{a_{12}}{2}\sum_{r=1}^{m}\sum_{s=1}^{m}\sum_{p=1}^{m}\left(\psi^{w\prime T}R^w\right)_r\left(\psi^{u\prime T}R^u\right)_s\left(\psi^{\phi T}R^\phi\right)_p\vartheta_r\vartheta_s\vartheta_p - \\
&a_{44}\sum_{r=1}^{m}\sum_{s=1}^{m}\sum_{p=1}^{m}\left(\psi^{u\prime T}R^u\right)_r\left(\psi^{\phi\prime T}R^\phi\right)_s\left(\psi^{y\prime T}R^y\right)_p\vartheta_r\vartheta_s\vartheta_p - \\
&a_{22}\sum_{r=1}^{m}\sum_{s=1}^{m}\sum_{p=1}^{m}\left(\psi^{u\prime T}R^u\right)_r\left(\psi^{yT}R^y\right)_s\left(\psi^{\phi T}R^\phi\right)_p\vartheta_r\vartheta_s\vartheta_p - \\
&a_{22}\sum_{r=1}^{m}\sum_{s=1}^{m}\sum_{p=1}^{m}\left(\psi^{u\prime T}R^u\right)_r\left(\psi^{u\prime T}R^u\right)_s\left(\psi^{\phi T}R^\phi\right)_p\vartheta_r\vartheta_s\vartheta_p + \\
&a_{22}\sum_{r=1}^{m}\sum_{s=1}^{m}\sum_{p=1}^{m}\left(\psi^{v\prime T}R^v\right)_r\left(\psi^{v\prime T}R^v\right)_s\left(\psi^{\phi T}R^\phi\right)_p\vartheta_r\vartheta_s\vartheta_p + \\
&a_{33}\sum_{r=1}^{m}\sum_{s=1}^{m}\sum_{p=1}^{m}\left(\psi^{v\prime T}R^v\right)_r\left(\psi^{xT}R^x\right)_s\left(\psi^{\phi T}R^\phi\right)_p\vartheta_r\vartheta_s\vartheta_p + \\
&a_{33}\sum_{r=1}^{m}\sum_{s=1}^{m}\sum_{p=1}^{m}\left(\psi^{v\prime T}R^v\right)_r\left(\psi^{v\prime T}R^v\right)_s\left(\psi^{\phi T}R^\phi\right)_p\vartheta_r\vartheta_s\vartheta_p - \\
&a_{33}\sum_{r=1}^{m}\sum_{s=1}^{m}\sum_{p=1}^{m}\left(\psi^{u\prime T}R^u\right)_r\left(\psi^{u\prime T}R^u\right)_s\left(\psi^{\phi T}R^\phi\right)_p\vartheta_r\vartheta_s\vartheta_p
\end{aligned} \tag{E.18}$$

$$
\begin{aligned}
N_{\phi}^{3}\Big|_{2} &= \frac{a_{88}}{2}\sum_{r=1}^{m}\sum_{s=1}^{m}\sum_{p=1}^{m}\left(\psi^{\phi' T}R^{\phi}\right)_{r}\left(\psi^{\phi' T}R^{\phi}\right)_{s}\left(\psi^{\phi' T}R^{\phi}\right)_{p}\vartheta_{r}\vartheta_{s}\vartheta_{p} - \\
&2a_{56}\sum_{r=1}^{m}\sum_{s=1}^{m}\sum_{p=1}^{m}\left(\psi^{v' T}R^{v}\right)_{r}\left(\psi^{\phi' T}R^{\phi}\right)_{s}\left(\psi^{\phi T}R^{\phi}\right)_{p}\vartheta_{r}\vartheta_{s}\vartheta_{p} + \\
&\left(a_{55}+\frac{a_{18}}{2}\right)\sum_{r=1}^{m}\sum_{s=1}^{m}\sum_{p=1}^{m}\left(\psi^{\phi' T}R^{\phi}\right)_{r}\left(\psi^{u' T}R^{u}\right)_{s}\left(\psi^{u' T}R^{u}\right)_{p}\vartheta_{r}\vartheta_{s}\vartheta_{p} - \\
&a_{55}\sum_{r=1}^{m}\sum_{s=1}^{m}\sum_{p=1}^{m}\left(\psi^{x' T}R^{x}\right)_{r}\left(\psi^{v' T}R^{v}\right)_{s}\left(\psi^{\phi T}R^{\phi}\right)_{p}\vartheta_{r}\vartheta_{s}\vartheta_{p} + \\
&\left(a_{44}+\frac{a_{18}}{2}\right)\sum_{r=1}^{m}\sum_{s=1}^{m}\sum_{p=1}^{m}\left(\psi^{\phi' T}R^{\phi}\right)_{r}\left(\psi^{v' T}R^{v}\right)_{s}\left(\psi^{v' T}R^{v}\right)_{p}\vartheta_{r}\vartheta_{s}\vartheta_{p} - \\
&a_{44}\sum_{r=1}^{m}\sum_{s=1}^{m}\sum_{p=1}^{m}\left(\psi^{y' T}R^{y}\right)_{r}\left(\psi^{u' T}R^{u}\right)_{s}\left(\psi^{\phi T}R^{\phi}\right)_{p}\vartheta_{r}\vartheta_{s}\vartheta_{p}
\end{aligned}
\tag{E.19}
$$

G. MASS, DAMPING AND STIFFNESS MATRICES

G1. Mass, Damping and Stiffness Matrices of the Beam-Blade Considering Only Incompressible Unsteady Aerodynamics

A1. The non-zero sub-matrices ($\boldsymbol{m}_{rp}^{s}$) of the structural mass matrix ($\boldsymbol{M}_{s}$) of dimension $5N \times 3N$

$$\boldsymbol{m}_{11}^{s} = \sum_{i=1}^{17} \int_{L_i}^{L_{i+1}} \left(b_1^i\right) \boldsymbol{\Psi}_{v_0} \boldsymbol{\Psi}_{v_0}^{T} dz, \qquad \boldsymbol{m}_{22}^{s} = \sum_{i=1}^{17} \int_{L_i}^{L_{i+1}} \left(b_4^i + b_5^i\right) \boldsymbol{\Psi}_{\phi} \boldsymbol{\Psi}_{\phi}^{T} dz$$

$$\boldsymbol{m}_{33}^{s} = \sum_{i=1}^{17} \int_{L_i}^{L_{i+1}} \left(b_4^i\right) \boldsymbol{\Psi}_{\theta_x} \boldsymbol{\Psi}_{\theta_x}^{T} dz$$

where i is the number of blade sections, L_i is the length of the i^{th} section b_1, b_4, b_5 are the mass and inertia terms defined by Eqn.(25) and $\boldsymbol{\Psi}_{\Delta} = \left\{\Psi_{\Delta}(z)\right\}$ is the shape function vector given by Eqn.(60).

A2. The non-zero sub-matrices ($\boldsymbol{k}_{rp}^{s}$) of the structural stiffness matrix ($\boldsymbol{K}_{s}$) of dimension $5N \times 5N$

$$\boldsymbol{k}_{11}^{s} = \sum_{i=1}^{17} \int_{L_i}^{L_{i+1}} \left(a_{33}^i \boldsymbol{\Psi}'_{v_0} \boldsymbol{\Psi}'^{T}_{v_0} + b_1^i \Omega^2 R(z) \boldsymbol{\Psi}'_{v_0} \boldsymbol{\Psi}'^{T}_{v_0} \right) dz, \qquad \boldsymbol{k}_{13}^{s} = \boldsymbol{k}_{31}^{s} = \sum_{i=1}^{17} \int_{L_i}^{L_{i+1}} a_{33}^i \boldsymbol{\Psi}'_{v_0} \boldsymbol{\Psi}_{\theta_x}^{T} dz$$

$$\boldsymbol{k}_{22}^{s} = \sum_{i=1}^{17} \int_{L_i}^{L_{i+1}} \left(a_{66}^i \boldsymbol{\Psi}'_{\phi} \boldsymbol{\Psi}'^{T}_{\phi} + (b_4^i - b_5^i) \Omega^2 \boldsymbol{\Psi}_{\phi} \boldsymbol{\Psi}_{\phi}^{T} + (b_4^i + b_5^i) \Omega^2 R(z) \boldsymbol{\Psi}'_{\phi} \boldsymbol{\Psi}'^{T}_{\phi} \right) dz$$

$$\boldsymbol{k}_{23}^{s} = \boldsymbol{k}_{32}^{s} = \sum_{i=1}^{17} \int_{L_i}^{L_{i+1}} a_{66}^i \boldsymbol{\Psi}'_{\phi} \boldsymbol{\Psi}'^{T}_{\theta_x} dz, \quad \boldsymbol{k}_{33}^{s} = \sum_{i=1}^{17} \int_{L_i}^{L_{i+1}} \left(a_{33}^i \boldsymbol{\Psi}_{\theta_x} \boldsymbol{\Psi}_{\theta_x}^{T} + a_{55}^i \boldsymbol{\Psi}_{\phi} \boldsymbol{\Psi}_{\phi}^{T} - b_4^i \Omega^2 \boldsymbol{\Psi}_{\theta_x} \boldsymbol{\Psi}_{\theta_x}^{T} \right) dz$$

A3. The non-zero sub-matrices ($\boldsymbol{m}_{rp}^{a-inc}$) of the incompressible aerodynamic mass matrix ($\boldsymbol{M}_{a}^{inc}$) of dimension $5N \times 3N$

$$\boldsymbol{m}_{11}^{a-inc} = \sum_{i=1}^{17} \int_{L_i}^{L_{i+1}} \left(\pi \rho b_i^2 \boldsymbol{\Psi}_{v_0} \boldsymbol{\Psi}_{v_0}^T \right) dz, \qquad \boldsymbol{m}_{12}^{a-inc} = \sum_{i=1}^{17} \int_{L_i}^{L_{i+1}} \left(\pi \rho b_i^3 a_i \boldsymbol{\Psi}_{\phi} \boldsymbol{\Psi}_{v_0}^T \right) dz$$

$$\boldsymbol{m}_{21}^{a-inc} = \sum_{i=1}^{17} \int_{L_i}^{L_{i+1}} \left(\pi \rho b_i^3 a_i \boldsymbol{\Psi}_{\phi} \boldsymbol{\Psi}_{v_0}^T \right) dz, \qquad \boldsymbol{m}_{22}^{a-inc} = \sum_{i=1}^{17} \int_{L_i}^{L_{i+1}} \left(\pi \rho b_i^4 \left(\frac{1}{8} + a_i^2 \right) \boldsymbol{\Psi}_{\phi} \boldsymbol{\Psi}_{\phi}^T \right) dz$$

$$\boldsymbol{m}_{41}^{a-inc} = \sum_{i=1}^{17} \int_{L_i}^{L_{i+1}} \left(\boldsymbol{\Psi}_{v_0} \boldsymbol{\Psi}_{B_1}^T \right) dz, \qquad \boldsymbol{m}_{42}^{a-inc} = \sum_{i=1}^{17} \int_{L_i}^{L_{i+1}} -b_i (0.5 - a_i) \boldsymbol{\Psi}_{\phi} \boldsymbol{\Psi}_{B_1}^T dz$$

$$\boldsymbol{m}_{51}^{a-inc} = \sum_{i=1}^{17} \int_{L_i}^{L_{i+1}} \left(\boldsymbol{\Psi}_{v_0} \boldsymbol{\Psi}_{B_2}^T \right) dz, \qquad \boldsymbol{m}_{52}^{a-inc} = \sum_{i=1}^{17} \int_{L_i}^{L_{i+1}} -b_i (0.5 - a_i) \boldsymbol{\Psi}_{\phi} \boldsymbol{\Psi}_{B_2}^T dz$$

A4. The non-zero sub-matrices ($\boldsymbol{c}_{rp}^{a-inc}$) of the incompressible aerodynamic damping matrix ($\boldsymbol{C}_a^{inc}$) of dimension $5N \times 5N$

$$\boldsymbol{c}_{11}^{a-inc} = \sum_{i=1}^{17} \int_{L_i}^{L_{i+1}} C_{L\phi_i} \rho U_r b_i \boldsymbol{\Psi}_{v_0} \boldsymbol{\Psi}_{v_0}^T dz,$$

$$\boldsymbol{c}_{12}^{a-inc} = \sum_{i=1}^{17} \int_{L_i}^{L_{i+1}} \left(-\pi \rho b_i^2 U_r \boldsymbol{\Psi}_{\phi} \boldsymbol{\Psi}_{v_0}^T + C_{L\phi_i} \rho U_r b_i^2 \left(a_i - \frac{C_{L\phi_i}}{2\pi} + 0.5 \right) \boldsymbol{\Psi}_{\phi} \boldsymbol{\Psi}_{v_0}^T \right) dz$$

$$\boldsymbol{c}_{21}^{a-inc} = \sum_{i=1}^{17} \int_{L_i}^{L_{i+1}} C_{L\phi_i} \rho U_r b_i^2 \left(0.5 + a_i \right) \boldsymbol{\Psi}_{v_0} \boldsymbol{\Psi}_{\phi}^T dz$$

$$\boldsymbol{c}_{22}^{a-inc} = \sum_{i=1}^{17} \int_{L_i}^{L_{i+1}} \left(\begin{array}{l} \pi \rho b_i^3 U_r \left(\dfrac{C_{L\phi_i}}{2\pi} - 0.5 - a_i \right) \boldsymbol{\Psi}_{\phi} \boldsymbol{\Psi}_{\phi}^T + \\ C_{L\phi_i} \rho U_r b_i^3 (0.5 + a_i) \left(a_i - \dfrac{C_{L\phi_i}}{2\pi} + 0.5 \right) \boldsymbol{\Psi}_{\phi} \boldsymbol{\Psi}_{\phi}^T \end{array} \right) dz$$

$$\boldsymbol{c}_{42}^{a-inc} = \sum_{i=1}^{17} \int_{L_i}^{L_{i+1}} -U_r \boldsymbol{\Psi}_{\phi} \boldsymbol{\Psi}_{B_1}^T dz, \qquad \boldsymbol{c}_{44}^{a-inc} = \sum_{i=1}^{17} \int_{L_i}^{L_{i+1}} -\boldsymbol{\Psi}_{B_1} \boldsymbol{\Psi}_{B_1}^T dz$$

$$\boldsymbol{c}_{52}^{a-inc} = \sum_{i=1}^{17} \int_{L_i}^{L_{i+1}} -U_r \boldsymbol{\Psi}_{\phi} \boldsymbol{\Psi}_{B_2}^T dz, \qquad \boldsymbol{c}_{55}^{a-inc} = \sum_{i=1}^{17} \int_{L_i}^{L_{i+1}} -\boldsymbol{\Psi}_{B_2} \boldsymbol{\Psi}_{B_2}^T dz$$

where, U_r is the relative velocity $\left(U_r = \sqrt{U_i^2 + (z\Omega)^2}\right)$, U_i is the inflow velocity, Ω is the rotating speed, ρ is the air density, b is the half chord and a is the offset coefficient.

A5. The non-zero sub-matrices ($\boldsymbol{k}_{r,p}^{a-inc}$) of the incompressible aerodynamic stiffness matrix ($\boldsymbol{K}_a^{inc}$) of dimension $5N \times 5N$

$$\boldsymbol{k}_{12}^{a-inc} = \sum_{i=1}^{17} \int_{L_i}^{L_{i+1}} -C_{L\phi_i} \rho U_r^2 b_i \boldsymbol{\Psi}_\phi \boldsymbol{\Psi}_{v_0}^T dz, \quad \boldsymbol{k}_{14}^{a-inc} = \sum_{i=1}^{17} \int_{L_i}^{L_{i+1}} -C_{L\phi_i} \rho U_r b_i \alpha_1 \boldsymbol{\Psi}_{B_1} \boldsymbol{\Psi}_{v_0}^T dz$$

$$\boldsymbol{k}_{15}^{a-inc} = \sum_{i=1}^{17} \int_{L_i}^{L_{i+1}} -C_{L\phi_i} \rho U_r b_i \alpha_2 \boldsymbol{\Psi}_{B_2} \boldsymbol{\Psi}_{v_0}^T dz,$$

$$\boldsymbol{k}_{22}^{a-inc} = \sum_{i=1}^{17} \int_{L_i}^{L_{i+1}} -C_{L\phi_i} \rho U_r^2 b_i^2 (0.5 + a_i) \boldsymbol{\Psi}_\phi \boldsymbol{\Psi}_\phi^T dz$$

$$\boldsymbol{k}_{24}^{a-inc} = \sum_{i=1}^{17} \int_{L_i}^{L_{i+1}} -C_{L\phi_i} \rho U_r b_i^2 (0.5 + a_i) \alpha_1 \boldsymbol{\Psi}_{B_1} \boldsymbol{\Psi}_\phi^T dz$$

$$\boldsymbol{k}_{25}^{a-inc} = \sum_{i=1}^{17} \int_{L_i}^{L_{i+1}} -C_{L\phi_i} \rho U_r b_i^2 (0.5 + a_i) \alpha_2 \boldsymbol{\Psi}_{B_2} \boldsymbol{\Psi}_\phi^T dz$$

$$\boldsymbol{k}_{44}^{a-inc} = \sum_{i=1}^{17} \int_{L_i}^{L_{i+1}} -\beta_1 \frac{U_r}{b_i} \boldsymbol{\Psi}_{B_1} \boldsymbol{\Psi}_{B_1}^T dz, \qquad \boldsymbol{k}_{55}^{a-inc} = \sum_{i=1}^{17} \int_{L_i}^{L_{i+1}} -\beta_2 \frac{U_r}{b_i} \boldsymbol{\Psi}_{B_2} \boldsymbol{\Psi}_{B_2}^T dz$$

G2. Mass, Damping and Stiffness Matrices of the Beam-Blade Considering both Incompressible and Compressible Unsteady Aerodynamics

Figure G1 shows the schematic of the wind turbine blade studied including all the aerodynamic and structural parameters used in the formulation to calculate the flutter characteristics of wind turbine blades. It is assumed that for a length of l_a from the blade root, the blade is in the incompressible flow regime, and in the outboard portion of the blade, blade is in the compressible flow regime. In Figure G1, N_e^{inc} is the number of blade sections over which incompressible aerodynamics acts.

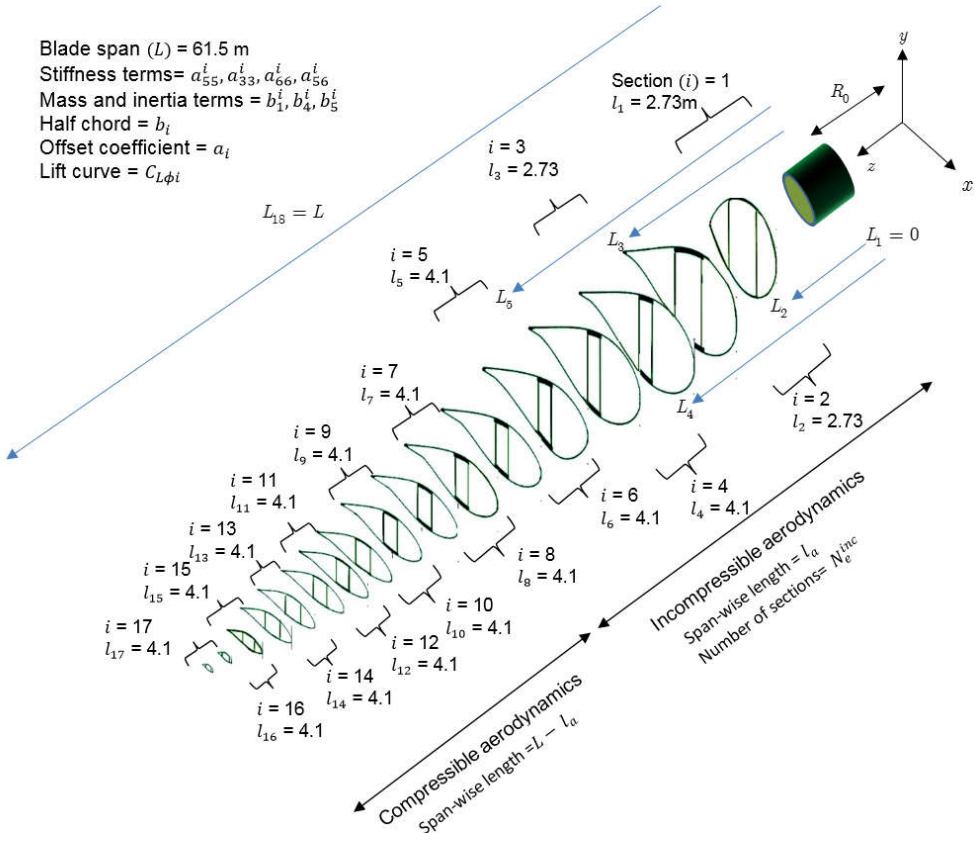

Figure G1. Wind turbine blade sections in the incompressible and compressible flow regime

B1. The non-zero sub-matrices ($\boldsymbol{m}_{rp}^{s}$) of the structural mass matrix ($\boldsymbol{M}_s$) of dimension $15N \times 3N$ and the non-zero sub-matrices ($\boldsymbol{k}_{rp}^{s}$) of the structural stiffness matrix ($\boldsymbol{K}_s$) of dimension $15N \times 5N$ are same as the incompressible case and they are given in items A1 and A2 in APPENDIX G1.

B2. The non-zero sub-matrices ($\boldsymbol{m}_{rp}^{a-t}$) of the total aerodynamic mass matrix ($\boldsymbol{M}_a^{total}$) of dimension $15N \times 3N$

$$\boldsymbol{m}_{11}^{a-t} = \sum_{i=1}^{N_e^{inc}} \int_{L_i}^{L_{i+1}} \left(\pi \rho b_i^2 \boldsymbol{\Psi}_{v_0} \boldsymbol{\Psi}_{v_0}^T \right) dz, \qquad \boldsymbol{m}_{12}^{a-t} = \sum_{i=1}^{N_e^{inc}} \int_{L_i}^{L_{i+1}} \left(\pi \rho b_i^3 a_i \boldsymbol{\Psi}_{\phi} \boldsymbol{\Psi}_{v_0}^T \right) dz$$

$$\boldsymbol{m}_{21}^{a-t} = \sum_{i=1}^{N_e^{inc}} \int_{L_i}^{L_{i+1}} \left(\pi \rho b_i^3 a_i \boldsymbol{\Psi}_{\phi} \boldsymbol{\Psi}_{v_0}^T \right) dz, \qquad \boldsymbol{m}_{22}^{a-t} = \sum_{i=1}^{N_e^{inc}} \int_{L_i}^{L_{i+1}} \left(\pi \rho b_i^4 \left(\frac{1}{8} + a_i^2 \right) \boldsymbol{\Psi}_{\phi} \boldsymbol{\Psi}_{\phi}^T \right) dz$$

$$\boldsymbol{m}_{41}^{a-t} = \sum_{i=1}^{N_e^{inc}} \int_{L_i}^{L_{i+1}} \boldsymbol{\Psi}_{v_0} \boldsymbol{\Psi}_{B_1}^T dz + \sum_{i=N_e^{inc}+1}^{17} \int_{L_i}^{L_{i+1}} \boldsymbol{\Psi}_{v_0} \boldsymbol{\Psi}_{B_{1c}}^T dz, \quad \boldsymbol{m}_{42}^{a-t} = \sum_{i=1}^{N_e^{inc}} \int_{L_i}^{L_{i+1}} -b_i (0.5 - a_i) \boldsymbol{\Psi}_{\phi} \boldsymbol{\Psi}_{B_1}^T dz$$

$$\boldsymbol{m}_{51}^{a-t} = \sum_{i=1}^{N_e^{inc}} \int_{L_i}^{L_{i+1}} \boldsymbol{\Psi}_{v_0} \boldsymbol{\Psi}_{B_2}^T dz + \sum_{i=N_e^{inc}+1}^{17} \int_{L_i}^{L_{i+1}} \boldsymbol{\Psi}_{v_0} \boldsymbol{\Psi}_{B_{2c}}^T dz, \quad \boldsymbol{m}_{52}^{a-t} = \sum_{i=1}^{N_e^{inc}} \int_{L_i}^{L_{i+1}} -b_i (0.5 - a_i) \boldsymbol{\Psi}_{\phi} \boldsymbol{\Psi}_{B_2}^T dz$$

$$\boldsymbol{m}_{61}^{a-t} = \sum_{i=N_e^{inc}+1}^{17} \int_{L_i}^{L_{i+1}} \boldsymbol{\Psi}_{v_0} \boldsymbol{\Psi}_{B_{3c}}^T dz$$

$$m_{72}^{a-t} = \sum_{i=N_e^{inc}+1}^{17} \int_{L_i}^{L_{i+1}} \boldsymbol{\Psi}_{\phi} \boldsymbol{\Psi}_{B_{1cq}}^T dz, \quad m_{82}^{a-t} = \sum_{i=N_e^{inc}+1}^{17} \int_{L_i}^{L_{i+1}} \boldsymbol{\Psi}_{\phi} \boldsymbol{\Psi}_{B_{2cq}}^T dz, \quad m_{92}^{a-t} = \sum_{i=N_e^{inc}+1}^{17} \int_{L_i}^{L_{i+1}} \boldsymbol{\Psi}_{\phi} \boldsymbol{\Psi}_{B_{3cq}}^T dz$$

$$m_{10,1}^{a-t} = \sum_{i=N_e^{inc}+1}^{17} \int_{L_i}^{L_{i+1}} \boldsymbol{\Psi}_{v_0} \boldsymbol{\Psi}_{B_{1cM}}^T dz, \quad m_{11,1}^{a-t} = \sum_{i=N_e^{inc}+1}^{17} \int_{L_i}^{L_{i+1}} \boldsymbol{\Psi}_{v_0} \boldsymbol{\Psi}_{B_{2cM}}^T dz, \quad m_{12,1}^{a-t} = \sum_{i=N_e^{inc}+1}^{17} \int_{L_i}^{L_{i+1}} \boldsymbol{\Psi}_{v_0} \boldsymbol{\Psi}_{B_{3cM}}^T dz$$

$$m_{13,2}^{a-t} = \sum_{i=N_e^{inc}+1}^{17} \int_{L_i}^{L_{i+1}} \boldsymbol{\Psi}_{\phi} \boldsymbol{\Psi}_{B_{1cMq}}^T dz, \quad m_{14,2}^{a-t} = \sum_{i=N_e^{inc}+1}^{17} \int_{L_i}^{L_{i+1}} \boldsymbol{\Psi}_{\phi} \boldsymbol{\Psi}_{B_{2cMq}}^T dz, \quad m_{15,2}^{a-t} = \sum_{i=N_e^{inc}+1}^{17} \int_{L_i}^{L_{i+1}} \boldsymbol{\Psi}_{\phi} \boldsymbol{\Psi}_{B_{3cMq}}^T dz$$

B3. The non-zero sub-matrices ($\boldsymbol{c}_{rp}^{a-t}$) of the total aerodynamic damping matrix ($\boldsymbol{C}_a^{total}$) of dimension $15N \times 15N$

$$
\begin{aligned}
\boldsymbol{c}_{11}^{a-t} &= \sum_{i=1}^{N_e^{inc}} \int_{L_i}^{L_{i+1}} C_{L\phi_i} \rho U_r b_i \boldsymbol{\Psi}_{v_0} \boldsymbol{\Psi}_{v_0}^T dz + \sum_{i=N_e^{inc}+1}^{17} \int_{L_i}^{L_{i+1}} C_{L\phi_i} \rho U_r b_i \overline{\alpha}_{0c} \boldsymbol{\Psi}_{v_0} \boldsymbol{\Psi}_{v_0}^T dz, \\
\boldsymbol{c}_{12}^{a-t} &= \sum_{i=1}^{N_e^{inc}} \int_{L_i}^{L_{i+1}} \left(-\pi \rho b_i^2 U_r \boldsymbol{\Psi}_\phi \boldsymbol{\Psi}_{v_0}^T + C_{L\phi_i} \rho U_r b_i^2 \left(a_i - \frac{C_{L\phi_i}}{2\pi} + 0.5 \right) \boldsymbol{\Psi}_\phi \boldsymbol{\Psi}_{v_0}^T \right) dz + \\
&\quad \sum_{i=N_e^{inc}+1}^{17} \int_{L_i}^{L_{i+1}} -2 C_{L\phi_i} \rho U_r b_i^2 \overline{\alpha}_{0cq} \boldsymbol{\Psi}_\phi \boldsymbol{\Psi}_{v_0}^T dz \\
\boldsymbol{c}_{21}^{a-t} &= \sum_{i=1}^{N_e^{inc}} \int_{L_i}^{L_{i+1}} C_{L\phi_i} \rho U_r b_i^2 \left(0.5 + a_i \right) \boldsymbol{\Psi}_{v_0} \boldsymbol{\Psi}_\phi^T dz + \sum_{i=N_e^{inc}+1}^{17} \int_{L_i}^{L_{i+1}} 2 C_{L\phi_i} \rho U_r b_i^2 \overline{\alpha}_{0cM} \boldsymbol{\Psi}_{v_0} \boldsymbol{\Psi}_\phi^T dz, \\
\boldsymbol{c}_{22}^{a-t} &= \sum_{i=1}^{N_e^{inc}} \int_{L_i}^{L_{i+1}} \begin{pmatrix} \pi \rho b_i^3 U_r \left(\dfrac{C_{L\phi_i}}{2\pi} - 0.5 - a_i \right) \boldsymbol{\Psi}_\phi \boldsymbol{\Psi}_\phi^T + \\ C_{L\phi_i} \rho U_r b_i^3 (0.5 + a_i) \left(a_i - \dfrac{C_{L\phi_i}}{2\pi} + 0.5 \right) \boldsymbol{\Psi}_\phi \boldsymbol{\Psi}_\phi^T \end{pmatrix} dz + \\
&\quad \sum_{i=N_e^{inc}+1}^{17} \int_{L_i}^{L_{i+1}} -4 C_{L\phi_i} \rho U_r b_i^3 \overline{\alpha}_{0cMq} \boldsymbol{\Psi}_\phi \boldsymbol{\Psi}_\phi^T dz
\end{aligned}
$$

$$
\begin{aligned}
\boldsymbol{c}_{42}^{a-t} &= \sum_{i=1}^{N_e^{inc}} \int_{L_i}^{L_{i+1}} -U_r \boldsymbol{\Psi}_\phi \boldsymbol{\Psi}_{B_1}^T dz + \sum_{i=N_e^{inc}+1}^{17} \int_{L_i}^{L_{i+1}} -U_r \boldsymbol{\Psi}_\phi \boldsymbol{\Psi}_{B_{1c}}^T dz, \\
\boldsymbol{c}_{44}^{a-t} &= \sum_{i=1}^{N_e^{inc}} \int_{L_i}^{L_{i+1}} -\boldsymbol{\Psi}_{B_1} \boldsymbol{\Psi}_{B_1}^T dz + \sum_{i=N_e^{inc}+1}^{17} \int_{L_i}^{L_{i+1}} -\boldsymbol{\Psi}_{B_{1c}} \boldsymbol{\Psi}_{B_{1c}}^T dz, \\
\boldsymbol{c}_{52}^{a-t} &= \sum_{i=1}^{N_e^{inc}} \int_{L_i}^{L_{i+1}} -U_r \boldsymbol{\Psi}_\phi \boldsymbol{\Psi}_{B_2}^T dz + \sum_{i=N_e^{inc}+1}^{17} \int_{L_i}^{L_{i+1}} -U_r \boldsymbol{\Psi}_\phi \boldsymbol{\Psi}_{B_{2c}}^T dz \\
\boldsymbol{c}_{55}^{a-t} &= \sum_{i=1}^{N_e^{inc}} \int_{L_i}^{L_{i+1}} -\boldsymbol{\Psi}_{B_2} \boldsymbol{\Psi}_{B_2}^T dz + \sum_{i=N_e^{inc}+1}^{17} \int_{L_i}^{L_{i+1}} -\boldsymbol{\Psi}_{B_{2c}} \boldsymbol{\Psi}_{B_{2c}}^T dz, \\
\boldsymbol{c}_{62}^{a-t} &= \sum_{i=N_e^{inc}+1}^{17} \int_{L_i}^{L_{i+1}} -U_r \boldsymbol{\Psi}_\phi \boldsymbol{\Psi}_{B_{3c}}^T dz, \quad \boldsymbol{c}_{66}^{a-t} = \sum_{i=N_e^{inc}+1}^{17} \int_{L_i}^{L_{i+1}} -\boldsymbol{\Psi}_{B_{3c}} \boldsymbol{\Psi}_{B_{3c}}^T dz \\
\boldsymbol{c}_{77}^{a-t} &= \sum_{i=N_e^{inc}+1}^{17} \int_{L_i}^{L_{i+1}} -\boldsymbol{\Psi}_{B_{1cq}} \boldsymbol{\Psi}_{B_{1cq}}^T dz, \quad \boldsymbol{c}_{88}^{a-t} = \sum_{i=N_e^{inc}+1}^{17} \int_{L_i}^{L_{i+1}} -\boldsymbol{\Psi}_{B_{2cq}} \boldsymbol{\Psi}_{B_{2cq}}^T dz, \quad \boldsymbol{c}_{99}^{a-t} = \sum_{i=N_e^{inc}+1}^{17} \int_{L_i}^{L_{i+1}} -\boldsymbol{\Psi}_{B_{3cq}} \boldsymbol{\Psi}_{B_{3cq}}^T dz \\
\boldsymbol{c}_{10,2}^{a-t} &= \sum_{i=N_e^{inc}+1}^{17} \int_{L_i}^{L_{i+1}} -U_r \boldsymbol{\Psi}_\phi \boldsymbol{\Psi}_{B_{1cM}}^T dz, \quad \boldsymbol{c}_{10,10}^{a-t} = \sum_{i=N_e^{inc}+1}^{17} \int_{L_i}^{L_{i+1}} -\boldsymbol{\Psi}_{B_{1cM}} \boldsymbol{\Psi}_{B_{1cM}}^T dz, \quad \boldsymbol{c}_{11,2}^{a-t} = \sum_{i=N_e^{inc}+1}^{17} \int_{L_i}^{L_{i+1}} -U_r \boldsymbol{\Psi}_\phi \boldsymbol{\Psi}_{B_{2cM}}^T dz \\
\boldsymbol{c}_{11,11}^{a-t} &= \sum_{i=N_e^{inc}+1}^{17} \int_{L_i}^{L_{i+1}} -\boldsymbol{\Psi}_{B_{2cM}} \boldsymbol{\Psi}_{B_{2cM}}^T dz, \quad \boldsymbol{c}_{12,2}^{a-t} = \sum_{i=N_e^{inc}+1}^{17} \int_{L_i}^{L_{i+1}} -U_r \boldsymbol{\Psi}_\phi \boldsymbol{\Psi}_{B_{3cM}}^T dz, \quad \boldsymbol{c}_{12,12}^{a-t} = \sum_{i=N_e^{inc}+1}^{17} \int_{L_i}^{L_{i+1}} -\boldsymbol{\Psi}_{B_{3cM}} \boldsymbol{\Psi}_{B_{3cM}}^T dz \\
\boldsymbol{c}_{13,13}^{a-t} &= \sum_{i=N_e^{inc}+1}^{17} \int_{L_i}^{L_{i+1}} -\boldsymbol{\Psi}_{B_{1cMq}} \boldsymbol{\Psi}_{B_{1cMq}}^T dz, \quad \boldsymbol{c}_{14,14}^{a-t} = \sum_{i=N_e^{inc}+1}^{17} \int_{L_i}^{L_{i+1}} -\boldsymbol{\Psi}_{B_{2cMq}} \boldsymbol{\Psi}_{B_{2cMq}}^T dz, \quad \boldsymbol{c}_{15,15}^{a-t} = \sum_{i=N_e^{inc}+1}^{17} \int_{L_i}^{L_{i+1}} -\boldsymbol{\Psi}_{B_{3cMq}} \boldsymbol{\Psi}_{B_{3cMq}}^T dz
\end{aligned}
$$

B4. The non-zero sub-matrices ($\boldsymbol{k}_{r,p}^{a-t}$) of the total aerodynamic stiffness matrix ($\boldsymbol{K}_a^{total}$) of dimension $15N \times 15N$

$$\boldsymbol{k}_{12}^{a-t} = \sum_{i=1}^{N_e^{inc}} \int_{L_i}^{L_{i+1}} -C_{L\phi_i} \rho U_r^2 b_i \boldsymbol{\Psi}_\phi \boldsymbol{\Psi}_{v_0}^T dz + \sum_{i=N_e^{inc}+1}^{17} \int_{L_i}^{L_{i+1}} -C_{L\phi_i} \rho U_r^2 b_i \overline{\alpha}_{0c} \boldsymbol{\Psi}_\phi \boldsymbol{\Psi}_{v_0}^T dz,$$

$$\boldsymbol{k}_{14}^{a-t} = \sum_{i=1}^{N_e^{inc}} \int_{L_i}^{L_{i+1}} -C_{L\phi_i} \rho U_r b_i \alpha_1 \boldsymbol{\Psi}_{B_1} \boldsymbol{\Psi}_{v_0}^T dz + \sum_{i=N_e^{inc}+1}^{17} \int_{L_i}^{L_{i+1}} -C_{L\phi_i} \rho U_r b_i \overline{\alpha}_{1c} \boldsymbol{\Psi}_{B_{1c}} \boldsymbol{\Psi}_{v_0}^T dz$$

$$\boldsymbol{k}_{15}^{a-t} = \sum_{i=1}^{N_e^{inc}} \int_{L_i}^{L_{i+1}} -C_{L\phi_i} \rho U_r b_i \alpha_2 \boldsymbol{\Psi}_{B_2} \boldsymbol{\Psi}_{v_0}^T dz + \sum_{i=N_e^{inc}+1}^{17} \int_{L_i}^{L_{i+1}} -C_{L\phi_i} \rho U_r b_i \overline{\alpha}_{2c} \boldsymbol{\Psi}_{B_{2c}} \boldsymbol{\Psi}_{v_0}^T dz,$$

$$\boldsymbol{k}_{16}^{a-t} = \sum_{i=N_e^{inc}+1}^{17} \int_{L_i}^{L_{i+1}} -C_{L\phi_i} \rho U_r b_i \overline{\alpha}_{3c} \boldsymbol{\Psi}_{B_{3c}} \boldsymbol{\Psi}_{v_0}^T dz, \quad \boldsymbol{k}_{17}^{a-t} = \sum_{i=N_e^{inc}+1}^{17} \int_{L_i}^{L_{i+1}} 2C_{L\phi_i} \rho U_r b_i^2 \overline{\alpha}_{1cq} \boldsymbol{\Psi}_{B_{1cq}} \boldsymbol{\Psi}_{v_0}^T dz,$$

$$\boldsymbol{k}_{18}^{a-t} = \sum_{i=N_e^{inc}+1}^{17} \int_{L_i}^{L_{i+1}} 2C_{L\phi_i} \rho U_r b_i^2 \overline{\alpha}_{2cq} \boldsymbol{\Psi}_{B_{2cq}} \boldsymbol{\Psi}_{v_0}^T dz, \quad \boldsymbol{k}_{19}^{a-t} = \sum_{i=N_e^{inc}+1}^{17} \int_{L_i}^{L_{i+1}} 2C_{L\phi_i} \rho U_r b_i^2 \overline{\alpha}_{3cq} \boldsymbol{\Psi}_{B_{3cq}} \boldsymbol{\Psi}_{v_0}^T dz$$

$$\boldsymbol{k}_{22}^{a-t} = \sum_{i=1}^{N_e^{inc}} \int_{L_i}^{L_{i+1}} -C_{L\phi_i} \rho U_r^2 b_i^2 (0.5 + a_i) \boldsymbol{\Psi}_\phi \boldsymbol{\Psi}_\phi^T dz + \sum_{i=N_e^{inc}+1}^{17} \int_{L_i}^{L_{i+1}} -2C_{L\phi_i} \rho U_r^2 b_i^2 \overline{\alpha}_{0cM} \boldsymbol{\Psi}_\phi \boldsymbol{\Psi}_\phi^T dz,$$

$$\boldsymbol{k}_{24}^{a-t} = \sum_{i=1}^{N_e^{inc}} \int_{L_i}^{L_{i+1}} -C_{L\phi_i} \rho U_r b_i^2 (0.5 + a_i) \alpha_1 \boldsymbol{\Psi}_{B_1} \boldsymbol{\Psi}_\phi^T dz, \quad \boldsymbol{k}_{25}^{a-t} = \sum_{i=1}^{N_e^{inc}} \int_{L_i}^{L_{i+1}} -C_{L\phi_i} \rho U_r b_i^2 (0.5 + a_i) \alpha_2 \boldsymbol{\Psi}_{B_2} \boldsymbol{\Psi}_\phi^T dz$$

$$\boldsymbol{k}^{a-t}_{2,10} = \sum_{i=N^{inc}_e+1}^{17} \int_{L_i}^{L_{i+1}} -2C_{L\phi_i}\rho U_r b_i^2 \overline{\alpha}_{1cM} \boldsymbol{\Psi}_{B_{1cM}} \boldsymbol{\Psi}^T_{\phi} dz, \quad \boldsymbol{k}^{a-t}_{2,11} = \sum_{i=N^{inc}_e+1}^{17} \int_{L_i}^{L_{i+1}} -2C_{L\phi_i}\rho U_r b_i^2 \overline{\alpha}_{2cM} \boldsymbol{\Psi}_{B_{2cM}} \boldsymbol{\Psi}^T_{\phi} dz,$$

$$\boldsymbol{k}^{a-t}_{2,12} = \sum_{i=N^{inc}_e+1}^{17} \int_{L_i}^{L_{i+1}} -2C_{L\phi_i}\rho U_r b_i^2 \overline{\alpha}_{3cM} \boldsymbol{\Psi}_{B_{3cM}} \boldsymbol{\Psi}^T_{\phi} dz, \quad \boldsymbol{k}^{a-t}_{2,13} = \sum_{i=N^{inc}_e+1}^{17} \int_{L_i}^{L_{i+1}} 4C_{L\phi_i}\rho U_r b_i^3 \overline{\alpha}_{1cMq} \boldsymbol{\Psi}_{B_{1cMq}} \boldsymbol{\Psi}^T_{\phi} dz,$$

$$\boldsymbol{k}^{a-t}_{2,14} = \sum_{i=N^{inc}_e+1}^{17} \int_{L_i}^{L_{i+1}} 4C_{L\phi_i}\rho U_r b_i^3 \overline{\alpha}_{2cMq} \boldsymbol{\Psi}_{B_{2cMq}} \boldsymbol{\Psi}^T_{\phi} dz, \quad \boldsymbol{k}^{a-t}_{2,15} = \sum_{i=N^{inc}_e+1}^{17} \int_{L_i}^{L_{i+1}} 4C_{L\phi_i}\rho U_r b_i^3 \overline{\alpha}_{3cMq} \boldsymbol{\Psi}_{B_{3cMq}} \boldsymbol{\Psi}^T_{\phi} dz,$$

$$\boldsymbol{k}^{a-t}_{44} = \sum_{i=1}^{N^{inc}_e} \int_{L_i}^{L_{i+1}} -\beta_1 \frac{U_r}{b_i} \boldsymbol{\Psi}_{B_1} \boldsymbol{\Psi}^T_{B_1} dz + \sum_{i=N^{inc}_e+1}^{17} \int_{L_i}^{L_{i+1}} -\beta_1 \frac{U_r}{b_i} \boldsymbol{\Psi}_{B_{1c}} \boldsymbol{\Psi}^T_{B_{1c}} dz,$$

$$\boldsymbol{k}^{a-t}_{55} = \sum_{i=1}^{N^{inc}_e} \int_{L_i}^{L_{i+1}} -\beta_2 \frac{U_r}{b_i} \boldsymbol{\Psi}_{B_2} \boldsymbol{\Psi}^T_{B_2} dz + \sum_{i=1}^{17} \int_{L_i}^{L_{i+1}} -\beta_2 \frac{U_r}{b_i} \boldsymbol{\Psi}_{B_{2c}} \boldsymbol{\Psi}^T_{B_{2c}} dz$$

$$\boldsymbol{k}^{a-t}_{66} = \sum_{i=N^{inc}_e+1}^{17} \int_{L_i}^{L_{i+1}} -\beta_3 \frac{U_r}{b_i} \boldsymbol{\Psi}_{B_{3c}} \boldsymbol{\Psi}^T_{B_{3c}} dz, \quad \boldsymbol{k}^{a-t}_{77} = \sum_{i=N^{inc}_e+1}^{17} \int_{L_i}^{L_{i+1}} -\beta_1 \frac{U_r}{b_i} \boldsymbol{\Psi}_{B_{1cq}} \boldsymbol{\Psi}^T_{B_{1cq}} dz$$

$$\boldsymbol{k}^{a-t}_{88} = \sum_{i=N^{inc}_e+1}^{17} \int_{L_i}^{L_{i+1}} -\beta_2 \frac{U_r}{b_i} \boldsymbol{\Psi}_{B_{2cq}} \boldsymbol{\Psi}^T_{B_{2cq}} dz, \quad \boldsymbol{k}^{a-t}_{99} = \sum_{i=N^{inc}_e+1}^{17} \int_{L_i}^{L_{i+1}} -\beta_3 \frac{U_r}{b_i} \boldsymbol{\Psi}_{B_{3cq}} \boldsymbol{\Psi}^T_{B_{3cq}} dz$$

$$\boldsymbol{k}^{a-t}_{10,10} = \sum_{i=N^{inc}_e+1}^{17} \int_{L_i}^{L_{i+1}} -\beta_1 \frac{U_r}{b_i} \boldsymbol{\Psi}_{B_{1cM}} \boldsymbol{\Psi}^T_{B_{1cM}} dz, \quad \boldsymbol{k}^{a-t}_{11,11} = \sum_{i=N^{inc}_e+1}^{17} \int_{L_i}^{L_{i+1}} -\beta_2 \frac{U_r}{b_i} \boldsymbol{\Psi}_{B_{2cM}} \boldsymbol{\Psi}^T_{B_{2cM}} dz$$

$$\boldsymbol{k}^{a-t}_{12,12} = \sum_{i=N^{inc}_e+1}^{17} \int_{L_i}^{L_{i+1}} -\beta_3 \frac{U_r}{b_i} \boldsymbol{\Psi}_{B_{3cM}} \boldsymbol{\Psi}^T_{B_{3cM}} dz, \quad \boldsymbol{k}^{a-t}_{13,13} = \sum_{i=N^{inc}_e+1}^{17} \int_{L_i}^{L_{i+1}} -\beta_1 \frac{U_r}{b_i} \boldsymbol{\Psi}_{B_{1cMq}} \boldsymbol{\Psi}^T_{B_{1cMq}} dz$$

$$\boldsymbol{k}^{a-t}_{14,14} = \sum_{i=N^{inc}_e+1}^{17} \int_{L_i}^{L_{i+1}} -\beta_2 \frac{U_r}{b_i} \boldsymbol{\Psi}_{B_{2cMq}} \boldsymbol{\Psi}^T_{B_{2cMq}} dz, \quad \boldsymbol{k}^{a-t}_{15,15} = \sum_{i=N^{inc}_e+1}^{17} \int_{L_i}^{L_{i+1}} -\beta_3 \frac{U_r}{b_i} \boldsymbol{\Psi}_{B_{3cMq}} \boldsymbol{\Psi}^T_{B_{3cMq}} dz$$